

# Waveguides in Large Bandgap Materials for Lasers and Quantum Photonics

A thesis presented in fulfilment of the requirements for the degree of Doctor of Philosophy



By

Loyd James M<sup>c</sup>Knight

2012

# Declaration of Authenticity

---

This thesis is the result of the author's original research. It has been composed by the author and has not been previously submitted for examination which has led to the award of a degree.

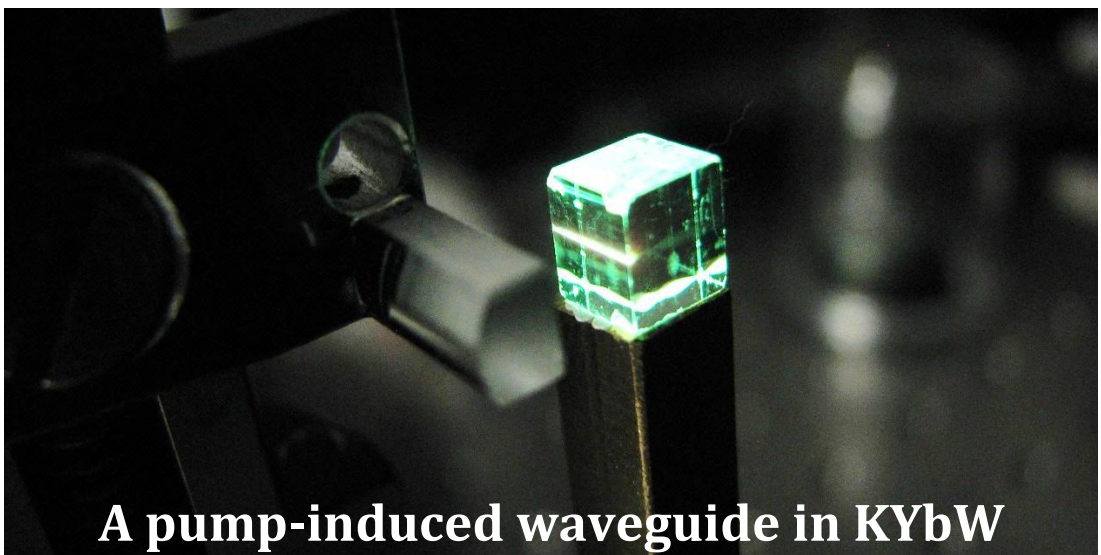
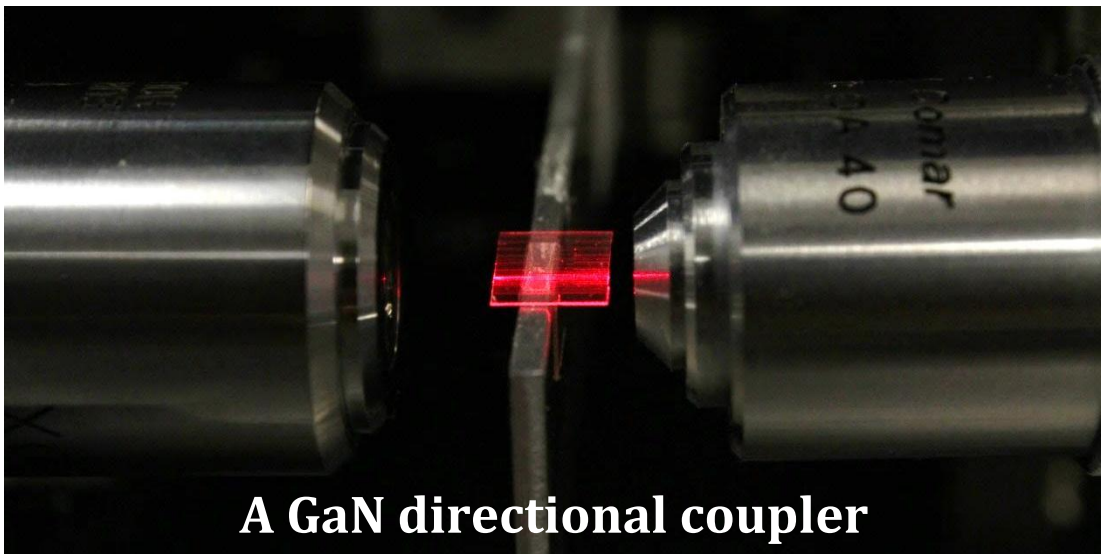
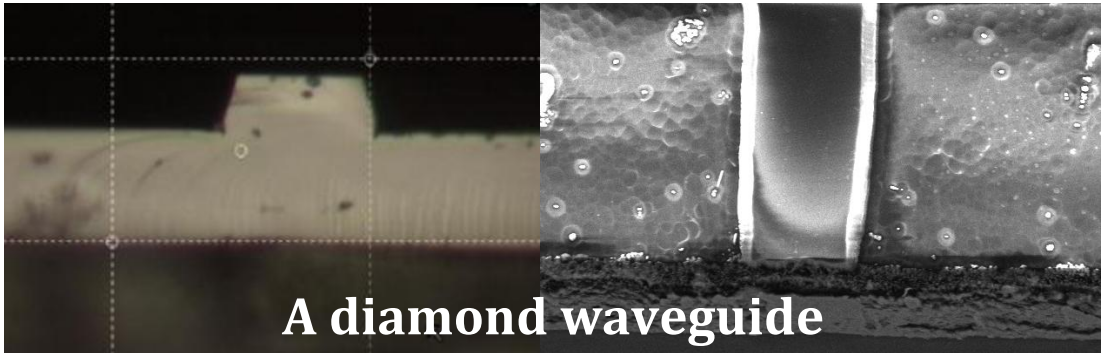
The copyright of this thesis belongs to the author under the terms of the United Kingdom Copyright Acts as qualified by University of Strathclyde Regulation 3.50. Due acknowledgement must always be made of the use of any material contained in, or derived from, this thesis.

Signed:

Date:

# Frontispiece

---



# Abstract

---

The spatial confinement of light with a waveguide offers the possibility for improved performance of many optical devices including lasers and nonlinear frequency converters. Furthermore, waveguide devices may be combined together to increase functionality reliably, in a field known as integrated optics. One application that may benefit from integration is quantum photonics: working with single photons for quantum logic.

The work presented in this thesis studies the development of waveguides for these aforementioned applications in three materials for which few waveguide devices have been previously reported: diamond, gallium nitride (GaN) and stoichiometric potassium ytterbium double tungstate (KYbW). Each material platform offers properties that are highly suited to the selected photonics application.

Diamond is a suitable material for quantum photonics and as a Raman laser gain material. A large-cross-sectional-area diamond rib waveguide has been designed, fabricated and characterised optically. Diamond waveguides of varying cross-section are considered for a Raman waveguide laser. A fully analytical model is developed incorporating scattering losses to optimise the design of such a laser system.

GaN has a range of material properties that are suited to the application of integrated quantum photonics. A directional coupler was designed and optimised for a small footprint with contact lithography. Devices were fabricated and optically characterised including for propagation loss. Two-photon interference was measured within a GaN directional coupler highlighting the suitability for quantum photonics.

KYbW is an atypical laser gain material with very high  $\text{Yb}^{3+}$  concentrations. The short absorption-length at a wavelength of 980 nm has been used in combination with a high nonlinear polarisability to form an optically-induced waveguide. Mode profiles have been characterised and transient analysis has been carried out at 633 nm. This pump-induced waveguide is used within a laser cavity to create laser action at 1080 nm, using the pumped region of the crystal to define the stability.

# Table of Contents

---

Frontispiece .....	iii
Abstract .....	iv
Technical Preliminaries .....	viii

<b>Chapter 1: Introduction</b> .....	1
1.1 Waveguides and integrated optics.....	1
1.1.1 Waveguide geometries and fabrication techniques.....	4
1.2 Thesis motivation and objectives.....	7
1.3 Waveguide lasers and nonlinear devices .....	8
1.3.1 Threshold reduction.....	9
1.3.2 Slope efficiency .....	10
1.3.3 Thermal management.....	11
1.3.4 Nonlinear frequency conversion.....	12
1.3.5 Raman waveguide lasers .....	13
1.4 Integrated quantum photonics.....	16
1.4.1 Sources and detectors.....	17
1.5 Diamond photonics: towards waveguides.....	20
1.5.1 Diamond waveguides and fabrication methods .....	21
1.5.2 Diamond N-V single-photon source.....	23
1.5.3 Diamond Raman lasers.....	24
1.6 GaN photonics: towards waveguides.....	25
1.6.1 GaN waveguide devices and applications.....	26
1.6.2 GaN for integrated quantum optics.....	27
1.7 KYbW for guided laser operation.....	29
1.8 Thesis outline.....	32
References .....	33

<b>Chapter 2: Theory and Modelling of Waveguides</b> .....	41
Abstract.....	41
2.1 Waveguide fundamental theory.....	41
2.1.1 Transverse resonance condition .....	42
2.1.2 Polarisation states and boundary conditions .....	49
2.1.3 Marcatili's analytical approximation for planar waveguides.....	49
2.1.4 Planar waveguide single-mode criteria.....	52
2.1.5 2D approximation with planar waveguide solutions .....	54
2.2 The rib waveguide – a single material waveguide .....	55
2.2.1 The effective index method .....	56
2.2.2 The single-mode criteria of the rib waveguide .....	58
2.2.3 Marcatili's method for rib waveguides .....	61
2.3 The four-layer waveguide.....	63
2.3.1 Rib waveguides.....	65
2.4 Computational methods .....	67
2.4.1 Finite element method (FEM) .....	67
2.4.2 Beam propagation Method .....	71
2.5 Hybrid polarisation modes and linear approximations.....	77
2.6 Comparison of methods .....	80
2.7 Conclusions.....	82
References .....	83

<b>Chapter 3: Diamond Waveguides</b> .....	85
Abstract.....	85
Preliminaries .....	85
3.1 Large area waveguide design.....	85
3.1.1 Useful waveguide criteria.....	86
3.1.2 Single-mode requirements .....	90
3.2 Large area diamond rib waveguides.....	92
3.2.1 Sample and design.....	92
3.2.2 Fabrication .....	93
3.2.3 Optical characterisation.....	98
3.3 Analytical scattering loss theory.....	101
3.4 Diamond Raman waveguide analysis .....	106
3.4.1 Coupled equations.....	106
3.4.2 Analytical solution for a Raman laser including the Lambert function.....	109
3.4.3 Variation with roughness and comparison to bulk .....	113
3.5 Conclusions.....	116
References .....	117
<b>Chapter 4: Gallium Nitride Waveguides</b> .....	121
Abstract.....	121
Preliminaries .....	121
4.1 Circuit design .....	121
4.1.1 Straight waveguide design.....	121
4.1.2 Directional coupler theory.....	122
4.1.3 Minimum bend radii .....	124
4.1.4 Directional coupler design.....	125
4.1.5 Tapers and length minimisation .....	127
4.2 Fabrication.....	130
4.2.1 GaN material growth.....	130
4.2.2 Waveguide definition.....	131
4.3 Optical characterisation .....	133
4.3.1 Mode profiling.....	133
4.3.2 Directional coupler splitting ratios .....	135
4.3.3 Propagation loss.....	137
4.3.4 Two-mode waveguide .....	145
4.4 Two-Photon quantum interference.....	147
4.4.1 The Hong-Ou-Mandel (HOM) effect.....	147
4.4.2 Experimental setup.....	149
4.5 Conclusions.....	151
References .....	153

<b>Chapter 5: Guiding and Laser Operation in KYbW</b> .....	156
Abstract.....	156
Preliminaries .....	156
5.1 Optically-induced guiding effects.....	156
5.1.1 Gain guiding .....	157
5.1.2 Thermal guiding.....	158
5.1.3 Electronic guiding.....	159
5.1.4 Guiding effects in KYbW .....	160
5.2 Gain-free guiding at 633 nm.....	163
5.2.1 Experimental setup.....	163
5.2.2 Guided mode analysis .....	166
5.2.3 Time-resolved guiding analysis.....	170
5.3 Laser operation.....	175
5.3.1 Fibre pumped system .....	175
5.3.2 Laser performance .....	176
5.3.3 Transverse cavity modes and temporal stability .....	180
5.3.4 Curved mirror cavity.....	182
5.3.5 Thermal analysis.....	185
5.4 Conclusions.....	187
References .....	188
<b>Chapter 6: Summary and Future Perspectives</b> .....	191
6.1 Summary.....	191
6.1.1 Theory and waveguide design; throughout thesis.....	191
6.1.2 Diamond devices; Chapter 3 .....	192
6.1.3 Analytical modelling of a diamond Raman waveguide laser; Chapter 3.....	192
6.1.4 GaN devices; Chapter 4.....	193
6.1.5 KYbW; Chapter 5.....	194
6.2 Future perspectives .....	195
6.2.1 Diamond and GaN for integrated quantum optics .....	195
6.2.2 Diamond and GaN nonlinear waveguide devices.....	196
6.2.3 Novel guiding techniques for laser operation.....	197
References .....	198
Appendix A Colour map scale.....	199
Appendix B Chapter 3, Equation 3.16 .....	200
Appendix C Jack-knife error analysis .....	201
Abbreviations.....	202
Publications .....	203
Acknowledgements .....	205

# Technical Preliminaries

---

## **a) Technical acknowledgements**

A full acknowledgement for people at the Institute of Photonics, University of Strathclyde, is available at the end of this thesis.

Yanfeng Zhang was involved in all the fabrication work presented in this thesis. Her skills and fabrication knowledge allowed for the successful demonstration of waveguide devices in diamond and GaN. This includes SEM images taken at the Physics department at the University of Strathclyde.

Erman Engin, Mark Thompson and the group at the Centre for Quantum Photonics, University of Bristol assisted with the experimental single-photon and focused ion beam milling work. Erman's technical knowledge and equipment skills were a great asset for the short time the author was in Bristol.

## **b) Technical points of note**

This thesis is intended to be read and printed in colour. There are a number of graphs that are only legible in colour; to cope with multiple functions in a visually pleasing way. The electronic colour version is widely available online through the University of Strathclyde library or directly from the author.

Throughout this thesis the guided mode is referred to in terms of the effective index. Readers may multiply this number by the free space angular wavenumber to obtain the guided mode propagation constant.

At the time of writing the Raman gain values in diamond are being measured in a precise manner within the Institute of Photonics. The diamond Raman waveguide laser analysis method described in Chapter 3 can take into account these new values in future work.

# Chapter 1

## Introduction

---

### 1.1 Waveguides and integrated optics

An optical waveguide is a physical structure that spatially confines and guides light. This is typically achieved by an increase in refractive index relative to the surroundings. Through the use of optical confinement, a wide array of photonic devices may be realised in micron-sized structures within an optically transparent material. The performance and functionality of these devices may be enhanced by optical confinement. New photonics properties and applications may be obtained through use of waveguides. Furthermore, these devices may be joined together to offer additional functionality by forming an integrated optical circuit.

Integrated optics was first introduced and summarised as a distinct field of research in 1969 by S. E. Miller [1]. The abstract is reproduced here as a point of reference:

*“This paper outlines a proposal for a miniature form of laser beam circuitry. Index of refraction changes of the order of  $10^{-2}$  or  $10^{-3}$  in a substrate such as glass allow guided laser beams of width near 10 microns. Photolithographic techniques may permit simultaneous construction of complex circuit patterns. This paper also indicates possible miniature forms for a laser, modulator, and hybrids. If realised this new art would facilitate isolating the laser circuit assembly from thermal, mechanical, and acoustic ambient changes through small overall size; economy should ultimately result.”*

The concept of waveguides, waveguide lasers, directional couplers, phase modulators, wavelength selective filters and fabrication and integration methods were all outlined in this concise paper. This paper summarised work by some of the founders of the field including E. A. J. Marcatili, D. Marcuse, P. K. Tien, R. Ulrich, H. Kogelnik and A. Yariv. At that time intercontinental fibre networks and diode lasers at room temperature did not exist. The underlying theory for many integrated optical devices was defined over the following couple of decades. It took some time for technology to catch up and realise a number of low-loss on-chip devices.

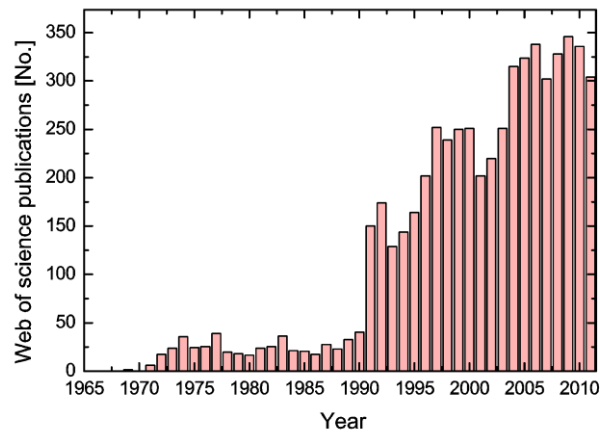


Figure 1. 1: Number of publications per year in the Thomson Reuters' Web of Science database with the term 'integrated optics' in the topic.

The internet revolution in the 1990s, with the aid of low-loss optical fibre, brought with it the desire to respond with integrated optics. Many start-up companies in this area were created and subsequently struggled through a lack of commercial demand. The predicted commercial revolution did not then take place. However, a number of successfully demonstrated systems now exist in a range of materials, of which many have commercial applications. Forty years after the initial proposal optical waveguides and the prospect of integration continue to offer functionality benefits and an increasing range of applications to the field of photonics.

Figure 1. 1 shows a list of publications with the term 'integrated optics' in the topic. The sudden rise in publications from the '90s may represent the response to the communication and internet boom, and subsequent production of low-loss integrated optical devices in a range of materials. Additionally, there is a large amount of research relating to optical waveguides that does not classify itself as 'integrated optics' because there is no intention to integrate with other devices on the same chip. Single devices such as some waveguide lasers, filters and sensors use the waveguide geometry to offer enhanced performance or sensitivity without the intention for integration.

The major near-future and commercial application of integrated optics lies with replacing electronic interconnects between processors in computing with optical analogues. Recently, there has been a change in personal computer architectures caused by the minimum feature size limitation of transistors and heat extraction problems. Personal computers now use as standard four or more processors, a trend that cannot continue unless interconnects are replaced with optical analogues. As a consequence there has been a recent concentrated effort in silicon-based photonics to

achieve this goal, and related applications, to integrate with the existing silicon based microelectronics industry [2, 3].

Other than optical communication or integration with the microelectronics industry, integrated optics and constituent devices have a very large range of applications. Almost all free-space bulk optical components have an on-chip analogue that may offer improved performance or enhanced functionality. Additionally, there are many areas of photonics where device functionality can only be achieved with use of a waveguide. Some key areas of interest are highlighted below, but this is by no means a comprehensive review:

Waveguide sensors use properties of the waveguide to increase sensitivity including refractive index changes or waveguide resonators. Applications include biosensors, chemical sensors and trace-gas sensors.

Waveguides may be used for optical modulation. Fundamental modulating components can use the properties of waveguides to control and/or measure a number of optical properties including optical power, frequency, polarisation or phase. Such components can be integrated into controllable optical switches and routers for spatial control and port selection.

Waveguide-based lasers and nonlinear frequency converters use properties of waveguides to enhance performance and offer integration potential. Many materials may only offer efficient nonlinear conversion with use of a waveguide for intensity enhancement for extended distances or for phase controlling properties. A detailed discussion on this topic is presented in Section 1.3.

More recently, waveguides have also found applications in the field of quantum photonics. Quantum photonics applications include; quantum communication, quantum metrology and quantum computation. These applications rely on single photon sources, single-photon detectors and circuitry that may all be implemented within an integrated circuit. A more detailed discussion on this topic is presented Section 1.4.

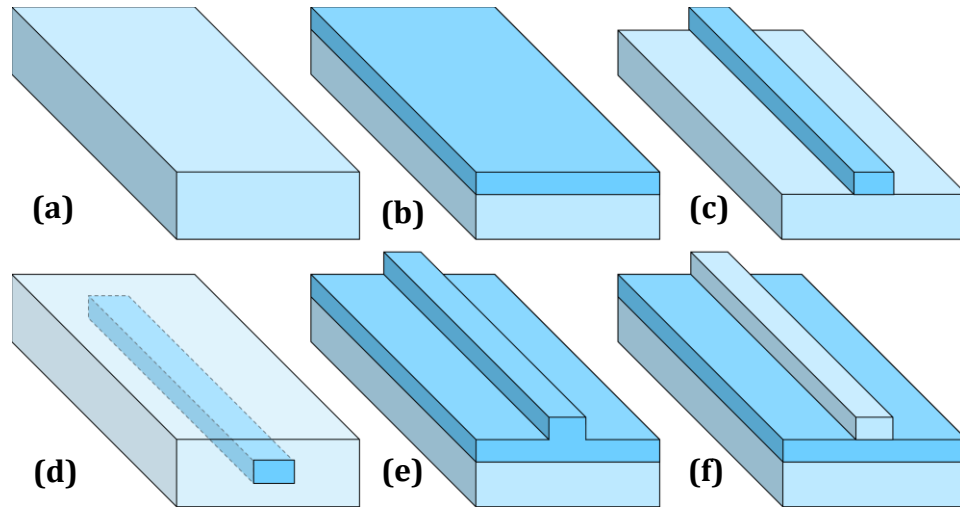


Figure 1. 2: 3D schematic of **(a)** bulk sample, **(b)** planar waveguide, **(c)** surface channel waveguide, **(d)** buried channel waveguide, **(e)** rib waveguide and **(f)** strip-loaded waveguide where the top layer may have a higher or lower refractive index than the middle layer. Dark blue represents a higher refractive index than light blue.

### 1.1.1 Waveguide geometries and fabrication techniques

One-dimensional optical confinement is referred to as a planar waveguide and two-dimensional confinement is referred to as a channel waveguide. The work in this thesis focuses on channel waveguides, however, planar waveguides are still very attractive for a range of applications. Channel waveguide fabrication often involves forming a planar waveguide first and lateral confinement may then be added using a different fabrication method. Alternatively, the channel waveguide may be formed with no prior definition of a planar waveguide with a 3D fabrication technique.

Figure 1. 2 shows 3D schematics of some representative planar and channel waveguide designs. Chapter 2 progresses from these designs to describe requirements for electromagnetic confinement. There is also a range of speciality waveguide geometries that include photonic crystal waveguides, slot waveguides, plasmonics, hollow-core waveguides and Bragg-mirror waveguides. Each of these waveguide geometries are suitable for different application areas, but will not be discussed at length in this thesis.

There is a wide array of waveguide fabrication techniques that may be used, each with different limitations and benefits. This section does not attempt to fully review the field and some detailed review papers are available on the topic [4, 5]. Table 1. 1 shows some fabrication techniques that are either well-established or relevant to the work presented in this thesis. Fabrication techniques may be categorised into those that form

waveguides through material growth, through physical structuring (removal) of the material or modification of the refractive index (positively or negatively).

It is difficult to concisely compare these techniques as the particular merits and short comings relate to the material in question, the required dimensions and the required functionality. A particular fabrication technique is selected based on the applicability to the material of interest and the ability to produce a functional device. Optimal device performance is usually achieved with low propagation-loss and the possibility for efficient integration with other devices. For commercial applications, the economics of the fabrication procedure is of utmost concern.

From Table 1. 1 it is clear that defining the waveguide during the growth process can produce high quality low-loss waveguides. However, the applicability of this technique relies on finding materials that are lattice- and thermal-matched whilst offering a refractive index change high enough to form a waveguide. Furthermore, a specialised and sometimes expensive growth facility is required. These techniques are thus limited to a few material systems.

Refractive index modification techniques are well-established and can be applied to a large range of materials to form planar or channel (with a mask) waveguides. Ion implantation [6] is suitable for many materials but often results in high propagation loss. Ion exchange [7] and metal indiffusion are some of the most established waveguide fabrication techniques but are limited in the range of suitable materials.

Mechanical structuring techniques (polishing and saws) have been used to fabricate waveguides with low losses. This is a flexible technique, however only a few devices have successfully been demonstrated, requiring high skill and suitable equipment. Similarly focused ion beam (FIB) milling may be used to structure waveguides in many materials but typically with high loss and this approach is only suitable for speciality applications like photonic crystals.

Laser waveguide writing through inducing stress or damage [8] is suitable for a range of materials although cannot achieve high refractive index changes required for some small footprint devices. Photosensitive waveguide formation is restricted to particular material systems [9].

Table 1. 1: Typical waveguide fabrication methods, including suitable materials, low loss fabrication example and comments. Abbreviated terms include; Plan. – planar, Lat. – lateral, struct. – structural changes, mod. – refractive index modification, Geom – geometry and chan. – channel.

<b>Fabrication Method</b>	<b>Category</b>	<b>Typical/Suitable Materials</b>	<b>Loss [dB/cm]</b>	<b>Geom.</b>	<b>Comments</b>
Liquid phase epitaxy	Plan. Growth	Garnates, double tungstates	0.05 [10]	Plan.	Limited materials
Pulsed laser deposition	Plan. Growth	Glasses, garnates, sapphire	0.10 [11]	Plan.	Low crystalline quality, impurity losses
Chemical vapour deposition	Plan. Growth	Glasses, oxides, III-V, diamond	0.01 [12]	Plan.	High quality, toxic precursors
Sputtering	Plan. Growth	III-V, sapphire	0.11 [13]	Plan.	Limited materials, impurity losses
Polishing/Saw	Plan./Lat. struc.	Any, Lithium niobate, diamond...	0.50 [14]	Rib	Fabrication skill or roughness losses
Sacrificial layer	Plan. struc.	III-V, diamond	2.20 [15]	Chan.	Limited materials, scattering losses
Ion implantation	Plan./Lat. mod.	Any, sapphire, diamond...	1.00 [16]	Chan.	$\Delta N \propto$ loss, damage & impurity losses
Ion exchange	Plan./Lat. mod.	Phosphates, silicates, borosilicates	0.10 [17]	Chan.	$\Delta N \propto$ loss, impurity loss, limited materials
Ion indiffusion	Plan./Lat. mod.	Ti&Zn ions, sapphire, lithium niobate	0.10 [18]	Chan.	$\Delta N \propto$ loss, impurity loss, limited materials
Laser writing	3D mod.	Glasses, double tungstates, garnates...	0.20 [19]	Chan.	Positive $\Delta N$ or stress variants, damage losses
Photosensitive writing	3D mod.	Silica, glasses	0.20 [20]	Chan.	Limited materials, good for Bragg gratings
Focused ion beam milling	3D struc.	Any, diamond, GaN...	High [21]	Chan.	Short lengths, scattering & impurity losses
Dry etching (RIE, ICP)	Lat. struc.	Sapphire, diamond, hard-crystals	0.10 [22]	Rib	Large vertical etch depths, low loss
Wet etching	Lat. struc.	Glasses, non-hard-crystals	0.30 [23]	Rib	Limited materials, used for sacrificial layers
Ion beam etching	Lat. struc.	Any, Sapphire, III-V, silicon...	0.20 [24]	Rib	Roughness & impurity losses

Reactive ion etching (RIE), inductively coupled plasma reactive ion etching (ICP-RIE) or wet etching may be used to define a structure laterally in the material and thus turn a planar waveguide into a channel waveguide. These techniques may be used in conjunction with photolithography to define integrated circuits in a parallel manner.

The fabrication techniques used in this work include polishing, ICP-RIE and chemical vapour deposition. The fabrication processes are outlined in the respective experimental chapters: Chapters 3 and 4. A more detailed discussion of the fabrication processes used in this work is available in the thesis of Y. Zhang [25].

## 1.2 Thesis motivation and objectives

The work presented in this thesis has a broad scope, considering novel optical waveguide materials for current and emerging photonics applications. The photonics applications include linear lasers and nonlinear Raman laser systems, and quantum information processing. The materials systems are diamond, gallium nitride (GaN) and potassium ytterbium double tungstate (KYbW).

The use of optical waveguides for lasers and nonlinear converters is well-established. However, this is still a topic of current and prospective research due to increased fabrication capabilities and an extended range of suitable materials of optical quality. Integrated quantum photonics is a new area of research that holds potential for performing quantum logic and metrology. Diamond, GaN and KYbW are all materials for which very few or no waveguide devices have been demonstrated. Table 1. 2 highlights the suitability these materials for the aforementioned photonics applications and shows applications which are considered in greater detail in this thesis.

Table 1. 2: Photonics applications and materials considered in thesis. Small green tick represents modest suitability whereas the large green tick represents a high level of suitability.

Application	Diamond Chapter 3		GaN Chapter 4		KYbW Chapter 5	
	Suitable	In thesis	Suitable	In thesis	Suitable	In thesis
Linear lasers	✓		✓		✓	✓
Single photon sources	✓		✓			
Quantum logic circuits	✓		✓	✓		
Raman lasers	✓	✓			✓	

The goals of this project are to design, demonstrate and characterise waveguides in each of these material systems and furthermore to consider or demonstrate the suitability of these waveguide devices to the highlighted photonics application areas. This will include a number of research topics that are not known to have been reported previously:

- Diamond for a Raman waveguide laser
- GaN as a material for integrated quantum photonics
- Pump-induced waveguides (in KYbW) for laser operation

Optical waveguide theory, design and modelling formed a significant component of the work and is presented in Chapter 2. The rest of this chapter will focus on the motivation for waveguides in the application areas of lasers and nonlinear devices (Section 1.3) and quantum photonics (Section 1.4). Furthermore, the motivation for waveguides in diamond (Section 1.5), GaN (Section 1.6), and KYbW (Section 0) with a focus on the highlighted application areas.

### 1.3 Waveguide lasers and nonlinear devices

Waveguide lasers have been a sustained area of research since the first demonstration in 1961 with a neodymium doped glass rod [26]. Waveguide lasers are usually divided into two separate strands; those for high power operation or those for integration and increased functionality, although there is usually some overlap. This work concentrates on the use of waveguide lasers in novel materials for integration and functionality.

High-power laser operation has included using gas as the waveguide and gain material which has produced some of the highest power (multi-kW) laser systems, using CO<sub>2</sub> [27]. The slab laser geometry has enabled the development of high power lasers in a range of gain materials, notably Nd:YAG, by allowing thermal control and heat extraction [28] and has enabled kW output powers [29].

Alternatively, separate to high power operation, waveguide lasers have been demonstrated in a range of materials. Recently, a number of impressive waveguide laser results have been reported that offer advantages over bulk systems including improved performance and the possibility for integration. A number of detailed review papers summarise these recent results and include the use of Lithium niobate [18], Ti:sapphire [30], double-tungstates [31] or a more general overview [4, 5, 32].

Table 1. 3: A list of motivations and potential benefits of the waveguide laser geometry and their origin.

Motivation/Benefit	Origin/Cause
Threshold reduction	Larger gain for longer lengths compared to bulk
Slope efficiency improvement	Better pump/signal overlap compared to bulk
Thermal management	Large area/volume ratio and strong guiding
Nonlinear enhancement	Larger gain for longer lengths compared to bulk
Increased functionality	Integration with other on-chip devices
Miniaturisation	Compact alignment-free systems

There are a large range of motivations for fabricating waveguide lasers or nonlinear devices some of which are summarised in Table 1. 3 and then discussed further in Sections 1.3.1 to 1.3.5. These discussions focus on some of the major applications that are well-established and some that relate to this work. There is a large range of waveguide laser and nonlinear device applications not listed here that are beyond the scope of this thesis.

### 1.3.1 Threshold reduction

Threshold reduction is most advantageous for gain materials which typically exhibit high threshold in bulk (guide-free) laser systems. Reduction in threshold can offer higher output powers with the same pump source; providing greater power conversion efficiencies. Higher power conversion efficiencies may then allow the use of cheaper or more compact pump sources. Materials with high reabsorption typically exhibit high thresholds; this includes most 3-level laser gain materials.

A threshold comparison between bulk and waveguide geometries can be made by considering the diffraction of a Gaussian beam optimised for minimum volume in a crystal [33]:

$$w_0 = \sqrt{\frac{\lambda l}{2\sqrt{3}\pi n}}, \quad \bar{w} = \sqrt{\frac{\lambda l}{\sqrt{3}\pi n}} \tag{1.1}$$

Where  $w_0$  is the waist radius of the volume minimised beam,  $\bar{w}$  is the average beam radius throughout the crystal,  $\lambda$  is the wavelength,  $l$  is the length of the crystal and  $n$  is the refractive index.

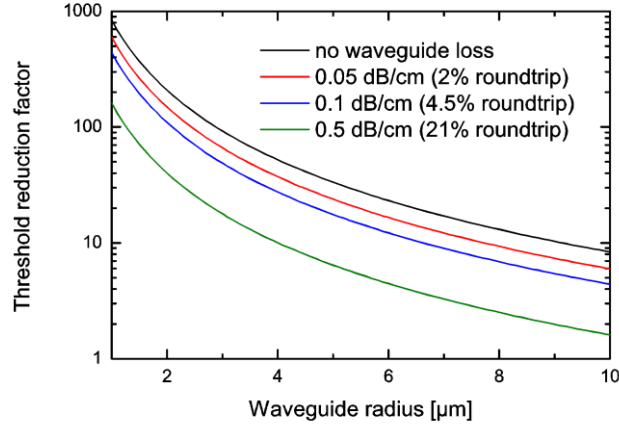


Figure 1. 3: The threshold reduction factor for a Ti:sapphire waveguide laser calculated with Equation (1.2) with  $l=1$  cm,  $\lambda=800$  nm,  $n=1.76$ ,  $T=1\%$  and  $L_b=4\%$  for varying propagation loss and waveguide radius.

The threshold reduction factor for a circular waveguide compared to bulk is then [4]:

$$\frac{P_{th\_b}}{P_{th\_w}} = \frac{l\lambda}{\sqrt{3}\pi n w_w^2} \frac{L_b + T}{L_b + L_w + T} \quad (1.2)$$

Where  $L_b$  is the bulk loss,  $L_w$  is the additional waveguide loss and  $T$  is the output coupler's transmission. The difference in overlap between pump and signal modes are ignored for simplicity here. From Equation (1.2) it can be seen that significant threshold reduction can be achieved for systems that have high bulk loss values and/or if the waveguide propagation loss is of a similar magnitude to or less than the output coupler's transmission and bulk-roundtrip loss.

Ti:Sapphire is a widely used laser gain material that suffers from re-absorption due to unwanted  $Ti^{4+}$  ions and typically requires argon-ion high-power-density green-emitting pump sources leading to relatively low wall-plug efficiency systems. Reduction of threshold may allow for a more efficient laser operation and allow the use of cheaper and more efficient laser diodes as pump sources. Figure 1. 3 shows the possible reduction in threshold for a Ti:sapphire laser with various parameters.

### 1.3.2 Slope efficiency

The laser slope efficiency has the prospect to be improved compared to bulk alternatives with use of a waveguide. This is possible due to the improved overlap between pump and signal (laser) beams. The optimum overlap of perfect Gaussian free-space beams will always be limited by their wavelength difference to roughly  $\lambda_p/\lambda_s$ . For  $Yb^{3+}$  tungstate systems this may be as high as 95% but for Ti:sapphire systems may be as low as 50%. Furthermore, nonlinear conversion may produce beams with large differences in wavelength for which bulk systems can no longer maintain an adequate overlap.

Mode overlaps for certain waveguide designs may be greater than 99% for large wavelength differences providing significant improvement. In order to produce good overlap within bulk systems, high pump beam quality is required and careful alignment must be employed, in some cases preventing the use of low beam quality diode pump lasers. The waveguide system can produce near unity overlap with no strict alignment tolerances other than coupling. In practice, many reported waveguide laser systems do not offer improvement in slope efficiency due to the increased propagation loss. In nonlinear converters however, the improvement in overlap is sometimes key to operational efficiency.

### 1.3.3 Thermal management

Improved thermal management in waveguide lasers has allowed for high power operation – larger than unguided bulk alternatives. High power operation is typically limited in bulk systems due to thermally-induced refractive index changes within the cavity referred to as thermal lensing. These thermal lens effects may be reduced by removing heat from the system. This can be achieved by increasing the surface to volume ratio of the pumped region. The slab waveguide laser system and thin-disk laser system both utilise this effect and are shown in Figure 1.4 a) and c). Slab and planar waveguide lasers are often  $\sim 10 \mu\text{m}$  thick, offering very large surface to volume ratios. It is also useful to bond high thermally conductive materials close to the pump region to extract heat to remove thermal gradients. This method is commonly used in thin-disk lasers [34, 35].

One important aspect of thermal management of slab/planar waveguide lasers is the dominance of the fabricated waveguide refractive index change over thermal index gradients. The cavity design is based on the dimensions of the waveguide, which are fixed with temperature. For free standing waveguides, the refractive index step is defined by the refractive index of the material, which is  $\Delta N \sim 1.8$  for YAG systems. This refractive index step is much larger than any thermal gradients and thus thermal effects offer minimal distortion to the cavity. Furthermore, the pump is absorbed in a uniform manner due to the distribution of the pump by the waveguide modes. This creates uniform refractive index gradients throughout the waveguide.

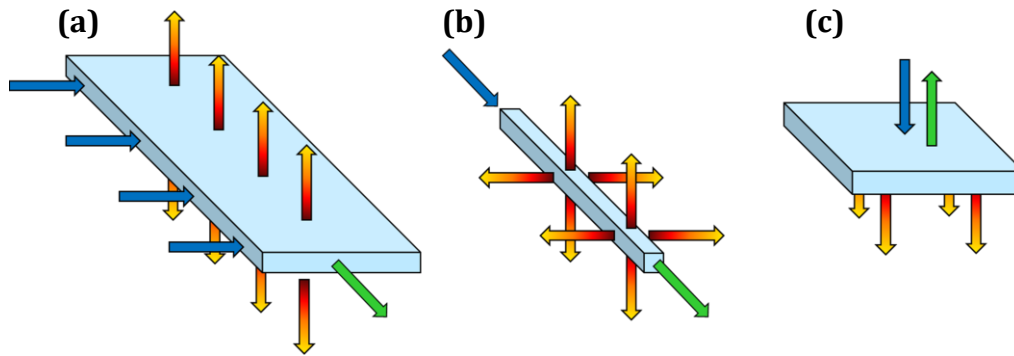


Figure 1. 4: Schematic of **(a)** Side (edge) pumped slab waveguide laser, **(b)** longitudinally pumped channel waveguide laser and **(c)** thin disk laser geometry. Red/yellow represents heat flow, blue represents pump direction and green represents laser output direction.

The channel waveguide laser geometry, shown in Figure 1. 4 b), does not offer the same improvement in surface to volume aspect ratio compared to bulk systems as does the planar waveguide. However, utilising strong refractive index guiding allows for an increase in cavity thermal stability. This is achieved with some ‘cane’ or ‘rod’ laser systems where the cavity is defined by the waveguide effects rather than a free-space cavity which would otherwise be subject to thermal refractive index gradients.

### 1.3.4 Nonlinear frequency conversion

Waveguides find important applications in the field of nonlinear frequency conversion [36]. This can be subdivided into  $\chi^{(2)}$  processes including doubling, sum and difference frequency conversion and  $\chi^{(3)}$  processes including Raman conversion and four-wave mixing. Raman conversion is discussed in Section 1.3.5 due to the relevance to work in this thesis.

Efficient nonlinear frequency conversion usually requires resonant enhancement with use of an optical cavity. Typically a nonlinear crystal which exhibits a high  $\chi^{(2)}$  is inserted within a laser or external cavity in order to achieve efficient frequency conversion. With the use of a waveguide, the threshold for conversion may be reduced, the efficiency at which conversion takes place may be enhanced and phase-matching control with use of a waveguide can be introduced to achieve nonlinear frequency conversion where it may otherwise not be possible.

Nonlinear effects have a strong intensity dependence which can be enhanced over long distances with the use of a waveguide. For bulk systems the  $\chi^{(2)}$  conversion efficiency can be considered to depend inversely on the spot size (area) because conversion will only occur within a small region around the focus spot within the Rayleigh range. This has been shown to be optimal when the spot size =  $\lambda/2n$  [4]. The efficiency can be described more concisely in a waveguide due to the constant beam profile and is known to be inversely

proportional to the waveguide mode area. By comparing these two efficiencies an improvement factor can be defined and is shown in equation (1.3):

$$\frac{\eta_w}{\eta_b} \propto \frac{\lambda l}{2n\pi w_w^2} \quad (1.3)$$

where terms have been described previously. Equation (1.3) is very close to equation (1.2), and thus produces a similar enhancement factor. A long length and small-cross section waveguide may easily offer several thousand times higher conversion efficiency than bulk alternatives. A similar, although more thorough, procedure for Raman resonators is described Chapter 3.

Results in periodically poled lithium niobate [37] have shown efficient doubling, sum and difference frequency conversion, and this is considered the benchmark material for nonlinear  $\chi^{(2)}$  processes in waveguides. The use of waveguides to enhance nonlinear processes has allowed efficient conversion in a range of materials and the necessity for high  $\chi^{(2)}$  coefficients is reduced. The range of frequency conversion is generally only restricted by the transparency range of the material. Nonlinear frequency conversion was originally limited to niobates, tantalates and potassium titanyl phosphate materials [38] but has now been demonstrated with waveguides in a range of materials including GaAs [39] and polymers [40].

There is an extensive range of nonlinear applications in waveguides. Supercontinuum generation consists of a combination of nonlinear effects that have only been possible due to tight confinement offered by photonic crystals and tapered fibres [41, 42]. Waveguide based optical parametric oscillators take advantage of a  $\chi^{(2)}$  nonlinear enhancement in the waveguide. Using dispersion control of the waveguide, phase matching can be achieved [43]. Frequency comb generation can be achieved with broadband phase matching in a waveguide resonator.

### **1.3.5 Raman waveguide lasers**

The Raman effect describes light interaction with vibrational modes within a material [44, 45]. When these vibrational modes are excited with a laser beam, new scattered light is produced, shifted from the original frequency due to the generation of an optical phonon. Two types of scattered light can be produced; that with a lower energy known as Stokes scattering and that with a higher energy known as anti-Stokes scattering. The Stokes scattering is many magnitudes more intense than the anti-Stokes. This effect is different to other third-order scattering processes such as Brillouin scattering, which is related to acoustic phonons and Rayleigh scattering which is not accompanied by a frequency shift.

Raman scattering may be stimulated, much like in a linear laser system, resulting in coherent emission and efficient transfer of energy from the pump beam to the Stokes beam. As with all stimulated emission processes; amplifiers or lasers may be developed exploiting stimulated Raman scattering. By using the Raman effect, laser sources can be produced with a range of materials without the requirement for doping. A range of new wavelength sources can thus be produced anywhere in the transparency range of the material, dependent only on the availability of pump sources and material quality.

The Raman gain coefficient is particularly low compared with the gain of typical linear laser systems and results in thresholds that are higher. To achieve laser operation, Raman active crystals are usually placed in high quality optical cavities to reduce threshold. The crystal length is usually selected to be long to increase the conversion efficiency, and preferably the pump quality is very high with a small line-width. Pulsed pumping is often employed to further enhance the pump intensity.

A range of materials are suitable for efficient Raman conversion. There is a disparity between reported values of Raman gain for several of these materials as it is dependent on wavelength, polarisation, pump direction, linewidth and temporal characteristics. For an accurate comparison between materials it is best to compare results from the same author. The materials with the some of the highest reported Raman gains are shown in Table 1. 4.

Bulk Raman lasers have been demonstrated in a range of materials and cavity geometries [46, 47]. There are a number of recent noteworthy Raman laser results reported in diamond which are discussed in Section 1.5.3.

Table 1. 4: Raman shift and Raman gain of common high gain crystalline materials. Silica fibre is shown for comparison.

<b>Material</b>	<b>Raman Shift [cm<sup>-1</sup>]</b>	<b>Measured gain [cm/GW] at wavelength [nm]</b>
Diamond	1333	21 at 1064 [48]
Ba(NO <sub>3</sub> ) <sub>2</sub>	1049	8.5 at 1064 [49]
KG(WO <sub>4</sub> ) <sub>2</sub>	768/901	5.7 at 1064 [48], 3.5 at 1064 [49]
KY(WO <sub>4</sub> ) <sub>2</sub>	767/906	5.1 at 1064 [49]
Silicon	517	7.5 at 1536 nm [50]
Silica	400	10 <sup>-2</sup> at 526 nm [51]

Every material produces Raman scattering with a characteristic frequency shift, hence it is a technique used widely in spectroscopy to identify materials. Raman spectroscopy techniques are routinely carried out with thin films, taking advantage of the confinement of the Stokes field with the waveguide effect to enhance the signal intensity. Fibre Raman lasers and converters take advantage of the long length and low loss of optical fibre, even though the gain in such fibre is typically very low compared to many crystalline materials.

A recent significant result has been the demonstration of the silicon Raman waveguide laser which highlights a number of advantages offered by the waveguide geometry [50, 52]. In one design [50], the cross-sectional area has been reduced to a very small mode size of 2.6  $\mu\text{m}^2$  which is near the diffraction limit. The length of the waveguide has been maximised with respect to area with use of an S-bend to 4.8 cm. Silicon suffers badly from two-photon absorption loss which acts to dramatically increase threshold. This is reduced with use of an electric field across the waveguide reducing threshold and increasing efficiency by significant factors. Such a system allows integration with other devices, with the scope for integration with the microelectronics industry, and would be difficult to implement in bulk Silicon. Raman cascading has been shown to provide additional laser wavelengths in Silicon [53].

Ring resonators with high Q values may be used to generate Raman lasers in materials with low Raman gains. Silica microspheres with Q values in excess of  $10^9$  offer  $\mu\text{W}$  Raman laser thresholds [54]. Microtoroid silica Raman lasers offer the possibility for integration on chip [55]. High Q CaF<sub>2</sub> rings have also been used to demonstrate Raman laser operation [56]. The fabrication of high quality resonators will enable a range of materials to be used to produce Raman waveguide lasers without the requirement for high Raman gain.

## 1.4 Integrated quantum photonics

Current classical computer systems are based on encoding 1's and 0's to electrical signals through the use of transistors. Quantum computational processes are based on encoding information to qubits, the quantum analogue of the bit, which through quantum mechanics is allowed to be in a superposition of both 1 and 0. For a system with  $n$  qubits the superposition state is considered to be in  $2^n$  states simultaneously. This allows a unique style of parallel processing that is not possible with classical computing. Peter Shor famously developed algorithms that allowed the factorisation of large numbers with quantum computing [57]. As a consequence there is a large amount of recent research activity in the field of quantum computing. Many governments and private companies are particularly interested in cryptanalysis and efficient database searching only made possible with quantum based logic.

There are many architectures to implement quantum logic circuits including using trapped ions, nuclear magnetic resonance, quantum dots in solids, superconductors and photons [58]. The use of photons for qubits is believed by many to be the most promising architecture due to the long coherence time of the photon and their suitability for quantum key distribution and communication over long distances [58]. Qubits can be encoded on the polarisation state of the photon. Unlike other quantum information architectures however, photon-photon interactions are difficult to obtain making communication between qubits problematic. A nonlinearity is required to cause reversible phase changes between photons and even with cavity enhancement this is difficult.

In 2001 Knill et al. [59, 60] showed that all-optical quantum logic could be performed with linear devices such as beam splitters. This important breakthrough for quantum optics allowed for the possibility of photon-based quantum logic without the requirement for a nonlinearity. This led to a number of experimental demonstrations of quantum logic in bulk systems [61-63].

Integrated optics provides an alternative platform for quantum logic and allows for many linear devices to be connected together on-chip to dramatically reduce the alignment and stability requirements the system [64]. The directional coupler is used as a direct waveguide analogue to a beam splitter as depicted in Figure 1. 5 a). Integrated optics allows for an alternative qubit encoding system to polarisation, called path encoding. Using integrated optics it is possible to accurately control the path length of the different arms using Mach-Zehnder-like phase changing devices. Similar accurate path length control is difficult to obtain with bulk optics. The qubit is encoded on an uncoupled pair of waveguides which is also known as the 'dual rail' representation [65]. A photon in one arm

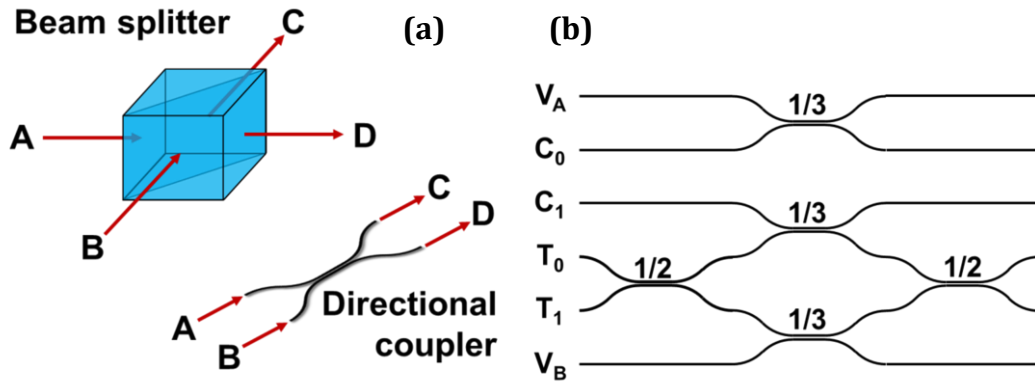


Figure 1. 5: **(a)** Schematic of a beam splitter and directional coupler showing the similarity of the device functionality. **(b)** Schematic of a C-NOT path encoded integrated quantum photonics circuit made up from 1/3 and 1/2 power splitting directional couplers.

of the waveguide indicates a qubit  $|1\rangle$  state and a photon on the other arm of the waveguide indicates a qubit  $|0\rangle$ . An arbitrary single photon qubit state is then the superposition of these states:  $|\psi\rangle = a|0\rangle + b|1\rangle$ , where  $|a|^2$  and  $|b|^2$  represent the probabilities of finding a photon in each arm and  $|a|^2 + |b|^2 = 1$ .

Integrated quantum optics was first demonstrated experimentally by Politi et al. in 2008 [66]. Since then there have been demonstrations of different systems including circuits in silica-on-silicon [67-69] including Shor’s algorithm [70] and different material systems including glass [71], lithium niobate [72], silicon [73] and in this work GaN [74].

An elementary quantum circuit, the controlled NOT gate, is shown in Figure 1. 5 b) using the path encoding system. The controlled NOT gate operates by switching the target state  $T$  only when the control state  $C$  is in state  $|1\rangle$ . The control state is defined such that  $C$  is in state  $|0\rangle$  when a photon is present in path  $C_0$  and in state  $|1\rangle$  a photon is present in path  $C_1$ . The target state  $T$  is defined in the same manner. When  $C$  is in state  $|0\rangle$ , state  $T$  remains unaffected with the photons exciting along the same path. When  $C$  is in state  $|1\rangle$  interference occurs at the central beam splitter to alter the output state of  $T$ .

#### 1.4.1 Sources and detectors

In order to carry out quantum information processing with photons, a source of high quality single-photons is required [75]. These photons are required to be indistinguishable with precisely the same frequency and a correlated polarisation state. The source is required to have a high repetition rate and be able to be coupled into the processing circuit with high efficiency – for this work a waveguide. Another key factor is noise limitation – the prevention of multi-photon emission, which could act to reduce the quality of the measurement. Spectral filtering may be applied to isolate the photon(s) of interest and improve the quality of the single-photon sources. Deterministic single-photons based

on single-emitter sources may take advantage of an optical cavity to further enhance their quality and improve collection through the Purcell effect.

Single ions/atoms may be isolated and trapped to be used as single-photon sources. To achieve efficient operation the atom may be held in an optical cavity [76]. The complexity of the typical atom trapping system may limit the suitability of this technique for a range of applications. Quantum dots provide an alternative to single atoms and may be isolated and enhanced in an optical cavity in a similar manner. InGaAs/GaAs quantum dots may be electrically driven [77]. InGaN/GaN quantum dots are also an interesting single-photon source as they may be produced over a wide transparency range and electrically driven and tuned [78]. The N-V centre in diamond has some of the most desirable characteristics of all deterministic single photon sources and is reviewed in Section 1.5.2.

Single-photons may also be produced in a probabilistic way rather than a deterministic way through parametric down conversion or four-wave mixing. In this case, the production of a photon is not on-demand. The photon is produced as part of a pair, where both photons are correlated. This source is often referred to as a heralded single photon source because the existence of one photon predicts the existence of the other half of the pair. A disadvantage of probabilistic single photon sources is the chance of producing multiple pairs simultaneously. Since some detectors types cannot detect multiple events this would increase the error in measurements. These sources must therefore be operated with low generation probabilities to prevent noise.

Spontaneous parametric down-conversion (SPDC) is a nonlinear technique that involves pumping a material with a  $\chi^{(2)}$  optical nonlinearity, creating two photons which have correlated characteristics due to momentum conservation [79]. In order for phase matching to occur, the two photons are emitted in different directions. This has the advantage that photon pairs may be easily spatially separated but provides difficulties in efficiently coupling to waveguides. Phase matching is possible for a certain range of wavelengths in different crystals using polarisation phase-matching. Periodic-poling may also be used to extend the range of wavelengths for which phase-matching is possible. When the two down-converted photons have the same polarisation it is referred to as type-I SPDC and when the photons have orthogonal polarisations it is referred to as type-II SPDC. For this work type-II SPDC in BBO was utilised for single-photon work and is discussed as part the experimental section in Chapter 4.

SPDC may also be achieved in a waveguide – which is of particular relevance to this work. The waveguide geometry ensures that pairs are produced within a waveguide, thus improving collection efficiency, and can be directly coupled to quantum logic circuits. Phase matching can be achieved with appropriate mode dispersion control in the waveguide. There are a number of recent results that demonstrate the use of waveguides to enhance efficient SPDC or to extend the wavelength range. This includes periodic poling of KTP [80] and lithium niobate [81].

Four-wave mixing is an alternative to SPDC to produce single photon pairs and takes advantage of the  $\chi^{(3)}$  rather than the  $\chi^{(2)}$  nonlinearity. Single-photon production by four-wave mixing has recently been shown as method that that can be integrated on chip for quantum logic circuits in silicon [82].

Single photon detectors are required to complete the quantum logic system. Photon detectors require conversion of a photon into an electrical signal. Desirable characteristics of a single photon detector are high detection efficiencies, low darkcount rates, minimum dead-time and low timing jitter. The detector needs sensitivity in the wavelength range of the source and ideally the possibility to integrate with the entire system on chip. There are a large range of single-photon detection systems, too extensive to list here. A review by M. D. Eisaman et al. is available that details their various merits and limitations [75]. Some well-known methods include using photomultiplier tubes, single-photon avalanche photodiodes and superconducting single-photon detectors. Electronics forms an important an integral part of the device because the timing requirements are non-trivial. There is limited commercial availability of many single-photon detectors and this work presented in this thesis aligns well with the wavelength sensitivity of silicon single-photon avalanche photodiodes (SPADs).

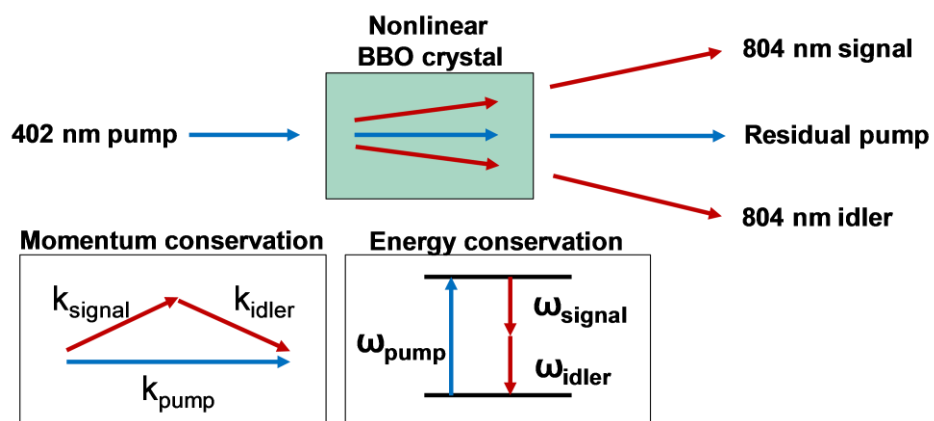


Figure 1. 6: Schematic of direction of pump and signal/idler photon pair outputs. **(inset left)** Requirements for photon momentum conservation that lead to directionality. **(inset right)** Energy conservation requirements leading to correlated output photons.

A major goal of integrated quantum photonics is to integrate sources, circuits and detectors on chip to offer scalability for complex logic and to operate efficiently at room temperature. There are a multitude of different methods and material systems than can be used to achieve this goal and much research still needs to be done. Many consider the N-V centre in diamond as one of the few suitable single-photon sources for this role and this source is discussed in Section 1.5.2.

### 1.5 Diamond photonics: towards waveguides

The name diamond appropriately derives from the ancient Greek word for unbreakable. Natural diamond is formed from carbon under immense temperature and pressure and is found in small quantities in diamond mines. The financial value of optical quality diamond has been set artificially high over the past century based on clever jewellery marketing and restrictions to trade. This continues to have an impact on scientific research, based on access to materials and artificial limitations applied to the availability of synthetic diamond. The jewellery market for diamond may, interestingly enough, stem from the optical properties of diamond including a low number of stable impurities, visible transparency and a high refractive index which offers significant light refraction.

Synthetic diamond may be formed using a high pressure high temperature technique from carbon – replicating natural formation processes. Samples produced in this manner are typically restricted to just below maximum optical quality. Synthetic diamond may also be formed using a chemical vapour deposition technique (CVD) from a hydrocarbon gas mixture on a range of substrates. This technique has only recently been fine-tuned to offer optical quality diamond [83]. The desirable properties for a range of optical applications, especially laser applications, include low loss, low birefringence (introduced by stress variation) and a low number of impurities. The development of high optical quality affordable diamond samples in mm<sup>3</sup> sizes has led to a large amount of recent research which would otherwise not have been possible.

Diamond has a very high mechanical strength with a large Young's modulus and is the hardest natural material known. This leads to a range of mechanical applications. By doping diamond with boron or phosphorus, diamond can be made into a semiconductor. Diamond electronics is an area of research that offers high power and high bandwidth transistors [84].

Table 1. 5: Photonics based applications of diamond.

Application	Contributing material property	Review
Quantum optics	Colour centre stability	[85]
Raman lasers	{ Large $\chi^{(3)}$ Thermal conductivity Transparency	[86]
UV diodes – LED/lasers	Large bandgap	[87]
Laser heat-spreaders	{ Thermal conductivity Transparency	[34]
Colour centre lasers/ Rare earth lasers	{ Colour centre stability Thermal conductivity Transparency	[88]/ [89]
Laser optical windows	{ Transparency Thermal conductivity	[90]

Diamond has a number of unique properties which allow for a range photonics based applications [91]. It has a large bandgap, which leads to a broad transparency range and opens up the possibility for UV LEDs and diode lasers. Diamond has high thermal conductivity, important for heat extraction. There are a number of high quality stable colour centres, at room temperature, in diamond which offer high quality single-photon sources. Diamond also has a high nonlinear  $\chi^{(3)}$  owing to a high Raman gain and potential four-wave mixing applications. A summary of some diamond photonics applications are listed in Table 1. 5.

### 1.5.1 Diamond waveguides and fabrication methods

As with all optical materials and applications areas there is a range of benefits that may arise with use of guided wave optics. Every application listed in Table 1. 5 may benefit from a waveguide, not only by enhancing the performance of the device but by allowing a range of increased functionality either through integration with other components or through a direct result of the waveguide.

Separate to the list of direct photonics based applications of diamond there are a number material properties of diamond which may benefit other applications of waveguides and integrated optics. The field of waveguide sensors may benefit from the high thermal conductivity, large bandgap and mechanical strength of diamond. These properties may extend the range of sensor based applications in high strain or temperature environments such as in structures or space/aerospace.

The refractive index of diamond ( $n \sim 2.4$ ) is intermediate compared to other optical materials typically used for waveguide fabrication including silica ( $n \sim 1.5$ ), and silicon and GaAs ( $n \sim 3.4$  in the infrared) and is relatively high for a material which has such broadband transparency through the visible. Diamond may offer a route to high density integrated nanowire waveguide circuits in the visible where other materials struggle. The refractive index closely matches that of GaN and is compared in Figure 1. 9. This may allow for integration between these materials.

Diamond has recently been highlighted as a material of great interest for integrated quantum photonics [92]. The application focus of nearly all of the (limited) waveguide structures fabricated to date in diamond is quantum photonics due to the suitability of the N-V centre as a single-photon source. It should be kept in mind, however, that these fabrication procedures may also be applied to a range of alternative applications.

At the time of writing there are very few demonstrations of guided light in diamond. Access to suitable material and control over the growth process has limited progress in this area. Existing waveguide structures have been fabricated using either well-established and or novel fabrication techniques.

Ion implantation has been used to change the refractive index of diamond: 2-3 MeV proton and 180 KeV boron ion beams have been used to directly introduce positive refractive index changes up to 0.1 which have been used to for waveguide fabrication [93, 94]. Alternatively, ion implantation has been used to create a sacrificial graphitisation layer which was then removed with acid etching: MeV carbon and oxygen ion beams have been used to create such a sacrificial damaged graphitisation layer in diamond. This layer was removed by acid or plasma etching leaving a free-standing diamond membrane waveguide layer [95-97]. In combination with CVD diamond regrowth the diamond membrane thickness can be controlled [98-100].

Three dimensional FIB has been used to fabricate diamond waveguide structures [101, 102]. This is a novel fabrication method but has a number of limitations in terms of device length is limited and the propagation loss is high.

Diamond may be thinned mechanically or via a deep etch to produce waveguide structures [103, 104]. Some thinned platelets are available commercially. Reactive ion etching or inductively coupled plasma of diamond provides a route to lateral definition of the waveguide structure [105, 106]. This method of diamond waveguide fabrication is used in this work and is presented in Chapter 3.

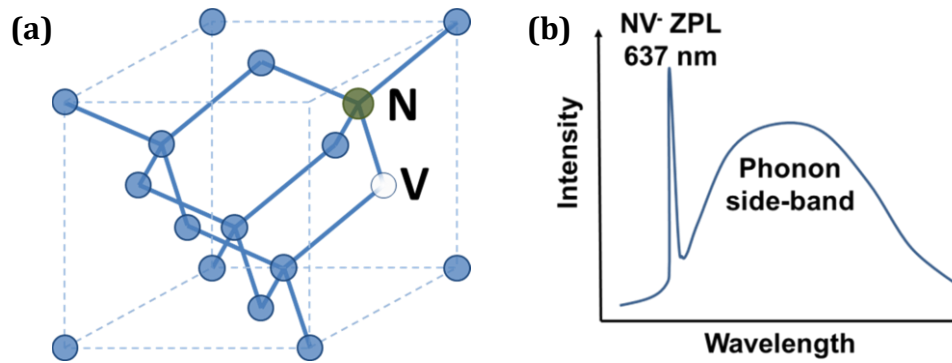


Figure 1. 7: **(a)** Schematic of diamond cubic lattice structure – a face centred cubic structure of carbon atoms separated by  $\frac{1}{4}$  of the unit cell in each dimension. **(b)** A sketch of the typical emission spectra from an N-V diamond single-photon source.

### 1.5.2 Diamond N-V single-photon source

There are over 500 documented colour centres in diamond [107], of which one of the most intensely studied is the nitrogen-vacancy (N-V) centre. The N-V centre is bright and stable at room temperature with a controllable spin-polarisation state [108]. This colour centre is created by substitution of a carbon atom with a nitrogen atom and an adjacent vacancy in the diamond lattice as shown in Figure 1. 7 a). The N-V centre may be neutral or negatively charged of which the negatively charged version is of most interest for quantum optics. One of the key properties of the N-V centre is the coherence time which is the time it takes the qubit state to become a mixed state and of no further use. Coherence times for photons from N-V centres have been measured to be as long as 350  $\mu$ s at room temperature [109] allowing for a significant number of processes to be carried out within that timeframe. No other suitable single-photon source has yet demonstrated the coherence time long enough to offer logic capabilities at room temperature. The N-V single-photon source has been used to demonstrate quantum key distribution [110] and single-photon interference [111].

By trapping the N-V centre in an optical cavity, through use of the Purcell effect, the contribution from the phonon sidebands may be reduced to enhance the zero-phonon line (ZPL) emission at 637 nm. Such cavities are vital in successful use of the N-V centre for quantum information applications. [108]

Waveguides may form an important role in the efficient collection, routing and subsequent quantum processing of the single-photons. Single-photon collection efficiency with a high NA objective can be as low as 8% from bulk diamond and it has been demonstrated that this can be significantly enhanced up to 91% by structuring the diamond into a waveguide [112]. The waveguide may also form part of the cavity required for zero-phonon-line enhancement. Remote qubit-qubit interaction can be achieved by coupling between N-V centres with a waveguide. Interaction between qubits in this manner would allow for on-

demand qubit interactions. 'Useful' quantum logic will involve the integration of many devices; hence the architecture is expected to be in waveguide form. If the single-photon sources could be integrated together with the logic system, the optical efficiency and practicality of the device would be significantly greater.

### 1.5.3 Diamond Raman lasers

There have been a number of recently reported demonstrations of diamond Raman lasers; largely due to the recent availability of high optical quality diamond in mm<sup>3</sup> sizes [83]. In pulsed operation this includes lasers that offer an optical conversion efficiency up to 63.5 % [113], a slope efficiency of 84 % [114] and a Stokes average output power of 24.5 W [115]. In continuous wave operation >5 W at 1217 nm has been obtained [48] and wavelength tunable operation has been demonstrated [116]. Operation in the UV has been reported [117] and using the anti-Stokes beam [118]. Through appropriate Raman cascading, it should be possible to develop a range of laser output wavelengths throughout the transparency window of diamond.

A diamond Raman waveguide laser may offer enhanced performance including a reduced threshold and higher optical conversion efficiency. Reduced thresholds may offer the possibility for new pump sources where less power is available.

Raman cascading to higher order Stokes beams may benefit from a number of advantages of the waveguide geometry including the enhanced overlap and reduced threshold. Maintaining an overlap between cascaded Stokes beams and pump beams in a bulk cavity becomes troublesome as the overlap is typically limited to  $\lambda_p/\lambda_s$ . The large Raman shift in diamond produces a maximum pump/Stokes overlap of ~92% which is compounded with each Stokes cascade. This can highly reduce the slope efficiency when attempting cascade outputs. Raman cascading in waveguides has already been demonstrated in Silicon where two-photon absorption loss is highly degrading to efficiency [53].

The waveguide geometry may offer increased functionality including efficient integration with other lasers, nonlinear doubling materials or waveguide optical parametric oscillators. Efficient on-chip coupling to fibre-optics may provide applications in the field of sensors or increase the portability and reliability of the device. Work presented in Chapter 3 considers diamond waveguides for Raman laser applications.

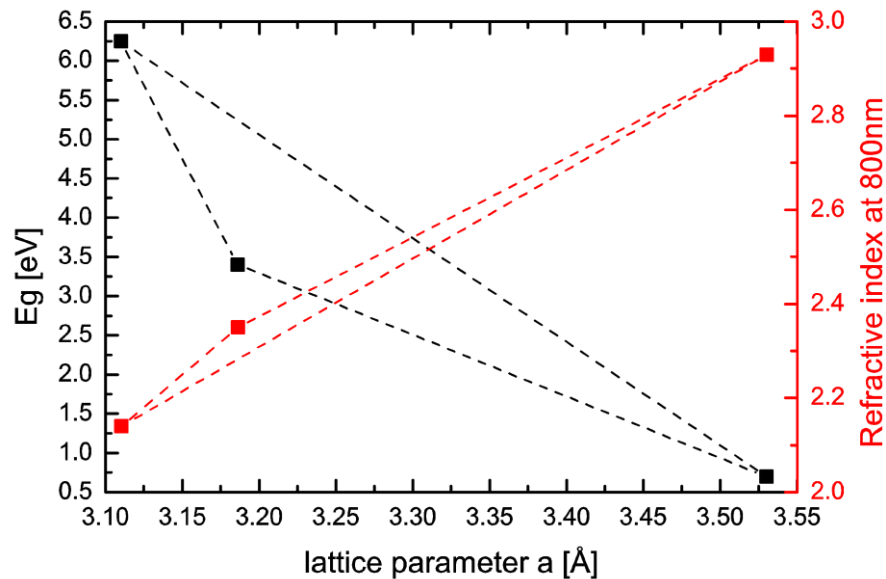


Figure 1. 8: **(black/left)** The bandgap of various III-nitride alloys. Significant bandgap bowing will shift the bandgap lower from the dashed line but is not shown here. **(red/right)** Estimate of the refractive index of various III-nitride alloys from the linear approximation between measured samples.

## 1.6 GaN photonics: towards waveguides

GaN was originally grown by CVD or sputtering and was not suitable for optical or electronic applications due to poor material quality. The development of plasma induced molecular beam epitaxy (MBE) and metalorganic chemical vapour deposition (MOCVD) in the 1990s made optical quality GaN available. A review of the material properties and growth techniques is available in ref. [119].

GaN is typically grown on sapphire substrates and this process has been fine-tuned to achieve optical quality layers with use of a buffer layer [120]. GaN is now widely available on a range of substrates. It may be grown on silicon using a low temperature buffer layer to manage with the thermal mismatch and has been directly grown onto diamond in order to take advantage of the high thermal conductivity of diamond [121]. Lattice matching is an important requirement to ensure defect free layers to maintain high optical quality. This work concentrates on the wurtzite (hexagonal) crystal structure of GaN, although it may also be grown in cubic form.

GaN has a direct bandgap of 3.4 eV and a large transparency range covering the visible and infrared. GaN belongs to a family of III-nitride semiconductors including InN, GaN and AlN that may be mixed into ternary or quaternary alloys allowing for bandgap engineering from the deep UV to the infrared. The range of achievable bandgaps is shown in Figure 1. 8.

The major optical application of GaN (and alloys) is for electrically LEDs and diode lasers [122] which operate in the UV/visible. The development of the GaN UV/blue LED led to the development of the white light LED [123]. Significant improvements in electrical-optical power efficiencies lead many to consider the white light LED as a potential replacement to existing lighting; to provide intelligent and green lighting.

The UV/blue diode laser is a recent development, largely motivated by the increased data capacity offered at shorter wavelengths in optical data storage [124]. Recent availability and increased power from these lasers has opened up a range of new pump schemes for solid-state lasers including the Ti:sapphire laser [125]. The true blue laser variety finds applications in laser projection displays.

### 1.6.1 GaN waveguide devices and applications

There are currently very few reported demonstrations of waveguide devices in GaN except for those in diode lasers. As with most diode lasers, the commercially available UV/blue diode laser benefits from a vertical and transverse waveguide structure for operation [124]. As such there is potential to efficiently extract and transport optical power with use of a waveguide. GaN based micro-LEDs have shown potential for visible light communication [126] which would also benefit from waveguide based functionality. Brief consideration was given to a monolithic integrated optics systems operating in visible wavelengths [127] however little work has been carried out in this area.

Some progress has been made in the development of GaN waveguide devices for communications applications working at a wavelength of 1550 nm [128-131]. This includes the possibility for erbium doping [132]. Fabricated devices include a directional coupler [128, 129] and free-standing GaN waveguides [130].

GaN and III-nitride alloys offer an interesting growth waveguide fabrication method. As outlined in Section 1.1.1, defining the waveguide during growth offers the possibility for low-loss and is an alternative to implantation or mechanical thinning to form planar waveguides. It is possible to use the refractive index difference of different nitride alloys to define the vertical waveguide during growth [131, 133]. An indication of the potential refractive index difference between nitride alloys is shown in Figure 1. 8. This can be achieved with low-loss, due to defect reduction, with lattice- and thermal-matching of the alloys.

Appropriate growth tailoring can be employed to create a waveguide that overlaps with nitride based quantum-wells [134]. This offers the possibility for a self-contained nitride based quantum-well waveguide laser system without the requirement for post-growth

waveguide definition. Such a system has the possibility to offer very low propagation loss due to lattice- and thermal-matched layer growth.

GaN has a high  $\chi^{(2)}$  making it suitable for nonlinear conversion. A number of recent measurements in bulk GaN agree and calculate the quadratic nonlinear optical coefficients of GaN to be  $\chi_{31}^{(2)} = 5\text{pm/V}$  [135, 136], which is similar to that of lithium niobate  $\chi_{31}^{(2)} = 8.8\text{pm/V}$  [137]. Nonlinear frequency conversion can be enhanced with use of a waveguide and has been demonstrated with a GaN photonic crystal [138] and in a ring resonator [139]. It has been proposed that waveguide dispersion can be used as an alternative to quasi-phase matching with use of a waveguide in GaN [140]. Although lithium niobate nonlinear frequency conversion waveguide technology is mature, GaN is available on a range of substrates, offers the possibility to guide with lattice matched alloys with the prospect to be integrated with other GaN light sources.

GaN has been identified as a material suitable for biosensor applications as it is biocompatible and chemically stable. There are a number of biosensors based on III-nitride materials using MEMs-based structures [141] however no known report of a GaN optical biosensor. The use of optical waveguides in other materials for label-free biosensors is well-established [142]. With appropriate waveguide design, the guided mode's evanescent field can be used to detect molecular interactions. Structures can be based on straight waveguides, photonic-crystals and ring resonators, connected remotely with optical fibre.

### **1.6.2 GaN for integrated quantum optics**

As part of this work, presented in Chapter 4, GaN is proposed as a platform for integrated quantum optics. GaN has a number of advantages over existing and proposed architectures.

The high  $\chi^{(2)}$  of GaN is a suitable for spontaneous parametric down-conversion to probabilistically produce single-photon pairs. With use of a waveguide, appropriate phase-matching and pair separation may be achieved; as has been demonstrated in a lithium niobate waveguide [81].

GaN is proposed as a suitable material to integrate with diamond due to the broadband transparency of both materials and the similar refractive index. The dispersion curve of the refractive index of GaN is compared to diamond in Figure 1. 9 from Ref. [143, 144]. Further precise index matching can be achieved with appropriate III-nitride alloy selection. The N-V colour centre in diamond is very attractive as a deterministic single-photon source for quantum information applications and thus could be integrated into a

GaN material system relatively easily. GaN may be grown directly onto diamond to assist with this integration [121].

GaN offers transparency through the visible and NIR for which existing and commercially available SPADS are available. This allows for a range of single-photon experiments to be carried out with high efficiency and low integration times. SPADs could be integrated with the GaN material system to offer efficient systems that operate at room temperature. A typical wavelength sensitivity curve for a SPAD is shown in Figure 1. 9.

The refractive index of GaN is relatively high offering the possibility for compact single-mode nanowire waveguides. This waveguide geometry would allow for the integration of numerous components on-chip as would be required for complex quantum calculations.

Some of the discussed applications of GaN to optics and integrated optics are highlighted in Table 1. 6.

Table 1. 6: Summary of material properties of GaN and optical applications.

<b>GaN Property</b>	<b>Application/Benefit</b>
Bandgap tuning with nitride alloys	{ UV-visible-Infrared diode-lasers or LEDs Quantum-well lasers
Lattice matched alloy growth	Low-loss waveguide possibilities
Available on a range of substrates	Cheap and versatile
High $\chi^{(2)}$	{ Nonlinear frequency conversion SPDC for integrated quantum photonics
Broadband transparency	{ Compatible with SPAD sensitivity range Visible lasers and integrated optics
Refractive index matched to diamond	Possibility for hybrid structures

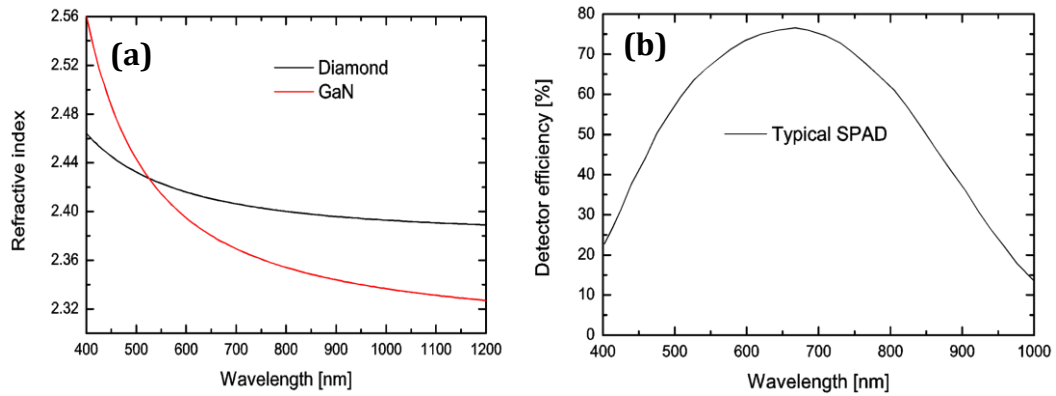


Figure 1. 9: **(a)** Dispersion curve of crystalline GaN and diamond. **(b)** SPAD wavelength sensitivity. Data taken from a commercial SPAD device offered by PicoQuant.

## 1.7 KYbW for guided laser operation

Monoclinic potassium ytterbium double-tungstate,  $\text{KYb}(\text{WO}_4)_2$ , hereafter referred to as KYbW, is a stoichiometric (equivalent to 100%  $\text{Yb}^{3+}$  doped) optically active crystal [145]. It belongs to a family of well-known double-tungstates that also include  $\text{KY}(\text{WO}_4)_2$ ,  $\text{KGd}(\text{WO}_4)_2$  and  $\text{KLu}(\text{WO}_4)_2$  which have a wide range of applications in the field of optics. A large variety of rare-earth atoms have been doped into these host materials for efficient laser operation including erbium, holmium, neodymium, praseodymium and ytterbium. The host KYW material offers high absorption and emission cross-sections.

Rare-earth doped double tungstate materials are suitable for diode-pumping [146], mode-locking [147], thin-disk operation (power scaling) [148, 149] and for waveguide lasers [31]. With or without doping, the large third-order nonlinear optical susceptibility of these host materials allows for efficient Raman conversion [47].

Due to the similar ionic radius of yttrium and ytterbium, KYbW has similar properties to Yb:KYW and allows for high doping without additional stress in the crystal.  $\text{Yb}^{3+}$  does not suffer from quenching at high concentrations due to the simple three-level laser system and no excited state absorption [145]. In this work only trivalent ytterbium ions are used, typically referred to as  $\text{Yb}^{3+}$ , and for convenience are simply referred to as Yb.

The high concentration of Yb ions combined with the high absorption-cross section of Yb in the host material creates a very high absorption coefficient. A 1% doped Nd:YAG crystal is a typical laser gain material and has an absorption length at peak absorption of 950  $\mu\text{m}$ . KYbW has an absorption length of 13.3  $\mu\text{m}$  which is nearly 70 times shorter. KYbW has similar absorption lengths as other stoichiometric materials such as YbAG and  $\text{YbVO}_4$ . High Yb concentrations can be achieved, creating high absorption coefficients in these stoichiometric materials. Table 1. 7 shows a comparison of the absorption properties of some stoichiometric Yb materials and other optically active ions in KYW.

Table 1. 7: Absorption properties of various stoichiometric Yb materials and KYW doped with other rare-earth ions.

Material	Peak absorption cross-section (for doping level) [ $\times 10^{-20} \text{ cm}^2$ ]	Wavelength at peak absorption [nm]	Yb Concentration [ $\times 10^{21} \text{ cm}^{-3}$ ]	Absorption length [ $\mu\text{m}$ ]
KYbW [145]	11.7	981	6.4	13
YbAG [150]	0.7	940	13.7	96
YbVO <sub>4</sub> [151]	1.0	970	12.4	129
Tm:KYW [152]	(15%) 1.9	1850		
Er:KYW [153]	(0.5%) 2.7	1535		
Nd:KYW [154]	(5%) 5.8	812		

The crystallographic unit cell parameters of KYbW are  $a=10.590 \text{ \AA}$ ,  $b=10.290 \text{ \AA}$ ,  $c=7.478 \text{ \AA}$ ,  $\beta=130.70^\circ$ , and  $Z=4$ , with the space group  $C2/c$ . The crystallographic axes are non-orthogonal. KYbW is a biaxial crystal with three orthogonal optical axes defined here as  $N_g$ ,  $N_m$ , and  $N_p$ . The optical axis  $N_p$  is parallel with the crystallographic  $b$  axis and  $N_g$  and  $N_m$  lie in the  $a$ - $c$  plane. The optical axes are shown in relation to the crystallographic axes inset in Figure 1. 11. In order to achieve high cross-sections, the polarisation must be parallel to the appropriate optical axis  $N_m$ . The cross-sections and absorption coefficients are shown in Figure 1. 10.

The high absorption coefficient of KYbW is unusual and may offer the possibility for a number of novel laser configurations. The thin-disk laser cavity design allows for some of the highest average output power due to efficient heat extraction due to the high area/volume ratio [35]. A thin disk KYbW laser would allow for micron sized disks with near 100% pump absorption with a single-pass [149]. The large absorption coefficient allows for the use of low-quality pump sources whilst maintaining good pump/signal overlaps. Materials with lower absorption coefficients require longer crystal lengths in order to absorb the pump. In that situation high quality pump beams are required to maintain a good overlap between pump and signal beams limiting the use of diode-lasers.

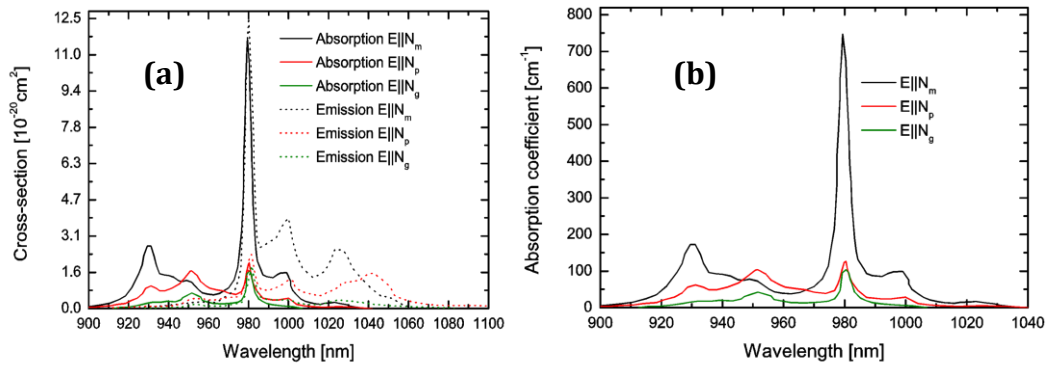


Figure 1. 10: **(a)** Absorption and emission cross-section of KYbW. **(b)** Absorption coefficient of KYbW. Data and taken from.

It has been noted by several authors [30, 145, 155] that the short absorption length could find applications in the field of waveguide laser designs. However, outside of this work there is no known demonstration of KYbW for guided wave applications. The absorption length of KYbW is of the order of the same cross-sectional size of many waveguide lasers and thus it is possible to consider side-pumping fabricated structures or inducing waveguides in KYbW. Other material systems would require multiple pump passes to efficiently side pump waveguides; increasing the complexity.

There are limited reported laser demonstrations of KYbW including operation with a chopper [155] and continuous wave (cw) operation [156], both in a thin-disk-like geometry. The chopped operation was achieved with a 500  $\mu$ m thick sample at Brewster’s angle with no thermal cooling pumping at 922 nm or 963 nm. The cw operation was achieved with a 125  $\mu$ m thick sample, thermal cooling and pumping at 1025 nm to reduce the thermal load. In both cases negative thermal lensing limited performance and temporal fluctuations were observed. It is clear that for efficient thin-disk operation thermal lensing is an issue and heat extraction is important.

The Raman gain coefficient of KYbW is high, similar to that of KYW as listed in Table 1. 4. Raman nonlinear frequency conversion is a possibility to reach a range of output

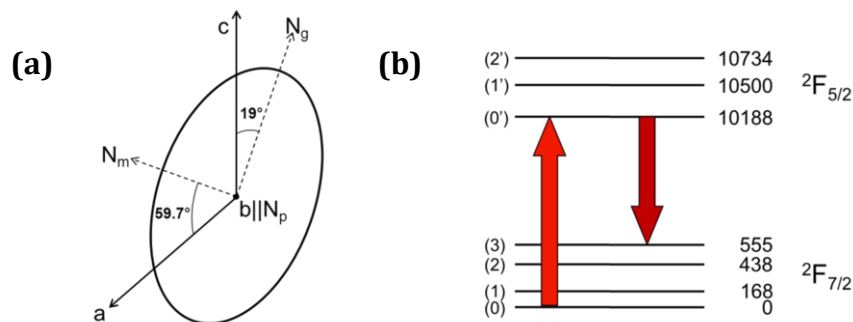


Figure 1. 11: **(a)** The optical ellipsoid of KYbW in relation to the crystallographic axis. **(b)** The Stark energy levels and most pronounced transitions of the  $2F_{5/2}$  and  $2F_{7/2}$  levels. Highlighted are the transitions used for laser operation as part of this work.

wavelengths with the same laser system. The waveguide geometry may be key to achieving such conversion efficiently as was highlighted in Section 1.3.5.

Pump-induced guiding is an effect that will be enhanced by the high concentration of the Yb ion. In Chapter 5 this topic is discussed at length. This method of waveguide formation is not widely reported and could lead to a number of new laser geometries.

### 1.8 Thesis outline

The work presented in this thesis relates to waveguides in three different materials for which optical guiding is not widely reported. The thesis is thus subdivided into chapters based on each material system. There are however significant overlap of both underlying theory and applications of optical guiding. Novel guiding mechanisms, Raman lasers and quantum optics are all highlighted as significant themes throughout the thesis.

Chapter 2 presents the underlying theory of waveguides. It describes many of the techniques used throughout the rest of the thesis to model or simulate guiding behaviour. The effective index, Marcatili's approximation, the finite element and the beam propagation methods are all introduced and described in this chapter. Their application to the rib waveguide is compared and a new accurate analytical method to describe narrow rib waveguides is introduced based on the four-layer solution.

Chapter 3 presents waveguide work in diamond with a focus on Raman laser applications. This chapter describes the criteria required to produce, measure and justify large cross-sectional area single-mode waveguides, in any material system but particularly diamond. It presents the fabrication and optical characterisation of such waveguide designs in diamond. A theoretical study on the performance of a diamond Raman waveguide laser is presented for 532 nm or 1064 nm cw pumping incorporating scattering losses. Properties such as output power and threshold are investigated for different cross-sectional sizes and mirror reflectivities.

Chapter 4 presents waveguide work in GaN. GaN waveguides have a large range of potential applications and are considered here as a platform for integrated quantum photonics. Design and operational theory of GaN directional couplers are considered in order to minimise footprint with relaxed fabrication requirements. The fabrication process and optical characterisation of straight waveguides and directional couplers is presented including mode profiles, propagation loss and splitting ratios. The results of two-photon quantum interference within the directional couplers are presented.

Chapter 5 presents optically induced guiding and laser operation results in KYbW. The mechanisms of optically induced refractive index change and their guiding effects are introduced. Optically induced guiding at 633 nm is performed and the refractive index change is calculated. Guided quasi-continuous-wave laser operation in KYbW is demonstrated and analysis of the power transfers, mode profiles, cavity stability and thermal effects are presented.

Chapter 6 provides a summary of the work presented in this thesis and outlines potential applications of the research and suggests further work that may be carried out to continue and compliment this research.

## References

- [1] S. E. Miller, "Integrated Optics - an Introduction," Bell System Technical Journal, **48**, 2059 (1969).
- [2] D. A. B. Miller, "Device Requirements for Optical Interconnects to Silicon Chips," Proceedings of the IEEE, **97**, 1166-1185 (2009).
- [3] B. Jalali, M. Paniccia, and G. Reed, "Silicon photonics," IEEE Microwave Magazine, **7**, 58 (2006).
- [4] C. Grivas, "Optically pumped planar waveguide lasers, Part I: Fundamentals and fabrication techniques," Progress in Quantum Electronics, **35**, 159-239 (2011).
- [5] E. Cantelar, D. Jaque, and G. Lifante, "Waveguide lasers based on dielectric materials," Optical Materials, **34**, 555-571 (2012).
- [6] F. Chen, X. L. Wang, and K. M. Wang, "Development of ion-implanted optical waveguides in optical materials: A review," Optical Materials, **29**, 1523-1542 (2007).
- [7] A. Tervonen, B. R. West, and S. Honkanen, "Ion-exchanged glass waveguide technology: a review," Optical Engineering, **50**, 071107 (2011).
- [8] M. Ams, G. D. Marshall, P. Dekker, J. A. Piper, and M. J. Withford, "Ultrafast laser written active devices," Laser & Photonics Reviews, **3**, 535-544 (2009).
- [9] G. D. Emmerson, S. P. Watts, C. B. E. Gawith, V. Albanis, M. Ibsen, R. B. Williams, and P. G. R. Smith, "Fabrication of directly UV-written channel waveguides with simultaneously defined integral Bragg gratings," Electronics Letters, **38**, 1531-1532 (2002).
- [10] I. Chartier, B. Ferrand, D. Pelenc, S. J. Field, D. C. Hanna, A. C. Large, D. P. Shepherd, and A. C. Tropper, "Growth and Low-Threshold Laser Oscillation of an Epitaxially Grown Nd Yag Wave-Guide," Optics Letters, **17**, 810-812 (1992).
- [11] C. Grivas, T. C. May-Smith, D. P. Shepherd, and R. W. Eason, "Laser operation of a low loss (0.1 dB/cm) Nd : Gd<sub>3</sub>Ga<sub>5</sub>O<sub>12</sub> thick (40 μm) planar waveguide grown by pulsed laser deposition," Optics Communications, **229**, 355-361 (2004).
- [12] H. Y. Ou, "Different index contrast silica-on-silicon waveguides by PECVD," Electronics Letters, **39**, 212-213 (2003).
- [13] K. Worhoff, J. D. B. Bradley, F. Ay, D. Geskus, T. P. Blauwendraat, and M. Pollnau, "Reliable Low-Cost Fabrication of Low-Loss Al<sub>2</sub>O<sub>3</sub>:Er<sup>3+</sup> Waveguides With 5.4-dB Optical Gain," IEEE Journal of Quantum Electronics, **45**, 454-461 (2009).
- [14] T. Nishikawa, A. Ozawa, Y. Nishida, M. Asoke, F. L. Hong, and T. W. Hansch, "Efficient 494 mW sum-frequency generation of sodium resonance radiation at 589 nm by using a periodically poled Zn:LiNbO<sub>3</sub> ridge waveguide," Optics Express, **17**, 17792-17800 (2009).
- [15] D. P. Kelly, M. W. Pruessner, K. Amarnath, M. Datta, S. Kanakaraju, L. C. Calhoun, and R. Ghodssi, "Monolithic suspended optical waveguides for InP MEMS," IEEE Photonics Technology Letters, **16**, 1298-1300 (2004).
- [16] C. Grivas, D. P. Shepherd, R. W. Eason, L. Laversenne, P. Moretti, C. N. Borca, and M. Pollnau, "Room-temperature continuous-wave operation of Ti : sapphire buried channel-waveguide lasers fabricated via proton implantation," Optics Letters, **31**, 3450-3452 (2006).

- [17] G. Jose, G. Sorbello, S. Taccheo, E. Cianci, V. Foglietti, and P. Laporta, "Active waveguide devices by Ag-Na ion exchange on erbium-ytterbium doped phosphate glasses," *Journal of Non-Crystalline Solids*, **322**, 256-261 (2003).
- [18] C. Becker, T. Oesselke, J. Pandavenes, R. Ricken, K. Rochhausen, G. Schreiber, W. Sohler, H. Suche, R. Wessel, S. Balsamo, I. Montrosset, and D. Sciancalepore, "Advanced Ti : Er : LiNbO<sub>3</sub> waveguide lasers," *IEEE Journal of Selected Topics in Quantum Electronics*, **6**, 101-113 (2000).
- [19] W. Yang, C. Corbari, P. G. Kazansky, K. Sakaguchi, and I. C. S. Carvalho, "Low loss photonic components in high index bismuth borate glass by femtosecond laser direct writing," *Optics Express*, **16**, 16215-16226 (2008).
- [20] D. Zauner, K. Kulstad, J. Rathje, and M. Svalgaard, "Directly UV-written silica-on-silicon planar waveguides with low insertion loss," *Electronics Letters*, **34**, 1582-1584 (1998).
- [21] P. Olivero, S. Rubanov, P. Reichart, B. C. Gibson, S. T. Huntington, J. Rabeau, A. D. Greentree, J. Salzman, D. Moore, D. N. Jamieson, and S. Praver, "Ion-beam-assisted lift-off technique for three-dimensional micromachining of freestanding single-crystal diamond," *Advanced Materials*, **17**, 2427 (2005).
- [22] J. D. B. Bradley, F. Ay, K. Worhoff, and M. Pollnau, "Fabrication of low-loss channel waveguides in Al<sub>2</sub>O<sub>3</sub> and Y<sub>2</sub>O<sub>3</sub> layers by inductively coupled plasma reactive ion etching," *Applied Physics B-Lasers and Optics*, **89**, 311-318 (2007).
- [23] H. Hu, R. Ricken, W. Sohler, and R. B. Wehrspohn, "Lithium niobate ridge waveguides fabricated by wet etching," *IEEE Photonics Technology Letters*, **19**, 417-419 (2007).
- [24] C. Grivas, T. C. May-Smith, D. P. Shepherd, R. W. Eason, M. Pollnau, and M. Jelinek, "Broadband single-transverse-mode fluorescence sources based on ribs fabricated in pulsed laser deposited Ti : sapphire waveguides," *Applied Physics A-Materials Science & Processing*, **79**, 1195-1198 (2004).
- [25] Y. F. Zhang, Phd Thesis, "Diamond and GaN Waveguides and Microstructures for Integrated Quantum Photonics," (Institute of Photonics, University of Strathclyde, 2012).
- [26] E. Snitzer, "Optical Maser Action of Nd<sup>+3</sup> in a Barium Crown Glass," *Physical Review Letters*, **7**, 444 (1961).
- [27] A. D. Colley, H. J. Baker, and D. R. Hall, "Planar Wave-Guide, 1-kW cw, Carbon-Dioxide Laser-Excited by a Single Transverse RF Discharge," *Applied Physics Letters*, **61**, 136 (1992).
- [28] T. J. Kane, J. M. Eggleston, and R. L. Byer, "The Slab Geometry Laser .2. Thermal Effects in a Finite Slab," *IEEE Journal of Quantum Electronics*, **21**, 1195-1210 (1985).
- [29] B. Comaskey, G. Albrecht, R. Beach, S. Velsko, S. Sutton, S. Mitchell, C. Petty, K. Jancaitis, W. Benett, B. Freitas, and R. Solarz, "A One Kilowatt Average Power Diode-Pumped Ndyag Folded Zigzag Slab Laser," *Diode Pumping of Average-Power Solid State Lasers*, **1865**, 9 (1993).
- [30] M. Pollnau, C. Grivas, L. Laversenne, J. S. Wilkinson, R. W. Eason, and D. P. Shepherd, "Ti : Sapphire waveguide lasers," *Laser Physics Letters*, **4**, 560-571 (2007).
- [31] M. Pollnau, Y. E. Romanyuk, F. Gardillou, C. N. Borca, U. Griebner, S. Rivier, and V. Petrov, "Double tungstate lasers: From bulk toward on-chip integrated waveguide devices," *IEEE Journal of Selected Topics in Quantum Electronics*, **13**, 661-671 (2007).
- [32] J. I. Mackenzie, "Dielectric solid-state planar waveguide lasers: A review," *IEEE Journal of Selected Topics in Quantum Electronics*, **13**, 626-637 (2007).
- [33] M. J. F. Digonnet, and C. J. Gaeta, "Theoretical-Analysis of Optical Fiber Laser-Amplifiers and Oscillators," *Applied Optics*, **24**, 333-342 (1985).
- [34] P. Millar, R. B. Birch, A. J. Kemp, and D. Burns, "Synthetic diamond for intracavity thermal management in compact solid-state lasers," *IEEE Journal of Quantum Electronics*, **44**, 709-717 (2008).
- [35] C. R. E. Baer, O. H. Heckl, C. J. Saraceno, C. Schriber, C. Krankel, T. Sudmeyer, and U. Keller, "Frontiers in passively mode-locked high-power thin disk laser oscillators," *Optics Express*, **20**, 7054-7065 (2012).
- [36] G. I. Stegeman, and C. T. Seaton, "Nonlinear Integrated-Optics," *Journal of Applied Physics*, **58**, R57-R78 (1985).
- [37] R. V. Roussev, C. Langrock, J. R. Kurz, and M. M. Fejer, "Periodically poled lithium niobate waveguide sum-frequency generator for efficient single-photon detection at communication wavelengths," *Optics Letters*, **29**, 1518-1520 (2004).
- [38] C. J. Van der poel, J. D. Bierlein, J. B. Brown, and S. Colak, "Efficient Type-I Blue second-Harmonic Generation in Periodically Segmented Ktiopo<sub>4</sub> Wave-Guides," *Applied Physics Letters*, **57**, 2074 (1990).

- [39] B. Bijlani, P. Abolghasem, and A. S. Helmy, "Second harmonic generation in ridge Bragg reflection waveguides," *Applied Physics Letters*, **92**, 101124 (2008).
- [40] K. D. Singer, M. G. Kuzyk, W. R. Holland, J. E. Sohn, S. J. Lalama, R. B. Comizzoli, H. E. Katz, and M. L. Schilling, "Electro-Optic Phase Modulation and Optical 2nd-Harmonic Generation in Corona-Poled Polymer-Films," *Applied Physics Letters*, **53**, 1800 (1988).
- [41] J. M. Dudley, G. Genty, and S. Coen, "Supercontinuum generation in photonic crystal fiber," *Reviews of Modern Physics*, **78**, 1135-1184 (2006).
- [42] T. A. Birks, W. J. Wadsworth, and P. S. Russell, "Supercontinuum generation in tapered fibers," *Optics Letters*, **25**, 1415-1417 (2000).
- [43] L. E. Myers, and W. R. Bosenberg, "Periodically poled lithium niobate and quasi-phase-matched optical parametric oscillators," *IEEE Journal of Quantum Electronics*, **33**, 1663-1672 (1997).
- [44] R. Boyd, "Nonlinear Optics" (Academic Press, 2008).
- [45] R. Singh, "C. V. Raman and the discovery of the Raman effect," *Physics in Perspective*, **4**, 399-420 (2002).
- [46] H. M. Pask, "The design and operation of solid-state Raman lasers," *Progress in Quantum Electronics*, **27**, 3 (2003).
- [47] J. A. Piper, and H. M. Pask, "Crystalline Raman lasers," *IEEE Journal of Selected Topics in Quantum Electronics*, **13**, 692-704 (2007).
- [48] V. G. Savitski, I. Friel, J. E. Hastie, M. D. Dawson, D. Burns, and A. J. Kemp, "Characterization of Single-Crystal Synthetic Diamond for Multi-Watt Continuous-Wave Raman Lasers," *IEEE Journal of Quantum Electronics*, **48**, 328-337 (2012).
- [49] P. Cerny, P. G. Zverev, H. Jelinkova, and T. T. Basiev, "Efficient Raman shifting of picosecond pulses using BaWO<sub>4</sub> crystal," *Optics Communications*, **177**, 397-404 (2000).
- [50] H. S. Rong, A. S. Liu, R. Jones, O. Cohen, D. Hak, R. Nicolaescu, A. Fang, and M. Paniccia, "An all-silicon Raman laser," *Nature*, **433**, 292-294 (2005).
- [51] R. H. Stolen, and E. P. Ippen, "Raman Gain in Glass Optical Waveguides," *Applied Physics Letters*, **22**, 276 (1973).
- [52] H. S. Rong, S. B. Xu, Y. H. Kuo, V. Sih, O. Cohen, O. Raday, and M. Paniccia, "Low-threshold continuous-wave Raman silicon laser," *Nature Photonics*, **1**, 232-237 (2007).
- [53] H. S. Rong, S. B. Xu, O. Cohen, O. Raday, M. Lee, V. Sih, and M. Paniccia, "A cascaded silicon Raman laser," *Nature Photonics*, **2**, 170-174 (2008).
- [54] S. M. Spillane, T. J. Kippenberg, and K. J. Vahala, "Ultralow-threshold Raman laser using a spherical dielectric microcavity," *Nature*, **415**, 621-623 (2002).
- [55] T. J. Kippenberg, S. M. Spillane, D. K. Armani, and K. J. Vahala, "Ultralow-threshold microcavity Raman laser on a microelectronic chip," *Optics Letters*, **29**, 1224-1226 (2004).
- [56] I. S. Grudin, and L. Maleki, "Ultralow-threshold Raman lasing with CaF<sub>2</sub> resonators," *Optics Letters*, **32**, 166-168 (2007).
- [57] P. W. Shor, "Algorithms for Quantum Computation - Discrete Logarithms and Factoring," 35Th Annual Symposium on Foundations of Computer Science, Proceedings, 124-134 (1994).
- [58] J. L. O'Brien, "Optical quantum computing," *Science*, **318**, 1567-1570 (2007).
- [59] E. Knill, R. Laflamme, and G. J. Milburn, "A scheme for efficient quantum computation with linear optics," *Nature*, **409**, 46 (2001).
- [60] P. Kok, W. J. Munro, K. Nemoto, T. C. Ralph, J. P. Dowling, and G. J. Milburn, "Linear optical quantum computing with photonic qubits," *Reviews of Modern Physics*, **79**, 135-174 (2007).
- [61] J. L. O'Brien, G. J. Pryde, A. G. White, T. C. Ralph, and D. Branning, "Demonstration of an all-optical quantum controlled-NOT gate," *Nature*, **426**, 264-267 (2003).
- [62] C. Y. Lu, D. E. Browne, T. Yang, and J. W. Pan, "Demonstration of a compiled version of Shor's quantum factoring algorithm using photonic qubits," *Physical Review Letters*, **99**, 250504 (2007).
- [63] J. Chen, J. B. Altepeter, M. Medic, K. F. Lee, B. Gokden, R. H. Hadfield, S. W. Nam, and P. Kumar, "Demonstration of a quantum controlled-NOT gate in the telecommunications band," *Physical Review Letters*, **100**, 133603 (2008).
- [64] M. G. Thompson, A. Politi, J. C. F. Matthews, and J. L. O'Brien, "Integrated waveguide circuits for optical quantum computing," *IET Circuits Devices & Systems*, **5**, 94-102 (2011).
- [65] I. L. Chuang, and Y. Yamamoto, "Simple Quantum Computer," *Physical Review A*, **52**, 3489-3496 (1995).
- [66] A. Politi, M. J. Cryan, J. G. Rarity, S. Y. Yu, and J. L. O'Brien, "Silica-on-silicon waveguide quantum circuits," *Science*, **320**, 646-649 (2008).

- [67] B. J. Smith, D. Kundys, N. Thomas-Peter, P. G. R. Smith, and I. A. Walmsley, "Phase-controlled integrated photonic quantum circuits," *Optics Express*, **17**, 13516-13525 (2009).
- [68] A. Laing, A. Peruzzo, A. Politi, M. R. Verde, M. Halder, T. C. Ralph, M. G. Thompson, and J. L. O'Brien, "High-fidelity operation of quantum photonic circuits," *Applied Physics Letters*, **97**, 211109 (2010).
- [69] G. D. Marshall, A. Politi, J. C. F. Matthews, P. Dekker, M. Ams, M. J. Withford, and J. L. O'Brien, "Laser written waveguide photonic quantum circuits," *Optics Express*, **17**, 12546-12554 (2009).
- [70] A. Politi, J. C. F. Matthews, and J. L. O'Brien, "Shor's Quantum Factoring Algorithm on a Photonic Chip," *Science*, **325**, 1221-1221 (2009).
- [71] L. Sansoni, F. Sciarrino, G. Vallone, P. Mataloni, A. Crespi, R. Ramponi, and R. Osellame, "Polarization Entangled State Measurement on a Chip," *Physical Review Letters*, **105**, 200503 (2010).
- [72] D. Bonneau, M. Lobino, P. S. Jiang, C. M. Natarajan, M. G. Tanner, R. H. Hadfield, S. N. Dorenbos, V. Zwiller, M. G. Thompson, and J. L. O'Brien, "Fast Path and Polarization Manipulation of Telecom Wavelength Single Photons in Lithium Niobate Waveguide Devices," *Physical Review Letters*, **108**, 053601 (2012).
- [73] D. Bonneau, E. Engin, K. Ohira, N. Suzuki, H. Yoshida, N. Iizuka, M. Ezaki, C. M. Natarajan, M. G. Tanner, R. H. Hadfield, S. N. Dorenbos, V. Zwiller, J. L. O'Brien, and M. G. Thompson, "Quantum interference and manipulation of entanglement in silicon wire waveguide quantum circuits," *New Journal of Physics*, **14**, 045003 (2012).
- [74] Y. F. Zhang, L. McKnight, E. Engin, I. M. Watson, M. J. Cryan, E. D. Gu, M. G. Thompson, S. Calvez, J. L. O'Brien, and M. D. Dawson, "GaN directional couplers for integrated quantum photonics," *Applied Physics Letters*, **99**, 161119 (2011).
- [75] M. D. Eisaman, J. Fan, A. Migdall, and S. V. Polyakov, "Invited Review Article: Single-photon sources and detectors," *Review of Scientific Instruments*, **82**, 071101 (2011).
- [76] J. McKeever, A. Boca, A. D. Boozer, R. Miller, J. R. Buck, A. Kuzmich, and H. J. Kimble, "Deterministic generation of single photons from one atom trapped in a cavity," *Science*, **303**, 1992-1994 (2004).
- [77] Z. L. Yuan, B. E. Kardynal, R. M. Stevenson, A. J. Shields, C. J. Lobo, K. Cooper, N. S. Beattie, D. A. Ritchie, and M. Pepper, "Electrically driven single-photon source," *Science*, **295**, 102-105 (2002).
- [78] A. F. Jarjour, R. A. Oliver, and R. A. Taylor, "Nitride-based quantum dots for single photon source applications," *Physica Status Solidi A-Applications and Materials Science*, **206**, 2510-2523 (2009).
- [79] P. G. Kwiat, K. Mattle, H. Weinfurter, A. Zeilinger, A. V. Sergienko, and Y. H. Shih, "New High-Intensity Source of Polarization-Entangled Photon Pairs," *Physical Review Letters*, **75**, 4337-4341 (1995).
- [80] T. A. Zhong, F. N. C. Wong, T. D. Roberts, and P. Battle, "High performance photon-pair source based on a fiber-coupled periodically poled KTiOPO4 waveguide," *Optics Express*, **18**, 20114-20114 (2010).
- [81] G. Fujii, N. Namekata, M. Motoya, S. Kurimura, and S. Inoue, "Bright narrowband source of photon pairs at optical telecommunication wavelengths using a type-II periodically poled lithium niobate waveguide," *Optics Express*, **15**, 12769-12776 (2007).
- [82] E. Engin, D. Bonneau, C. M. Natarajan, A. Clark, M. G. Tanner, R. H. Hadfield, S. N. Dorenbos, V. Zwiller, K. Ohira, N. Suzuki, H. Yoshida, N. Iizuka, M. Ezaki, J. L. O'Brien, and M. G. Thompson, "Photon Pair Generation in Silicon Micro-Ring Resonator and Enhancement via Reverse Bias," arXiv:1204.4922v1, (April 2012).
- [83] I. Friel, S. L. Geoghegan, D. J. Twitchen, and G. A. Scarsbrook, "Development of high quality single crystal diamond for novel laser applications," *Optics and Photonics for Counterterrorism and Crime Fighting Vi and Optical Materials in Defence Systems Technology Vii*, 7838 (2010).
- [84] M. Kasu, K. Ueda, Y. Yamauchi, A. Tallaire, and T. Makimoto, "Diamond-based RF power transistors: Fundamentals and applications," *Diamond and Related Materials*, **16**, 1010-1015 (2007).
- [85] S. Praver, and A. D. Greentree, "Applied physics - Diamond for quantum computing," *Science*, **320**, 1601-1602 (2008).
- [86] R. P. Mildren, "The Outlook for Diamond in Raman Laser Applications," in *Materials Research Society* (2010).
- [87] P. John, "Applied physics - Toward diamond lasers," *Science*, **292**, 1847-1848 (2001).

- [88] V. G. Vins, and E. V. Pestryakov, "Color centers in diamond crystals: Their potential use in tunable and femtosecond lasers," *Diamond and Related Materials*, **15**, 569-571 (2006).
- [89] K. D. Jamison, and H. D. Schmidt, "Doped diamond laser - 5504767," U. S. Patent, ed. (1996).
- [90] J. R. Brandon, S. E. Coe, R. S. Sussmann, K. Sakamoto, R. Spörl, R. Heidinger, and S. Hanks, "Development of CVD diamond r.f. windows for ECRH," *Fusion Engineering and Design*, **53**, 553-559 (2001).
- [91] I. Aharonovich, A. D. Greentree, and S. Praver, "Diamond photonics," *Nature Photonics*, **5**, 397-405 (2011).
- [92] A. D. Greentree, B. A. Fairchild, F. M. Hossain, and S. Praver, "Diamond integrated quantum photonics," *Materials Today*, **11**, 22 (2008).
- [93] F. Bosia, N. Argiolas, M. Bazzan, P. Olivero, F. Picollo, A. Sordini, M. Vannoni, and E. Vittone, "Modification of the structure of diamond with MeV ion implantation," *Diamond and Related Materials*, **20**, 774-778 (2011).
- [94] A. Battiato, F. Bosia, S. Ferrari, P. Olivero, A. Sytchkova, and E. Vittone, "Spectroscopic measurement of the refractive index of ion-implanted diamond," *Optics Letters*, **37**, 671-673 (2012).
- [95] I. Bayn, B. Meyler, A. Lahav, J. Salzman, R. Kalish, B. A. Fairchild, S. Praver, M. Barth, O. Benson, T. Wolf, P. Siyushev, F. Jelezko, and J. Wrachtrup, "Processing of photonic crystal nanocavity for quantum information in diamond," *Diamond and Related Materials*, **20**, 937-943 (2011).
- [96] B. A. Fairchild, P. Olivero, S. Rubanov, A. D. Greentree, F. Waldermann, R. A. Taylor, I. Walmsley, J. M. Smith, S. Huntington, B. C. Gibson, D. N. Jamieson, and S. Praver, "Fabrication of Ultrathin Single-Crystal Diamond Membranes," *Advanced Materials*, **20**, 4793 (2008).
- [97] M. P. Hiscocks, K. Ganesan, W. R. McKenzie, B. C. Gibson, F. Ladouceur, and S. Praver, "Towards characterisation of millimetre length waveguides and new fabrication method for nanoscale diamond photonic structures," *Diamond and Related Materials*, **20**, 556-559 (2011).
- [98] Y. Tzeng, J. Wei, J. T. Woo, and W. Lanford, "Freestanding Single-Crystalline Chemically Vapor-Deposited Diamond Films," *Applied Physics Letters*, **63**, 2216 (1993).
- [99] I. Aharonovich, J. C. Lee, A. P. Magyar, B. B. Buckley, C. G. Yale, D. D. Awschalom, and E. L. Hu, "Homoeptaxial Growth of Single Crystal Diamond Membranes for Quantum Information Processing," *Advanced Materials*, **24**, Op54-Op59 (2012).
- [100] H. Yamada, A. Chayahara, Y. Mokuno, N. Tsubouchi, S. Shikata, and N. Fujimori, "Developments of elemental technologies to produce inch-size single-crystal diamond wafers," *Diamond and Related Materials*, **20**, 616-619 (2011).
- [101] I. Bayn, B. Meyler, J. Salzman, and R. Kalish, "Triangular nanobeam photonic cavities in single-crystal diamond," *New Journal of Physics*, **13**, 025018 (2011).
- [102] L. Marseglia, J. P. Harrison, J. P. Hadden, A. Young, F. Jelezko, B. Naydenov, J. Meijer, A. C. Stanley-Clarke, Y. L. D. Ho, J. L. O'Brien, and J. G. Rarity, "Photonic crystal defect cavities coupled to N-V centres in diamond," in 36th European Conference and Exhibition on Optical Communication (Ecoc) (2010).
- [103] A. Faraon, P. E. Barclay, C. Santori, K. M. C. Fu, and R. G. Beausoleil, "Resonant enhancement of the zero-phonon emission from a colour centre in a diamond cavity," *Nature Photonics*, **5**, 301-305 (2011).
- [104] B. J. M. Hausmann, B. Shields, Q. M. Quan, P. Maletinsky, M. McCutcheon, J. T. Choy, T. M. Babinec, A. Kubanek, A. Yacoby, M. D. Lukin, and M. Loncar, "Integrated Diamond Networks for Quantum Nanophotonics," *Nano Letters*, **12**, 1578-1582 (2012).
- [105] E. Gu, H. W. Choi, C. Liu, C. Griffin, J. M. Girkin, I. M. Watson, M. D. Dawson, G. McConnell, and A. M. Gurney, "Reflection/transmission confocal microscopy characterization of single-crystal diamond microlens arrays," *Applied Physics Letters*, **84**, 2754 (2004).
- [106] C. L. Lee, E. Gu, and M. D. Dawson, "Micro-cylindrical and micro-ring lenses in CVD diamond," *Diamond and Related Materials*, **16**, 944-948 (2007).
- [107] A. M. Zaitsev, "Optical Properties of Diamond: A Data Handbook" (Springer, Berlin, 2001).
- [108] I. Aharonovich, S. Castelletto, D. A. Simpson, C. H. Su, A. D. Greentree, and S. Praver, "Diamond-based single-photon emitters," *Reports on Progress in Physics*, **74**, 076501 (2011).
- [109] T. Gaebel, M. Domhan, I. Popa, C. Wittmann, P. Neumann, F. Jelezko, J. R. Rabeau, N. Stavrias, A. D. Greentree, S. Praver, J. Meijer, J. Twamley, P. R. Hemmer, and J. Wrachtrup, "Room-

- temperature coherent coupling of single spins in diamond*," Nature Physics, **2**, 408-413 (2006).
- [110] A. Beveratos, R. Brouri, T. Gacoin, A. Villing, J. P. Poizat, and P. Grangier, "Single photon quantum cryptography," Physical Review Letters, **89**, 187901 (2002).
- [111] V. Jacques, E. Wu, F. Grosshans, F. Treussart, P. Grangier, A. Aspect, and J. F. Roch, "Experimental realization of Wheeler's delayed-choice gedanken experiment," Science, **315**, 966-968 (2007).
- [112] D. Le Sage, L. M. Pham, N. Bar-Gill, C. Belthangady, M. D. Lukin, A. Yacoby, and R. L. Walsworth, "Efficient photon detection from color centers in a diamond optical waveguide," Physical Review B, **85**, 121202 (2012).
- [113] R. P. Mildren, and A. Sabella, "Highly efficient diamond Raman laser," Optics Letters, **34**, 2811-2813 (2009).
- [114] A. Sabella, J. A. Piper, and R. P. Mildren, "1240 nm diamond Raman laser operating near the quantum limit," Optics Letters, **35**, 3874-3876 (2010).
- [115] J. P. M. Feve, K. E. Shortoff, M. J. Bohn, and J. K. Brasseur, "High average power diamond Raman laser," Optics Express, **19**, 913-922 (2011).
- [116] D. C. Parrotta, A. J. Kemp, M. D. Dawson, and J. E. Hastie, "Tunable continuous-wave diamond Raman laser," Optics Express, **19**, 24165-24170 (2011).
- [117] E. Granados, D. J. Spence, and R. P. Mildren, "Deep ultraviolet diamond Raman laser," Optics Express, **19**, 10857-10863 (2011).
- [118] R. P. Mildren, D. W. Coutts, and D. J. Spence, "All-solid-state parametric Raman anti-Stokes laser at 508 nm," Optics Express, **17**, 810-818 (2009).
- [119] O. Ambacher, "Growth and applications of Group III nitrides," Journal of Physics D-Applied Physics, **31**, 2653-2710 (1998).
- [120] S. Nakamura, "GaN Growth Using GaN Buffer Layer," Japanese Journal of Applied Physics Part 2-Letters, **30**, L1705-L1707 (1991).
- [121] P. R. Hageman, J. J. Schermer, and P. K. Larsen, "GaN growth on single-crystal diamond substrates by metalorganic chemical vapour deposition and hydride vapour deposition," Thin Solid Films, **443**, 9 (2003).
- [122] H. X. Jiang, and J. Y. Lin, "III-nitride quantum devices - Microphotonics," Critical Reviews in Solid State and Materials Sciences, **28**, 131-183 (2003).
- [123] S. Nakamura, T. Mukai, and M. Senoh, "High-Power GaN P-N-Junction Blue-Light-Emitting Diodes," Japanese Journal of Applied Physics Part 2-Letters, **30**, L1998-L2001 (1991).
- [124] S. Nakamura, S. J. Pearton, and G. Fasol, "The blue laser diode: the complete story" (Springer, 2000).
- [125] P. W. Roth, A. J. Maclean, D. Burns, and A. J. Kemp, "Directly diode-laser-pumped Ti:sapphire laser," Optics Letters, **34**, 3334-3336 (2009).
- [126] J. D. McKendry, D. Massoubre, S. Zhang, B. R. Rae, R. P. Green, E. Gu, R. K. Henderson, A. E. Kelly, and M. Dawson, "Visible-Light Communications Using a CMOS-Controlled Micro-Light-Emitting-Diode Array," Journal of Lightwave Technology, **30**, 61 (2012).
- [127] O. Skorka, B. Meyler, and J. Salzman, "Propagation loss in GaN-based ridge waveguides," Applied Physics Letters, **84**, 3801 (2004).
- [128] R. Hui, S. Taherion, Y. Wan, J. Li, S. X. Jin, J. Y. Lin, and H. X. Jiang, "GaN-based waveguide devices for long-wavelength optical communications," Applied Physics Letters, **82**, 1326-1328 (2003).
- [129] R. Q. Hui, Y. T. Wan, J. Li, S. X. Jin, J. Y. Lin, and H. X. Jiang, "III-nitride-based planar lightwave circuits for long wavelength optical communications," IEEE Journal of Quantum Electronics, **41**, 100-110 (2005).
- [130] R. Geiss, A. Chowdhury, C. M. Staus, H. M. Ng, S. S. Park, and J. Y. Han, "Low loss GaN at 1550 nm," Applied Physics Letters, **87**, 132107 (2005).
- [131] A. Lupu, F. H. Julien, S. Golka, G. Pozzovivo, G. Strasser, E. Baumann, F. Giorgetta, D. Hofstetter, S. Nicolay, M. Mosca, E. Feltn, J. F. Carlin, and N. Grandjean, "Lattice-matched GaN-InAlN waveguides at  $\lambda=1.55 \mu m$  grown by metal-organic vapor phase epitaxy," IEEE Photonics Technology Letters, **20**, 102-104 (2008).
- [132] R. Dahal, C. Ugolini, J. Y. Lin, H. X. Jiang, and J. M. Zavada, "Erbium-doped GaN optical amplifiers operating at  $1.54 \mu m$ ," Applied Physics Letters, **95**, 111109 (2009).
- [133] A. Stolz, E. Cho, E. Dogheche, Y. Androussi, D. Troadec, D. Pavlidis, and D. Decoster, "Optical waveguide loss minimized into gallium nitride based structures grown by metal organic vapor phase epitaxy," Applied Physics Letters, **98**, 161903 (2011).

- [134] H. Sodabanlu, J. S. Yang, T. Tanemura, M. Sugiyama, Y. Shimogaki, and Y. Nakano, "Intersubband absorption saturation in AlN-based waveguide with GaN/AlN multiple quantum wells grown by metalorganic vapor phase epitaxy," *Applied Physics Letters*, **99**, 151102 (2011).
- [135] M. Abe, H. Sato, I. Shoji, J. Suda, M. Yoshimura, Y. Kitaoka, Y. Mori, and T. Kondo, "Accurate measurement of quadratic nonlinear-optical coefficients of gallium nitride," *Journal of the Optical Society of America B-Optical Physics*, **27**, 2026-2034 (2010).
- [136] N. A. Sanford, A. V. Davydov, D. V. Tsvetkov, A. V. Dmitriev, S. Keller, U. K. Mishra, S. P. DenBaars, S. S. Park, J. Y. Han, and R. J. Molnar, "Measurement of second order susceptibilities of GaN and AlGaIn," *Journal of Applied Physics*, **97**, 053512 (2005).
- [137] R. C. Miller, W. A. Nordland, and Bridenba.Pm, "Dependence of Second-Harmonic-Generation Coefficients of Linbo3 on Melt Composition," *Journal of Applied Physics*, **42**, 4145 (1971).
- [138] D. Coquillat, G. Vecchi, C. Comaschi, A. M. Malvezzi, J. Torres, and M. L. d'Yerville, "Enhanced second- and third-harmonic generation and induced photoluminescence in a two-dimensional GaN photonic crystal," *Applied Physics Letters*, **87**, 101106 (2005).
- [139] C. Xiong, W. Pernice, K. K. Ryu, C. Schuck, K. Y. Fong, T. Palacios, and H. X. Tang, "Integrated GaN photonic circuits on silicon (100) for second harmonic generation," *Optics Express*, **19**, 10462-10470 (2011).
- [140] S. Pezzagna, J. Brault, M. de Micheli, P. Vennéguès, A. D. Wieck, and J. Massies, "GaN, a new material for integrated nonlinear optics," in *European Conference on Integrated Optics (Copenhagen, 2007)*.
- [141] I. Cimalla, F. Will, K. Tonisch, M. Niebelschutz, V. Cimalla, V. Lebedev, G. Kittler, M. Himmerlich, S. Krischok, J. A. Schaefer, M. Gebinoga, A. Schober, T. Friedrich, and O. Ambacher, "AlGaIn/GaN biosensor - effect of device processing steps on the surface properties and biocompatibility," *Sensors and Actuators B-Chemical*, **123**, 740-748 (2007).
- [142] X. D. Fan, I. M. White, S. I. Shopova, H. Y. Zhu, J. D. Suter, and Y. Z. Sun, "Sensitive optical biosensors for unlabeled targets: A review," *Analytica Chimica Acta*, **620**, 8 (2008).
- [143] M. Bass, "Handbook of Optics" (2009).
- [144] D. Brunner, H. Angerer, E. Bustarret, F. Freudenberg, R. Hopler, R. Dimitrov, O. Ambacher, and M. Stutzmann, "Optical constants of epitaxial AlGaIn films and their temperature dependence," *Journal of Applied Physics*, **82**, 5090-5096 (1997).
- [145] M. C. Pujol, M. A. Bursukova, F. Guell, X. Mateos, R. Sole, J. Gavalda, M. Aguilo, J. Massons, F. Diaz, P. Klopp, U. Griebner, and V. Petrov, "Growth, optical characterization, and laser operation of a stoichiometric crystal KYb(WO4)2," *Physical Review B*, **65**, 165121 (2002).
- [146] A. A. Lagatsky, N. V. Kuleshov, and V. P. Mikhailov, "Diode-pumped CW lasing of Yb : KYW and Yb : KGW," *Optics Communications*, **165**, 71 (1999).
- [147] U. Griebner, S. Rivier, V. Petrov, M. Zorn, G. Erbert, M. Weyers, X. Mateos, M. Aguilo, J. Massons, and F. Diaz, "Passively mode-locked Yb : KLu(WO4)2 oscillators," *Optics Express*, **13**, 3465-3470 (2005).
- [148] R. Peters, C. Krankel, K. Petermann, and G. Huber, "Power scaling potential of Yb : NGW in thin disk laser configuration," *Applied Physics B-Lasers and Optics*, **91**, 25 (2008).
- [149] K. Petermann, D. Fagundes-Peters, J. Johannsen, M. Mond, V. Peters, J. J. Romero, S. Kutovoi, J. Speiser, and A. Giesen, "Highly Yb-doped oxides for thin-disc lasers," *Journal of Crystal Growth*, **275**, 135-140 (2005).
- [150] F. D. Patel, E. C. Honea, J. Speth, S. A. Payne, R. Hutcheson, and R. Equall, "Laser demonstration of Yb3Al5O12 (YbAG) and materials properties of highly doped Yb : YAG," *IEEE Journal of Quantum Electronics*, **37**, 135-144 (2001).
- [151] H. J. Zhang, Y. G. Yu, Y. Cheng, J. H. Liu, H. X. Li, W. W. Ge, X. F. Cheng, X. G. Xu, J. Y. Wang, and M. H. Jiang, "Growth of YbVO4 stoichiometric crystal," *Journal of Crystal Growth*, **283**, 438-443 (2005).
- [152] S. N. Bagaev, S. M. Vatnik, A. P. Maiorov, A. A. Pavlyuk, and D. V. Plakushchev, "The spectroscopy and lasing of monoclinic Tm : KY(WO4)2 crystals," *Quantum Electronics*, **30**, 310-314 (2000).
- [153] N. V. Kuleshov, A. A. Lagatsky, A. V. Podlipensky, V. P. Mikhailov, A. A. Kornienko, E. B. Dunina, S. Hartung, and G. Huber, "Fluorescence dynamics, excited-state absorption, and stimulated emission of Er3+ in KY(WO4)2," *Journal of the Optical Society of America B-Optical Physics*, **15**, 1205-1212 (1998).
- [154] M. M. Han, and G. F. Wang, "Crystal growth and spectral properties of Nd3+ : KY(WO4)2 crystal," *Journal of Crystal Growth*, **247**, 551-554 (2003).

- [155] P. Klopp, U. Griebner, V. Petrov, X. Mateos, M. A. Bursukova, M. C. Pujol, R. Sole, J. Gavaldà, M. Aguilo, F. Guell, J. Massons, T. Kirilov, and F. Diaz, "*Laser operation of the new stoichiometric crystal KYb(WO<sub>4</sub>)<sub>2</sub>*," Applied Physics B-Lasers and Optics, **74**, 185-189 (2002).
- [156] P. Klopp, V. Petrov, U. Griebner, V. Nesterenko, V. Nikolov, M. Marinov, M. A. Bursukova, and M. Galan, "*Continuous-wave lasing of a stoichiometric Yb laser material: KYb(WO<sub>4</sub>)<sub>2</sub>*," Optics Letters, **28**, 322-324 (2003).

# Chapter 2

## Theory and Modelling of Waveguides

---

### **Abstract**

This chapter presents the theory and modelling required for a description of the waveguide devices used throughout this thesis. The transverse resonance condition is derived with analytical alternatives and extended to describe the rib waveguide. The single-mode design requirements for the rib waveguide are considered. A new extension to the effective index method is proposed. Computational techniques including the finite element method and beam propagation method are described. This results in 5 different methods to calculate the effective mode index and the accuracy of all models is compared.

### **2.1 Waveguide fundamental theory**

Light was shown to be a form of electromagnetic radiation by J. C. Maxwell. As such, the propagation of light in a dielectric may be described by Maxwell's equations [1]. Light may be confined in regions of increased refractive index relative to the surroundings in a structure known as a waveguide. This optical confinement may be described simply and elegantly with Maxwell's equations. Yet, research in the field of optical waveguides continues to discover novel guiding structures, such as the slot [2] and plasmonic [3] waveguide, 150 years after the complete description of electromagnetic radiation. The waveguide geometries considered in this work are traditional in the sense that guiding occurs in areas of increased refractive index that are larger than the diffraction limit. The focus is on large cross-sectional area rib waveguides with moderately high refractive index differences. This waveguide geometry offers some atypical transverse mode characteristics that are only recently well-reported in the literature.

Much of the fundamental theory and its application to integrated optics is discussed in a range of textbooks, including references [4-8]. Some topics less well reported in the literature include Marcatili's approximations, the rib waveguide and the four-layer waveguide. The simulation processes involved in more modern computational methods are also not widely documented.

## Chapter 2 – Theory and Modelling of Waveguides

The time-harmonic Maxwell equations in vector form are the starting point for this work:

$$\nabla \times \mathbf{E} = -\mu \frac{d\mathbf{H}}{dt}, \quad \nabla \times \mathbf{H} = \varepsilon \frac{d\mathbf{E}}{dt}, \quad \nabla \cdot \varepsilon \mathbf{E} = 0, \quad \nabla \cdot \mu \mathbf{H} = 0 \quad (2.1)$$

Where  $\mathbf{E}$  is the electric field,  $\mathbf{H}$  is the magnetic field,  $\varepsilon$  is the permittivity of the material. It is assumed that there is no magnetic field, no free charge and no free current. The angular wavenumber, magnitude of the  $k$  vector, or free space propagation constant is defined as:

$$k = \frac{2\pi}{\lambda} \quad (2.2)$$

Where  $\lambda$  is the free-space wavelength. The adjusted wavelength inside the medium will not be referred to in this work. The refractive index of the material is defined as:

$$n = \sqrt{\varepsilon_r \mu_r} \quad (2.3)$$

Where  $\varepsilon_r$  is the material relative permittivity and  $\mu_r$  is the material relative permeability. For convenience it is useful to use the vector Helmholtz form of Maxwell's equations which can be derived from vector identities:

$$\begin{aligned} \nabla \times (\nabla \times \mathbf{E}) &= k^2 n^2 \mathbf{E}, & \nabla \times \frac{1}{n^2} (\nabla \times \mathbf{E}) &= k^2 \mathbf{E} \\ \nabla \mathbf{E} + k^2 n^2 \mathbf{E} &= -\nabla (\nabla \ln n^2 \cdot \mathbf{E}), & \nabla \mathbf{H} + k^2 n^2 \mathbf{H} &= -\nabla (\ln n^2) \times \nabla \times \mathbf{H} \end{aligned} \quad (2.4)$$

For homogeneous media these equations simplify to:

$$\nabla \mathbf{E} + k^2 n^2 \mathbf{E} = 0, \quad \nabla \mathbf{H} + k^2 n^2 \mathbf{H} = 0 \quad (2.5)$$

These can be expressed in scalar form as shown here for the electric field:

$$\frac{\partial^2 E}{\partial x^2} + \frac{\partial^2 E}{\partial y^2} + \frac{\partial^2 E}{\partial z^2} + k^2 n(x, y, z)^2 E = 0 \quad (2.6)$$

Equation (2.6) is the foundation for the derivation of the transverse resonance condition that will form the basis for the description of light confinement.

### 2.1.1 Transverse resonance condition

The transverse resonance condition may be described with an equation and is the fundamental criterion used to describe the behaviour of light in a waveguide. It predicts that the transverse field is split into a number of discrete solutions known as

## Chapter 2 – Theory and Modelling of Waveguides

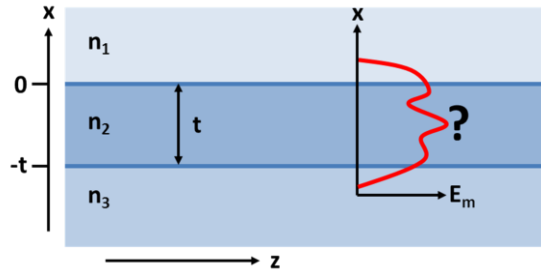


Figure 2. 1: Schematic of the 3-layer planar waveguide problem with distinct separate homogeneous refractive index regions.

modes. Each mode is a solution to the transverse resonance equation that determines the number of guided modes and the properties of these modes. These solutions provide the data required to calculate the distribution of the electromagnetic field in relation to the waveguide structure. The transverse resonance equation may be derived from the fundamental Maxwell equations or interestingly and intuitively from a geometrical approach. To be concise, the transverse resonance condition is derived here for the transverse electric (TE) 3-layer planar waveguide scenario. This restricts the electric field to the transverse direction  $y$  (in the direction of the page) as shown in Figure 2. 1.

### a) Derivation from the scalar Helmholtz equation

From the one-dimensional scalar form of the Helmholtz equation, from Equation (2.6), three regions can be defined which depend on the three respective refractive indices as shown in Figure 2. 1. It is possible to consider each region as a homogenous material allowing Equation (2.5) to hold true. At the boundaries, however, different conditions must be met, and this is described in 2.1.2. The solution to the transverse resonance criterion involves the introduction of an effective index  $N$  which is used to describe the propagation characteristics of each discrete guided mode which is considered initially to spread over all three regions:

$$\begin{aligned}
 \frac{\partial^2}{\partial x^2} E_y(x, z, t) + k^2(n_1^2 - N^2)E_y(x, z, t) &= 0 \\
 \frac{\partial^2}{\partial x^2} E_y(x, z, t) + k^2(n_2^2 - N^2)E_y(x, z, t) &= 0 \\
 \frac{\partial^2}{\partial x^2} E_y(x, z, t) + k^2(n_3^2 - N^2)E_y(x, z, t) &= 0 \\
 E_y(x, z, t) &= E_m(x)e^{i(\omega t - Nkz)}
 \end{aligned}
 \tag{2.7}$$

## Chapter 2 – Theory and Modelling of Waveguides

To find a description of the guided mode, consideration of the two outer regions of lower refractive index can be simplified by assuming that the amplitude of the transverse electric field must reduce to zero at infinity. There are solutions for which it does not and these are known as radiation modes which are not of interest for this section. Secondly, the electric field  $E_y$  is considered to be continuous at material boundaries of  $x=0$  and  $x=-t$ , which is valid for TE modes as discussed in section 2.1.2. For convenience, terms  $h$ ,  $p$  and  $q$  are introduced which are in a similar format to those chosen by A. Yariv [9]. These terms refer to distinct regions of the waveguide and are sometimes called the transverse propagation constants.

$$h = k\sqrt{n_2^2 - N^2}, \quad q = k\sqrt{N^2 - n_1^2}, \quad p = k\sqrt{N^2 - n_3^2} \quad (2.8)$$

Equation (2.7) may now be solved considering these restrictions and new terms:

$$E_m = \begin{cases} C \exp(-qx), & 0 \leq x < \infty \\ C \left[ \cos(hx) - \frac{q}{h} \sin(hx) \right], & 0 \leq x \leq -t \\ C \left[ \cos(-ht) - \frac{q}{h} \sin(-ht) \right] \exp p(x+t), & -t \leq x < -\infty \end{cases} \quad (2.9)$$

Equation (2.9) is an important result and describes fully the electric component of the electromagnetic field for a guided mode in a waveguide.

The third restriction considers the continuity of the magnetic field at the boundary in the  $z$  direction.  $H_z$  is proportional to the derivative of  $E_y$  from Maxwell equations. Thus the transverse resonance can be found by examining the derivative of the function  $E_m$  at the point  $x=-t$ .

$$\begin{aligned} \frac{\delta}{\delta x} \left[ \cos(hx) - \frac{q}{h} \sin(hx) \right] &= \frac{\delta}{\delta x} \left[ \cos(-ht) - \frac{q}{h} \sin(-ht) \right] \exp p(x+t) \\ h \sin(ht) - q \cos(ht) &= p \cos(ht) + \frac{pq}{h} \sin(ht) \\ \tan(ht) &= \frac{p+q}{h - \frac{pq}{h}} \end{aligned} \quad (2.10)$$

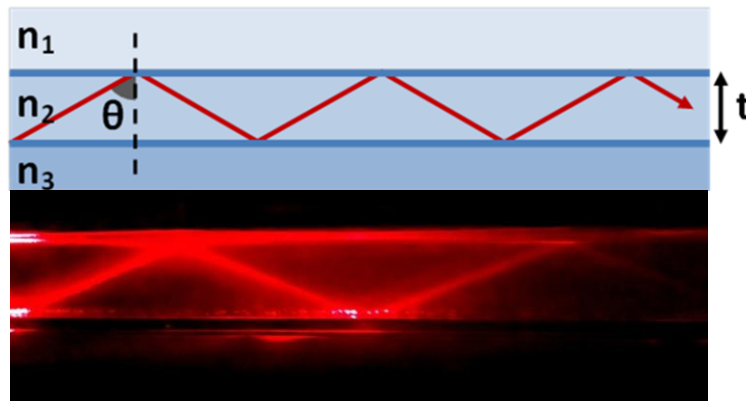


Figure 2. 2: **(a)** Schematic of geometrical optics approach and terms used. **(b)** Photograph of an in-house made total internal reflection of a collimated red diode-laser output beam in water with milk for scattering.

Equation (2.10) is the transverse resonance equation in tangent form. The tangent function is repetitive thus will describe all the discrete modes supported by the waveguide in the range  $n_2 < N < n_3$ .

### **b) Derivation from the geometrical optics approach**

Although the geometrical optics approach has a number of limitations it is surprisingly accurate for a range of situations. It was the method first used to accurately describe the behaviour of waveguides [10, 11] and is the most intuitive. It can be used to accurately derive the same transverse resonance condition for waveguides and is shown here for completeness. A relevant schematic and photograph are shown in Figure 2. 2.

By examining the critical angle at a boundary between two materials it is easy to understand the mechanism for guiding light down a region with increased refractive index. If the horizontal propagation were ignored for a moment, it is possible to think of the light bouncing up and down as if it were in a Fabry-Perot resonator. Thus, for resonance to occur, each round trip must produce a change of phase of  $2m\pi$ , where  $m$  is an integer. The phase for each round-trip bounce can be found from the vertical component of the zig-zag which will depend on the bounce angle. There is a further phase change from each reflection that can be determined from the Goos-Hänchen shift [12] and is defined for each boundary with the term  $\Phi$ :

## Chapter 2 – Theory and Modelling of Waveguides

$$2m\pi = kn_2t \cos \theta - 2\Phi_{21} - 2\Phi_{23}$$

$$\Phi_{21} = \tan^{-1} \left( \frac{\sqrt{n_2^2 \sin^2 \theta - n_1^2}}{n_2 \cos \theta} \right), \quad \Phi_{23} = \tan^{-1} \left( \frac{\sqrt{n_2^2 \sin^2 \theta - n_3^2}}{n_2 \cos \theta} \right) \quad (2.11)$$

By using the definition of the effective index,  $N$ , this can be re-written from Equation (2.11) without angles:

$$N = n_2 \sin \theta, \quad \cos \theta = \sqrt{1 - \sin^2 \theta}$$

$$kt\sqrt{n_2^2 - N^2} = \tan^{-1} \left( \frac{\sqrt{N^2 - n_1^2}}{\sqrt{n_2^2 - N^2}} \right) + \tan^{-1} \left( \frac{\sqrt{N^2 - n_3^2}}{\sqrt{n_2^2 - N^2}} \right) + m\pi \quad (2.12)$$

Using the predefined terms for simplification from Equation (2.8) this may be further simplified:

$$ht = \tan^{-1} \left( \frac{q}{h} \right) + \tan^{-1} \left( \frac{p}{h} \right) + m\pi, \quad \tan^{-1}(x) + \tan^{-1}(y) = \tan^{-1} \left( \frac{x+y}{1-xy} \right)$$

$$\tan(ht) = \frac{p+q}{h - \frac{pq}{h}} \quad (2.13)$$

Where this is the transverse resonance equation and is identical to that found with a complete description from Maxwell equations in Equation (2.10).

### c) Solutions to the transverse resonance condition

The transverse resonance equation is transcendental, meaning it is not expressed explicitly ( $h$  appears on both sides of the equation). Solutions to the transverse resonance transcendental equation can be found numerically by iteration and are often displayed graphically. It is preferable to introduce new terms to simplify the description of these solutions.

Two new unitless parameters are introduced that indicate the capability for a waveguide to guide modes. Increasing the thickness or refractive index difference of the waveguide or reducing the wavelength all have the same effect. These are useful parameters to identify quickly the guiding properties of the waveguide. It is typical to only refer to the  $v$ -parameter, although the  $u$ -parameter provides similar information:

$$u = tk\sqrt{n_2^2 - n_1^2}, \quad v = tk\sqrt{n_2^2 - n_3^2} \quad (2.14)$$

Another convenient parameter to introduce is the normalised guide parameter,  $b$ . This normalised guide index is 0 when the guided mode has the same effective index as the

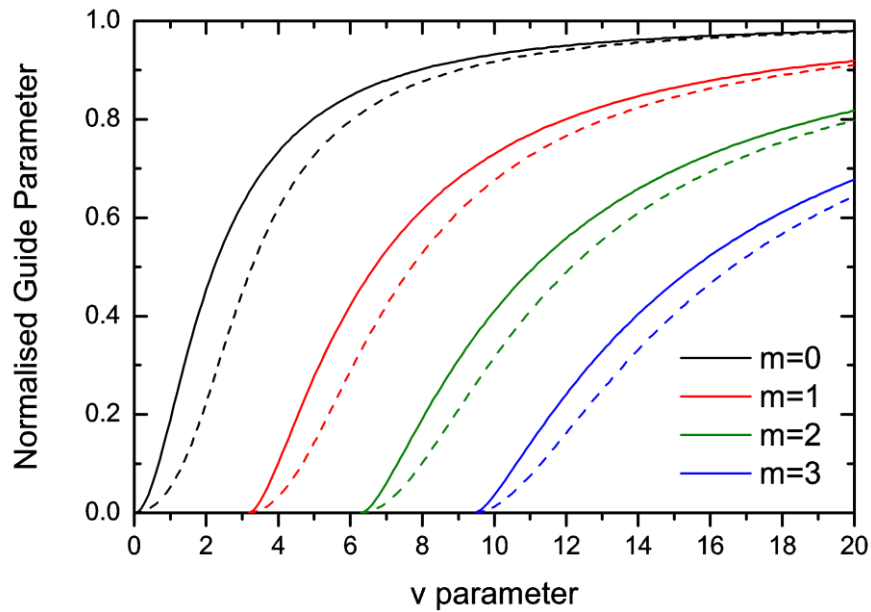


Figure 2. 3: The normalised guide parameter for the first four modes of a symmetrical planar waveguide with varying v-parameter. The solid lines indicate TE solutions and the dashed lines indicate TM solutions. No specific data on the refractive indices, wavelengths or dimensions are required for TE modes. The TM modes are calculated with a guide index of 1.5 and a cladding index of 1.

cladding and is 1 when the guided mode has the same effective index as the guide core. The mode effective index lies between these points:

$$b = \frac{N^2 - n_3^2}{n_2^2 - n_3^2} \quad (2.15)$$

The root-finding algorithm Ridder’s method [13] was used to find solutions to the transverse resonance equation. Many commercial mathematical computing packages have embedded fast root-solvers and all are suitable. The normalised guide parameter is calculated for varying v-parameter for TE and TM modes in a symmetrical ( $n_1=n_3$ ) waveguide and is shown in Figure 2. 3. Conveniently TE solutions only depend on the v-parameter itself and not different ratios of parameters that produce the same v-parameter. TM solutions require additional specification of each refractive index.

Figure 2. 3 shows that a symmetrical waveguide will always support at least one guided mode because the normalised guide parameter is always above zero for the fundamental mode. In practice, however, a guided mode is usually found to be impractical before this point due to the increasing mode size. Successive modes become supported when the v-parameter is a multiple of  $\pi$  for symmetrical waveguides. This can lead to a great deal of simplification of parameters and simple criteria for single-

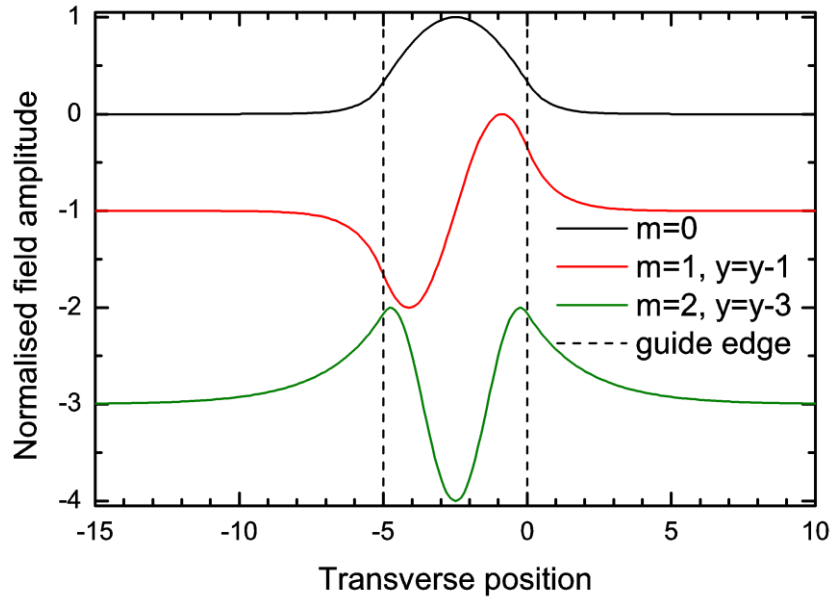


Figure 2. 4: The normalised electric field amplitude is shown for the three guided modes of a symmetrical waveguide with  $n_1=n_3=1$ ,  $n_2=1.01$ ,  $\lambda=600$  nm and  $t=5$   $\mu\text{m}$ . The waveguide/cladding interface is shown with a dotted line. The  $v$ -parameter for this waveguide is calculated to be 7.4 thus it is capable of supporting only 3 modes. The curves are displaced vertically respectively by 0, -1 and -3 for improved visibility.

mode behaviour. The normalised guide parameter is below  $\sim 0.6$  for single-mode waveguides. This requirement means that nearly all single-mode waveguides are weakly guiding with a significant proportion of their power in the cladding. It is shown that TM modes will always have a lower normalised guide parameter due to the different requirements at the boundaries.

Solutions to the transverse resonance equation only indicate the modal properties, but not their electromagnetic profiles. The mode profiles can be calculated with Equation (2.9). A waveguide design was selected such that it would only support 3 modes by appropriate selection of refractive index change, dimensions and wavelength. The transverse mode profiles are shown in Figure 2. 4. As the mode order is increased the effective index decreases and an increasing proportion of the power is guided in the cladding. It is not simple enough to presume that the guided mode's effective index is simply a 'weighting factor'. The effective index takes into account the transverse mode structure. This can be understood by the geometrical optics approximation where higher order modes have lower effective indices simple due to multiple bounces as they travel down the waveguide.

## Chapter 2 – Theory and Modelling of Waveguides

### 2.1.2 Polarisation states and boundary conditions

Waveguides are capable of guiding two orthogonal polarisation states referred to as transverse electric (TE) and transverse magnetic (TM). The TE mode is defined for when the electric field is parallel with the plane of the waveguide interface, and the TM is when the electric field is perpendicular to the interface.

The TE mode has electric field,  $E_y$ , parallel to the interface, a magnetic field,  $H_x$ , which is perpendicular to the interface and a magnetic field,  $H_z$ , in the propagation direction. These fields are related in the following way:

$$H_x = -\frac{kN}{\omega\mu_0} E_y, \quad H_z = -\frac{i}{\omega\mu_0} \frac{dE_y}{dx} \quad (2.16)$$

The TE polarisation state will observe continuity of all fields at the boundary.

The TM mode has magnetic field,  $H_y$ , parallel to the interface, an electric field,  $E_x$ , which is perpendicular to the interface and an electric field,  $E_z$ , in the propagation direction. These fields are related in the following way:

$$E_x = \frac{kN}{n_m^2 \omega \epsilon_0} H_y, \quad E_z = \frac{i}{n_m^2 \omega \epsilon_0} \frac{dH_y}{dx}, \quad m=1,2,3 \quad (2.17)$$

The inclusion of the material index in Equation (2.17) results in a discontinuity in the electric field at interfaces between high and low refractive index regions. For a material system such as diamond with an air cladding this will result in the electric field being 5.8 times larger on the air side of the interface than on the diamond side.

In a two-dimensional waveguide, guided modes will have TE-like interactions in one direction and TM like interactions in the other. TE modes are usually defined in this case with the electric field in the horizontal plane, parallel with any substrate interface. Furthermore, in a two-dimensional waveguide there are small regions in the waveguide, near the corners, where the fields are no longer parallel to any surface. Thus, sometimes the polarisation states are referred to as quasi-TE and quasi-TM, however the scalar approximation is accurate for most geometries.

### 2.1.3 Marcattili's analytical approximation for planar waveguides

The transcendental transverse resonance equation (2.10) and (2.13) is non-analytical, in the sense that computational methods are required, and thus makes the task of optimisation inconvenient. Large multi-order optimisations can become cumbersome

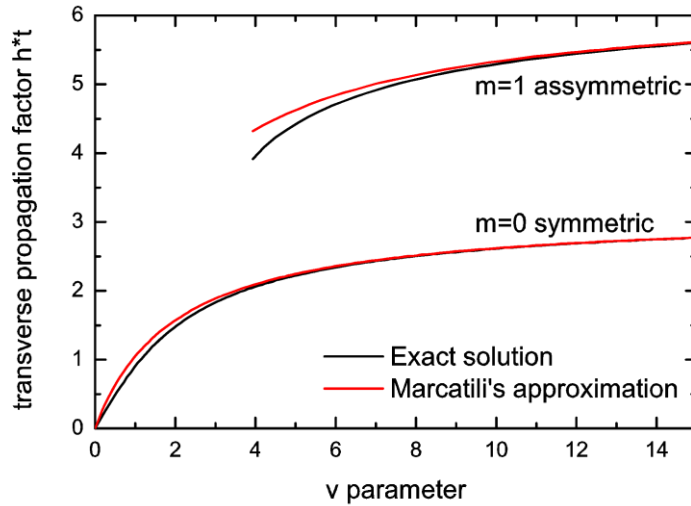


Figure 2. 5: The transverse propagation factor  $h^*t$  is shown for the fundamental mode of a symmetrical waveguide where no definition of refractive index, waveguide thickness or wavelength is required for calculation and the second mode in an asymmetrical waveguide with a cladding index of 1 and a substrate index of 2 to define the asymmetry.

and time consuming. A typical design process involves selecting a geometry that produces a guide with a specific mode area, thus a great number of calculations must be performed for optimisation. It is desirable to reduce this problem to an analytical solution to reduce computational demand. Furthermore, this provides a greater intuitive understanding of the problem and variables.

E. A. J. Marcatili proposed an analytical solution to the transverse resonance equation based on an asymptote which holds true for large  $v$ -parameters [14]. For large  $v$ -parameters  $h$  becomes negligibly small in comparison to  $u$  and  $v$ . The inverse tangents in equation (2.13) then becomes close to zero so the approximation  $\tan(x) \rightarrow x$  can be used.  $h$  can then be described by an asymptote which is explicit and only depends on the physical parameters of the waveguide. The  $K$  parameters are introduced for TM guiding:

$$h \rightarrow \frac{1}{t} \frac{\pi(m+1)}{1 + \frac{K_1}{u} + \frac{K_3}{v}}, \quad K_{1,3} = \begin{cases} \frac{n_{1,3}^2}{n_2^2}, & \text{for TM modes} \\ 1, & \text{for TE modes} \end{cases} \quad (2.18)$$

Where  $u$  and  $v$  are defined in Equation (2.14),  $m$  is the mode number,  $t$  is the waveguide thickness and  $n_{1,2,3}$  are the refractive indices as defined in Figure 2. 2. The guided mode effective index can be found from the definition of  $h$  in Equation (2.8):

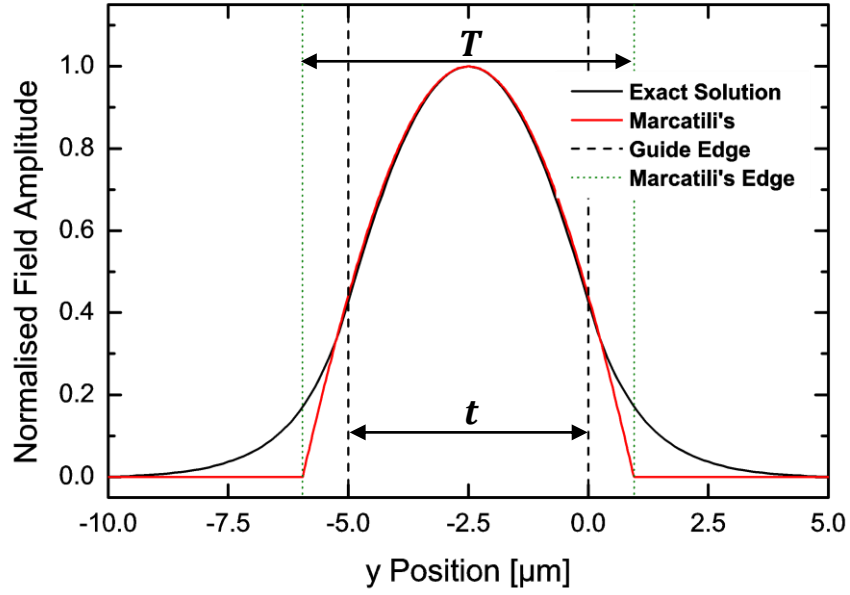


Figure 2. 6: Normalised electric field amplitude for the fundamental mode of a waveguide with  $n_1=n_3=1$ ,  $n_2=1.005$ ,  $t=5\mu\text{m}$  and  $\lambda=600\text{ nm}$ . Using Marcatili's approximation the modified width,  $T$ , is  $6.9\mu\text{m}$ .

$$N \rightarrow \sqrt{n_2^2 - \left( \frac{1}{t} \frac{\pi(m+1)}{1 + \frac{K_1}{u} + \frac{K_3}{v}} \right)^2} \quad (2.19)$$

Figure 2. 5 shows plots of  $h \cdot t$ , a convenient term which provides values of a similar order to the  $v$ -parameter. Marcatili's approximation in Equation (2.18) is compared to precise computation solutions for varying  $v$ -parameters in Figure 2. 5. The asymptotic solution is most accurate for high values of the  $v$ -parameter, away from cut-off conditions. This is when the planar waveguide is highly multimode. The approximation is also more accurate for symmetric waveguides and for the fundamental mode. This approximation is particularly useful for work in this thesis as the refractive index of diamond/GaN is high, and large-area waveguides are considered.

In order to calculate the transverse profile of the guided mode it is appropriate to define a new waveguide thickness  $T$  beyond which the electromagnetic field is set to 0:

$$T = t \left( 1 + \frac{K_1}{u} + \frac{K_3}{v} \right) \quad (2.20)$$

Figure 2. 6 shows how Marcatili's approximation may be used to calculate the guided mode profile. It should be noted that within the guide region and including at the waveguide boundary, the analytical solution remains fairly accurate.

### 2.1.4 Planar waveguide single-mode criteria

The precise number of transverse modes supported by a waveguide depends on the refractive index, the physical dimensions of the waveguide and the wavelength of the guided light. With use of the transverse resonance equation, a waveguide can be designed such that it guides only a single mode.

There are a number of applications which require the restriction of one guided transverse mode. These include optimal beam quality for light output from a waveguide, to prevent waveguide dispersion and to allow correct operation of various integrated optics devices such as directional couplers [15] and ring resonators. Charles K. Kao was awarded the 2009 Nobel Prize in Physics for theoretical work on the single-mode fibre [16]. A key design requirement for many waveguide based applications is therefore single-mode operation.

Single-mode operation can be defined as the region below cut-off of the second guided mode. The strict way to define cut-off, the point at which waveguiding begins (or ends) for a particular guided mode, has the following definition:

*The point at which a guided mode is supported in a waveguide is when the mode effective index is equal to that of the surrounding cladding or substrate's refractive index. – Strict cut-off criteria*

To locate the strict cut-off points the transverse resonance condition is solved by setting the guided mode effective index as the cladding index. So for cut-off of the second mode,  $N_{m=1} = n_3$ . This position defines the end of the single-mode region.

In practice, guided modes that are near cut-off are not useful, in the sense that they are weakly guided and exhibit large mode sizes that fill the cladding region. Alternative methods of defining single-mode behaviour based on 'usefulness' of mode area are presented in Chapter 3.

The cut-off condition for the fundamental mode is another interesting point – it can be seen in Figure 2. 3 that the cut-off point is  $v=0$  for a symmetrical waveguide, thus a mode will always be supported. This is also true for optical fibre due to symmetry. Asymmetrical waveguides do have a cut-off condition for the fundamental mode. This can be important for the design of high-index strip-loaded waveguides [17].

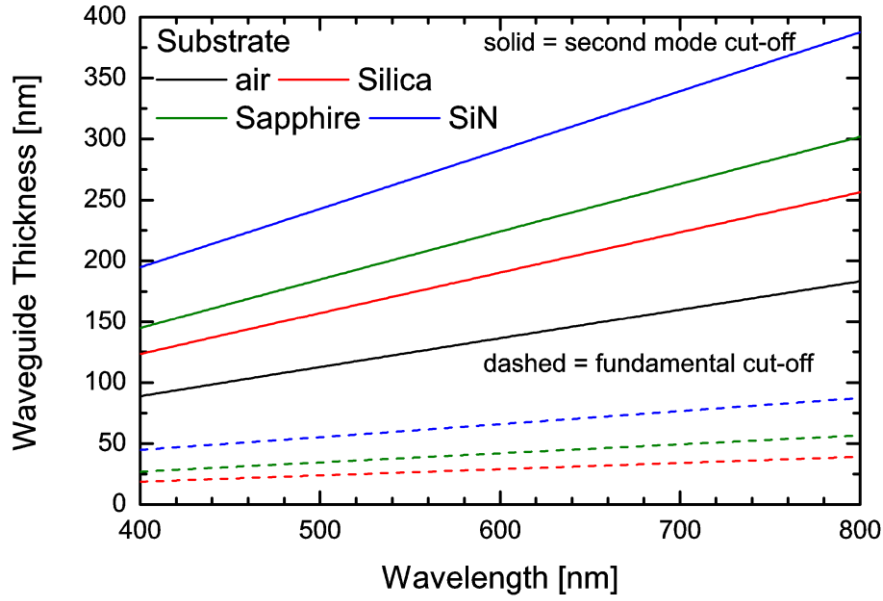


Figure 2. 7: The waveguide thickness for single mode operation and at cut-off for a planar diamond waveguide with different substrate materials for varying wavelength. The cladding is air with  $n_1=1$ . The refractive indices are calculated from their dispersion curves and are  $n_{\text{diamond}} = 2.41$ ,  $n_{\text{silicon nitride}} = 2.01$ ,  $n_{\text{sapphire}} = 1.77$ ,  $n_{\text{silica}} = 1.54$  at 630 nm. The material dispersion has negligible effect on the result for these materials. Below the solid line is single-mode and below the dashed line is cut-off (does not support a mode).

For the symmetrical waveguide the single-mode criteria is  $v < \pi$ . Figure 2. 7 (in black) shows the single-mode criteria for a symmetrical diamond waveguide, when the substrate and cladding is air. Waveguide dimensions for this diamond membrane are required to be below 180 nm for single-mode operation at visible wavelengths.

The asymmetrical single-mode criteria is different. From Equation (2.13) it can be seen that the phase change component for the cladding does not reduce to 0. Here  $n_1 < n_2 < n_3$  and  $N_{m=1} = n_3$  at the cut-off conditions. Thus the asymmetric single-mode criterion becomes:

$$V = \tan^{-1} \left( \frac{\sqrt{n_3^2 - n_1^2}}{\sqrt{n_2^2 - n_3^2}} \right) + \pi \quad (2.21)$$

Figure 2. 7 shows a range of single-mode criteria for asymmetric diamond waveguides with different substrate indices and a cladding of air.

By reducing the index difference between the core and substrate/cladding the waveguide can remain single mode for larger dimensions. When this substrate index is close to the core index, waveguide sizes can be significantly large whilst maintaining single-mode operation. To allow for simple fabrication methods and efficient

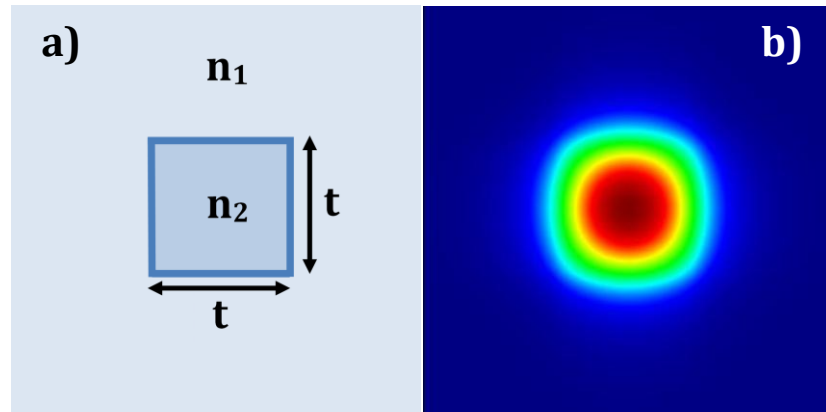


Figure 2. 8: **(a)** Schematic of a buried square channel waveguide where  $n_2 > n_1$ . **(b)** Electric field magnitude of the fundamental mode of a buried channel waveguide with  $t=5 \mu\text{m}$ ,  $\lambda=630 \text{ nm}$ ,  $n_2 = 1.005$  and  $n_1 = 1$ . Calculation performed by approximating the waveguide into two planar waveguides; horizontal and vertical.

input/output coupling it is typically necessary to use materials with low index contrasts to allow for large micron sized waveguides above the diffraction limit.

### 2.1.5 2D approximation with planar waveguide solutions

This work is focussed on the implementation of two-dimensional waveguides such that guiding occurs both the  $x$  and  $y$  directions. Full and correct solutions to Maxwell's equations in 2D usually require extensive and complete computation with mode solving software. However, it is possible to produce accurate approximations for a range of practical 2D waveguides with use of the planar transverse resonance condition. For situations where there are large amounts of symmetry, the solution of a 2D waveguide can be approximated by splitting the waveguide into constituent one dimensional waveguides. This simplification can be used to find solutions for the guided mode profiles and cut-off criteria using the planar waveguide equations.

A buried channel waveguide is considered for which the refractive index of the guide region is increased relative to the surroundings. This waveguide can be analysed by separating it into two constituent vertical and horizontal planar waveguide equivalents. Using Equations (2.9) and (2.10) for the vertical direction and the corresponding TM versions for the horizontal direction and is shown in Figure 2. 8. The approximation loses validity near the corners but remains accurate when taking slices through the centre of the mode profile.

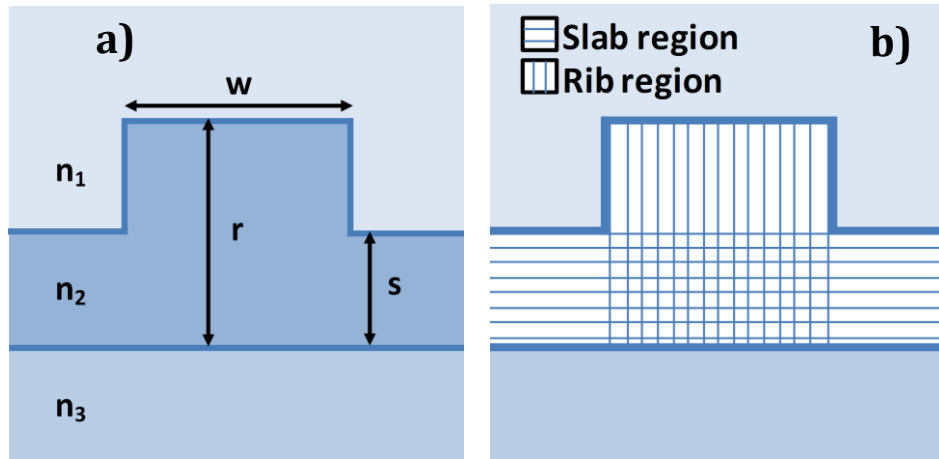


Figure 2. 9: **(a)** Schematic of a rib waveguide.  $r$  is the rib height,  $s$  is the slab height and  $w$  is the rib width. **(b)** Schematic of the same rib waveguide with slab and rib regions defined.

## 2.2 The rib waveguide – a single material waveguide

The rib waveguide is a special type of channel waveguide with two-dimensional confinement that is categorised as a single material waveguide. The key property of a single material waveguide is that the guided mode is restricted to a specific sub-region of one homogeneous material. On first inspection the structure should not offer two-dimensional confinement as the physical basis for confinement requires an increased refractive index relative to the surroundings. However, it can be shown that with the correct geometry, confinement can be maintained within a sub-region of one material. The rib waveguide and other single material waveguides have a number of unique properties which have historically been overlooked. Attention will be paid to the guiding properties of these waveguides, as they are investigated further in Chapters 3 and 4 for fabrication.

Figure 2. 9 shows a schematic of a rib waveguide with various dimensions and terms defined therein. The guided mode is confined in the rib region although there is no refractive index change between the rib and slab regions. The slab region is assumed to extend infinitely in the horizontal direction.

The slab thickness,  $s$ , does not need to be reduced such that the slab cannot support a mode. This is a point that is missed by some people that are new to the topic. In fact the modal characteristics rely on the slab waveguide being able to extract higher order modes. All dimensions may be much greater than the wavelength of light whilst maintaining single-mode operation. The simplest way to understand the guiding

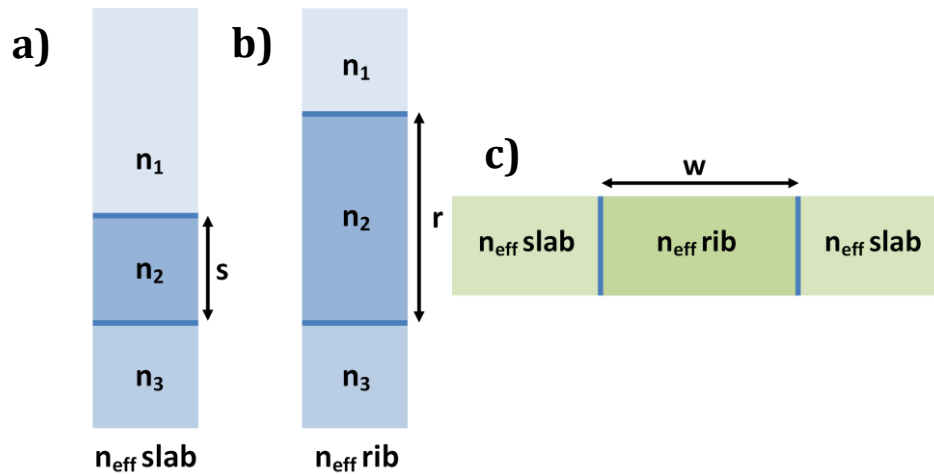


Figure 2. 10: Schematic of **(a)** the vertical planar waveguide equivalent of the slab region, **(b)** the vertical planar waveguide equivalent of the rib region and **(c)** the horizontal planar equivalent of the rib region using the effective indices calculated in a and b.

properties of this waveguide structure is through the technique of the effective index method (EIM).

### 2.2.1 The effective index method

As discussed in section 2.1.5, approximate 2D mode profile solutions can be found by subdividing a 2D problem into constituent 1D problems and convolving their solutions. In the same way we can find the guided mode effective index using a method known as the effective index method (EIM) [18].

Ignoring horizontal confinement for a moment: from planar waveguide analysis, fundamental mode light propagating in the rib region propagates with a guided mode index that is higher than if it were propagating in the slab region. Thus, fundamental mode light in the rib region must observe a reduction in effective index in order to ‘escape’ into the slab. The difference in these effective mode indices may be used to describe the horizontal confinement. This methodology is referred to as ‘the effective index method’ and involves the subdivision of the problem into constituent planar waveguides and using the effective indices to calculate a new 2D guided mode index as shown in Figure 2. 11.

Using the planar waveguide transverse resonance equation the  $n_{\text{eff slab}}$  and  $n_{\text{eff rib}}$  can be found based on their different thicknesses,  $s$  and  $r$ . The difference between these two values forms the basis for horizontal guiding as the rib region will always have a higher effective index than a thinner slab. Figure 2. 10 shows the planar waveguide effective index and the difference in  $N_{\text{eff}}$  between different thicknesses.

The horizontal guide strength is then defined by the difference in thickness between the rib and slab region. A large  $r/s$  provides a large horizontal effective index difference, or guide strength. This guiding mechanism is different to a channel waveguide where the guide strength is set purely by the refractive index difference. Figure 2. 10 b) shows that the index difference between these regions is found to vary with wavelength, among other parameters. Figure 2. 12 shows the horizontal  $v$ -parameter for different rib waveguide designs in comparison to a channel waveguide with a fixed index difference. The  $v$ -parameter is defined in Equation (2.14) where here the core region is the rib and the cladding region is the slab.

Figure 2. 12 highlights an often overlooked point; there is only a small change in the horizontal  $v$ -parameter for rib waveguides for changing wavelengths. This means that the rib waveguide can be single-mode for a large range of wavelengths which would not otherwise be possible for channel waveguides such as typical fibres. The near constant  $v$ -parameter for rib waveguides is due to the increase in effective index difference with wavelength, as shown in Figure 2. 10 b). This counteracts the normal reduction in  $v$ -parameter with increasing wavelength. The channel waveguide, conversely, has a rapidly decreasing  $v$ -parameter for increasing wavelength, creating wavelength dependent single-mode and multi-mode regions.

The effective index method is used to calculate the 2D guided mode index and is shown at the end of this chapter in Figure 2. 29 where it is compared to other methods. The effective index method is also extended beyond the typical 3-layer approach for greater accuracy in section 2.3.

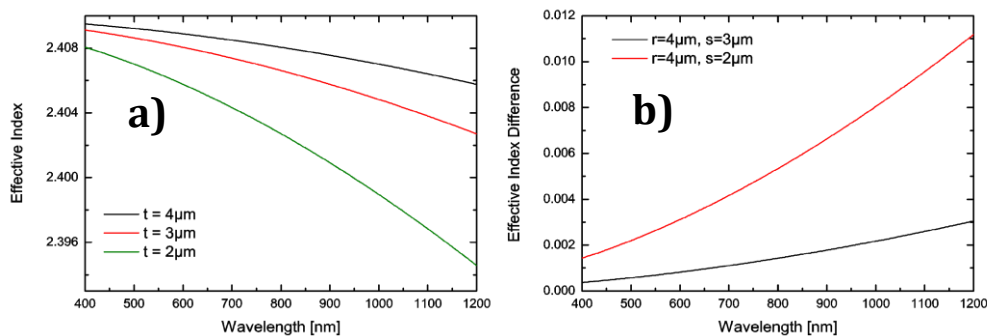


Figure 2. 11: **(a)** The effective index of planar waveguides with different thicknesses for varying wavelength. **(b)** The effective index difference between planar waveguides. The larger thickness represents the rib region and the smaller thickness represents the slab region.  $n_1=1, n_2=2.41, n_3=1.77$  for a and b.

### 2.2.2 The single-mode criteria of the rib waveguide

Understanding the full single-mode criteria of the single-material waveguide is non-trivial. However, some simplifications can offer great insight into the guiding properties of these waveguides. The single-mode criteria of the rib waveguide consist of a criterion for single-mode horizontal guidance and a separate criterion for single-mode vertical guidance.

The strict cut-off criteria, as used for the planar waveguides, can be applied to the rib waveguide: the mode is no longer guided when the mode effective index reaches that of the surrounding planar slab. At this point mode will have spread out laterally into the slab and extend infinitely (throughout the cladding). Using the effective index method a two-dimensional single-mode criteria for the rib waveguide can be developed. Single-mode guidance occurs up until the cut-off point of the second mode. From Equation (2.14), because the rib waveguide is horizontally symmetric, this is when:

$$w_{sm} = \frac{\pi}{k \sqrt{(n_{eff\_rib})^2 - (n_{eff\_slab})^2}} \quad (2.22)$$

where  $n_{eff\_rib}$  and  $n_{eff\_slab}$  are found from solutions to the transverse resonance equation for the respective regions. It is then possible to calculate the minimum width required for single-mode operation for a range of parameters including rib and slab dimensions

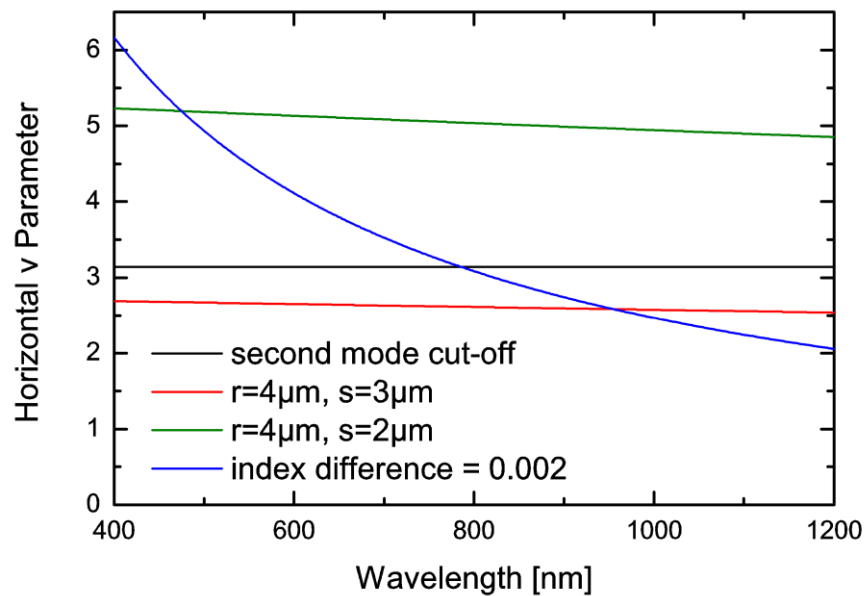


Figure 2. 12: The horizontal v-parameter is shown for a rib waveguide with width  $w=4\mu\text{m}$  in red and green. The horizontal indices used were those calculated using the effective index method based on the vertical dimensions shown in the figure. The single mode region is defined by the second mode cut-off and shown in black. For comparison a channel waveguide with a fixed index difference is shown in blue.  $n_1=1$ ,  $n_2=2.41$  and  $n_3=1.77$ .

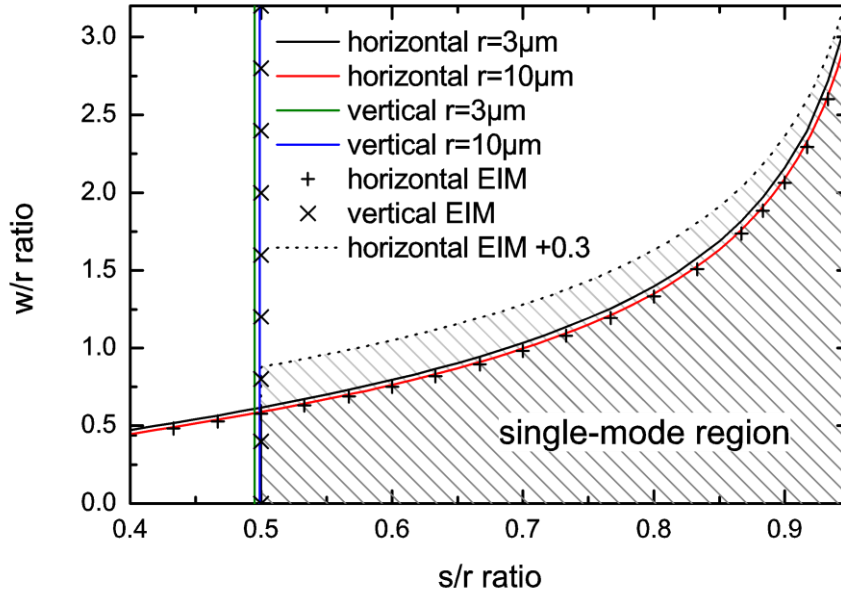


Figure 2. 13: Single-mode criteria of the rib waveguide. Solid lines are based on iterative calculations using Equations (2.22) and (2.23) with  $n_1=1$ ,  $n_2=2.41$  and  $n_3=1.77$   $\lambda=630\text{nm}$ . Symbols are for approximations using (2.24) and (2.25) with no definition of refractive index or wavelength. Dashed line shows adjustment to formula to agree with finite element analysis. Shaded region indicates the single-mode region.

and refractive indices. This requires iterative computation to find  $n_{\text{eff\_rib}}$  and  $n_{\text{eff\_slab}}$ . Results are shown in Figure 2. 13.

The rib waveguide is also capable of supporting multiple modes in the vertical direction. To find the cut-off position of the second vertical mode: the effective index of the 2<sup>nd</sup> guided vertical mode in the rib region is considered. This effective index is set equal to the slab fundamental effective index to find the point at which horizontal guiding ceases. Both these rib and slab modes then have the same values of  $h$ ,  $p$  and  $q$ , differing only in mode number and waveguide size:

$$hs = \tan^{-1}\left(\frac{q}{h}\right) + \tan^{-1}\left(\frac{p}{h}\right), \quad hr = \tan^{-1}\left(\frac{q}{h}\right) + \tan^{-1}\left(\frac{p}{h}\right) + \pi \quad (2.23)$$

$$hr = hs + \pi$$

These dimensions can be calculated using iterative computation and do not depend on the rib width. Results are shown in Figure 2. 13.

From Figure 2. 13, it is clear that there is little variation of the single-mode criteria for waveguides with different dimensions. This important result shows that although the waveguide dimensions individually suggest highly multimode behaviour as planar

## Chapter 2 – Theory and Modelling of Waveguides

waveguides in both horizontal and vertical directions; the rib waveguide remains single-mode.

Upon further analysis it is possible to identify that if the constituent v-parameters are much larger than  $\pi$ , the rib waveguide single-mode criteria is independent of absolute dimensions, wavelength and refractive index and found to depend on a ratio of dimensions alone.

For the horizontal single-mode criterion, as the v-parameters in the vertical direction become large, the guided mode effective index becomes close to  $n_2$  and the total phase change components in Equation (2.10) reduce to  $\pi$  such that:

$$n_{eff\_rib} \rightarrow \sqrt{n_2^2 - \left(\frac{\pi}{kr}\right)^2}, \quad n_{eff\_slab} \rightarrow \sqrt{n_2^2 - \left(\frac{\pi}{ks}\right)^2}$$

$$w_{sm} \rightarrow \frac{1}{\sqrt{\left(\frac{1}{s}\right)^2 - \left(\frac{1}{r}\right)^2}} \quad (2.24)$$

This approximation is shown on Figure 2. 13 and results show that it matches closely to precise calculations for large dimensions or large refractive indices. In a similar way the vertical single-mode criteria can be simplified. Since the second vertical rib mode and fundamental slab mode have the same effective index at cut-off, the same values of h can be used. The phase change components become  $\pi$  for v-parameter waveguides:

$$hs \rightarrow \pi, \quad hr \rightarrow 2\pi, \quad \frac{s}{r} \rightarrow 0.5 \quad (2.25)$$

This vertical approximation is shown in Figure 2. 13 and matches closely the iterative criteria for large v-parameter waveguides.

There is still currently a great deal of confusion over the precise single-mode criteria for large-area rib waveguides. Equations (2.22) to (2.25) are based on the EIM and derived from the transverse resonance condition. Prior to the EIM, alternative criteria were proposed by E.A.J. Marcatili [14] and were later shown to be less accurate. Soref et al. [19] developed single-mode criteria based on a mode-matching technique introduced by Peterman [20]. This provided a result which is identical to that found by EIM, but shifted by an addition of 0.3 and is shown in Figure 2. 13 and in Equation (2.26). This criteria was later corrected by Pogossian et al. [21] through use of the effective index method described above (based on agreement with experimental results)

## Chapter 2 – Theory and Modelling of Waveguides

to remove this addition of 0.3. More recently finite element, work that solves accurately in two-dimensions, has been used to show that the addition of 0.3 is significantly more accurate [22, 23]. This addition is also in agreement with finite element work carried out as part of this work:

$$w < 0.3 + \frac{1}{\sqrt{\left(\frac{1}{s}\right)^2 - \left(\frac{1}{r}\right)^2}}, \quad \frac{s}{r} > 0.5 \quad (2.26)$$

The single-mode criteria are further complicated by the presence of low-loss modes which are by definition unguided but remain due to low-loss such that further analysis is required [23]. The waveguide length must be taken into account to ensure sufficient removal of higher-order low-loss modes to fully define the single-mode criteria. Further consideration is given to this requirement in Chapter 3 for large cross-sectional area diamond waveguides. The simplified single-mode criteria are used widely in modern fabrication processes including that of the recent silicon Raman waveguide laser to achieve single-mode operation with low fabrication-related propagation loss [24].

### 2.2.3 Marcatili's method for rib waveguides

Marcatili's method used previously for a planar waveguide, in section 2.1.3, can be extended to two dimensions allowing for analytical calculation of the guided mode effective index in a rib waveguide. This topic is discussed extensively by Maractili [2] and the technique is briefly outlined here. This approach allows for full analysis of the guiding properties of the rib waveguide without the requirement for time consuming and unintuitive computational work.

For planar waveguides, a new waveguide thickness,  $T$ , was defined and the electromagnetic field was set to zero at this waveguide boundary such that it produced the same mode effective index as that of the actual waveguide. This method can be applied for all dimensions of the rib waveguide and is shown schematically in Figure 2.14.

New adjusted dimensions of rib height,  $R$ , rib width,  $W$ , for the rib above the slab and slab height,  $S$ , are introduced. Two new related parameters are also introduced;  $W_b$  represents the width of the guided mode due to the horizontal effective index guiding of the rib/slab and  $W_e$  represents the adjusted width of the actual guided mode which is

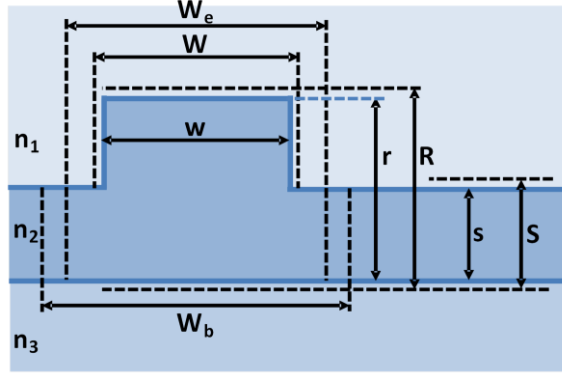


Figure 2. 14: Schematic of the rib waveguide with new adjusted dimensions used for Marcatili's analytical approximation for the rib waveguide.

assumed to be a linear combination of  $W$  and  $W_b$ .  $W$ ,  $R$  and  $S$  are all related to the physical dimension sizes in a similar manner to the planar waveguide approximation:

$$W = w\left(1 + \frac{2K_w}{v_w}\right), \quad R = r\left(1 + \frac{K_1}{u_h} + \frac{K_3}{v_h}\right), \quad S = s\left(1 + \frac{K_1}{u_s} + \frac{K_3}{v_s}\right) \quad (2.27)$$

$W_b$ , the adjusted width due to horizontal effective index guiding in the slab, is defined from the effective index method as:

$$W_b = W \left[ 1 + \frac{2S}{\pi W} \frac{1}{\sqrt{1 - \left(\frac{(m+1)S}{R}\right)^2}} \right] \quad (2.28)$$

$W_e$ , the adjusted width of the guided rib mode, is a linear combination of rib top width and slab guided width:

$$W_e = \frac{W(R-S) + W_b}{R}, \quad W_e = W(1 + c_q) \quad (2.29)$$

$$c_q = \frac{2}{\pi} \frac{S^2}{WR} \frac{1}{\sqrt{1 - \left(\frac{(m+1)S}{R}\right)^2}}$$

The effective index of the rib waveguide mode can then be defined explicitly by using known parameters of the waveguide:

$$N = \frac{1}{k} \sqrt{k^2 n_2^2 - \left[ \frac{\pi(m_v+1)}{W(1+c_q)} \right]^2 - \left( \frac{\pi(m_h+1)}{R} \right)^2} \quad (2.30)$$

## Chapter 2 – Theory and Modelling of Waveguides

Where  $m_v$  is the vertical mode number and  $m_h$  is the horizontal mode number, with this notation starting from 0. The calculation of the guided mode effective index using Marcatili's method is shown in Figure 2. 29 where it is compared to other methods. This method is used in Chapter 3 to develop a fully analytical model of a diamond Raman waveguide laser.

### 2.3 The four-layer waveguide

Full derivation of the four-layer transverse resonance equation is extensive and thus only limited descriptions are presented in papers and textbooks. The four-layer solution is required for a complete description of the strip loaded waveguides [17, 25]. Later, it will be shown that rib waveguides with narrow ribs may be described with an effective index method which is applied in four-layers rather than three to provide improved accuracy. This method describes the basis for inverse rib waveguide tapers. In Chapter 4, rib waveguide tapers are designed and fabricated in order to reduce the footprint of directional couplers. The following theory helps underpin a description of their operation.

The methodology followed is similar to that for the 3-layer problem as presented in Section 2.1.1. Guiding is assumed to occur in the two middle layers and a description of the profile is interesting for this work:

$$E_m = \begin{cases} A \exp(-qx), & t_1 \leq x < \infty \\ B \cos(hx) + C \sin(hx), & 0 \leq x \leq t_1 \\ D \cos(mx) + E \sin(mx) & -t_2 \leq x \leq 0 \\ F \exp(px) & -\infty \leq x \leq -t_2 \end{cases} \quad (2.31)$$

The schematic shown in Figure 2. 15 defines the new dimensions and refractive indices used. The transverse propagation constants are redefined to take into account the new layer:

$$p = k\sqrt{N^2 - n_1^2}, \quad h = k\sqrt{n_2^2 - N^2}, \quad m = k\sqrt{n_3^2 - N^2}, \quad q = k\sqrt{N^2 - n_4^2} \quad (2.32)$$

If the guided mode effective index is higher than one of the guiding layers but lower than the other, one of the transverse constants becomes imaginary. Using Euler's formula, this leads to the field being described by real exponential terms if one constant is allowed to become complex:

## Chapter 2 - Theory and Modelling of Waveguides

$$B \cos hx + C \sin hx = \left( \frac{B}{2} - \frac{D}{2i} \right) e^{ihx} + \left( \frac{B}{2} + \frac{D}{2i} \right) e^{-ihx} \quad (2.33)$$

The field is then described by an exponential and has two real values at each boundary. If the field decays rapidly to zero before the boundary, then it is no longer necessary to consider the waveguide as a four level system and the outer region can be ignored.

The set of equations can be solved to find the transverse resonance condition for the four-layer system with use of the boundary conditions at the material interfaces. They may be reduced such that the coefficients A-F are not required. The solution is a transcendental equation which is a function of the refractive indices, the wavelength and the thickness of the guide regions. This can be shown in a variety of forms including with the use of hyperbolic tangents, inverse tangents and restrictions, in order to specify mode numbers. It is displayed here in an unsimplified form based on the boundary condition for the derivative at the interface between  $n_3$  and  $n_4$ :

$$C = F, \quad Bh = Dm, \quad \tan(ht_1) = \frac{Bh + Cp}{Ch - Bp}, \quad \tan(-mt_2) = \frac{Dm - Cq}{Dq + Cm}$$

$$\tan(-mt_2) = \frac{h - q \frac{h + p \tan(ht_1)}{h \tan(ht_1) - p}}{\frac{hq}{m} + m \frac{h + p \tan(ht_1)}{h \tan(ht_1) - p}} \quad (2.34)$$

Equation (2.34) fully describes all the guided modes supported by the waveguide for any given refractive index, dimension or wavelength. Solutions for this transcendental equation can be found with the aid of a computer using an iteration method.

The transverse field of a guided mode in a four-layer waveguide is shown in Figure 2.15 for different values of  $n_2$ . Results show several properties of the four-layer waveguide solution. When the index difference between  $n_2$  and  $n_3$  is sufficiently large, the field will decay rapidly in region 2 such that the field magnitude drops to 0 prior to the  $n_1/n_2$  boundary. This means the four layer solution is not required and the solution matches that provided by the three-layer solution where  $n_2$  becomes a cladding index. Similarly when  $n_2$  equals  $n_3$  the four-layer solution can be described by the three-layer solution with  $t = t_1 + t_2$ .

When  $n_2$  is slightly lower than  $n_3$ , the field is described by sinusoidal functions in both region 2 and region 3 with slightly differing transverse propagation constants such that the peak of the field lies closer to the  $n_3/n_4$  interface than the  $n_1/n_2$  interface. This is

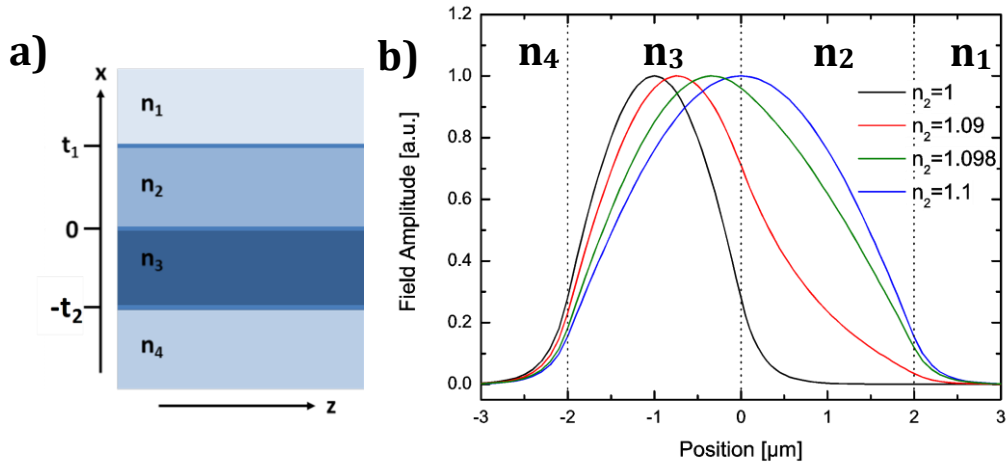


Figure 2. 15: **(a)** Schematic of the four-layer planar waveguide terms. **(b)** Normalised electric field magnitude for  $t_1=2 \mu\text{m}$ ,  $t_2=2 \mu\text{m}$ ,  $n_1=1$ ,  $n_3=1.1$ ,  $n_4=1$ ,  $\lambda=630 \text{ nm}$  and varying  $n_2$ . The coefficient D was imaginary for  $n_2=1$  and  $n_2=1.09$  leading to an exponential decay in this region for these indices.

shown in Figure 2. 15 with  $n_2=1.098$  and with real coefficients A-F. The guided mode effective index is smaller than  $n_2$  and  $n_3$  and larger than  $n_1$  and  $n_4$ .

When  $n_2$  is reduced, as shown by  $n_2=1.09$  in Figure 2. 15, the field is sinusoidal in region 3 and decays exponentially in region 2. This exponential decay extends beyond region 2 and continues to decay at a different rate in region 1, thus the mode extends throughout all four regions. This solution is characterised by an imaginary coefficient D and has a guided mode index which is larger than  $n_1$ ,  $n_2$  and  $n_4$  but smaller than  $n_3$ .

### 2.3.1 Rib waveguides

It is proposed, in this work, to describe the profile of the guided mode in a rib waveguide with use of the four-layer model as part of the effective index method. The use of this model is not known to be reported for rib waveguides elsewhere.

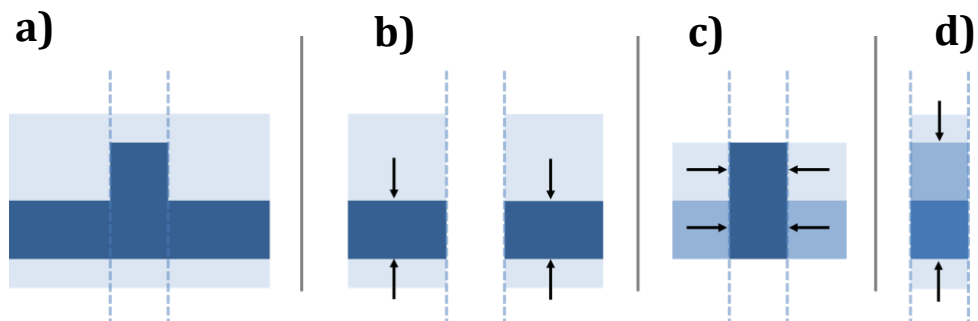


Figure 2. 16: Schematic of **(a)** the rib waveguide design, **(b)** Step 1; effective index of slab region due to vertical confinement, **(c)** Step 2: effective index of rib region due to horizontal confinement and **(d)** four-layer effective index of rib region due to vertical confinement.

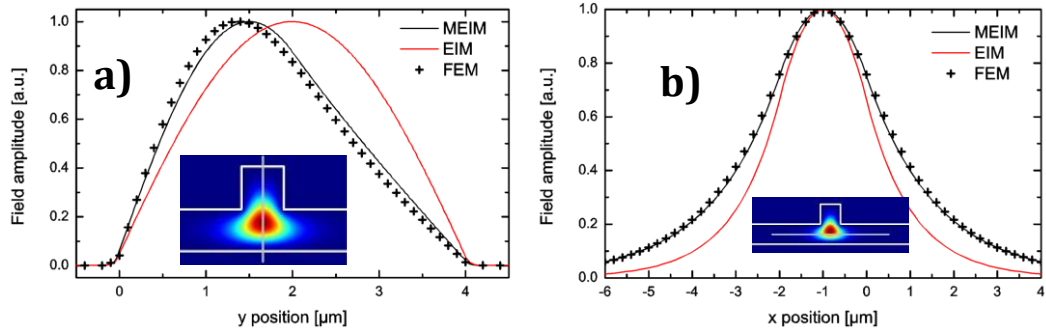


Figure 2. 17: Normalised electric field amplitude of **(a)** a vertical cut and **(b)** a horizontal cut through a rib waveguide. The modified effective index method (MEIM) includes a 4-layer solution. The effective index method (EIM) uses only 3-layer solutions. FEM simulations were performed with COMSOL. Solutions are for  $r=4\ \mu\text{m}$ ,  $s=2\ \mu\text{m}$ ,  $w=2\ \mu\text{m}$ ,  $n_1 = 1$ ,  $n_2=2.4$ ,  $n_3=1.76$  and  $\lambda=630\ \text{nm}$ .

Close examination of field profiles of the guided modes in rib waveguides reveals that the vertical approximation to a 3-layer waveguide in the rib region is insufficient. This effect is highlighted in Figure 2. 17. The field maximum is significantly closer to the bottom of the rib rather than the top of the rib for a range of dimensions. It is proposed that a modification is applied to the EIM to better describe the rib waveguide mode profiles and guided mode effective index.

By applying the EIM in the vertical direction, characteristics of the rib region can be described with the four-layer solution. Using the EIM described previously the confinement is calculated in a process outlined in Figure 2. 16. The new addition to the standard method involves describing the rib region with the four-layer planar solution using the effective index of the rib top and rib bottom separately.

In order to confirm that the proposed method is an accurate representation of the guiding mechanisms of rib waveguides, a numerical example was considered and the proposed modified EIM (MEIM) was compared to the original EIM. This is shown in Figure 2. 17 for a set of fixed parameters. The finite element method (FEM), a more accurate 2D technique discussed in Section 2.4.1, is shown alongside to allow close comparison with the approximations.

It can be seen that the basic three-layer EIM deviates significantly from the more accurate finite element method. The MEIM matches closely for both the vertical and horizontal directions. Accuracy in predicting horizontal spread can have significant effects on directional couplers which are discussed in Chapter 4.

In order to confirm the accuracy of this technique for a range of rib waveguide dimensions: a rib waveguide with fixed  $r$  and  $s$  with a varying rib width  $w$  was

## Chapter 2 – Theory and Modelling of Waveguides

considered. The guided mode effective index was calculated using the EIM, the MEIM and FEM and is shown in Figure 2. 18. The proposed MEIM provides a more accurate solution for a range of dimensions in comparison to the three-layer EIM. The FEM is introduced next in Section 2.4.1.

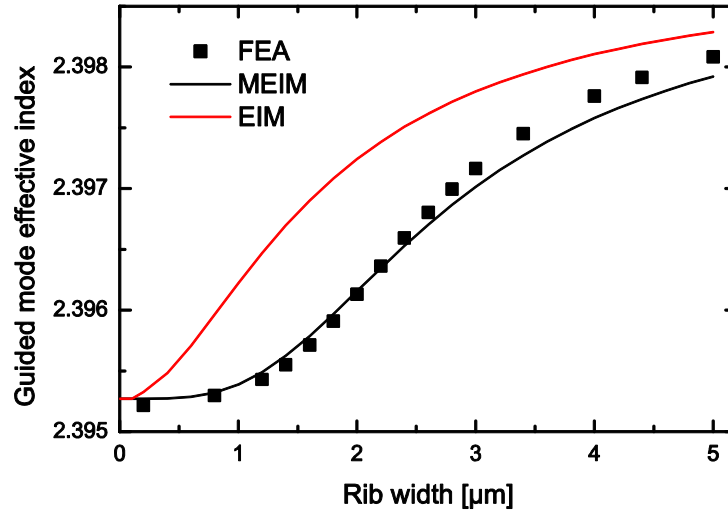


Figure 2. 18: Guided mode effective index for changing rib width. The modified effective index method (MEIM) includes a 4-layer solution. The effective index method (EIM) uses only 3-layer solutions. Finite element analysis (FEA) was performed with COMSOL. Solutions are for  $r=4 \mu\text{m}$ ,  $s=2 \mu\text{m}$ ,  $n_1 = 1$ ,  $n_2=2.4$ ,  $n_3=1.76$  and  $\lambda=630 \text{ nm}$ .

## 2.4 Computational methods

In Sections 2.1 and 2.2, solutions to describe the electromagnetic field in a waveguide were found starting from the one-dimensional scalar form of the Helmholtz equation. These have been applied precisely to the case of the planar waveguide, but approximations were used to describe two-dimensional confinement. Although this provides accurate results for a range of symmetrical geometries, it is not complete and may not be sufficient to describe some waveguide geometries. To achieve the complete solution, Maxwell's equations should be solved in all dimensions. This is possible through use of a computer to search iteratively for a solution. Several methods may be used to solve Maxwell's equations numerically [26] and for this work the finite element method (FEM) and beam propagation method (BPM) are considered.

### 2.4.1 Finite element method (FEM)

The finite element method (FEM) involves solving Maxwell's equations precisely in two or three-dimensions [27]. It may require significant computational power, depending on the required accuracy and waveguide geometry. As with any computational

## Chapter 2 – Theory and Modelling of Waveguides

technique, a good understanding of the methodology is required to assess the results and the limitations of the method. The FEM process and limitations of the technique are now outlined:

### a) The geometry is specified

The cross-section of the waveguide is defined within a simulation region. These parameters include the physical dimensions and refractive index of each material that forms the guiding structure. Figure 2. 19 shows an example of a cross-section of a rib waveguide. The region size is important and will affect the boundary conditions.

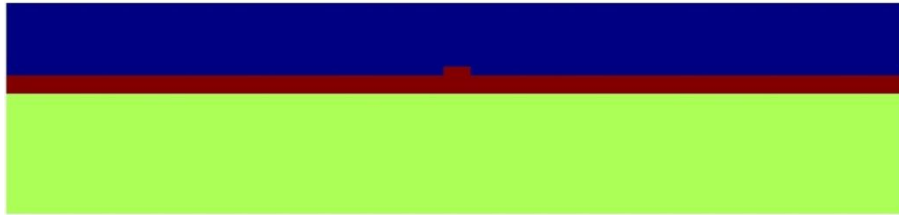


Figure 2. 19: An example of a geometry of a rib waveguide by commercial software COMSOL multiphysics. The standard colour map has been applied to the refractive index (Appendix A).

### b) The boundary conditions are specified

The boundary conditions are specified by setting the electric and magnetic components to zero at the edge of the simulation region. This requires knowledge that the fields will drop to zero at the edge of simulation region, thus that region needs to be sufficiently large to contain the entire guided mode. In the example shown in Figure 2. 19, the simulation region is much wider than the expected guided mode. This is deliberate, because some rib waveguides offer weak horizontal guidance and produce modes that extend significantly beyond the rib region. It is necessary to extend the simulation region to prevent the boundary conditions of the simulation affecting the results.

### c) The mesh is generated

The mesh is a grid, usually triangular but not necessarily, that is formed by nodes connected together by lines called elements. FEM has a limited finite resolution defined by the mesh and this is key to the accuracy of the technique. Greater resolution and accuracy is achieved by reducing the size of the elements such that there are many nodes. Each node on the mesh will have a specific electric and magnetic field component associated with it. To accurately retrieve profile information many nodes must sit within the guided mode profile.

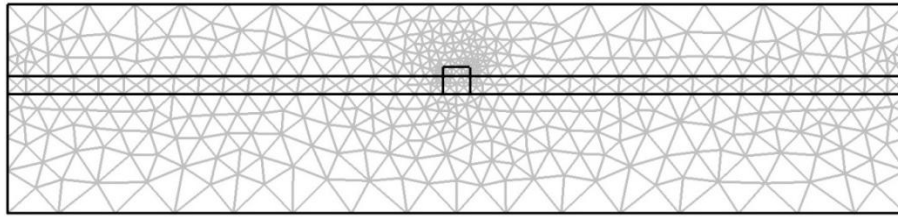


Figure 2. 20: An example of a mesh with 949 elements. This mesh is used for demonstration purposes and has a low resolution.

It is not necessary to have a high mesh resolution around the boundaries of the simulation, as the influence of these sections on the solution is minimal due to the small field magnitude away from the waveguide. For this reason, the resolution of the mesh should be increased in and just around the waveguide region and reduced towards the simulation edges (Figure 2. 20). This increases accuracy whilst minimising computational requirements.

### **d) The mode characteristics are solved**

Maxwell's equations are applied to the overall structure as a constraint to the simulation region. Similar to the processes followed in section 2.1, a number of requirements to obey Maxwell's equations include: continuity of E and H fields in homogeneous regions and boundary conditions at the interfaces between different refractive index regions as detailed in section 2.1.2.

Due to the large simulation region there are numerous solutions, as they may extend to the edge of the simulation region. The solutions of interest are confined to a small sub-region around the waveguide core. For this reason it is necessary to provide a solution estimate, often in the form of an effective index. This can be done by specifying the effective index of interest and the number of solutions of interest. It is usually sufficient to specify the refractive index of the waveguide core material as an estimate.

The algorithm then works by applying an initial field to the problem based on the estimated solution. This field is then spread through the defined structure conforming to Maxwell's equations. This process is iterated, working towards a solution, until there is no change in the field profile, resulting in a solution. The point at which there is no change between iterations will depend on the algorithm accuracy, which may be defined. Increasing this accuracy will be of no benefit unless the mesh has sufficient accuracy to make the result meaningful.

## Chapter 2 – Theory and Modelling of Waveguides

There are a number of solving algorithms suitable for FEM, each with a number of advantages and disadvantages usually relating to the processing time and memory requirements for different types of problems. The work presented in this thesis was carried out using commercially available software COMSOL using the RF module. The typical algorithm used was the direct UMFPACK. A typical concern involves the resolution of the mesh where a compromise between accuracy and computational time must be selected. Figure 2. 21 shows a close up of the rib waveguide and the guided mode solution.

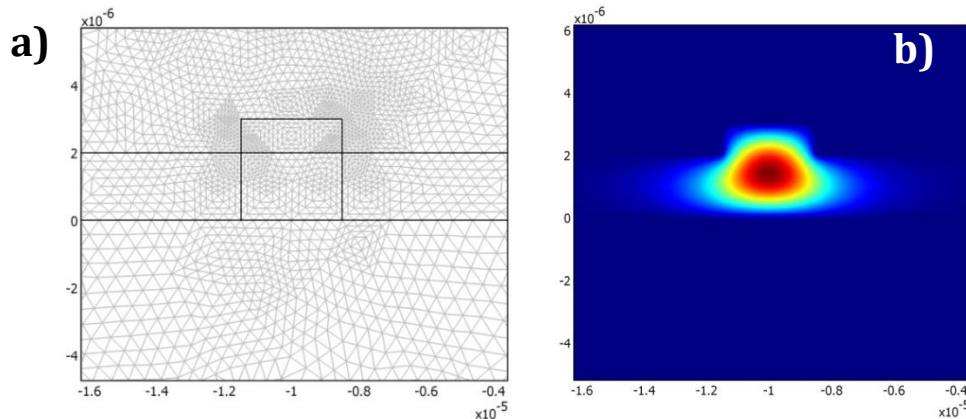


Figure 2. 21: **(a)** Typical medium resolution mesh with 27000 elements. Solution time takes 6.8s and is shown in **(b)** for the geometry shown in Figure 2. 19.

In order to understand the limitations and the selection criteria for various algorithms an example with a dense mesh was considered and the element density is shown in Figure 2. 22. Since the solution is 2D and not 3D a standard desktop computer was suitable for mode solving. It is preferable to use personal computers, as the number of simulations required to converge to a design may be large and the timeshare of powerful computers is not always possible. The computer specifications are important to the calculation times and in this case the processor was an Intel Core 2 Duo E650 operating at 2.33GHz. One core was used for solving which is typical of most algorithm capabilities. It is possible to extend the algorithm to two cores, but care must be taken to ensure the operating system supports this. The operating system used was Windows XP. The system had 3GB of RAM installed, but Windows restricts memory allocation to single tasks resulting in errors well below the maximum RAM. Alternative operating systems may fully exploit the hardware. The solution requirements for this example are shown in Table 2. 1 for different algorithms.

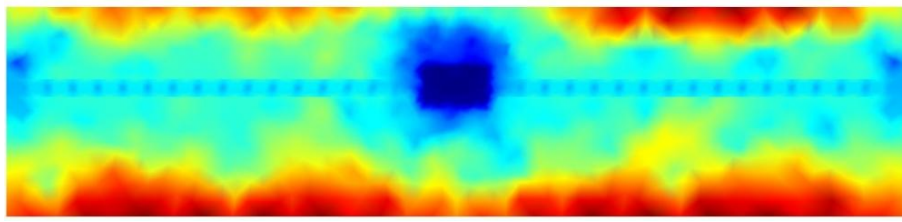


Figure 2. 22: Element density, blue highest and red lowest. This mesh was specifically optimised around the rib region where the guided mode was expected to lie. The minimum element size shown in blue was 22 nm, maximum element size shown in red was 3.3 $\mu$ m. There was a total of 43000 elements with 22000 of them in the rib region alone.

Table 2. 1: Computational time and memory requirements for fundamental mode solution using various algorithms

Algorithm	TE Only		Hybrid	
	Peak Memory Used [MB]	Time [s]	Peak Memory Used [MB]	Time [s]
UMFPACK	360	9.2	Out of Memory	
SPOOLES	310	62.4	600	487
PARDISO	230	5.5	Out of Memory	
CHOLESKY TAUCS	230	5.6	Out of Memory	

It was observed that some algorithms used less memory such as the SPOOLES algorithm but required longer processing time. Other algorithms converged much quicker which allows for rapid design testing.

### e) Post Analysis

After the solution has been obtained, the electric and magnetic field may be plotted in a range of convenient forms. An important step of the process is to ensure that the result is not mesh dependent. To confirm this, both the guided mode effective index and the mode profile should be examined for a fine mesh. The resolution of the mesh may then be reduced to the point at which there is no observable change in the result.

### 2.4.2 Beam propagation Method

The beam propagation method (BPM) [26, 28] is different to the analytical techniques and FEM described previously, now the extension of the waveguide in the propagation direction,  $z$ , is considered. Similar to FEM, the waveguide cross-section is subdivided in  $x$  and  $y$  by a grid. The beam propagation method also involves subdivision in the  $z$  direction. For this work, finite difference BPM is used and should not be confused with

## Chapter 2 – Theory and Modelling of Waveguides

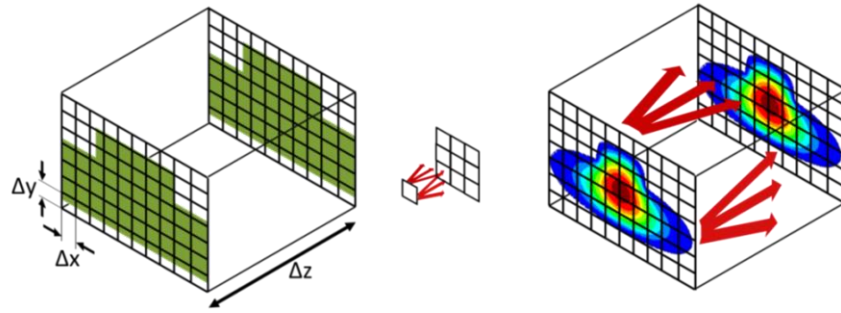


Figure 2. 23: Example of the subdivision of the waveguide cross-section into small components usually smaller than the wavelength of the light. The subdivision in the z direction can be much larger than the wavelength of the light but depends on the refractive index and guiding properties of the waveguide.

the finite difference time domain (FDTD) method. FDTD is an invaluable tool for precise modelling but uses extensive computational power and, as such, is not the focus of this work due to the limitations in the modelling of large devices.

BPM is based on the paraxial approximation, which differentiates it from other finite difference techniques. This approximation allows computation of structures which extend into the millimetre and centimetre scale that would otherwise not be possible with the FDTD technique. The approximation hinges on the restriction to slowly varying fields across the plane in the direction of propagation. This approximation restricts modelling to waveguides which propagate mainly in one direction and is not suitable for large angles of curvature such as ring-resonators.

The paraxial approximation states that the angle between the optical axis and the wave vector must be small enough such that  $\sin\theta \approx \theta$  and  $\tan\theta \approx \theta$ . This restricts simulations to waveguides with separation angles well below 20 degrees, with the precise limitations depending on required accuracy. This restriction also limits the suitability for multi-mode waveguides, where higher order modes rapidly diverge from the axis. The consideration of high refractive index changes, which is of particular relevance for this work, is another limitation that will require high grid resolution to remain accurate.

The BPM approximation can be shown by considering the Helmholtz equation for wave propagation. From Equation (2.6) but for all dimensions:

$$\frac{\partial^2 E}{\partial x^2} + \frac{\partial^2 E}{\partial y^2} + \frac{\partial^2 E}{\partial z^2} + k(x, y, z)^2 E = 0 \quad (2.35)$$

$$E(x, y, z) = E_m(x, y, z)e^{i(\omega t - kNz)}$$

## Chapter 2 – Theory and Modelling of Waveguides

where the terms have been defined previously. For a beam propagating in the  $z$  direction with an effective index  $N$  in a material with refractive index  $n$  this becomes:

$$\frac{\partial^2 E_m}{\partial z^2} + 2ikN \frac{\partial E_m}{\partial z} + \frac{\partial^2 E_m}{\partial x^2} + \frac{\partial^2 E_m}{\partial y^2} + (k^2 n^2 - k^2 N^2) E_m = 0 \quad (2.36)$$

If variation of  $E_m$  with  $z$  is sufficiently small, the second derivative can be ignored as it is much smaller than the first derivative. This is also known as the slowly varying envelope approximation (SVEA). This allows the  $z$  grid to be much coarser than the wavelength thus increasing efficiency:

$$\frac{\partial E_m}{\partial z} \rightarrow \frac{i}{2kN} \left( \frac{\partial^2 E_m}{\partial x^2} + \frac{\partial^2 E_m}{\partial y^2} + (k^2 - k^2 N^2) E_m \right) \quad (2.37)$$

The field may then be calculated for propagation in the  $z$  direction, by projecting the field in the current  $z$  position to the next  $z$  position through use of Equation (2.37). A simplified schematic is shown in Figure 2. 23. The process and limitations of the BPM are now outlined:

### a) The geometry is specified

Similarly to FEM, the waveguide cross-section and refractive index profile is defined. Although typical commercial software packages allow only limited geometries, it is possible to define more complex structures by combining basic components such as channel waveguides. The rib waveguide structures used in this work were defined using two channel guides, one for the rib region and one for the slab region which extends horizontally beyond the simulation region. An example is shown in Figure 2. 24.

### b) The simulation region is specified

As with many computational mode solvers, a prior knowledge of the guided modes is required to effectively define the simulation region. This could be acquired through trial and error of multiple simulation regions or from analytical work. It is important to select a simulation region which is significantly larger than the guided mode such that mode lies well-confined within the simulation region. A typical error may be underestimating the width of the exponential wings that extend into the slab region. Cutting these off results in loss as the guided mode propagates, because power will leak out of the simulation region. A typical simulation region for a rib waveguide is shown in Figure 2. 24.

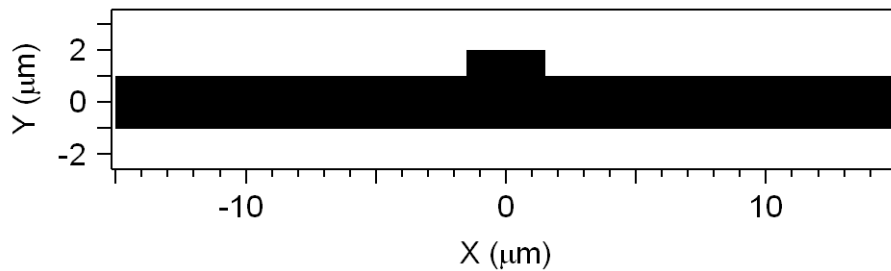


Figure 2. 24: A cross-section of the waveguide considered where the area shown is the simulation region. The black area represents the waveguide and has a refractive index is defined differently for various simulations. The white area represents the background index which is 1. Image from commercial software BeamProp™ by RSoft.

### c) The grid is defined

The cross-sectional grid resolution is first defined as an approximation that should be finer for modes with high confinement. It is necessary to perform a convergence study on every new type of waveguide structure to ascertain its sensitivity to varying grid sizes. There is a reduced grid resolution in the  $z$  direction due to the slowly varying field approximation. The slowly varying field assumption holds true for only a range of structures. Attention must be paid when modelling waveguides with large refractive index changes and dealing with sharp bends.

### d) The launch conditions are selected

The launch profile of the mode must be defined. Unlike FEM, a well-defined starting profile is required. This profile is then propagated through the waveguide structure defined following Maxwell's equations.

### e) Monitoring and analysis

BPM, as with other finite element computational solutions to Maxwell's propagation equations, offers a range of powerful outputs which can add to analysis of a given waveguide structure. The electromagnetic field is calculated at every point during propagation. It is possible to calculate how much the field has deviated from the original input field, thus loss can easily be calculated.

### f) Mode solving

BPM can be utilised to solve for modes of a waveguide structure. A guided mode can be found by launching an arbitrary profile in a waveguide with fixed cross-sectional dimensions over a long propagation distance. The closer this profile is to the actual guided mode the quicker the simulation will converge. If the field profile remains constant over a long distance a guided mode is found. Complications arise when dealing with multi-mode waveguides.

## Chapter 2 – Theory and Modelling of Waveguides

The iterative imaginary distance mode-solving technique is used in this work and works as follows. An arbitrary excitement field is launched into the waveguide structure off axis. This field should be capable of exciting all the possible guided modes which make up the waveguide structure and also some radiation modes which will exit the simulation region.

Instead of using a real distance as the finite propagation step,  $\Delta z$ , an imaginary distance  $\Delta z = i\Delta z$  is used. As a consequence every guided mode has an exponential growth rate equal to the real propagation constant. The guided mode with the lowest order mode, with the highest effective index, is preferentially guided. All other modes are selectively removed during the simulation, retaining the fundamental mode of the waveguide. This method can be extended to identify the higher order modes by successively applying this technique and removing the profile of the lower order modes from the simulation.

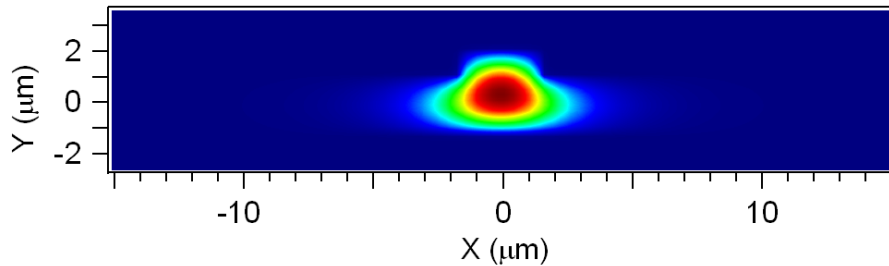


Figure 2. 25: The solution of the guided mode for the refractive index profile shown in Figure 2. 24 at a free-space wavelength of 800nm and an index 2. The guided mode effective index is 1.9943 and 1.0918 for a material index of 2 and 1.1 respectively.

### g) Convergence Study

To clarify the necessity for a convergence study, a rib width taper structure was considered and is shown in Figure 2. 26. This simple device was used to highlight the considerations and complications of grid size selection. The chosen taper caused a range of complexities for the simulation. In particular the finite size of the grid causes the taper to be split into jagged step-like sections. In order to comply with the slowly varying field assumption of the BPM, it was necessary that these steps were sufficiently small and caused limited effect to the guided mode. The previously calculated guided modes were used as the launch field for the taper structure and the transverse field was monitored during propagation. A number of parameters taken from the various simulations are shown in Table 2. 2.

## Chapter 2 – Theory and Modelling of Waveguides

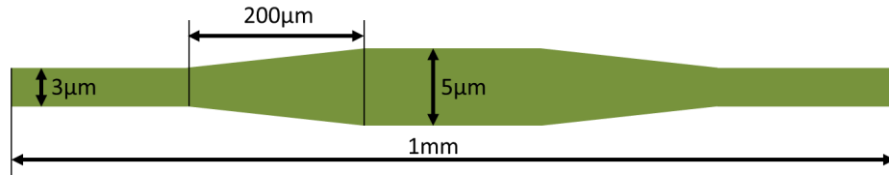


Figure 2. 26: Rib width taper waveguide structure. The rib height  $r$  and slab thickness  $t$  remains constant throughout this structure. This consists of 5 separate sections each with  $200\ \mu\text{m}$  length: a straight section with  $w=3\ \mu\text{m}$ , a linear taper from  $w=3\ \mu\text{m}$  to  $w=5\ \mu\text{m}$ , a straight section with  $w=5\ \mu\text{m}$ , a linear taper from  $w=5\ \mu\text{m}$  to  $w=3\ \mu\text{m}$  followed by a further straight section with  $w=3\ \mu\text{m}$ .

Table 2. 2: The effect of grid sizes on processing time and output results for the structure shown in Figure 2. 26 at a wavelength of  $800\ \text{nm}$ .

Refractive Index	X and Y Grid [ $\mu\text{m}$ ]	Z Grid [ $\mu\text{m}$ ]	Processing Time [s]	Convolution with input field	Std Dev on $1/e$ width on last $200\ \mu\text{m}$ [ $\mu\text{m}$ ]
2	0.05	0.1	160	0.995	0.023
2	0.05	0.4	96	0.995	0.032
2	0.05	1	16	0.996	0.042
2	0.05	10	1.6	0.935	0.103
2	0.1	1	2.5	0.992	0.044
2	0.2	1	0.84	0.963	0.028
1.01	0.05	1	16	0.998	0.024
1.01	0.05	10	1.6	0.98	0.056
1.01	0.05	5	8	1	0.027
1.01	0.1	1	2.5	0.997	0.025
1.01	0.2	1	0.84	0.997	0.021
1.01	0.2	10	0.09	0.99	0.063

Several important observations were made that affected both the accuracy of the result and gave an indication of the appropriate grid parameters. By initially observing the convolution with the input field, an initial indication of the accuracy was obtained. It was not assumed that the correct result was 1 as it was possible the structure exhibited loss. Rather, the convolution was compared for different grid sizes, with the highest resolution grid typically offering the most accurate result.

The convolution alone was not enough information to assess accuracy as there was mode beating in the structure which was only evident if the field variation in the  $z$  direction was monitored. For this reason the mode width was monitored for a significant propagation distance.

## Chapter 2 – Theory and Modelling of Waveguides

For  $n=2$  it was clear that both the  $x,y$  and  $z$  grid sizes have an influence on the formation of mode beating. For accurate results all grid sizes has to be roughly the same size as the wavelength. For  $n=1.01$  the influence of the grid size was lower, highlighting that the errors in the simulation are geometry and refractive index dependent. Most of these simulation errors are however well below the required accuracy for many applications.

### 2.5 Hybrid polarisation modes and linear approximations

Previously in this chapter polarisation states of the waveguide modes were categorised into TE (transverse electric) and TM (transverse magnetic) as defined in Section 2.1.2. A pure TE mode is defined by having no electric field in the direction of propagation  $E_z=0$ ,  $H_x$  and  $E_y$  are real and  $H_z$  is imaginary and nonzero. A pure TM mode is defined by having no magnetic field in the direction of propagation  $H_z=0$ ,  $E_x$  and  $H_y$  are real and  $E_z$  is imaginary and nonzero.

In practice all nonplanar waveguides produce modes which have nonzero values for both  $E_z$  and  $H_z$ . This is due to the nonzero  $\nabla \ln n^2$  term, shown in Equation (2.4), which is the result of the refractive index difference between the core and the cladding. These refractive index changes acts to affect the polarisation states of the waveguide. This can be understood by considering the ray-optical approximation of dielectric waveguides: in general the ray follows a skew trajectory and changes direction upon each reflection along the waveguide and rotating the electric field in all directions. This produces modes which have components of  $E_z$  and  $H_z$ . These modes are known as hybrid or full vector modes, these modes cannot be decoupled into TE and TM.

It is common practice when considering single-mode waveguides to neglect the  $\nabla \ln n^2$  term because the refractive index difference is usually small to ensure single-mode operation. This is known as the weakly guiding waveguide approximation. This approximation reduces hybrid modes into TE or TM modes. For fibre optics (cylindrically symmetric waveguides) this results in the simplification of hybrid modes into linearly polarised (LP) modes.

The designation of the hybrid modes is based on the relative contributions of E and H to a transverse component of the field. If  $E_z$  makes the larger contribution, the mode is considered E-like and designated  $EH_{mn}$ . If  $H_z$  makes the larger contribution the mode is

## Chapter 2 – Theory and Modelling of Waveguides

considered H-like and designated  $HE_{mn}$ . This follows the historical designation of modes [29]. In this work the numbering  $m$  and  $n$  follows that of Soref et al. [19] where  $m$  represents modes in the vertical direction and  $n$  represents modes in the horizontal direction, both starting from 0. Where one polarisation state dominates the other by a very large amount, modes may be referred to as quasi-TE and quasi-TM, however it should be made clear whether full hybrid calculations or scalar approximations are used.

To fully simulate hybrid modes, finite element software and extensive computational power is usually required. For demonstration purposes the first 12 hybrid modes of a  $4\ \mu\text{m} \times 4\ \mu\text{m}$  diamond channel waveguide in air were found using FEM analysis and are shown in Figure 2. 27. In each case it is clear that one polarisation state dominates the other by a significant factor. Each polarisation state is sometimes referred to as major or minor. In Figure 2. 27 the minor polarisation state is multiplied by a magnification factor to allow comparison with the major polarisation state. It is clear that for all of these modes that the major polarisation state is significantly dominant that for most forms of analysis it is possible to neglect the minor component.

Figure 2. 28 shows the two fundamental modes of a rib waveguide with dimensions  $h=4\ \mu\text{m}$ ,  $w=4\ \mu\text{m}$  and  $s=2\ \mu\text{m}$ . This structure has a high index contrast  $\Delta n=2.4$  and so the modes are hybrid. The significant component of each hybrid mode lies in one polarisation direction. Each corner at the bottom of the rib has a field in the minor polarisation direction. By integrating the components of the fields that contribute to the power of the guided mode it is possible to calculate what fraction of power lies in each polarisation state. For the  $HE_{00}$  mode (quasi-TE), the contribution to power of the major component ( $E_x H_y^*$ ) is  $1.6 \times 10^5$  times larger than the contribution of the minor component ( $-E_y H_x^*$ ).

For the rest of this thesis the linear approximation is made and the contribution from the minor component is neglected. This is because the structures considered are large and this rib waveguide design has minimal components in the minor polarisation state. Care should be taken for structures that deviate from this rib design. Small channel waveguides with high index contrast are known to have significant components in their minor field that can't be ignored.

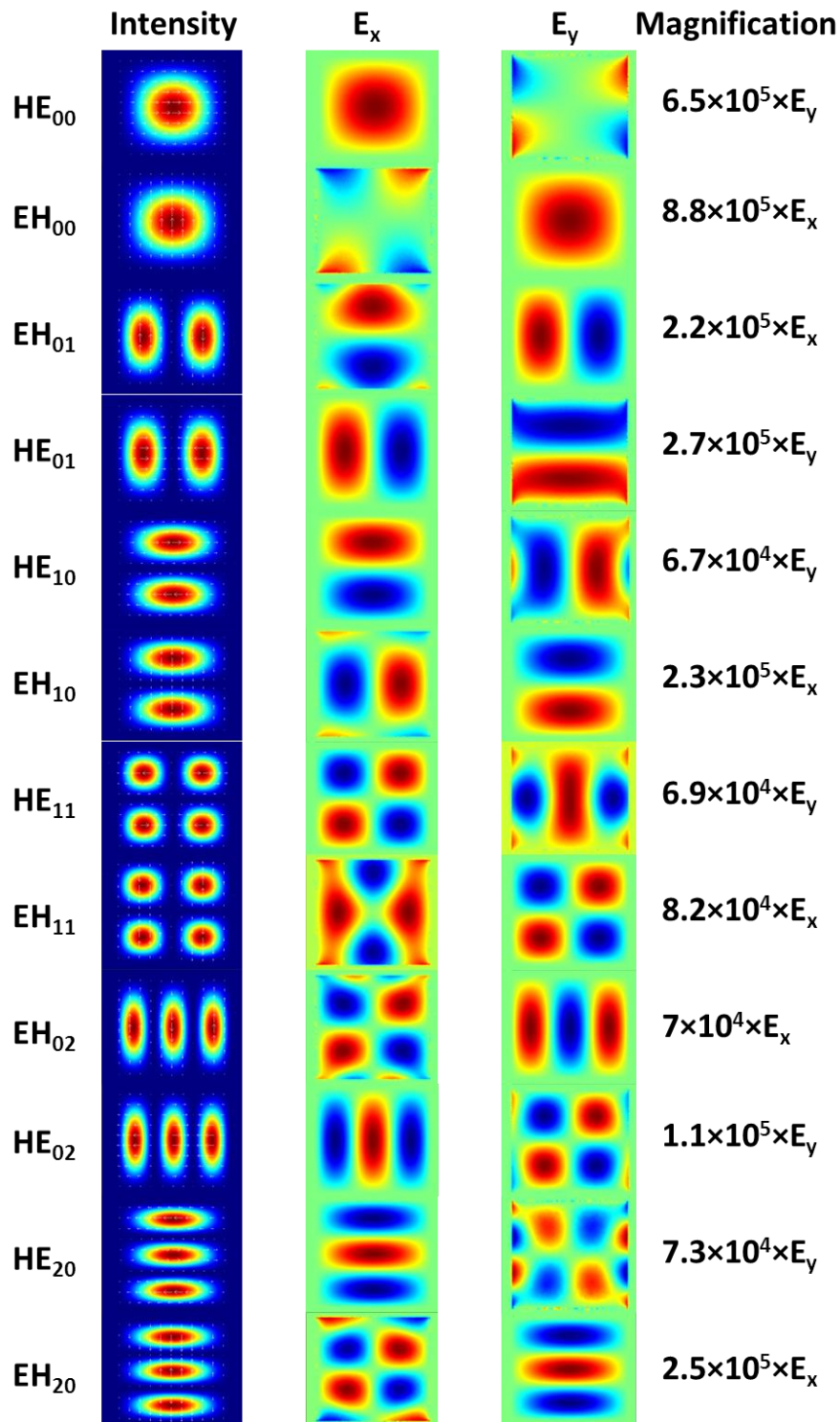


Figure 2. 27: The intensity of the guided mode  $=0.5\text{Re}[E_x H_y^* - E_y H_x^*]$ , horizontal electric field and vertical electric field for a  $4 \mu\text{m} \times 4 \mu\text{m}$  diamond waveguide surrounded by air at a wavelength of 532 nm calculated by FEM. The magnetic field components and components in the z direction are not shown here but are related to the electric field with Equation (2.16) and (2.17). The minor component has been multiplied by a magnification factor in order to compare the field patterns. All plots follow the colour scale shown in Appendix A. For  $E_x$  and  $E_y$  plots green is 0 and blue represents negative values. For intensity plots blue represents 0 and all values are positive. Each square represents a  $5 \mu\text{m} \times 5 \mu\text{m}$  area. A positive y is upward, a positive x is to the right and z is into the page.

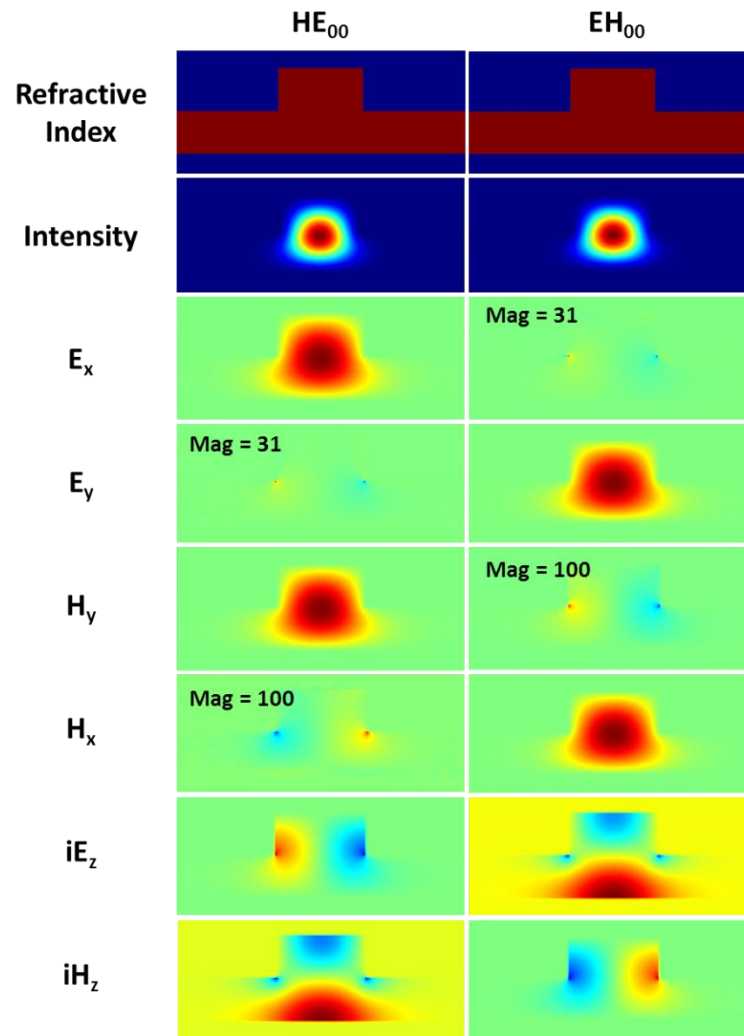


Figure 2. 28: Properties of the two fundamental modes of a rib waveguide. The refractive index profile is shown where the rib in red is  $n=2.4$  and the surrounding cladding is  $n=1$ . The intensity of the guided mode  $=0.5\text{Re}[E_x H_y^* - E_y H_x^*]$ . horizontal electric field and vertical electric field for a  $4\ \mu\text{m} \times 4\ \mu\text{m}$  diamond waveguide surrounded by air at a wavelength of  $532\ \text{nm}$  calculated by FEM. The minor component has been multiplied by a magnification factor in order to compare the field patterns. All plots follow the colour scale shown in Appendix A. Each square represents a  $5\ \mu\text{m} \times 5\ \mu\text{m}$  area. A positive  $y$  is upward, a positive  $x$  is to the right and  $z$  is into the page.

## 2.6 Comparison of methods

Five separate techniques for mode solving have been detailed with their numerical foundations explained. It is clear that each method is suitable for different reasons including accuracy, analysis or for time constraints. However it is important to consider the accuracy of each technique in comparison to each other. A numerical comparison of these techniques is shown in Figure 2. 29 with varying rib width for fixed rib height, slab height, refractive indices and wavelength.

## Chapter 2 – Theory and Modelling of Waveguides

A number of properties of each method are evident from examining Figure 2. 29. Firstly, all of these techniques predict a similar guided mode effective index, at worst  $\pm 0.03\%$ . However such an index difference can refer to very different mode widths in a rib waveguide. It can be seen that the EIM deviates from the other techniques most, especially for narrow ribs due to the 3-layer approximation. The MEIM performs well in comparison to finite element techniques which are considered most accurate. Marcatili's method does not include an inflection in the gradient as the mode nears cut off, thus it predicts a clear and quick cut-off due to the inaccuracies of the approximation. It is accurate, however, for a range of dimensions away from cut-off, considering it is completely analytical. FEM is considered most accurate, however to accurately predict values near cut-off, when the mode is very large, the technique becomes computationally demanding as large simulation regions are needed. Similarly the BPM is particularly poor near cut-off for the same simulation region requirements.

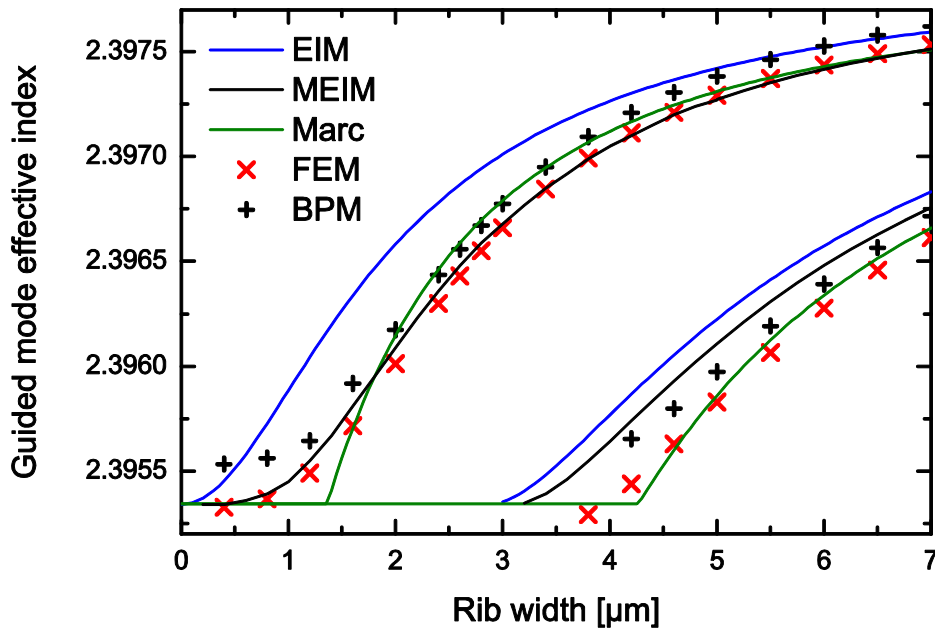


Figure 2. 29: Guided mode effective index for changing rib width. The effective index method (EIM) uses only 3-layer solutions, the modified effective index method (MEIM) includes a 4-layer solution, Marcatili's approximation (Marc) uses an asymptotic approximation, finite element analysis (FEA) was performed with COMSOL and the beam propagation method (BPM) was used in imaginary distance mode with BeamPROP™ by RSOFT. Solutions are for  $r=3 \mu\text{m}$ ,  $s=2 \mu\text{m}$ ,  $n_1 = 1$ ,  $n_2=2.4$ ,  $n_3=1.76$  using the 3-layer notation defined previously and a free space wavelength of  $\lambda=630 \text{ nm}$ .

### 2.7 Conclusions

A number of different mode-solving techniques for waveguides, and in particular rib waveguides, have been outlined including analytical and computational.

The effective index method was the earliest, most simple and intuitive solution to 2D problems. Although this technique is not analytical (without modification) the computational demand is minimal if not negligible in comparison to the computational finite element techniques. The key motivation for this technique is that it can be used to optimise parameters for a desired output characteristic in near real-time.

It has been shown in this work that the EIM can be enhanced to provide greater accuracy to the rib waveguide problem by considering the finite width of the top of the rib and the four-layer planar waveguide solution. Without greatly increasing computational demand, in comparison to finite element techniques, accurate solutions can be obtained. This allows the EIM to be extended to a range of situations where previously accuracy limits prevented the usefulness of this technique.

Marcatili's analysis offers a completely analytical solution for not only planar waveguides but 2D structures such as the rib waveguide. The technique is based on an asymptotic solution which holds true only far from the cut-off criteria, however is accurate within this region. Marcatili's approximation allows for quick optimisation based on its analytical nature.

The finite element method is considered to be the most flexible and accurate technique for mode solving. It allows solutions for a range of waveguide designs where semi-analytical techniques are not suitable. It offers greater accuracy than other techniques due to a full implementation of Maxwell's equations in all directions. The main limitation of this technique is the computational demand that prevents accurate optimisation. A further limitation is in the consideration of modes near cut-off. Due to the finite size of the simulation window and the limits of memory and computational power, it is not possible to simulate modes which extend to very large areas.

The beam propagation method offers the possibility to solve modes using the imaginary distance method. This technique is similar to FEM in that the cross-section is subdivided into small  $x$  and  $y$  regions which are the resolution limit of the technique. As a consequence the technique is computationally demanding and is typically not the method used for optimisation. As with FEM a major limitation of this technique is

## Chapter 2 – Theory and Modelling of Waveguides

modelling modes with extended mode profiles as the computation region must be large to achieve accuracy and thus increases computational demands.

### References

- [1] J. C. Maxwell, "A Dynamical Theory of the Electromagnetic Field," Philosophical Transactions of the Royal Society of London, **155**, 459 (1865).
- [2] V. R. Almeida, Q. F. Xu, C. A. Barrios, and M. Lipson, "Guiding and confining light in void nanostructure," Optics Letters, **29**, 1209-1211 (2004).
- [3] J. Takahara, S. Yamagishi, H. Taki, A. Morimoto, and T. Kobayashi, "Guiding of a one-dimensional optical beam with nanometer diameter," Optics Letters, **22**, 475-477 (1997).
- [4] D. Marcuse, "Theory of Dielectric Optical Waveguides" (Academic Press, 2nd Ed. 1991, 1st Ed. 1974).
- [5] T. Tamir, and H. Kogelnik, "Topics in Applied Physics, Volume 7, Integrated Optics" (Springer, 1975).
- [6] M. J. Adams, "An Introduction to Optical Waveguides" (John Wiley & Sons, 1981).
- [7] R. G. Hunsperger, "Integrated Optics: Theory and Technology" (Springer, 5th Ed. 2002, 1st Ed. 1981).
- [8] M. Reinhard, "Integrated Optics: Design and Modelling" (Artech House, 1994).
- [9] H. F. Taylor, and A. Yariv, "Guided Wave Optics," Proceedings of the IEEE, **62**, 1044-1060 (1974).
- [10] J. Tyndall, "Notes of a Course of Nine Lectures on Light" (At the Royal Institution of Great Britain, 1870).
- [11] P. K. Tien, "Propagation of Light Waves in Thin Films," Journal of the Optical Society of America, **60**, 723 (1970).
- [12] F. Goos, and H. Hänchen, "Ein neuer und fundamentaler Versuch zur Totalreflexion," Ann. Phys., **436**, 333 (1947).
- [13] C. Ridder, "A new algorithm for computing a single root of a real continuous function," IEEE Transactions on Circuits and Systems, **26**, 979 (1979).
- [14] E. A. J. Marcatili, "Slab-Coupled Waveguides," Bell System Technical Journal, **53**, 645-674 (1974).
- [15] E. A. J. Marcatili, "Dielectric Rectangular Waveguide and Directional Coupler for Integrated Optics," Bell System Technical Journal, **48**, 2071 (1969).
- [16] K. C. Kao, and G. A. Hockham, "Dielectric-Fiber Surface Wave-Guides for Optical Frequencies," IEE Proceedings-J Optoelectronics, **133**, 191-198 (1986).
- [17] N. Uchida, "Optical-Waveguide Loaded with High Refractive-Index Strip Film," Applied Optics, **15**, 179-182 (1976).
- [18] G. B. Hocker, and W. K. Burns, "Mode Dispersion in Diffused Channel Waveguides by Effective Index Method," Applied Optics, **16**, 113-118 (1977).
- [19] R. A. Soref, J. Schmidtchen, and K. Petermann, "Large Single-Mode Rib Wave-Guides in GeSi-Si and Si-on-SiO<sub>2</sub>," IEEE Journal of Quantum Electronics, **27**, 1971-1974 (1991).
- [20] K. Petermann, "Properties of Optical Rib-Guides with Large Cross-Section," Aeu-International Journal of Electronics and Communications, **30**, 139-140 (1976).
- [21] S. P. Pogossian, L. Vescan, and A. Vonsovici, "The single-mode condition for semiconductor rib waveguides with large cross section," IEEE Journal of Lightwave Technology, **16**, 1851-1853 (1998).
- [22] O. Powell, "Single-mode condition for silicon rib waveguides," IEEE Journal of Lightwave Technology, **20**, 1851-1855 (2002).

## Chapter 2 – Theory and Modelling of Waveguides

- [23] J. Lousteau, D. Furniss, A. B. Seddon, T. M. Benson, A. Vukovic, and P. Sewell, "*The single-mode condition for silicon-on-insulator optical rib waveguides with large cross section,*" IEEE Journal of Lightwave Technology, **22**, 1923-1929 (2004).
- [24] H. S. Rong, S. B. Xu, O. Cohen, O. Raday, M. Lee, V. Sih, and M. Paniccia, "*A cascaded silicon Raman laser,*" Nature Photonics, **2**, 170-174 (2008).
- [25] Ramaswam.V, "*Strip-Loaded Film Waveguide,*" Bell System Technical Journal, **53**, 697-704 (1974).
- [26] R. Scarmozzino, A. Gopinath, R. Pregla, and S. Helfert, "*Numerical techniques for modeling guided-wave photonic devices,*" IEEE Journal of Selected Topics in Quantum Electronics, **6**, 150-162 (2000).
- [27] E. Schweig, and W. B. Bridges, "*Computer-Analysis of Dielectric Waveguides - a Finite-Difference Method,*" IEEE Transactions on Microwave Theory and Techniques **32**, 531-541 (1984).
- [28] D. Yevick, and B. Hermansson, "*Efficient Beam Propagation Techniques,*" IEEE Journal of Quantum Electronics, **26**, 109-112 (1990).
- [29] E. Snitzer, "*Cylindrical Dielectric Waveguide Modes,*" Journal of the Optical Society of America, **51**, 491-& (1961).

# Chapter 3

## Diamond Waveguides

---

### Abstract

This chapter presents theoretical studies and experimental results of large cross-sectional area diamond waveguides and their potential use as a Raman waveguide laser system. Design requirements for large cross-sectional area diamond rib waveguides are developed considering single-mode operation. Experimental results of a novel design and fabrication method are presented. A fully analytical model is developed to describe the operation of a diamond Raman waveguide laser incorporating scattering losses from all surfaces and the potential device performance is investigated.

### Preliminaries

Some of the results presented in this chapter relating to fabrication are published in reference [1] and theoretical work including for Raman lasers in reference [2], although no content is directly duplicated. Acknowledgements of contributions by others to the work presented in this chapter are listed at the front and back of this thesis. The motivation and background to this work is detailed in Chapter 1. The cross-sectional waveguide designs presented in this chapter build upon simulation work presented in Chapter 2.

### 3.1 Large area waveguide design

It has been identified, as detailed in Chapter 2 and in refs [3-6], that the single-mode criteria of large-area rib waveguides do not depend on the wavelength, refractive index or absolute dimensions of the waveguide but rather on a ratio of the dimensions of rib width  $w$ , rib height  $r$  and slab thickness  $s$ . Rib waveguides can maintain single-mode guiding whilst extending in size well beyond the single-mode criteria of planar/channel waveguides for the same material and wavelength. There is no requirement for the slab region surrounding the rib region to be below cut-off in order to maintain horizontal guiding. Single-mode guiding can occur for a large range of wavelengths in one material based simply on a ratio of dimensions. The rib waveguide does not have the same wavelength dependence as a single-mode fibre, as discussed in Chapter 2. The

fabrication requirements are greatly reduced as precise control over the refractive index is not required in order to control the modal properties.

The large rib waveguide single-mode criteria, as developed in Chapter 2, suggests it is possible to create single-mode waveguides with no upper limit on the cross-section for any wavelength or material. This may appear like an error with the approximation of the effective index method, however it is possible to confirm this result with either the finite element method or beam propagation method for both TE and TM polarisations for a range of wavelengths and sizes of hundreds of micrometres and larger. This result is hard to interpret practically and some new criteria should be developed to consider what is practical, useful and what other single-mode requirements exist.

### 3.1.1 Useful waveguide criteria

In order for light to be guided, the natural diffraction of light must be compensated. For this work, it is desirable to make a distinction between guiding effects and a useful waveguide. A guiding effect will compensate for diffraction but perhaps for only a short propagation distance, like a lens. In this work, a definition for a useful waveguide is developed based on similar analysis for waveguide lasers [7, 8]:

*A useful waveguide guide must compensate for diffraction such that it offers greater cross-sectional area confinement than free-space propagation of an optimised Gaussian beam over the same propagation length. – Useful Waveguide Definition*

Laser engineers are familiar with the diffraction of a Gaussian beam as this beam profile is readily produced in lasers and offers the minimum diffraction in free-space. If a waveguide is to offer functionality, it must offer greater cross-sectional confinement than that offered by an optimised Gaussian beam. The propagation of a free-space beam can be described with Equation (3.1) [9]:

$$W^2 = W_0^2 + \left( \frac{\lambda M^2}{\pi n W_0} \right)^2 (z - z_0)^2 \quad (3.1)$$

Where  $W$  is the beam radius,  $W_0$  is the radius at the waist,  $z$  is the propagation distance,  $z_0$  is the  $z$  position of the waist,  $\lambda$  is the wavelength of the light and  $n$  is the refractive index of the material. The  $M^2$  parameter is the beam propagation factor and describes the quality of the beam with respect to a pure Gaussian beam. A Gaussian profile beam has an  $M^2$  of 1. The definition of the beam radius for Gaussian beams is the  $1/e^2$  power radius. For other profiles the second moment radius should be used. It is possible to

### Chapter 3 - Diamond Waveguides

calculate the average area of any Gaussian beam over a given propagation distance from  $z=0$  to  $z=L$  and this will have minimum average area when  $z_0=L/2$  [7]:

$$\begin{aligned} \text{average area} &= \frac{\pi}{L} \int_0^L W_0^2 + \left( \frac{\lambda M^2}{\pi n W_0} \right)^2 \left( z - \frac{L}{2} \right)^2 dz \\ &= \frac{\pi}{L} \left( W_0^2 L + \left( \frac{\lambda M^2}{\pi n W_0} \right)^2 \frac{L^3}{12} \right) \end{aligned} \quad (3.2)$$

It is then possible to find the optimal waist,  $W_m$ , to provide the smallest possible average area for a circular channel waveguide at any given distance:

$$\begin{aligned} W_m &= \sqrt{\frac{\lambda M^2 L}{\sqrt{12} \pi n}} \\ \text{Minimum average area} &= \pi \left( W_m^2 + \left( \frac{\lambda M^2}{\pi n W_m} \right)^2 \frac{L^2}{12} \right) \end{aligned} \quad (3.3)$$

For convenience this can be defined in terms of an average radius:

$$\text{average beam radius for minimum area} = \sqrt{W_m^2 + \left( \frac{\lambda M^2}{\pi n W_m} \right)^2 \frac{L^2}{12}} \quad (3.4)$$

The definition of a useful waveguide is then dependent on propagation distance. For large propagation distances, a moderately large area waveguide can offer greater cross-sectional confinement and for small propagation distances small-area waveguides are required to offer any advantage over free-space propagation. The  $M^2$  is 1 for a pure Gaussian beam, but a diode laser however may have a higher  $M^2$  and as such occupy a larger volume for the same propagation distance.

In order to make a comparison between the cross-sectional area of a guided mode and an optimised Gaussian beam it is necessary to consider the guided mode width rather than the waveguide width. Waveguide transverse modes are not Gaussian but are sinusoidal in the guide region and exponentially decaying in the claddings. For waveguides it is important to consider the second moment width as this follows the parabolic propagation rule and may be significantly different to the  $1/e^2$  width [10]. The second moment width is defined as:

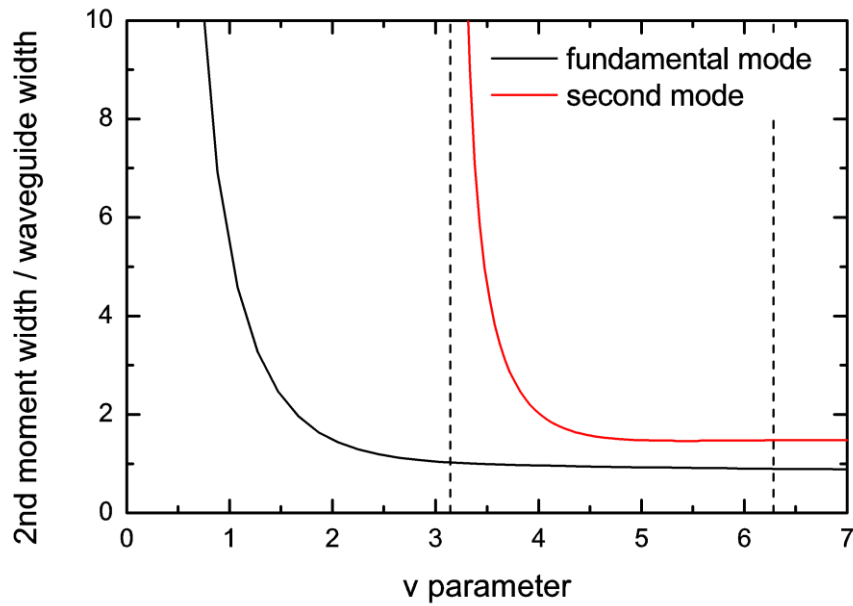


Figure 3. 1: A ratio of the second moment width to the guide width for varying v parameter for a TE symmetric planar waveguide and also applies to channel waveguide. This curve is consistent for any waveguide thickness, wavelength or index difference and is defined only by the v- Parameter. The single mode region is to the left of the first dashed line and between the first and second dashed lines is the region where two modes are guided.

$$W_{sm} = 2 \sqrt{\frac{\int_{-\infty}^{\infty} (x - x_0)^2 I dx}{\int_{-\infty}^{\infty} I dx}} \quad (3.5)$$

where  $x$  is the transverse direction,  $x_0$  is the centre of the guided mode and  $I$  is the intensity.  $W_{sm}$  can be substituted for  $W$  in equation (3.1) to describe the propagation of the guided mode as it leaves the waveguide. The second moment width has been calculated for a range of v parameters for a channel waveguide and is shown in Figure 3. 1.

Figure 3. 1 shows that for v-parameters lower than 1.5 there is a significant increase in the second moment width of the fundamental mode as much of the power is contained in the exponentially decaying wings. This weakly-guided mode is undesirable, due to poor confinement of light offering little or no benefit in comparison to that offered by free-space optics.

Single-mode channel waveguides are usually selected to operate just below cut-off of the second-order mode, in order to offer maximum confinement for the fundamental mode. At this position, the second moment width is roughly 1.1 times the waveguide width. A useful waveguide for this design would require dimensions that are 90% of Equation (3.4).

Rib waveguides offer single-mode propagation whilst maintaining high  $v$  parameters in individual component directions. The vertical confinement in the rib region may have  $v$  parameters well in excess of 100 for  $>10 \mu\text{m}$  sized waveguides and high refractive index changes (2.4-1 at visible wavelengths). In this situation the second moment height is 0.8 times the waveguide height ( $h_{sm}=0.8h$ ). Both the vertical confinement and horizontal confinement in the rib top may be described with the similarly high  $v$ -parameters. The horizontal confinement in the rib bottom will spread towards the typical definition in a channel waveguide. The horizontal confinement can be approximated with a linear combination of the two and is only valid for  $w \geq r$ :

$$w_{sm} = 0.8 \frac{1-s}{r} + 1.1 \frac{s}{r} \quad (3.6)$$

For a rib waveguide with  $s=0.65r$  this provides  $w_{sm}=0.995w$ . The averaged confinement may be calculated by considering an elliptical mode with a width of  $0.995w$  and height of  $0.8h$ , which is equivalent to a circular beam with  $w_{sm}=0.89w$ . Through use of equation (3.4) and (3.6) the minimum guide dimensions of a useful waveguide can be found and is shown in Figure 3. 2 for a rib waveguide with  $s=0.65r$ ,  $w=r$ . Figure 3. 2 shows the relationship between useful guide width and propagation length for the rib waveguide design described. This shows that the useful waveguide area can be significantly large, much greater than the mode area of single-mode fibre for short millimetre-length propagation distances. Consequently, there may be practical use for large area waveguides  $>20 \mu\text{m}$  in size.

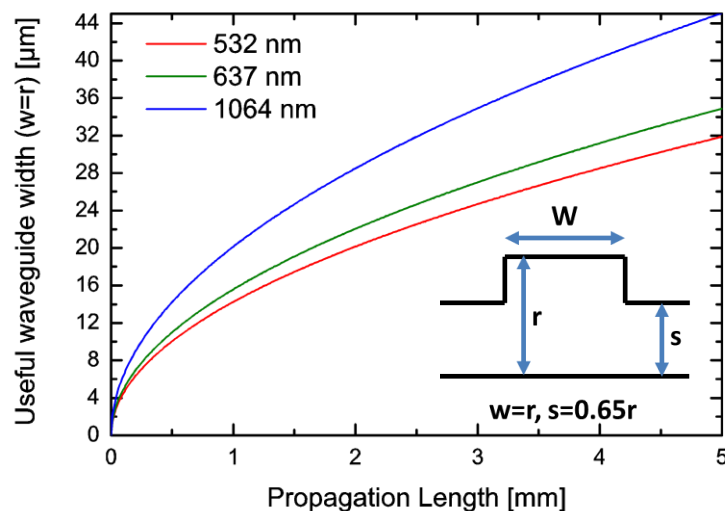


Figure 3. 2: Useful waveguide width(=height) for a rib waveguide (with ratio of dimensions defined inset) following the ‘useful waveguide definition’. Material considered to be diamond with  $n=2.42$  and negligible dispersion.

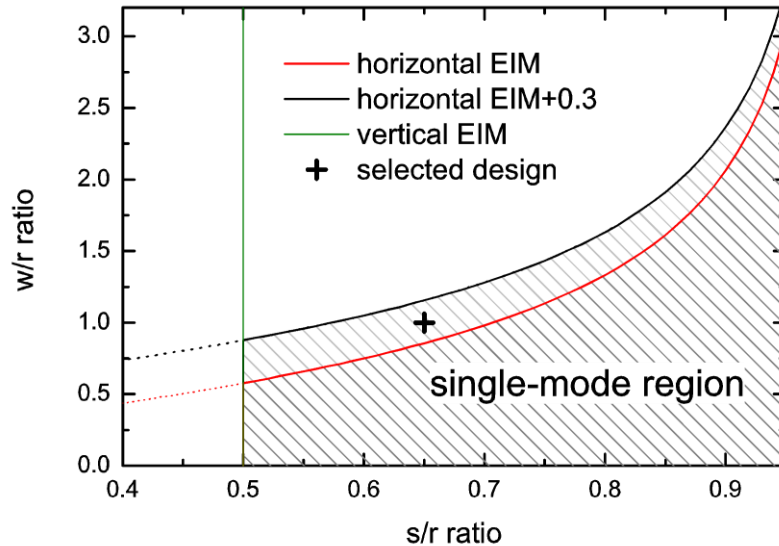


Figure 3. 3: Single-mode criteria for large rib waveguides calculated from the EIM and the addition of 0.3 to match the corrected criteria measured from FEM and BPM simulations. Equations shown in Chapter 2. The selected design falls within the single-mode region and offers a near-circular profile.

### 3.1.2 Single-mode requirements

The single-mode criteria for rib waveguides was discussed and defined in Chapter 2 and was derived using the EIM. For large rib waveguides, the single-mode criteria are developed into a ratio of dimensions that does not depend on wavelength, refractive index or polarisation. FEM and BPM simulations in this work, confirmed analysis performed by others [5, 11-13] that the single-mode criteria is better defined by an addition of 0.3 to the EIM single-mode criteria.

A design was initially selected based on the requirement for near-circular profile for optimal coupling. Circular profiles are obtained in channel waveguides when the waveguide width is equal to the height (for equal confinement). Initially the rib width is selected to be equal to the rib height,  $w=r$ , and a slab thickness,  $s$ , is selected preferably as low as possible whilst maintaining single-mode operation. The ratio of  $s=0.65r$  and  $w=r$  was selected. This is slightly away from the cut-off of the second mode to allow for fabrication related tolerances. This is shown in conjunction with the single-mode criteria in Figure 3. 3.

These criteria may be correct according to Maxwell equations but it does not take into account that unguided modes may remain within the rib region for a significant propagation distances. Since unguided modes may exhibit low loss, it is required to perform propagation analysis on the selected design. This has been shown by Lousteau et al. [13] to significantly alter the simplified considerations shown in Figure 3. 3. Some

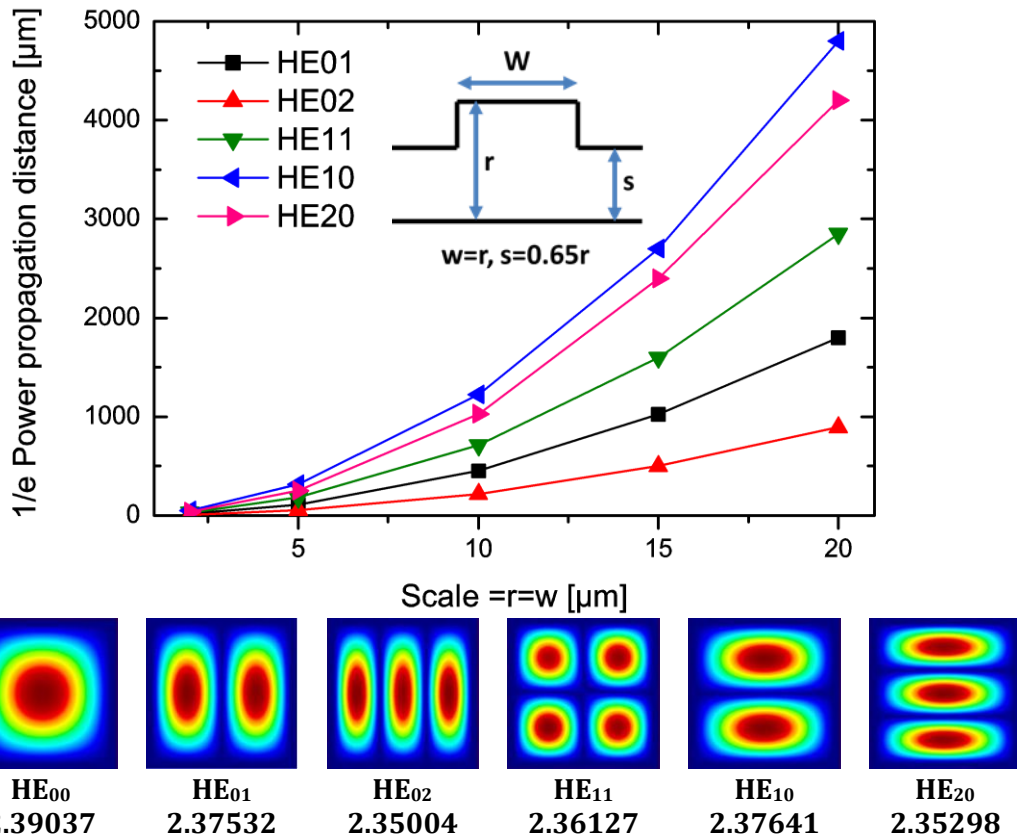


Figure 3. 4: The propagation distance required for the power in the rib region to drop to 1/e of the launch power for various higher order channel modes and cross-sectional areas. The HE<sub>00</sub> will have an infinite 1/e power propagation distance due to significant coupling to the fundamental rib mode. All higher order modes will excite a significant number of radiation modes that leak horizontally through the slab. Wavelength = 637 nm, refractive index = 2.42. Shown below is the field magnitude of the modes used for excitation for a scale of 2 μm.

designs create geometry-dependent loss for the higher order modes. This type of analysis will also have significance for short waveguides in resonators, where the effective resonator length can be considered as the propagation distance.

In order to ascertain the propagation distance required for unguided modes to leave the rib region, analysis was performed using BPM simulations. Rib waveguides with a fixed ratio of  $s=0.65r$  and  $w=r$  and varying scale, were excited with channel-like higher order mode profiles which have the potential to remain guided for the waveguide length. These are hybrid modes were modelled for both polarisation states and are discussed in more length in Section 2.5. Exciting the waveguide with higher-order channel modes preferentially excites the waveguide modes with least loss. These modes will have the lowest possible effective index change between the mode and the surrounding slab and are thus expected to propagate away from the rib region slowly. The results of this analysis are shown in Figure 3. 4.

The results shown in Figure 3. 4 highlight several important considerations for the large cross-sectional-area rib waveguide design. Results show that higher-order lossy modes in the rib have complex relationships with the surrounding slab. The  $HE_{10}$  and  $HE_{20}$  modes propagate the longest distance before diffracting out of the guide. This is because a significant proportion of the mode's power remains in the rib top and the opportunity for this power to leak into the slab is reduced due to poor interaction between the rib top and the slab. This effect causes higher order vertical modes to remain guided over significant distances in the waveguide even though they are theoretically unguided modes. For this reason it is always necessary to perform propagation analysis for every waveguide geometry to ensure the removal of these higher-order modes over the propagation distance of interest.

### 3.2 Large area diamond rib waveguides

Recent interest in diamond quantum information technologies [14] and advances in material growth and processing techniques [15] have led to significant progress in the fabrication of single-crystal diamond waveguides. Various methods to define a membrane or planar waveguide layers include ion implantation [16-20], growth on sacrificial layers [21] and etching mechanically-thinned substrates [22, 23]. Membranes require transverse waveguide definition by either reactive ion etching [19] or focussed ion beam writing [20, 21]. In this work mechanical substrate thinning is used to define the waveguide in the vertical direction with reactive ion etching to provide transverse confinement.

#### 3.2.1 Sample and design

Synthetic single crystal diamond platelets were obtained commercially from Element 6 Ltd. This synthetic diamond exhibits low birefringence with low defects and colour centres, and can be of higher optical quality than natural diamond. These properties are essential for optical work, to reduce bulk losses and further defects that could be produced by sample processing. The variety of diamond samples for this work was restricted by cost and commercial availability. Mechanically thinned samples were considered for fabrication of large cross-section waveguides. At the time of this research, the thinning techniques used consequently limited the area of the sample. 2 mm × 2 mm × 20 µm free-standing diamond samples were obtained with 6 optically polished surfaces to which further processing could be applied.

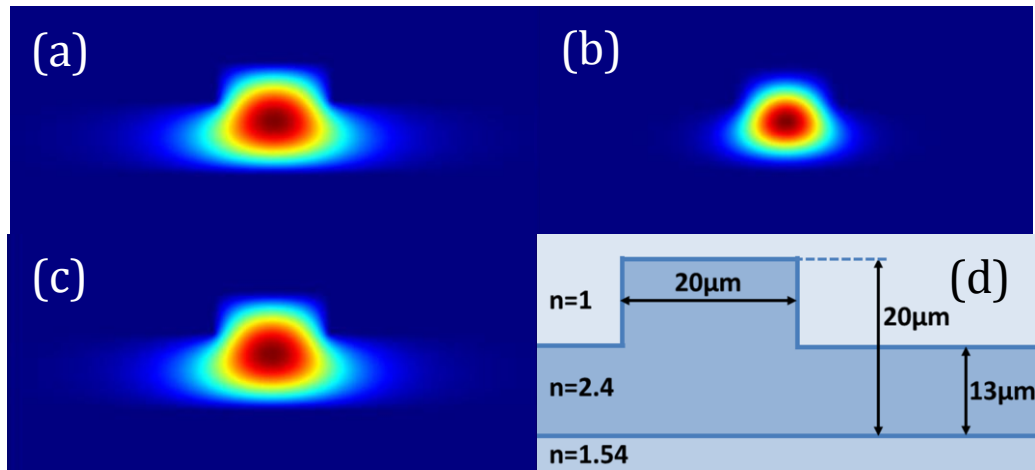


Figure 3. 5: **(a)-(c)** Finite element simulation of the waveguide design shown in schematic d) with  $w=r=20\ \mu\text{m}$  and  $s=0.65r$ ,  $s=13\ \mu\text{m}$ . **(a)** Normalised electric field for a TE mode at a wavelength of 532nm when the diamond refractive index=2.43. **(b)** Normalised electric field for a TE mode at a wavelength of 1064nm when the diamond refractive index = 2.4. **(c)** Normalised intensity for the guided mode shown in b).

In order to limit processing requirements for both technological reasons and in order to maintain a high quality sample, a simple one-etch-step rib waveguide design was considered. A design was selected as discussed previously in this chapter, in order to maintain single-mode requirements whilst obtaining mode profiles that are guided well within the rib region. A design with  $s=0.65r$  and  $w=r$  was selected. For the diamond sample used, this corresponded to a rib width  $w = 20\ \mu\text{m}$ , a rib height  $r = 20\ \mu\text{m}$  and a slab height of  $s = 13\ \mu\text{m}$ . This could be obtained with a single etch depth of  $7\ \mu\text{m}$ . The waveguide was selected to propagate with a constant cross-section for the length of the sample of 2 mm. This waveguide design is shown alongside the single-mode criteria in Figure 3. 3 and is the same as that selected for simulation in Figure 3. 4. The guided mode profile is shown in Figure 3. 5.

### 3.2.2 Fabrication

Fabrication was carried out by Y. Zhang in conjunction with this work [24]. The process flow is outlined in Figure 3. 6 (right).

$1\ \mu\text{m}\ \text{SiO}_2$  was deposited on the underside of the diamond using plasma enhanced chemical vapour deposition (PECVD). Analysis of the guided mode profile with finite element software showed that the power dropped to negligible levels within a few hundred nanometres and thus a  $1\ \mu\text{m}$  thick  $\text{SiO}_2$  layer was more than sufficient to ensure that the exponential decay in this region is not disturbed by any mechanical holders.

### Chapter 3 – Diamond Waveguides

An SiO<sub>2</sub> layer was also deposited using PECVD for use as a hard mask on the topside of the diamond. The minimum thickness of this layer was critical to the final etch depth of the diamond. To achieve a 7 µm etch depth in diamond using ICP it was calculated from Table 3. 2 that 750 nm of SiO<sub>2</sub> was required.

A novel photolithography method was developed in conjunction with this work to ensure that an accurate photoresist pattern and thickness could be maintained up to the edge of the 4 mm<sup>2</sup> chip. Photolithography typically uses a spin coating process to deposit a precise thickness of photoresist across the device. However, photoresist builds up on the edges of the chip during this process and it is difficult to obtain a constant thickness for the last 100 µm from the edge. This effect causes a problem during the transfer of the pattern and usually results in rib guides with reduced etch depth close to the edges of the sample which can distort the desired profile significantly.

Usually this effect is overcome by using chip sizes that are significantly larger than the desired waveguide structure and a post-fabrication cleave is carried out to remove the poor quality sample edge. This technique was unsuitable for this work due to the small area of the diamond sample, as it is not only very difficult to cleave samples whose side length is smaller than 2 mm but, if successful, the remaining sample size would be undesirable. Hiscocks et al. have proposed an alternative solution that consists of artificially extending the surface to be processed by embedding the diamond sample in a polydimethylsiloxane casing [25].

The method developed in this work involves the deposition of the photoresist using inkjet printing to ensure uniform deposition over the entire sample right up to the edge. An inkjet printer (Dimatix DMP-2800) was used in conjunction with photoresist S1805 which offers a high etch selectivity 1:4 to SiO<sub>2</sub>. This inkjet printer deposited 10 pl drops onto the diamond sample and was controlled with a piezo actuator. By carefully selecting the spacing between the photoresist drops a continuous photoresist strip was formed on the SiO<sub>2</sub>/diamond sample. Printed photoresist dots have a ring shape produced by the 'coffee-stain effect' [26] due to differential evaporation rates across the surface that create a lower height in the centre compared to the edges. This problem was overcome by deposition of several printed layers as shown in Figure 3. 6.

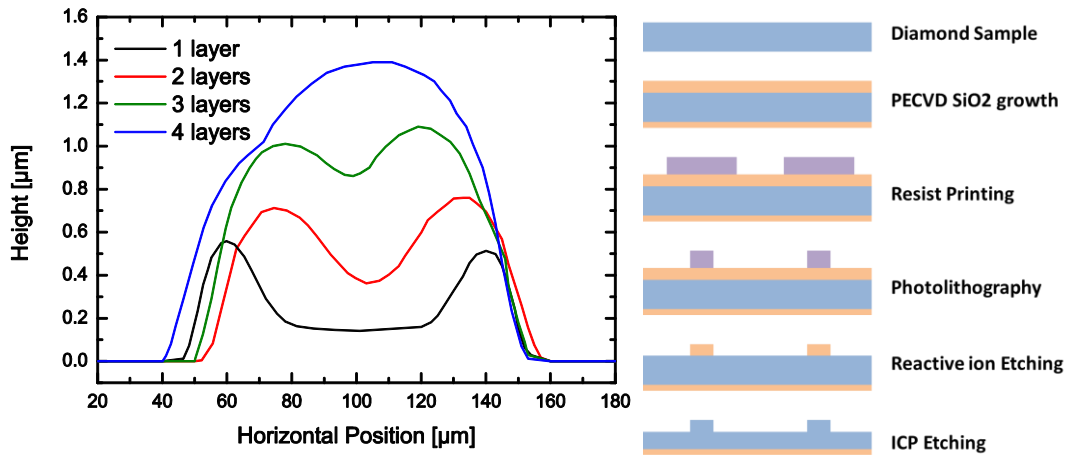


Figure 3. 6: **(left)** Surface profilometer measurements of a typical sample with 1-4 layers of photoresist deposited using inkjet printing. A typical strip was 1.5  $\mu\text{m}$  high and 100  $\mu\text{m}$  wide after 4 layers of photoresist. Manual alignment explains the horizontal offset between measurements and depositions and did not affect the definition of the much smaller waveguide widths. **(right)** Fabrication process flow from top to bottom.

Using standard contact photolithography techniques the waveguide width was defined in the deposited (uncured) strips of photoresist which extended to the sample edges. A mask was designed and fabricated commercially for the diamond waveguide structure that consisted of 2-mm-long straight lines with width progressing from 17  $\mu\text{m}$  to 25  $\mu\text{m}$ . A Karl Suss MA-6 contact mask aligner was used to transfer this mask design to the photoresist stripes and results are shown in Figure 3. 7.

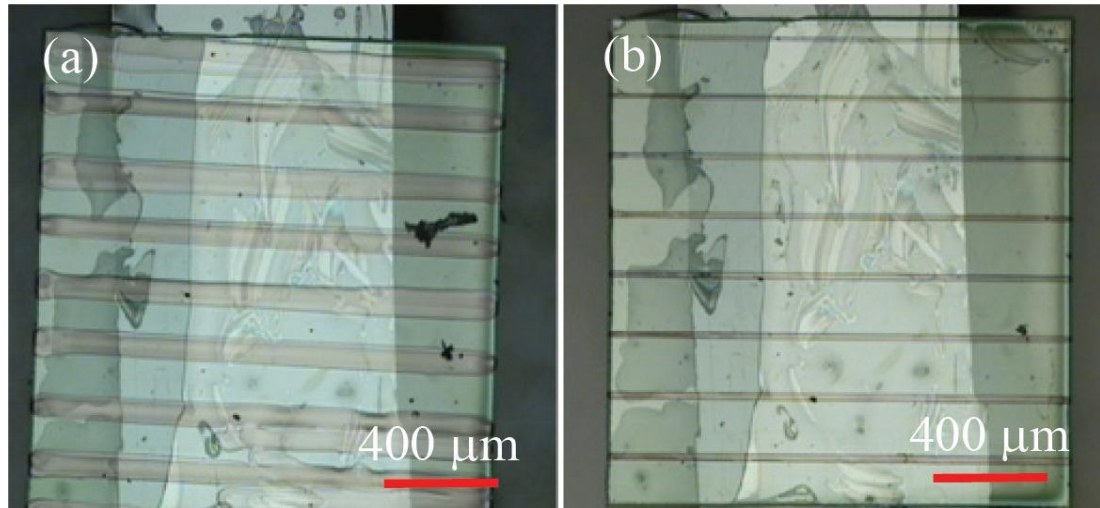


Figure 3. 7: Optical microscopy top-down images of **(a)** The photoresist stripes after inkjet printing and **(b)** the photoresist after transferring the waveguide mask design to the stripes. Diamond samples are transparent and the underlying glue and holder are visible.

Reactive ion etching (RIE) was used to transfer the pattern of the photoresist to the 750 nm SiO<sub>2</sub> hard mask. The etching recipe used for the hard mask is shown in Table 3. 1 and this process took around 18 minutes. The photoresist layer was sufficiently thick

### Chapter 3 – Diamond Waveguides

such that after patterning of the hard mask the remaining photoresist had to be removed with acetone and methanol. An optical image shows the patterned hard mask in Figure 3. 8 a).

Table 3. 1: RIE recipe for SiO<sub>2</sub> with etch rate of SiO<sub>2</sub> and S1805 photoresist.

Pressure	Ar Flow	CHF <sub>3</sub> Flow	Platen Power	SiO <sub>2</sub> Etching Rate	S1805 Etching Rate
66 mTorr	15 sccm	5 sccm	200 W	41 nm/min	10 nm/min

Inductively coupled plasma reactive ion etching was used to transfer the hard mask pattern into the diamond. The etching recipe used for diamond is shown in Table 3. 2 and the etching time took 25 minutes to reach an etch depth of 7 μm. An optical image shows the patterned diamond in Figure 3. 8 b).

Table 3. 2: ICP recipe for diamond with etch rate of diamond and SiO<sub>2</sub>.

Pressure	Ar Flow	O <sub>2</sub> Flow	CHF <sub>3</sub> Flow	Platen Power	Diamond Etching Rate	SiO <sub>2</sub> Etching Rate
5 mTorr	15 sccm	40 sccm	1200 W	300 W	280 nm/min	30 nm/min

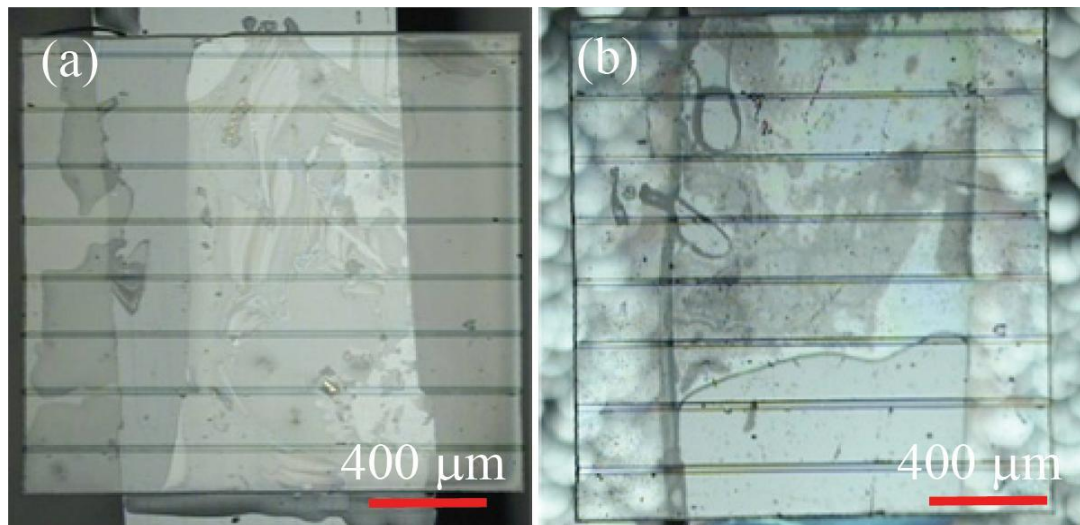


Figure 3. 8: Optical microscopy top-down images of (a) The SiO<sub>2</sub> hard mask after RIE and (b) The final sample with patterned diamond. Diamond samples are transparent and the underlying glue and holder are visible.

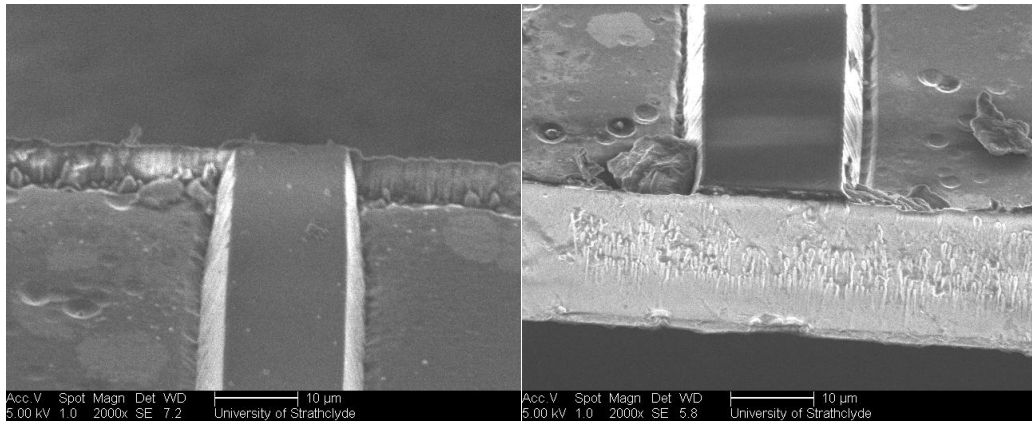


Figure 3. 9: Scanning electron microscope images of a facet of the diamond waveguide at the edge of the sample.

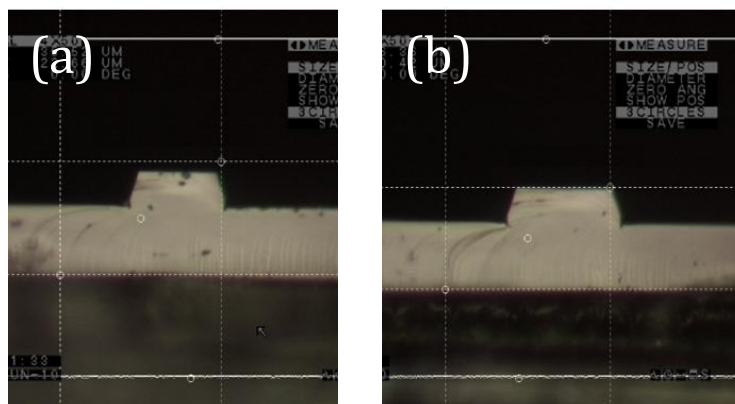


Figure 3. 10: Optical image of a cross-section of the waveguide. **(a)** A cleave through the sample showing the cross-section of a 17 µm wide waveguide. **(b)** A cleave through the sample showing the cross-section of a 25 µm wide waveguide.

As shown in Figure 3. 8 to Figure 3. 10, the waveguide ridge extends up to the edges of the sample and its cross-section is in agreement with the chosen design specifications. From the SEM image, the side slope angle of the diamond waveguide was measured to be about  $16^\circ$  from verticality. The roughness observed on the edge facet in Figure 3. 9 shows the (non-ideal) quality of the supplied polished platelet since these (side) surfaces remained unaffected by sample handling and waveguide processing steps. It is noticed that the etched (top) surface contains some etch pits and trenches. These etch-related defects and surface roughness should be reduced by further optimising etching parameters and processes. Here again, readily-achievable improvements in the platelet preparation and fabrication process would lead to waveguides of enhanced quality and characteristics.

### 3.2.3 Optical characterisation

Coupling into and out of most waveguides is a non-trivial task. There is a large range of coupling methods employed for waveguides of different types. Early waveguides were in the form of sub-micron planar waveguide films, for which coupling was particularly tricky. Prism coupling [27-29] and grating couplers [30-32] were best suited for these types of waveguides. Facet coupling is only suitable for waveguides which have a cross-sectional area greater than the wavelength of light, as free-space light cannot be focussed to smaller spot sizes.

For the large cross-sectional area waveguide fabricated as part of this work, free-space facet coupling was a simple and appropriately targeted means of waveguide coupling. Neither prism coupling nor grating coupling would be appropriate for these short length waveguides due to the limited length of the sample in comparison to the waveguide cross-section. Fibre to waveguide butt-coupling is not suitable for this type of waveguide due to the large area mismatch between single-mode fibres at visible wavelengths and the waveguide.

Optical characterisation was carried out at a wavelength of 633 nm with a red He-Ne laser, as this wavelength is close to that of the nitrogen vacancy centre emission at 637 nm, one of the potential applications for diamond waveguides. Several different free-space end-coupling arrangements were employed in order to optimise the coupling. It was necessary to ensure that unguided light diverged sufficiently for high contrast between guided modes and unguided light. For this reason optimal results were obtained using a tight focus, with a large divergence, hitting the waveguide facet with a mode-area-matched beam but with a curved wavefront. Simulation work was carried out to predict the propagation characteristics of the He-Ne beam in the diamond and is shown in Figure 3. 11.

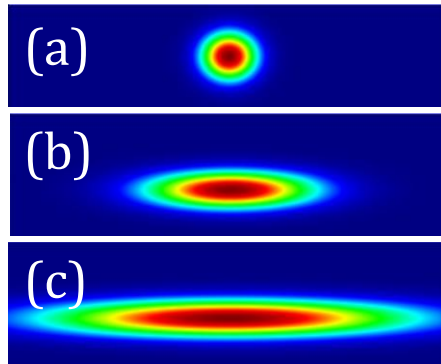


Figure 3. 11: Theoretical plots of **(a)** Gaussian approximation of guided light in the waveguide. **(b)** Horizontal spread of profile in a) after 2 mm propagation in diamond. **(c)** Horizontal spread of unguided light in slab after propagating 2 mm with a highly diverging coupling profile as described in the text.

This work shows that the additional spread of the unguided diverging beam in Figure 3. 11 c) allows for easy discrimination between guided and unguided light. The experimental setup as shown in Figure 3. 12 was used to determine the guiding properties of the waveguides.

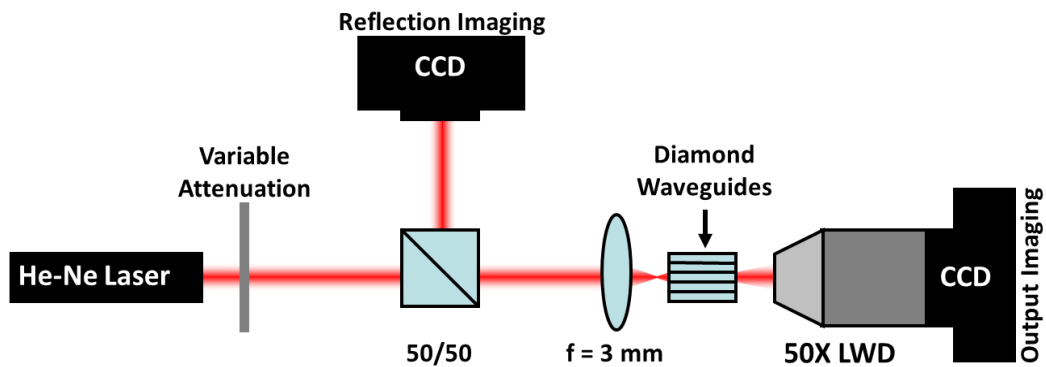


Figure 3. 12: Schematic of experimental setup used for optical characterisation.

Coupling was achieved with a 3 mm focus lens which provided a spot diameter at focus of  $5\ \mu\text{m}$ . This coupling beam was allowed to diverge until hitting the sample with a spot size which matched the guided mode. Output coupling was achieved with a 50X magnification long working distance (LWD) objective. Variable attenuation was used to prevent saturation of the camera. Reflection imaging allowed the tailoring of the mode profile on the input facet. Images of the output facet were recorded with a CCD, one set of which are shown in Figure 3. 13.

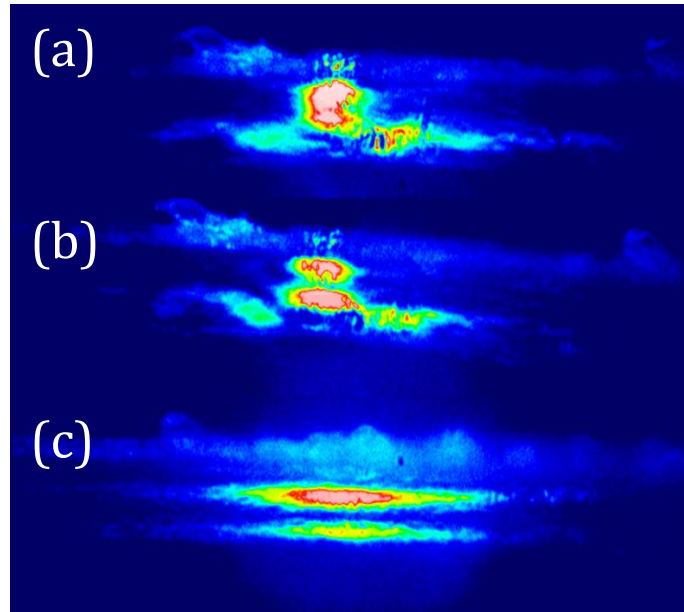


Figure 3. 13: Measured optical power at waveguide exit facet. **(a)** Guided fundamental mode **(b)** Guided 1<sup>st</sup> order vertical mode **(c)** Horizontally unguided light, measured away from the rib region.

The output profile was examined whilst changing the coupling conditions in order to excite various guided modes. Results in Figure 3. 13 show that the waveguide is capable of guiding the fundamental (a) and second vertical mode  $HE_{10}$  (b). The unguided light, which is a high order planar waveguide solution of the slab, is shown in (c) as a reference.

The surface quality of the output facet of the waveguide as seen in Figure 3. 9 is proposed to be a significant source of distortions measured on the guiding profile. Similar distortions on the input facet reduce the coupling coefficients and increase the component of unguided light in the measurement. It should be noted that this is a proof-of-principle demonstration and improved results should be possible with better platelet preparation.

The observation of the guided  $HE_{10}$  mode was not an unexpected result. It was shown in Figure 3. 4 that the  $HE_{10}$  mode is the mode which has the lowest leakage into the slab and when excited directly will remain guided for propagation distances exceeding the length of this fabricated waveguide. This observation shows that this waveguide cannot be considered single-mode for this short propagation distance. It is expected however, that this higher order mode is will leak out of the waveguide over a longer distance.

The demonstration of this diamond waveguide adds to the very limited number of fabricated waveguides to date [25, 33]. The processing steps employed here may be

used to fabricate waveguides of varying cross-section. Diamond waveguides may find application in the field of integrated quantum photonics [14] and this work outlines one method to fabricate such devices. An alternative application for diamond waveguides is for Raman lasers [34]. Raman lasers may benefit from small increases in confinement and lengths. These are different requirements to that of integrated quantum photonics. The rest of this chapter theoretically investigates the possibility for a diamond waveguide Raman laser and what performance it may have. Propagation loss is considered to be a key factor in the consideration of all diamond waveguides due to the high refractive index and processing quality concerns. As such, a method to estimate losses is considered and then implemented into Raman laser performance analysis.

### 3.3 Analytical scattering loss theory

Scattering loss is a source of propagation loss caused by the interaction of the guided mode with imperfect waveguide surfaces. Scattering, bulk absorption, radiation (leaky modes), and nonlinear effects such as two-photon absorption make up the predominant propagation loss mechanisms of most dielectric waveguides. Bulk losses are minimised by obtaining high quality defect and stress free materials. Radiation losses are prevented by appropriate waveguide design. Loss by two-photon absorption is not of concern when operating at photon energies below half the bandgap. Scattering is a source of loss for waveguides characterised by high index contrasts and is of particular concern for waveguides with small cross-sectional areas. This loss is likely to be significant in diamond waveguide structures, because the minimisation of process-induced roughness is difficult to perform due to the limited availability of samples.

The prediction of scattering loss is fundamental to assessing the practical benefits of waveguides, especially for systems where gain and loss relate to device performance such as waveguide amplifiers or lasers. There are several methods to model and predict the magnitude of scattering loss. These include the integration of radiation modes [35], simplifications based on the geometrical optics approach [36], the volume current method [37, 38] and adaption of coupled mode theory [39-41].

In the work of Payne and Lacey [42, 43], a simple and intuitive description of scattering loss was obtained by integration of radiation modes. This model has been shown to agree well with experimental results [44, 45] and theoretical methods offered by

### Chapter 3 – Diamond Waveguides

Marcuse [35]. This has been developed into an easy-to-use formula for calculating scattering loss based on the parameters of the waveguide.

For this work, it is important to understand the applicability of this simplified equation and to develop it further into a full solution of the rib waveguide. It is necessary to examine some of the simplifications made within the model, rather than using the final equation as more widely known:

$$\alpha = \frac{k^3}{4\pi n_2} (n_2^2 - n_1^2)^2 \phi_s^2 S_c, \quad S_c = \int_0^\pi \mathbf{R}(\beta - n_1 k \cos \theta) d\theta \quad (3.7)$$

$$\mathbf{R}(u) = \sigma^2 \exp\left(-\frac{|u|}{L_c}\right), \quad \int_{-\infty}^{\infty} \phi_s^2 dy = 1$$

$\alpha$  is the propagation loss from both surfaces of a symmetrical planar waveguide, where  $n_2$  is the refractive index of the waveguide,  $n_1$  is the refractive index of the cladding,  $\beta$  is the propagation constant of the guided mode,  $\sigma$  is the root mean square of the roughness and  $L_c$  is the correlation length of the roughness. Here, the exponential description of the scattering loss is used.  $\Phi_s$  is the electric field on the waveguide surface and is normalised by the integral in Equation (3.7). The integral  $S_c$  can be solved:

$$S_c = \sqrt{2} \sigma^2 \pi \frac{1}{p} f_e, \quad f_e = \frac{x \sqrt{\sqrt{(1+x^2)^2 + 2x^2 \gamma^2} + 1 - x^2}}{\sqrt{(1+x^2)^2 + 2x^2 \gamma^2}} \quad (3.8)$$

$$x = pL_c, \quad \gamma = \frac{n_1 v}{n_2 t p} \sqrt{\frac{2n_2^2}{n_2^2 - n_1^2}}$$

$$h = k \sqrt{n_2^2 - N^2}, \quad p = k \sqrt{N^2 - n_1^2}, \quad v = kt \sqrt{n_2^2 - n_1^2}$$

where the parameters  $h$ ,  $p$  and  $v$  are used as described in Chapter 2 making use of  $t$  the thickness of a planar waveguide which later can be adapted to terms  $r$ ,  $w$  and  $s$  for a rib waveguide. This gives a simple description of the loss which has four major components: terms that are independent of the guided mode solution, the electric field on the boundary squared and normalised, the inverse transverse propagation constant in the cladding and a term which depends on the correlation length of the scattering surface:

$$\alpha = \frac{\sigma^2 k^3}{\sqrt{2} n_2} (n_2^2 - n_1^2)^2 \phi_s^2 \frac{1}{p} f_e \quad (3.9)$$

The normalised field on the boundaries can be found by integrating over the three regions with use of the transverse resonance equation from Chapter 2:

$$\phi_{s\ TE}^2 = \frac{2}{h^2 + p^2 \left( t + \frac{2}{p} \right)}, \quad \phi_{s\ TM}^2 = \frac{2}{\frac{h^2 n_1^4 + p^2 n_2^4}{2h^2 n_2^4 n_1^4} \left( t + \frac{2n_2^2 n_1^2 \left( \frac{n_2^2}{n_1^2} h^2 + p^2 \right)}{p(h^2 n_1^4 + p^2 n_2^4)} \right)} \quad (3.10)$$

It is important to understand that the normalised waveguide surface field,  $\Phi_s$ , plays a role in defining how much power is in the exponential tails of the waveguide, which is shown to be the dominant source of loss. When considering the discontinuity at the waveguide boundary, the TM mode produces a higher E field. This dictates that significantly more power is propagated in the cladding than the weak guide approximation would predict. Equation (3.10) can be solved with an iterative method or Marcatili’s analytical solution as proposed here. It is interesting to compare the difference between these polarisations and this is shown in Figure 3. 14.

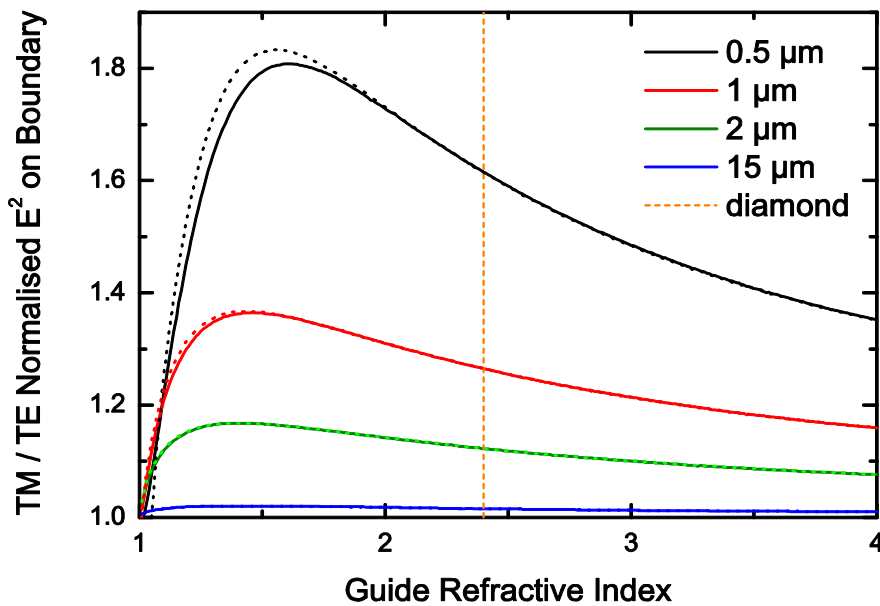


Figure 3. 14: Ratio of TM to TE normalised  $E^2$  on the waveguide boundary calculated with equation (3.10) with a cladding index of 1 at a wavelength of 630 nm for different guide thicknesses. Solid lines are calculated with numerical iteration and the dotted lines shows Marcatili’s analytical approximation.

Figure 3. 14 shows that there is insignificant difference for the E field on the boundary between TE and TM modes for large area waveguides. The TM interaction is expected to only have more loss for waveguides with a small cross-section. Furthermore it shows the suitability to use the analytical solution in order to calculate  $\Phi_s$ .

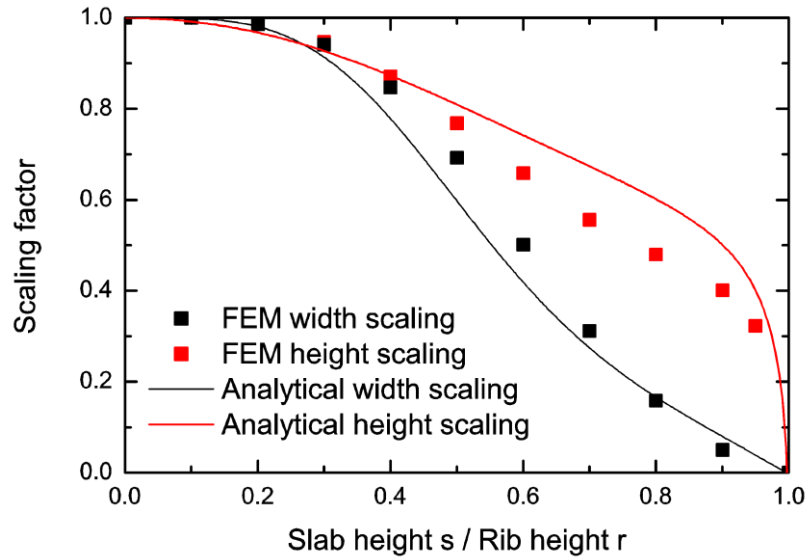


Figure 3. 15: Scaling factors shown in Equation (3.12) that represent the planar waveguide components of the rib waveguide. Analytical solutions using Marcatili’s solution are compared with finite element method results for a diamond waveguide with  $r=w=2\ \mu\text{m}$  at a wavelength of 630nm for varying  $s$ .

Term  $f_e$  depends on the correlation length of the roughness, and is described in equation (3.8). This is a statistical measure of the repetitive nature of the roughness. It can be calculated for a range of waveguide parameters and correlation lengths and is shown to reach a maximum of:

$$f_e = \frac{1}{\sqrt{2}} \quad (3.11)$$

This geometry and wavelength-independent value for  $f_e$  can greatly simplify calculations and assumes a value of maximum loss. In practice, with careful fabrication, significant loss reduction below this value can be achieved. In this work, the maximum scattering loss is of interest and equation (3.11) is used.

In order to extend equation (3.9) from planar waveguides to rib waveguides, methods used in Chapter 2 to describe the rib waveguide in terms of planar waveguide components will be used. This has also been proposed by Yap et al. [45]. Three component planar waveguides are considered: a vertical planar waveguide with thickness  $r$ , which describes vertical confinement in the rib region, a vertical planar waveguide with thickness  $s$ , which describes vertical confinement in the slab region and a horizontal planar waveguide, with thickness  $w$ , which describes horizontal confinement in the rib above the slab.

### Chapter 3 – Diamond Waveguides

In order to describe what fraction of the power is guided by these various planar waveguides, some scaling factors are introduced using variational theory. Yap et al. introduce a scaling factor which takes into account the proportion of power guided horizontally by the rib sidewalls. Here, another scaling factor is proposed to take into account the power guided vertically by the rib region in comparison to the slab:

$$\chi_w = \frac{dN_{rib} / dw}{dN_{channel} / dw}, \quad \chi_r = \frac{dN_{rib} / dr}{dN_{channel} / dr} \quad (3.12)$$

These two scaling factors allow direct comparison to a channel waveguide which can be approximated separately in both the horizontal and vertical direction by planar waveguide solutions as shown in Figure 3. 15.

A full account of scattering loss for any dimension rib waveguide can now be calculated through analytical solutions from Marcatili's approximations to all components of Equation (3.9). For this work, the rib top, rib sidewall and slab top are considered as scattering surfaces and the bottom surface is neglected due to the higher roughness induced by etching:

$$\begin{aligned} \alpha_{TE} &= \frac{k^3}{2n_2} (n_2^2 - n_1^2)^2 \left[ \chi_w \frac{\phi_{s\_w\_TM}^2 \sigma_w^2}{P_{w\_TM}} + \frac{1}{2} \chi_r \frac{\phi_{s\_r\_TE}^2 \sigma_r^2}{P_{r\_TE}} + \frac{1}{2} (1 - \chi_r) \frac{\phi_{s\_s\_TE}^2 \sigma_s^2}{P_{s\_TE}} \right] \\ \alpha_{TM} &= \frac{k^3}{2n_2} (n_2^2 - n_1^2)^2 \left[ \chi_w \frac{\phi_{s\_w\_TE}^2 \sigma_w^2}{P_{w\_TE}} + \frac{1}{2} \chi_r \frac{\phi_{s\_r\_TM}^2 \sigma_r^2}{P_{r\_TM}} + \frac{1}{2} (1 - \chi_r) \frac{\phi_{s\_s\_TM}^2 \sigma_s^2}{P_{s\_TM}} \right] \end{aligned} \quad (3.13)$$

Equation (3.13) is used to calculate the scattering loss of a diamond rib waveguide, with a fixed geometry matching that shown in Figure 3. 5, for various scaled sizes operating at 532nm and is shown in Figure 3. 16. Values of root mean square roughness are used from a typical study of a Silicon rib waveguide fabricated with a similar methodology to the diamond waveguide fabricated as part of this work [46]. These values will vary from sample to sample and with careful fabrication procedures can be greatly reduced. It is shown that scattering loss greatly reduces with increasing size, something that is perhaps not evident by examining equation (3.13) alone as the waveguide size does not appear in the equation. Sidewall scattering is shown to dominate the loss as the sidewalls are expected to have a much higher roughness.

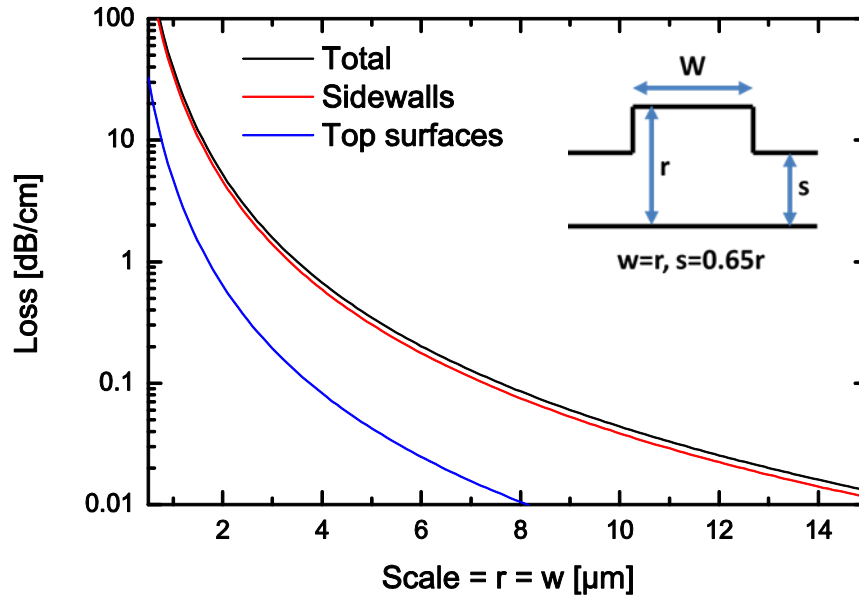


Figure 3. 16: TE mode maximum scattering loss for a rib waveguide with  $s=0.65r$  and  $w=r$  at a wavelength of 532 nm with a refractive index of 2.4. The top surfaces and sidewalls are only considered to contribute to scattering loss. A sidewall roughness of 17 nm and a top surface roughness of 4 nm is used. The TM mode differs negligibly for the range of dimensions considered.

### 3.4 Diamond Raman waveguide analysis

Diamond has been identified for some time as a suitable Raman laser material due to its high Raman gain, high thermal conductivity, broadband transparency and mechanical robustness [47-49]. However, efficient and CW Raman laser operation has only been demonstrated recently [34, 50-53] due to the increased availability of high optical quality diamond of suitable dimensions. The objective of this work is to scope out the feasibility and potential operating characteristics of a waveguide-based approach to a diamond Raman laser. In particular, it should be noted that increased confinement, increased interaction lengths, higher pump/signal overlaps are some of the arguments for such a system. The good pump/signal overlap in a waveguide may offer efficient cascading to higher-order Stokes beams. Furthermore, the possibility for integration with other waveguide devices is an additional motivation. The waveguide geometry has been utilised to develop a Raman laser in silicon where high two-photon absorption (TPA) loss occurs [54]. A similar diamond version of such a device should offer superior characteristics due to the lack of TPA.

#### 3.4.1 Coupled equations

Raman laser output at the first Stokes wavelength depends on the Raman gain coefficient, the pump intensity, the crystal length and incurred losses. Due to this

nonlinear process, it is clear that a significant increase in output power for a fixed input power can be obtained by reducing the mode area of the Stokes beam and optimising the material length. This is the technique used to great success in silica Raman fibre lasers with low Raman gain coefficients. This same technique of reducing the mode area of the Stokes cavity can be applied to crystals by use of a waveguide. The reduction in guided mode area is not, on its own, enough information to calculate the increase in output powers; the waveguide losses, material loss, Raman gain, crystal length and cavity reflectivities must also be taken into account. This makes accurate prediction of waveguide propagation loss, as discussed in Section 3.3, a key task in the optimisation of Raman waveguide laser design.

In order to optimise the design of the Raman laser, the well-known coupled equations (3.14) need to be integrated. Here, these equations are shown for a double-pump-pass system, as this geometry is easily achievable and offers a number of algebraic simplifications. The model neglects cascading to the second Stokes, which can be achieved by anti-reflection coating the facets at the second Stokes wavelength.

$$\begin{aligned}
 \pm \frac{1}{P_p^\pm} \frac{dP_p^\pm}{dz} &= -\alpha_p - \frac{g}{a} \frac{\lambda_s}{\lambda_p} (P_s^+ + P_s^-) \\
 \pm \frac{1}{P_s^\pm} \frac{dP_s^\pm}{dz} &= -\alpha_s + \frac{g}{a} (P_p^+ + P_p^-) \\
 P_p^+(0) &= P_{in}, \quad P_p^-(L) = R_p^L P_p^+(L) \\
 P_s^+(0) &= R_s^0 P_s^-(0), \quad P_s^-(L) = R_s^L P_s^+(L)
 \end{aligned} \tag{3.14}$$

where  $P$  is the power,  $\alpha$  is the propagation loss,  $g$  is the Raman gain coefficient,  $a$  is the mode area,  $R$  is the reflectivity and  $L$  is the material length in the  $z$  direction. The subscripts  $p$  and  $s$  denote the pump and the Stokes beams respectively. The superscripts  $+$  and  $-$  denote the forwards and backwards directions, respectively.  $P_{in}$  is the pump power, with 100% coupling considered.

In contrast to fibre-based systems, the use of crystalline Raman gain media means that the gain coefficient depends on the selected sample cut with respect to the material crystallographic axes and to the polarisation orientation of the pump and Stokes fields. Analysis for diamond [55] has shown that the material gain is maximised for pump polarisations parallel to the crystallographic  $\langle 111 \rangle$  direction and propagation direction along  $\langle 110 \rangle$ . The associated gain coefficients for the main  $1332\text{cm}^{-1}$  Raman shift are

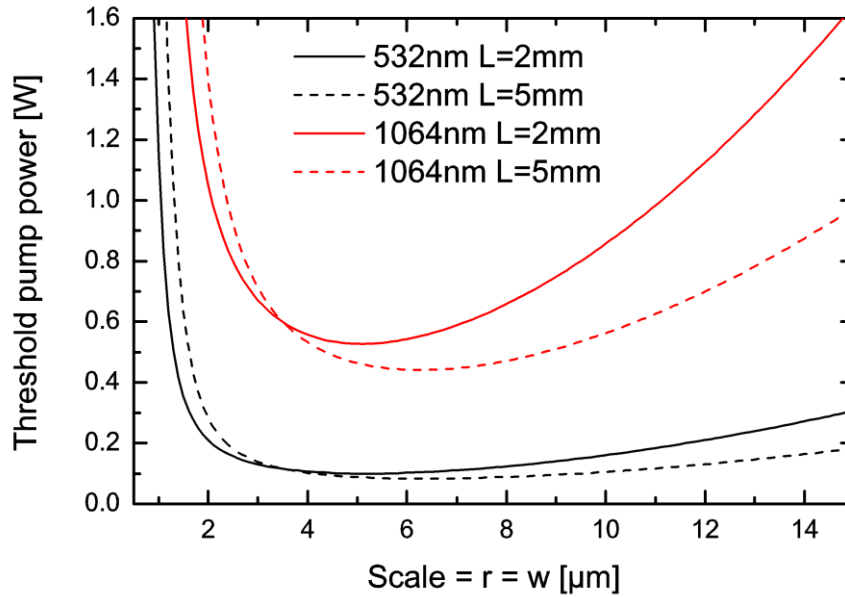


Figure 3. 17: Threshold power for a diamond Raman rib waveguide laser with different cross-sectional sizes, lengths and pump wavelengths calculated with equation(3.15). Parameters include: a fixed facet reflectivity of  $R_s^0=0.999$ ,  $R_s^L=0.99$ , a waveguide propagation loss calculated from equation (3.13) with  $\sigma_s= \sigma_r=4$  nm,  $\sigma_w=17$  nm and a bulk propagation loss of  $0.01$   $\text{cm}^{-1}$ .  $R_p^L$  is set to 1 making the system a double pump-pass system. A slab thickness of  $s=0.65r$  and  $w=r=\text{scale}$  is used for loss calculations whilst the mode area is taken to be the second moment width. The Raman gain coefficient used is  $75$   $\text{cm}/\text{GW}$  and  $14$   $\text{cm}/\text{GW}$  at a pump wavelength of  $532$  nm and  $1064$  nm respectively.

amongst the highest of all common Raman laser materials, taken here to be  $75\text{cm}/\text{GW}$  at  $532$  nm and  $14\text{cm}/\text{GW}$  at  $1064$  nm [56, 57]. These high gain values mean that samples of short length ( $<5$  mm) are sufficient to obtain Raman laser action with suitably designed laser resonators. Furthermore, this configuration is suitable for facet cleaving, simplifying the preparation of samples with high quality end faces, although it may not be optimal as far as growth is concerned since CVD samples are usually grown along the  $\langle 100 \rangle$  direction. Facet reflectivity coatings are assumed to be perfectly adhered to the diamond sample and with no graphitisation of the diamond during the coating process.

The pump wavelengths of  $532$  nm and  $1064$  nm are selected for analysis based on the wide availability of Nd:YAG and doubled Nd:YAG lasers. These pump sources offer high beam quality, narrow linewidth, the possibility for high pump powers and are cheap and versatile. Using the main Raman shift in diamond of  $1332\text{cm}^{-1}$  this produces Stokes beams at  $573$  nm and  $1240$  nm for  $532$  nm and  $1064$  nm pumping respectively.

Minimisation of the threshold power is one of the key motivations of Raman waveguide lasers, as Raman lasers typically exhibit high threshold powers in bulk operation

regimes requiring the use of complex high quality cavity systems, Q-switched and high power pump systems. This threshold power can be found by integrating equation (3.14):

$$P_{th} = \frac{a\alpha_p \left( 2\alpha_s + \ln \left( \frac{1}{R_s^0 R_s^L} \right) \right)}{2g(1 + (R_p^L - 1)e^{-\alpha_p L} - R_p^L e^{-2\alpha_p L})} \quad (3.15)$$

By using the values of scattering loss calculated in Section 3.3 with equation (3.13), in conjunction with a value of bulk loss, the threshold can be calculated for various Raman waveguide laser designs and is shown in Figure 3. 17. The value of bulk loss is here assumed to be 0.01cm<sup>-1</sup> [58]. These results highlight several important considerations for the design of a Raman waveguide laser. Although the threshold is known to reduce quite simply with the area of the guided mode, the effect of scattering loss increases dramatically towards smaller waveguide sizes. This creates an operating window to achieve the lowest threshold. The threshold calculation differs from typical linear laser systems in that lowest threshold is not achieved for the smallest volume. Results show that 5 mm long samples can offer lower thresholds than 2 mm samples. This is only the case when the propagation loss is low and for small-area waveguides the shorter sample length offers a lower threshold. This is due to round-trip loss competing with mode area reduction. Thus, a prediction of loss is always required to optimise the system. Scattering loss is shown to greatly increase threshold below a dimension of 3.5 μm which from Figure 3. 16 is when both Stokes and pump have a scattering loss around 1dBcm<sup>-1</sup>. Threshold for large-area devices is limited only by the bulk loss of diamond.

### 3.4.2 Analytical solution for a Raman laser including the Lambert function

When considering the solution to the coupled-equations above threshold, there is no correct and precise analytical solution to the problem. An accurate description of the output or intracavity power cannot be found with the use of the slope efficiency concept as is done with typical linear laser systems. The only way to find the Stokes and pump power within the cavity is to perform iterative analysis. An initial guess value can be selected for each point along the cavity and using iterative application of Equation (3.14) a solution may be converged for which after further iterations no change is observed is the power levels. This prevents the optimisation and design of the

waveguide without extensive computation time and prevents intuitive design. This is even more of a problem when propagation loss is highly structure-dependent, as here.

It can be shown that approximating the pump beam in the cavity (above threshold) to have linear attenuation that is larger than the propagation loss is an accurate approximation of the system [59, 60]. This linear attenuation can be described by use of the Lambert function that has been shown to match more complete iterative solutions [59, 60]. This approximation is shown as a set of equations in Appendix B and is referred to in the text as Equation (3.16):

See Appendix B (3.16)

It is convenient to define new terms for simplification such as gain factors  $\gamma$ , single-pass loss values  $\delta$  and effective lengths  $l_{\text{eff}}$  and are defined within Equation (3.16).

The Lambert function is itself non analytical, but can be approximated near zero and this approximation holds for the range of considered parameters. Here the sum of terms does not need to extend to infinity and 100 was found to be sufficiently accurate for this work:

$$Lb(x) = \sum_{n=1}^{n=100} \frac{(-n)^{n-1}}{n!} x^n \quad (3.17)$$

The accuracy of the analytical solution, equation (3.16), has been determined for a range of fibre based systems and is provided within reference [59]. It is proposed that the accuracy of this analytical method extends to shorter waveguides with larger cross-sections. In order to confirm the accuracy of this analytical solution an iterative algorithm was developed based on Equation (3.14). This iterative algorithm divides the waveguide into a number of steps, typically 100, and allows the pump and Stokes field to propagate forwards and backwards until the change after each repetition differs by less than 0.01%. Iterative algorithm results were confirmed to agree to those published by others [59].

Finally, the accuracy of the analytical method could be compared to a precise iterative method for the range of powers and device dimensions considered in this work. Figure 3. 18 shows the comparison between the two for one set of parameters. Results for a large range of parameters were found to agree with negligible error.

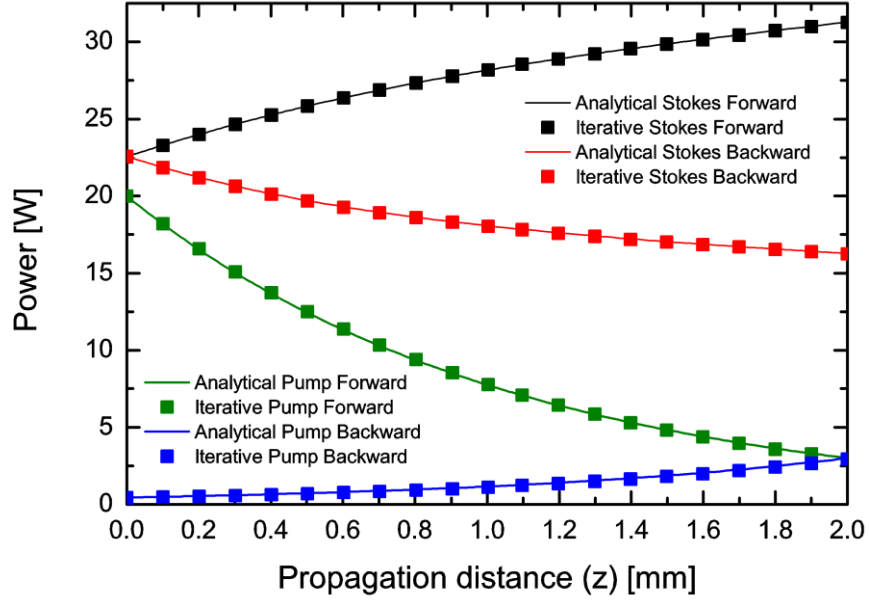


Figure 3. 18: Intracavity Stokes and pump powers in both directions calculated by analytical and iterative methods.  $P_{in} = 20$  W,  $R_s^0=0.999$ ,  $R_s^L=0.52$ ,  $R_s^L=1$ ,  $L=2$  mm,  $\lambda_p=1064$  nm,  $\lambda_s=1240$  nm and  $g=14$  cm/GW. Loss was calculated from equation (3.13) for  $r=w=4$   $\mu$ m,  $s=0.65r$  and was found to be  $\alpha_p=0.15$   $\text{cm}^{-1}$  and  $\alpha_s=0.148$   $\text{cm}^{-1}$  which was added to a bulk loss of  $1\text{cm}^{-1}$ . The second moment width was used for the mode area.

Laser output power is simply defined as  $(1-R_s^L)(P_s^+)$  at  $z=L$  and so optimisation can be performed to maximise output power. The usefulness of the analytical solution lies in the ability to optimise designs for a range of parameters. The one key outcome of the analytical description of the Raman laser is the ability to develop analytical functions to optimise the Stokes reflectivity of the output coupling facet for maximum output power for a fixed crystal length. This can be found by setting the derivative of the output power with respect to Stokes reflectivity to zero:

$$R_s^L \text{ Optimum} = \frac{d(1-R_s^L)P_s^+(z=L)}{dR_s^L} \quad (3.18)$$

$$R_s^L \text{ Optimum} = \exp \left[ 2L\alpha_s - \frac{4L \cdot P_{in} \cdot \frac{g}{a} - 2L\alpha_s}{\ln \left( 2P_{in} \frac{g}{a \cdot \alpha_s} \right)} \right]$$

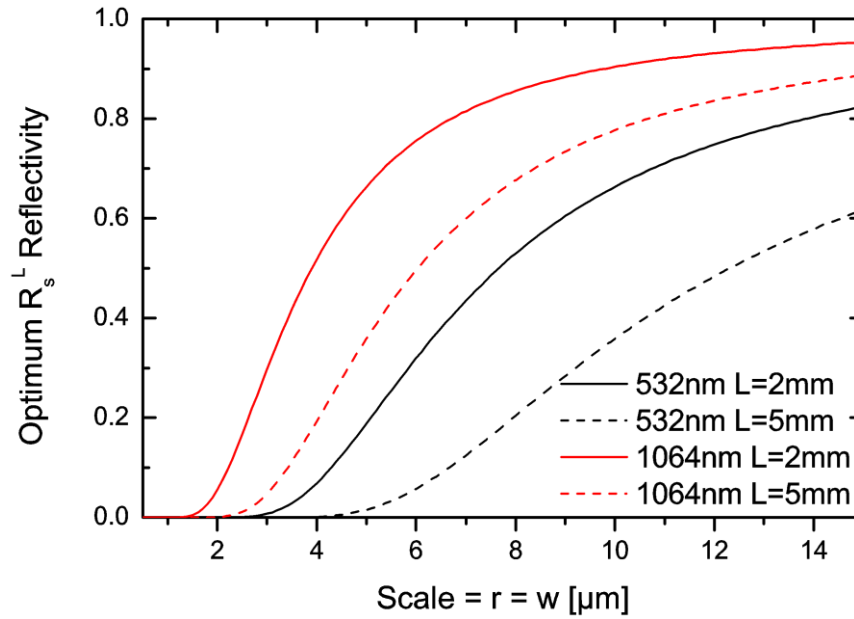


Figure 3. 19: Optimum reflectivity for maximum output power for a diamond Raman rib waveguide laser with different cross-sectional sizes, lengths and pump wavelengths calculated with equation (3.18) with a pump power of 20W. Parameters include:  $R_s^0=0.999$ , a waveguide propagation loss calculated from equation (3.13) with  $\sigma_s=\sigma_r=4$  nm,  $\sigma_w=17$  nm and a bulk propagation loss of  $0.01$   $\text{cm}^{-1}$ .  $R_p^L$  is set to 1 making the system a double pump-pass system. A slab thickness of  $s=0.65r$  and  $w=r=\text{scale}$  is used for loss calculations whilst the mode area is taken to be the second moment width. The Raman gain coefficient used is  $75\text{cm/GW}$  and  $14\text{cm/GW}$  at a pump wavelength of 532 nm and 1064 nm respectively.

Equation (3.18) is a powerful result that allows analytical optimisation of the reflectivity to maximise output power. It does not rely on the Lambert function and is thus not computationally demanding. The optimal reflectivity for a range of laser devices is shown in Figure 3. 19. The results in Figure 3. 19 show that a large range of reflectivity values may be suitable for different guide dimensions. As with linear laser systems for low gain materials, such as for 1064 nm pumping, the laser requires a large mirror reflectivity to maintain high intracavity power. This does not exceed 95% for the considered dimensions which is similar to bulk linear laser systems. For small cross-sections a very small Stokes reflectivity produces optimal output power, in some cases even lower than that offered by the Fresnel reflectivity of the sample (17%). This may reduce fabrication requirements and allow for no coating of one side of the sample. Reflectivities lower than the Fresnel reflection can be achieved with anti-reflection coatings.

The maximum output power for the optimal reflectivity shown in Figure 3. 19 is calculated and shown in Figure 3. 20. These results show that near quantum-efficiencies in principle can be obtained for a range of designs by appropriately

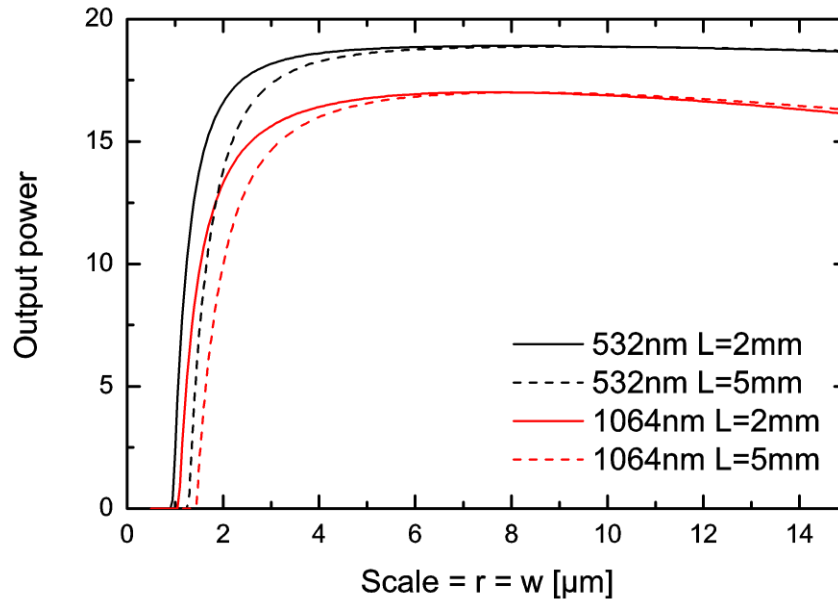


Figure 3. 20: Output power for 20W pump power for optimised reflectivity shown in Figure 3. 8. All parameters are consistent with and described in Figure 3. 8.

optimising the Stokes reflectivity. Output powers in excess of 15W for an injected power of 20W can be obtained for a large range of waveguide designs where scattering loss is minimal. There is a clear reduction in achievable output power for low cross-sections where scattering loss is in excess of a few dBcm<sup>-1</sup>.

### 3.4.3 Variation with roughness and comparison to bulk

Analytical results shown in Figure 3. 16 and in Section 3.4.2 are based on a sidewall roughness rms of 17 nm. This is an assumed value based on a study of silicon rib waveguide sidewall roughness [46] and estimates from SEM images of a number of diamond structures etched with the same ICP recipe [24]. AFM measurements have been performed on diamond samples using the same etch recipe after 1 μm ICP etching resulting in 1 nm rms roughness, indicating the possibility for low roughness with small waveguide dimensions and high quality samples [61]. However, SEM images of the diamond waveguides fabricated as part of this work, shown in Figure 3. 9, indicate high sidewall roughness, possibly up to 1 μm rms. A study on the effect of high sidewall roughness was carried out to determine what effect this has on laser performance.

Figure 3. 21 shows the waveguide propagation loss for varying sidewall roughness up to 200 nm rms. Waveguides smaller than 10 μm × 10 μm in cross-sectional size suffer much greater than 1 dB/cm loss for values of sidewall roughness greater than 100 nm. Care should therefore be taken to minimise sidewall roughness for low-loss operation.

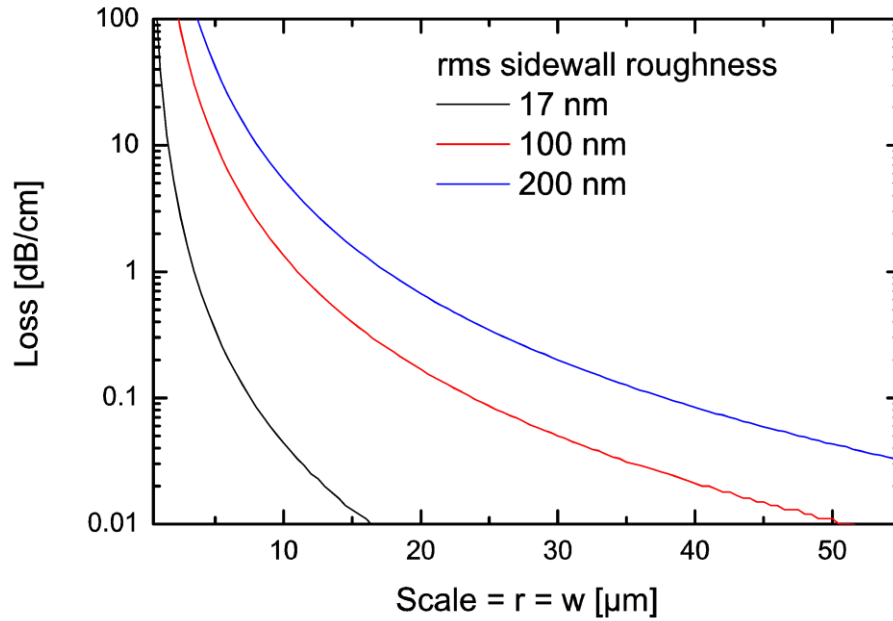


Figure 3. 21: TE mode maximum scattering propagation loss for varying cross-sectional sizes and varying rib sidewall roughness. The parameters include a rib waveguide with  $s=0.65r$  and  $w=r$  at a wavelength of 532 nm with a refractive index of 2.4. A top surface roughness of 4 nm is used.

For fabrication processes that result in large sidewall roughness compared to the top surfaces it is possible to select waveguide designs that minimise mode interaction with the rib sidewall. Rib waveguide designs with a large  $s/r$  ratio (large slab thicknesses and small rib heights) will cause the mode to spread into the slab. This will reduce interaction with the rib sidewall and reduce propagation loss significantly. However, this will result in a large guided mode area as the mode spreads to occupy the slab and forms a large elliptical mode. This will have the effect of reducing confinement and will increase Raman laser threshold. A compromise can be made between minimising propagation losses and minimising the mode area for optimal laser performance.

It is interesting to compare waveguide laser analytical results with approximations for bulk lasers. Intracavity beam waist sizes are usually limited by bulk optics, cavity stability regions and physical space limitations without the use of micro-optics. A typical value for a minimum intracavity waist radius is 20  $\mu\text{m}$  as previously reported in an intracavity diamond Raman laser [53]. This produces an average beam radius throughout a 5 mm long diamond crystal of 22  $\mu\text{m}$ . To estimate laser operation with analytical equations this beam can be approximated to a fixed average constant beam radius.

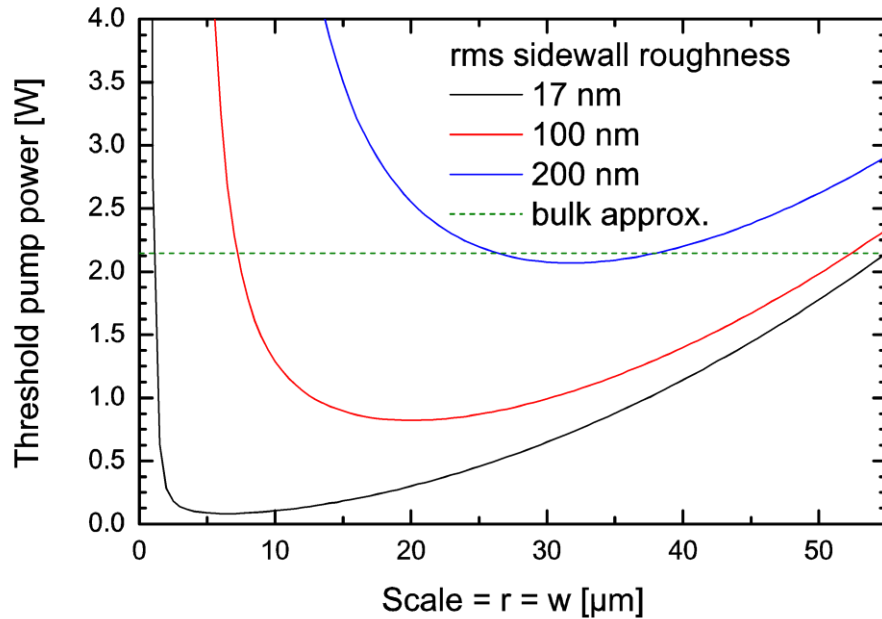


Figure 3. 22: Threshold power for a diamond Raman rib waveguide laser with different cross-sectional sizes and variable sidewall roughness. Parameters include: a fixed facet reflectivity of  $R_{s0}=0.999$ ,  $R_{sL}=0.99$ , a waveguide propagation loss shown in Figure 3. 10 and a bulk propagation loss of  $0.01/\text{cm}$ .  $R_{pL}$  is set to 1 making the system a double pump-pass system. A slab thickness of  $s=0.65r$  and  $w=r=\text{scale}$  is used for loss calculations whilst the mode area is taken to be the second moment width. The Raman gain coefficient used is  $75 \text{ cm/GW}$  at a pump wavelength of  $532 \text{ nm}$ . The bulk approximation uses a constant beam radius of  $22 \mu\text{m}$

Figure 3. 22 shows the effects of rib sidewall roughness variation on the threshold of the laser. Large values of sidewall roughness considerably increase the threshold. Calculations show that a sidewall roughness greater than  $200 \text{ nm rms}$  offers no reduction in threshold compared to a bulk laser with an average beam radius of  $22 \mu\text{m}$  based on the constant beam radius approximation.

Figure 3. 23 shows the output power of a Raman waveguide laser where the output coupler is optimised for  $20 \text{ W}$  pump power to offer maximum output. It can be seen that for values of sidewall roughness greater than  $\sim 150 \text{ nm rms}$ , bulk lasers (using the constant beam radius approximation) can offer larger output powers. This is due to the large value of Raman gain at this pump wavelength and bulk lasers may not perform as well in comparison to waveguide lasers for longer wavelengths such as in the infrared.

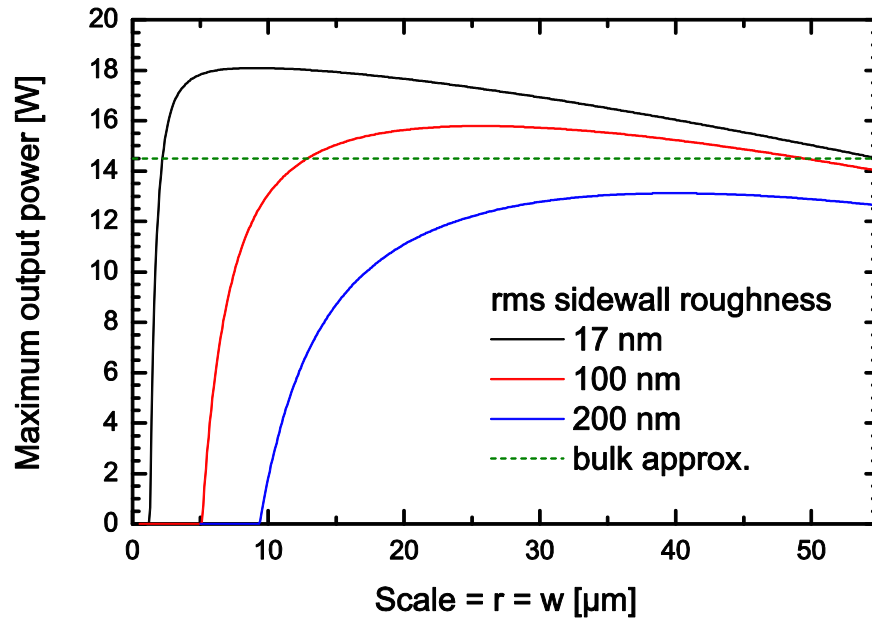


Figure 3. 23: Output power for 20W pump power for optimised reflectivity output facet, different cross-sectional sizes and varying sidewall roughness. Parameters include:  $R_{s0}=0.999$ , a waveguide propagation loss shown in Figure 3. 21 and a bulk propagation loss of  $0.01 \text{ cm}^{-1}$ .  $R_{pL}$  is set to 1 making the system a double pump-pass system. A slab thickness of  $s=0.65r$  and  $w=r=scale$  is used for loss calculations whilst the mode area is calculated from the second moment width. The Raman gain coefficient used is  $75\text{cm/GW}$  at a pump wavelength of 532 nm.

### 3.5 Conclusions

Criteria for a useful waveguide were developed on the basis for greater confinement compared to free-space propagation for the same propagation distance. This showed that diamond waveguides with large cross-sectional sizes can offer greater confinement than bulk alternatives. Work has shown that these waveguides can still operate as single-mode devices for large cross-sections. Beam propagation method simulations have shown that higher-order modes can remain guided in rib waveguides for significant distances, even though the cross-section of the waveguide suggests that the waveguide should be single mode. The waveguide length must thus be taken into account when defining the single-mode criteria of a waveguide.

Large-area diamond rib waveguides were designed and fabricated using a novel method to extend the waveguide uniformly to the sample edge. The waveguide design and fabrication method provides a much simpler alternative to other existing fabrication methods for diamond. The waveguides were optically characterised and were shown to support two modes, the fundamental and second vertical mode, over the 2 mm sample length. Simulations predict that the second guided mode would be

removed over longer propagation distances. The demonstration of this diamond waveguide adds to the limited number of waveguides fabricated in diamond to-date. The processing steps employed here may be used to fabricate waveguides of varying cross-section. Diamond waveguides may find application in areas including integrated quantum photonics or as Raman waveguide lasers.

The Payne and Lacey theory of surface scattering loss was extended to provide a full description from all surfaces of a rib waveguide. Marcatili's analytical solution was determined to be suitable for a range of large-cross-section rib waveguides. An analytical solution to the coupled equations to describe a Raman waveguide laser was extended to describe large cross-sectional rib waveguides. This solution was combined with analytical solutions for scattering loss to provide a full description of the Raman waveguide laser system. This model shows that a compromise should be made between scattering losses and gain when selecting the waveguide geometry.

Optimisations have shown that thresholds as low as 100mW could be obtained for optimised waveguides with a cross-section of 4-8  $\mu\text{m}^2$  for 2-5 mm sample lengths and 532 nm continuous wave pumping. Alternatively, continuous wave output power could be optimised to above 15 W for 20 W pump power at 532 or 1064 nm for waveguides with a cross-section above 2  $\mu\text{m}^2$ .

## References

- [1] Y. F. Zhang, L. McKnight, Z. S. Tian, S. Calvez, E. D. Gu, and M. D. Dawson, "Large cross-section edge-coupled diamond waveguides," *Diamond and Related Materials*, **20**, 564-567 (2011).
- [2] L. J. McKnight, M. D. Dawson, and S. Calvez, "Diamond Raman Waveguide Lasers: Completely Analytical Design Optimization Incorporating Scattering Losses," *IEEE Journal of Quantum Electronics*, **47**, 1069-1077 (2011).
- [3] E. A. J. Marcatil, "Slab-Coupled Waveguides," *Bell System Technical Journal*, **53**, 645 (1974).
- [4] J. Schmidtchen, A. Splett, B. Schuppert, K. Petermann, and G. Burbach, "Low-Loss Singlemode Optical Wave-Guides with Large Cross-Section in Silicon-on-Insulator," *Electronics Letters*, **27**, 1486-1488 (1991).
- [5] R. A. Soref, J. Schmidtchen, and K. Petermann, "Large Single-Mode Rib Wave-Guides in GeSi-Si and Si-on-SiO<sub>2</sub>," *IEEE Journal of Quantum Electronics*, **27**, 1971-1974 (1991).
- [6] S. P. Pogossian, L. Vescan, and A. Vonsovici, "The single-mode condition for semiconductor rib waveguides with large cross section," *Journal of Lightwave Technology*, **16**, 1851-1853 (1998).
- [7] M. J. F. Digonnet, and C. J. Gaeta, "Theoretical-Analysis of Optical Fiber Laser-Amplifiers and Oscillators," *Applied Optics*, **24**, 333-342 (1985).
- [8] J. I. Mackenzie, "Dielectric solid-state planar waveguide lasers: A review," *IEEE Journal of Selected Topics in Quantum Electronics*, **13**, 626-637 (2007).

- [9] H. Kogelnik, and T. Li, "*Laser Beams and Resonators*," Proceedings of the Institute of Electrical and Electronics Engineers, **54**, 1312 (1966).
- [10] A. E. Siegman, "*How to (Maybe) Measure Laser Beam Quality*," in Tutorial presentation at the Optical Society of America Annual Meeting (1997).
- [11] K. Petermann, "*Properties of Optical Rib-Guides with Large Cross-Section*," Aeu-International Journal of Electronics and Communications, **30**, 139-140 (1976).
- [12] O. Powell, "*Single-mode condition for silicon rib waveguides*," Journal of Lightwave Technology, **20**, 1851-1855 (2002).
- [13] J. Lousteau, D. Furniss, A. B. Seddon, T. M. Benson, A. Vukovic, and P. Sewell, "*The single-mode condition for silicon-on-insulator optical rib waveguides with large cross, section*," Journal of Lightwave Technology, **22**, 1923-1929 (2004).
- [14] S. Praver, and A. D. Greentree, "*Diamond for Quantum Computing*," Science, **320**, 1601-1602 (2008).
- [15] H. W. Choi, E. Gu, C. Liu, C. Griffin, J. M. Girkin, I. M. Watson, and M. D. Dawson, "*Fabrication of natural diamond microlenses by plasma etching*," Journal of Vacuum Science & Technology B, **23**, 130-132 (2005).
- [16] Y. Tzeng, J. Wei, J. T. Woo, and W. Lanford, "*Freestanding Single-Crystalline Chemically Vapor-Deposited Diamond Films*," Applied Physics Letters, **63**, 2216-2218 (1993).
- [17] B. A. Fairchild, P. Olivero, S. Rubanov, A. D. Greentree, F. Waldermann, R. A. Taylor, I. Walmsley, J. M. Smith, S. Huntington, B. C. Gibson, D. N. Jamieson, and S. Praver, "*Fabrication of Ultrathin Single-Crystal Diamond Membranes*," Advanced Materials, **20**, 4793 (2008).
- [18] A. P. Magyar, J. C. Lee, A. M. Limarga, I. Aharonovich, F. Rol, D. R. Clarke, M. B. Huang, and E. L. Hu, "*Fabrication of thin, luminescent, single-crystal diamond membranes*," Applied Physics Letters, **99**, 081913 (2011).
- [19] M. P. Hiscocks, K. Ganesan, B. C. Gibson, S. T. Huntington, F. Ladouceur, and S. Praver, "*Diamond waveguides fabricated by reactive ion etching*," Optics Express, **16**, 19512-19519 (2008).
- [20] P. Olivero, S. Rubanov, P. Reichart, B. C. Gibson, S. T. Huntington, J. Rabeau, A. D. Greentree, J. Salzman, D. Moore, D. N. Jamieson, and S. Praver, "*Ion-beam-assisted lift-off technique for three-dimensional micromachining of freestanding single-crystal diamond*," Advanced Materials, **17**, 2427 (2005).
- [21] J. Riedrich-Moller, L. Kipfstuhl, C. Hepp, E. Neu, C. Pauly, F. Mucklich, A. Baur, M. Wandt, S. Wolff, M. Fischer, S. Gsell, M. Schreck, and C. Becher, "*One- and two-dimensional photonic crystal microcavities in single crystal diamond*," Nature Nanotechnology, **7**, 69-74 (2012).
- [22] A. Faraon, P. E. Barclay, C. Santori, K. M. C. Fu, and R. G. Beausoleil, "*Resonant enhancement of the zero-phonon emission from a colour centre in a diamond cavity*," Nature Photonics, **5**, 301-305 (2011).
- [23] B. M. Hausmann, B. Shields, Q. Quan, P. Maletinsky, M. McCutcheon, J. T. Choy, T. M. Babinec, A. Kubanek, A. Yacoby, M. D. Lukin, and M. Lončar, "*Integrated diamond networks for quantum nanophotonics*," Nano Letters, **12**, 1578 (2012).
- [24] Y. F. Zhang, Phd Thesis, "*Diamond and GaN Waveguides and Microstructures for Integrated Quantum Photonics*," (Institute of Photonics, University of Strathclyde, 2012).
- [25] M. P. Hiscocks, C. H. Su, K. Ganesan, B. C. Gibson, A. D. Greentree, L. C. L. Hollenberg, F. Ladouceur, and S. Praver, "*Accessing diamond waveguides and future applications*," Integrated Optics: Devices, Materials, and Technologies XIV, **7604**, 760404 (2010).
- [26] R. D. Deegan, O. Bakajin, T. F. Dupont, G. Huber, S. R. Nagel, and T. A. Witten, "*Capillary flow as the cause of ring stains from dried liquid drops*," Nature, **389**, 827-829 (1997).
- [27] L. V. Iogansen, "*Theory of Resonant Electromagnetic Systems with Total Internal Reflection .3.*," Soviet Physics Technical Physics, **11**, 1529 (1967).
- [28] J. H. Harris, R. Shubert, and J. N. Polky, "*Beam Coupling to Films*," Journal of the Optical Society of America, **60**, 1007 (1970).
- [29] P. K. Tien, and R. Ulrich, "*Theory of Prism-Film Coupler and Thin-Film Light Guides*," Journal of the Optical Society of America, **60**, 1325 (1970).

### Chapter 3 – Diamond Waveguides

- [30] M. L. Dakss, L. Kuhn, P. F. Heidrich, and B. A. Scott, "Grating Coupler for Efficient Excitation of Optical Guided Waves in Thin Films," *Applied Physics Letters*, **16**, 523 (1970).
- [31] N. Neviere, R. Petit, and M. Cadilhac, "About the theory of optical grating coupler-waveguide systems," *Optics Communications*, **8**, 113 (1973).
- [32] T. Tamir, and S. T. Peng, "Analysis and Design of Grating Couplers," *Applied Physics*, **14**, 235-254 (1977).
- [33] I. Aharonovich, A. D. Greentree, and S. Prawer, "Diamond photonics," *Nature Photonics*, **5**, 397-405 (2011).
- [34] A. D. Greentree, and S. Prawer, "YELLOW LASERS A little diamond goes a long way," *Nature Photonics*, **4**, 202-203 (2010).
- [35] D. Marcuse, "Radiation losses of dielectric waveguides in terms of the power spectrum of the wall distortion function," *Bell System Technical Journal*, **48**, 3233 (1969).
- [36] P. K. Tien, "Light Waves in Thin Films and Integrated Optics," *Applied Optics*, **10**, 2395 (1971).
- [37] M. Kuznetsov, and H. A. Haus, "Radiation Loss in Dielectric Waveguide Structures by the Volume Current Method," *IEEE Journal of Quantum Electronics*, **19**, 1505-1514 (1983).
- [38] T. Barwicz, and H. A. Haus, "Three-dimensional analysis of scattering losses due to sidewall roughness, in microphotonic waveguides," *Journal of Lightwave Technology*, **23**, 2719-2732 (2005).
- [39] S. E. Miller, "Coupled Wave Theory and Waveguide Applications," *Bell System Technical Journal*, **33**, 661-719 (1954).
- [40] W. P. Huang, "Coupled-Mode Theory for Optical Wave-Guides - an Overview," *Journal of the Optical Society of America A-Optics Image Science and Vision*, **11**, 963-983 (1994).
- [41] C. G. Poulton, C. Koos, M. Fujii, A. Pfrang, T. Schimmel, J. Leuthold, and W. Freude, "Radiation modes and roughness loss in high index-contrast waveguides," *IEEE Journal of Selected Topics in Quantum Electronics*, **12**, 1306-1321 (2006).
- [42] J. P. R. Lacey, and F. P. Payne, "Radiation Loss from Planar Wave-Guides with Random Wall Imperfections," *IEE Proceedings-Journal of Optoelectronics*, **137**, 282-288 (1990).
- [43] F. P. Payne, and J. P. R. Lacey, "A Theoretical-Analysis of Scattering Loss from Planar Optical Wave-Guides," *Optical and Quantum Electronics*, **26**, 977-986 (1994).
- [44] Y. A. Vlasov, and S. J. McNab, "Losses in single-mode silicon-on-insulator strip waveguides and bends," *Optics Express*, **12**, 1622-1631 (2004).
- [45] K. P. Yap, A. Delage, J. Lapointe, B. Lamontagne, J. H. Schmid, P. Waldron, B. A. Syrett, and S. Janz, "Correlation of Scattering Loss, Sidewall Roughness and Waveguide Width in Silicon-on-Insulator (SOI) Ridge Waveguides," *Journal of Lightwave Technology*, **27**, 3999-4008 (2009).
- [46] Y. J. Wang, Z. L. Lin, X. L. Cheng, C. S. Zhang, F. Gao, and F. Zhang, "Scattering loss in silicon-on-insulator rib waveguides fabricated by inductively coupled plasma reactive ion etching," *Applied Physics Letters*, **85**, 3995-3997 (2004).
- [47] A. K. Mcquilla, W. R. Clements, and B. P. Stoichef, "Stimulated Raman Emission in Diamond - Spectrum, Gain, and Angular Distribution of Intensity," *Physical Review A*, **1**, 628 (1970).
- [48] A. M. Zaitsev, "Optical Properties of Diamond: A Data Handbook" (Springer, 2001).
- [49] S. A. Solin, and A. K. Ramdas, "Raman Spectrum of Diamond," *Physical Review B*, **1**, 1687 (1970).
- [50] R. P. Mildren, J. E. Butler, and J. R. Rabeau, "CVD-diamond external cavity Raman laser at 573 nm," *Optics Express*, **16**, 18950-18955 (2008).
- [51] R. P. Mildren, and A. Sabella, "Highly efficient diamond Raman laser," *Optics Letters*, **34**, 2811-2813 (2009).
- [52] W. Lubeigt, G. M. Bonner, J. E. Hastie, M. D. Dawson, D. Burns, and A. J. Kemp, "Continuous-wave diamond Raman laser," *Optics Letters*, **35**, 2994-2996 (2010).
- [53] D. C. Parrotta, A. J. Kemp, M. D. Dawson, and J. E. Hastie, "Tunable continuous-wave diamond Raman laser," *Optics Express*, **19**, 24165-24170 (2011).
- [54] H. S. Rong, A. S. Liu, R. Jones, O. Cohen, D. Hak, R. Nicolaescu, A. Fang, and M. Paniccia, "An all-silicon Raman laser," *Nature*, **433**, 292-294 (2005).

### Chapter 3 – Diamond Waveguides

- [55] A. P. Sabella, J. A., and R. P. Mildren, "1240 nm diamond Raman laser operating near the quantum limit," *Optics Letters*, **35**, 3874 (2010).
- [56] T. T. Basiev, A. A. Sobol, P. G. Zverev, V. V. Osiko, and R. C. Powell, "Comparative spontaneous Raman spectroscopy of crystals for Raman lasers," *Applied Optics*, **38**, 594-598 (1999).
- [57] J. A. Piper, and H. M. Pask, "Crystalline Raman lasers," *IEEE Journal of Selected Topics in Quantum Electronics*, **13**, 692-704 (2007).
- [58] G. Turri, Y. Chen, M. Bass, D. Orchard, J. E. Butler, S. Magana, T. Feygelson, D. Thiel, K. Fourspring, R. V. Dewees, J. M. Bennett, J. Pentony, S. Hawkins, M. Baronowski, A. Guenthner, M. D. Seltzer, D. C. Harris, and C. M. Stickley, "Optical absorption, depolarization, and scatter of epitaxial single-crystal chemical-vapor-deposited diamond at 1.064  $\mu\text{m}$ ," *Optical Engineering*, **46**, 064002 (2007).
- [59] C. H. Huang, Z. P. Cai, C. C. Ye, and H. Y. Xu, "Explicit solution for Raman fiber laser using Lambert W function," *Optics Express*, **15**, 4671-4676 (2007).
- [60] J. H. Zhou, J. P. Chen, X. W. Li, G. L. Wu, and Y. P. Wang, "Exact analytical solution for Raman fiber laser," *IEEE Photonics Technology Letters*, **18**, 1097-1099 (2006).
- [61] C. L. Lee, E. Gu, M. D. Dawson, I. Friel, and G. A. Scarsbrook, "Etching and micro-optics fabrication in diamond using chlorine-based inductively-coupled plasma," *Diamond and Related Materials*, **17**, 1292-1296 (2008).

# Chapter 4

## Gallium Nitride Waveguides

---

### Abstract

This chapter presents work in the field of Gallium Nitride (GaN) waveguides and directional couplers (DCs). Design and operational theory of GaN DCs is considered in order to minimise footprint with relaxed fabrication requirements. The fabrication process and optical characterisation is presented including mode profiles, propagation loss and splitting ratios. The results of two-photon quantum interference within the directional couplers are presented.

### Preliminaries

Some of the computational simulation and experimental results presented in this chapter are published in reference [1] although no content is directly duplicated. Acknowledgements of contributions by others to the work presented in this chapter are listed at the front and back of this thesis. The motivation and background to this work is detailed in Chapter 1. The cross-sectional waveguide designs presented in this chapter build upon work presented in Chapter 2 and Chapter 3 that will not be reiterated here.

## 4.1 Circuit design

### 4.1.1 Straight waveguide design

In a similar manner to that presented in Chapter 3, a Gallium Nitride (GaN) waveguide cross-section was selected based on a single etch-step for single-mode propagation and optimal coupling from a circular free-space Gaussian beam. The rib height,  $r$ , used as part of this design was based on the availability of in-house-grown GaN on sapphire substrates. The cross-section design selected for straight waveguides and the guided mode profile for this waveguide is shown in Figure 4. 1.

The 3.8  $\mu\text{m}$ -thick GaN layer with a cladding of air and a substrate of sapphire allows the large area rib waveguide single-mode criteria to be used as described in Chapter 2. This criteria does not require precise consideration of the wavelength or refractive index, within the optical range, as the  $v$ -parameters for the component planar waveguides

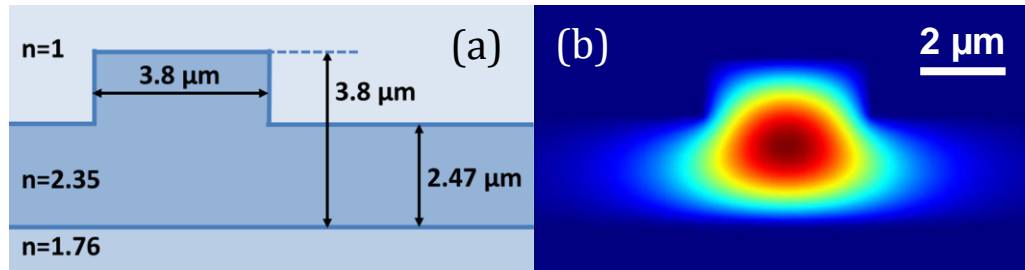


Figure 4. 1: **(a)** Schematic of rib waveguide design where refractive indices are shown for a free-space wavelength of 800 nm. **(b)** Normalised electric field profile of the guided TE mode for the rib waveguide design shown in (a).

remain high ( $>50$ ) for the dimensions considered. The geometry lies in the single-mode region described in Chapter 2 and was selected in order to maximise confinement and coupling efficiency from/to circular beams. FEM and BPM simulations have shown the guided mode profile is wavelength independent for the visible and near infrared with the possibility for high coupling coefficients  $> 97\%$  from circular Gaussian profiles.

#### 4.1.2 Directional coupler theory

Transfer of power between adjacent waveguides is known as directional coupling. A directional coupler (DC) is a device that contains two adjacent waveguides such that a specific proportion of power is transferred between them. A simple schematic is shown in Figure 4. 2. Theory to describe optical DCs [2-5] was extended from microwave DCs [6] and many devices were demonstrated as early as the '70s [7, 8]. Research continues in the design and fabrication of DCs based on requirements for reduced footprint [9, 10], relaxed fabrication [9, 10], additional functionality [11, 12], new waveguide geometries such as photonic crystals [13] and slot waveguides [14]. New fabrication processes [15, 16] and novel materials [17, 18] continue to extend the range of applications of DCs. Recent interest in integrated quantum photonics has renewed interest in DCs for quantum logic and metrology [19]. The application of DCs in this field was reviewed in Chapter 1.

DCs in GaN have only recently been demonstrated with 1550 nm communication applications in mind [20, 21]. That work produced a DC with a coupling region length of  $\sim 600 \mu\text{m}$  (inferred from images) and was fabricated using e-beam writing in order to achieve a sub-micron coupling gap. The losses of that waveguide were measured to be  $34.4 \text{ dBcm}^{-1}$ . This work concentrates on achieving similar device lengths, with a lower propagation loss and without the necessity for e-beam lithography; thus we are restricted to a coupling region gap of  $\sim 2 \mu\text{m}$  by contact lithography.

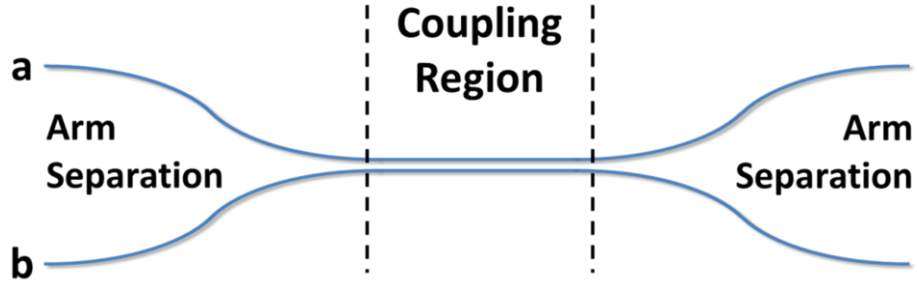


Figure 4. 2: Schematic top-down view of a simple directional coupler with coupling region and arm separation regions. The coupling region length is the physical distance for which coupling occurs between the waveguides. The arm separation distance is the distance between waveguides *a* and *b* at the beginning and end of the device.

With appropriate design of the DC, all of the power in one waveguide can be completely transferred to the adjacent waveguide. For this to occur, the waveguides must be symmetrical such that each constituent waveguide is identical and has the same guided mode effective index. For this work only symmetrical single-mode waveguides are considered and this allows for simplification of the descriptive theory. When power  $P_a(0)$  is launched into waveguide *a*, power will couple into waveguide *b*, and then back again after continued propagation in the coupling region. This follows a sinusoidal oscillation and can be described by introducing a coupling coefficient  $\kappa$ :

$$P_b(l) = P_a(0) \frac{(1 - \cos(\kappa l))}{2}, \quad P_a(l) = P_a(0) \frac{(\cos(\kappa l) + 1)}{2} \quad (4.1)$$

where  $P$  is the power in each mode/waveguide and  $l$  is the propagation length in the coupling region. The coupling coefficient can be calculated by considering the coupling region as a single waveguide structure, for which the modes of this larger structure are known as super-modes. From coupled-mode theory [2-5] the coupling coefficient is known to depend on the fundamental (symmetric) and second (asymmetric) super-modes of the coupling region:

$$\kappa = \frac{\beta_0 - \beta_1}{2} = \frac{k(N_0 - N_1)}{2} \quad (4.2)$$

where  $k$  is the angular wavenumber,  $2\pi/\lambda$ , and  $N_0$  and  $N_1$  are the effective indices of the symmetric and asymmetric super-modes respectively. It is convenient to define a “coupling length”,  $L_c$ , which refers to the propagation distance required for all the power to transfer from one waveguide to another:

$$L_c = \frac{\pi}{2\kappa} \quad (4.3)$$

An alternative description of the power transfer between waveguides can also be developed by considering the overlap between the guided modes of the constituent waveguides in the coupling region. Small coupling coefficients are known to be proportional to the overlap of the fields of the two modes:

$$\kappa \propto \iint \mathbf{E}_a \cdot \mathbf{E}_b^* dx dy \quad (4.4)$$

From Equation (4.4), the coupling length can be reduced by increasing the overlap of the modes of the two waveguides. This can be achieved by simply bringing the two waveguides close together and is why most directional coupler designs involve a narrow submicron coupling region gap. It will be shown in this work that small coupling lengths can also be obtained with a large coupling gap by appropriate tailoring of the mode profile to increase the overlap.

### 4.1.3 Minimum bend radii

In order to join and separate waveguides for the DC, curves or bends are required. When a waveguide is curved, the guided mode profile changes and is pushed towards the outer edge of the waveguide. This new mode profile can be described by a conformal transformation which is analogous to a linear increase in refractive index from the inside towards the outer edge of the waveguide [22, 23]. Small-radii curves cause a greater change in mode profile and push the guided mode towards the very edge of the waveguide. A mode that is confined by the outer edges of the waveguide alone is known as a whispering gallery mode [24]. As the bend radius is further reduced there comes a point when the refractive index change is no longer strong enough to guide the light around tight corners. The unguided light will cause a curvature loss which is pure radiation leakage loss rather than scattering or absorption loss. This loss is not the same as the bend transition loss, which is the loss that occurs at the transition between a bend and a straight section of waveguide due to the mode mismatch [25].

A minimum bend radius may be selected such that it exhibits an acceptable value of radiation loss for a given waveguide structure and mode profile. For optical fibres, the minimum bend radius is usually a few centimetres due to the low refractive index

change between the core and cladding [26]. Photonic wires can achieve very small bend radii due to the large refractive index change [27].

The rib waveguide has a small effective index change between core (rib) and cladding (slab) thus the minimum radius of curvature,  $R_{min}$ , is similar to that of single-mode fibres. A simple-to-use formula developed by Marcatili is used for this work, which was found to agree well with BPM simulations for curved waveguides [28]:

$$R_{min} = \frac{24\pi^2}{\lambda^2} N_{clad}^2 d_{clad}^3$$

$$d_{clad} = \frac{1}{k\sqrt{N_{core}^2 - N_{clad}^2}} \quad (4.5)$$

$N_{core}$  and  $N_{clad}$  are the refractive indices of the core and cladding, respectively. For rib waveguides these terms may be replaced with the effective indices of the rib and slab as calculated in Chapter 1.  $d_{clad}$  is the distance into the slab for which the field amplitude drops to 1/e of maximum and the effective index approximation to calculate this is shown in Equation (4.5). For radii above  $R_{min}$  the curvature loss can be considered negligible as discussed by Marcatili [28]. Equation (4.5) can be used to consider what separation distances can be achieved for various DC designs. The length required for joining and separating the waveguides in a directional coupler can often be the limiting factor in minimising device footprint for complex circuits.

### 4.1.4 Directional coupler design

For the waveguide cross-section shown in Figure 4. 1, a suitable directional coupler design was selected. For this work, standard contact photolithography was considered for which the feature size is fundamentally limited by the mask design and mask aligner optics. The mask was defined with a minimum feature size of 2  $\mu\text{m}$ , however it is expected that minimum feature sizes could be reduced to 1  $\mu\text{m}$  with the same technique and careful photolithographic procedures. The directional coupler has separate joining/separation and coupler regions which contribute to the length of the device. In order to minimise footprint both the coupling region and the separation regions were considered.

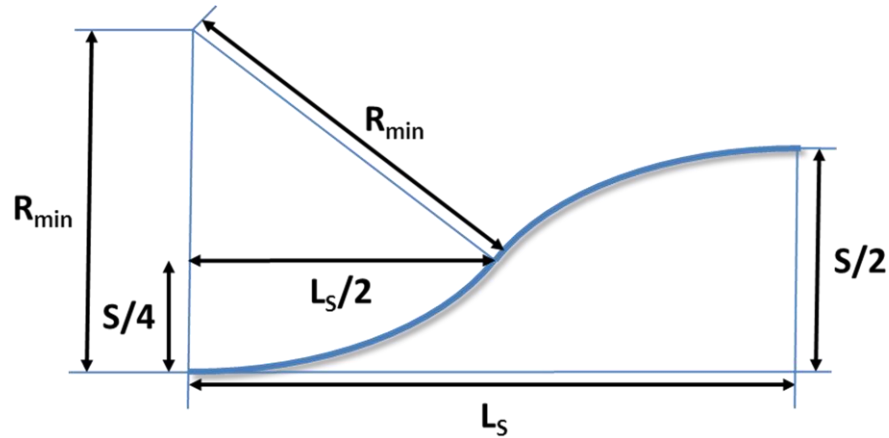


Figure 4. 3: Schematic top-down view of an s-bend. The length  $L_s$  for a required separation  $S$  may be calculated from the minimum radius of curvature  $R_{min}$  which can be calculated from Equation (4.5). The coupler region gap and waveguide width is not taken into consideration for simplicity.

FEM simulations were carried out, based on the design shown in Figure 4. 1, to find the coupling length. The effective indices of the symmetric and asymmetric super-modes were calculated when two identical waveguides were placed  $2\ \mu\text{m}$  apart. The coupling length was then calculated with Equation (4.3). Results gave  $N_0 = 2.346412$  and  $N_1 = 2.346255$  resulting in a coupling length of  $2550\ \mu\text{m}$ .

The propagation length required to separate the waveguide arms was calculated by considering the minimum bend radii of the waveguide and the separation distance required between the arms. The maximum separation for minimum distance is always achieved by an s-bend that changes direction after half the length. For a point of reference, fibre bundles with a standard separation distance,  $S$ , of  $250\ \mu\text{m}$  were considered for input/output coupling. With the aid of Equation (4.5) the length for separation,  $L_s$ , was calculated with geometrical considerations shown in Figure 4. 3.

For the design shown in Figure 4. 1, a minimum bend radius of  $4970\ \mu\text{m}$  was calculated for a wavelength of  $800\ \text{nm}$ . This corresponds to a length of  $1570\ \mu\text{m}$  to reach a fibre-to-fibre separation of  $250\ \mu\text{m}$  of standard fibre bundles. For input arm joining, 50% coupler length and output arm separation, this equals a complete device length of  $4.4\ \text{mm}$ . These results are presented in comparison to alternative designs in Table 4. 1.

In order to reduce the device length, a reduction in separation length would be advantageous. This can be achieved with a smaller minimum bend radius. A larger etch depth (smaller slab height) was considered, as this offers greater horizontal confinement and reduces the minimum bend radii. A 50% etch depth was considered and is shown in Figure 4. 4.

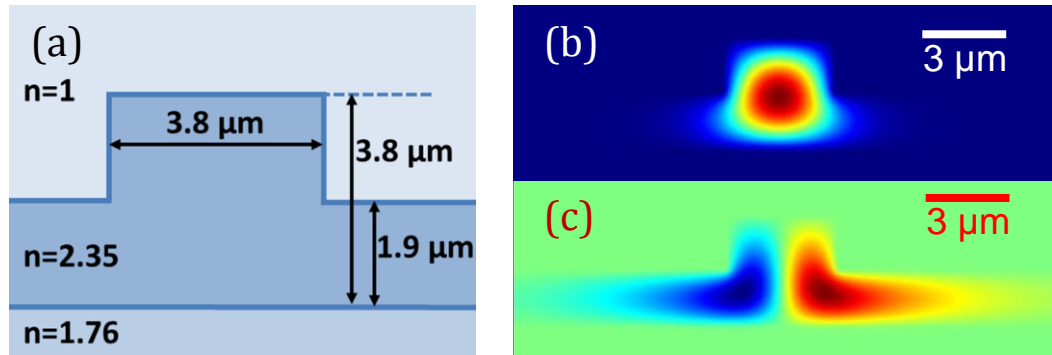


Figure 4. 4: **(a)** Schematic of rib waveguide design where refractive indices are shown for a free-space wavelength of 800 nm. **(b)** Normalised electric field profile for the fundamental TE mode of design shown in (a). **(c)** Normalised electric field profile for the second TE mode of design shown in (a).

A 1.9  $\mu\text{m}$  (50%) etch depth was calculated to significantly reduce the minimum bend radius to 1238  $\mu\text{m}$ , corresponding to roughly one quarter of the design with a 1.33  $\mu\text{m}$  (35%) etch depth. For 250- $\mu\text{m}$ -spaced fibre bundles a 390  $\mu\text{m}$  length for separation is then required. This reduction in length is a factor of four and reduces footprint significantly.

This new etch depth, however, creates a rib waveguide which is outside the single-mode operating regime, and the second guided mode can be clearly seen in Figure 4. 4 c). A further issue with the increased etch depth is the increase in coupling length. The guided mode is now well confined and no longer has the same coupling strength because the overlap between the modes of the waveguides in the coupler region is greatly reduced. The coupling length was calculated as previously with FEM simulations. The super-mode effective indices were calculated to be  $N_0=2.345832$   $N_1=2.345794$  corresponding to a coupler length which is 10530  $\mu\text{m}$ . This result is shown in Table 4. 1. In order ensure single-mode operation based on this design and reduce the coupling length, inverse tapers are considered in section 4.1.5.

#### 4.1.5 Tapers and length minimisation

The analysis in section 4.1.4 showed that a tightly confined mode offers the ability to greatly reduce the length required for a given arm separation distance. It also showed that a mode which is weakly confined offers good mode overlap with the adjacent waveguide and thus significantly reduces the coupling length. It is proposed that a mode converting taper is used to convert between these two desired mode profiles to take advantage of both scenarios.

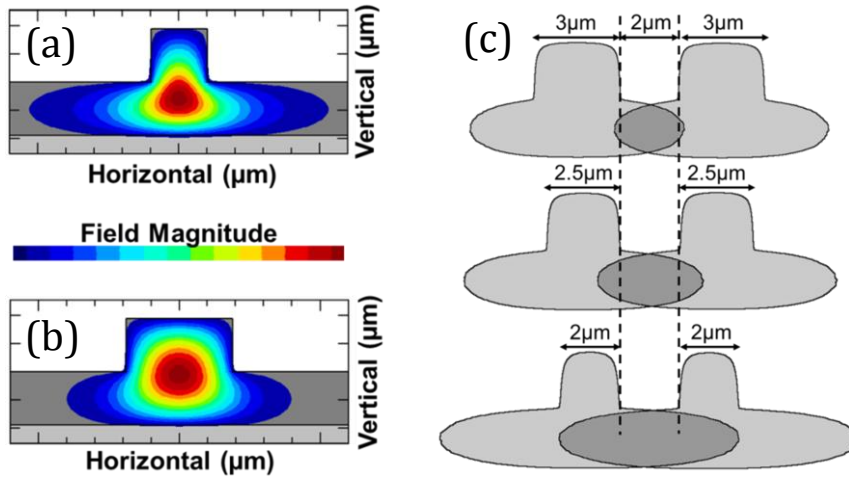


Figure 4. 5: **(a)** The mode profile for a rib waveguide with  $w=2\mu\text{m}$ ,  $r=3.8\mu\text{m}$ ,  $s=1.9\mu\text{m}$  and  $\lambda=800\text{ nm}$  for  $n_0=1, n_1=2.35$  and  $n_2=1.45$ . **(b)** The mode profile for a rib waveguide with the properties of (a) and  $w=3.8\mu\text{m}$ . **(c)** The 1% intensity contour, calculated by FEM simulation, for different rib widths with a fixed separation distance of  $2\mu\text{m}$ . The overlap is shown in dark grey.

Work in Chapter 2 showed that horizontal confinement in the rib top pushes the mode away from the top of the rib and into the slab. The 3-layer approximation was shown to be inaccurate to describe a vertical cross-section through the centre of the rib. It was necessary to use a 4-layer approximation and an effective index of the rib top in order to fully quantify the mode shifts from the rib top to the slab as the rib width is reduced.

The spread of the mode into the slab produces an enhancement of the coupling coefficient due to the increase of the mode overlap. This enhancement can be easily controlled by altering the width of the waveguide in the coupling region. This effect can be observed with the aid of Figure 4. 5. It is clear that smaller rib widths offer greater coupling strength for a fixed separation and thus can significantly reduce the coupling length.

Figure 4. 5 a) offers a reduced coupling length. Figure 4. 5 b) offers a reduced separation length and optimal coupling from circular Gaussian beams. In order to convert between these two modes, a mode-transforming taper is required. It is important that this taper converts between the two modes without increasing device length or introducing additional loss.

Mode-transforming tapers were introduced for microwaves [29] and extended to optical wavelengths [30] and are known as adiabatic tapers. The term ‘adiabatic’ refers to the fact that there is no loss and no conversion to other (leaky) modes. There are many types of tapers including lateral and vertical varieties [31]. Tapers have been a

topic of research for some time as they form the basis of many high power laser-diodes [32] and provide the only efficient method to couple to small nanowire waveguides [33]. The taper required in this work may be referred to as an inverse taper because as the width of the waveguide decreases, the mode width increases. This has some similarities to, although should not be confused with, tapers commonly used for efficient fibre to chip coupling [34].

It is desirable to have a short taper in order to minimise footprint. However, if this taper length is too short, the mode mismatch will cause a significant loss of power due to coupling to leaky radiation modes in the slab. As there is an exponential reduction of loss with taper length [34], it is necessary to consider an acceptable value of taper loss, otherwise tapers require excessive lengths to be truly lossless. For large mode-transformation, long tapers are required to minimise loss. Any footprint reduction due to enhanced coupling may be reduced by the requirement for long tapers.

In order to consider the effects of different rib widths in the coupler region on both required taper lengths and the coupler lengths a BPM study was carried out. The coupler region length that transfers 50% of the power was found by launching the guided mode profile and monitoring the power in the two waveguides. The required

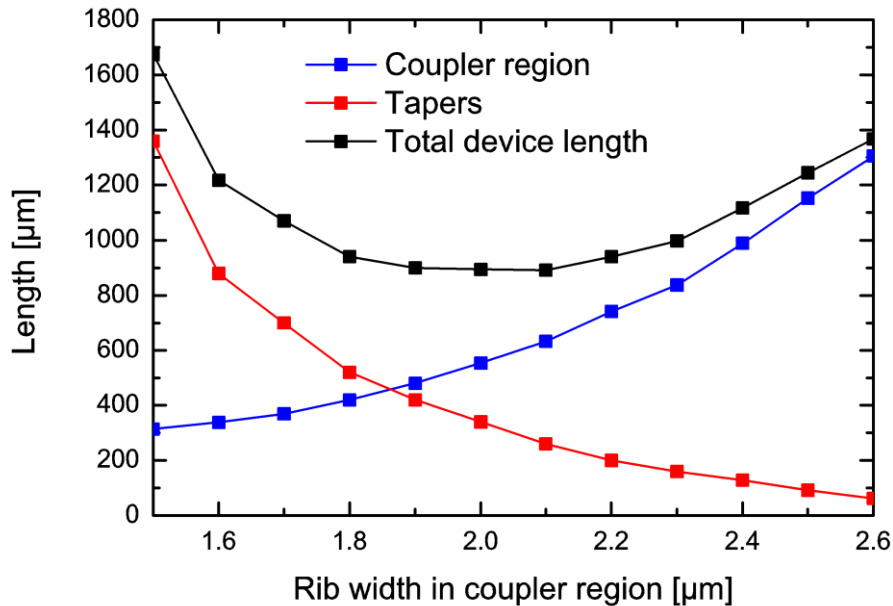


Figure 4. 6: The coupler region length for 50% power transfer ( $L_c/2$ ), taper length and device length is shown for various rib widths in the coupler region. The taper length is defined as the shortest that produces 0.05 dB radiation loss and is multiplied by 2 to give the total length of the input and output tapers. The taper converts from a width of 3.8  $\mu\text{m}$  to various rib widths in the coupler region. In all cases,  $r=3.8 \mu\text{m}$ ,  $s=1.9 \mu\text{m}$ ,  $\lambda=800 \text{ nm}$ ,  $n_0=1$ ,  $n_1=2.35$ ,  $n_2=1.76$  and the waveguide separation in the coupler region was fixed at 2  $\mu\text{m}$ .

taper length was defined as the shortest taper that introduced an acceptable loss of 0.05 dB. Results are shown in Figure 4. 6.

Results show that the device length is minimised when a compromise is made between minimising taper length and coupler region length. For the parameters considered, a rib width in the coupling region of 2  $\mu\text{m}$  is optimal in order to reduce footprint. The taper lengths could be integrated into the curved separation region to reduce device length further. A summary of device and component lengths are shown in Table 4. 1. This summary shows that a 2.6 times reduction in device length can be achieved with tapers and a 3.5 times reduction if these tapers are integrated within the separation region.

Table 4. 1: Directional coupler component lengths using different designs. Cross-sectional designs are shown in Figure 4. 1 and Figure 4. 4.

	<b><math>s=0.65r</math></b> <b>No Taper</b> <b>[<math>\mu\text{m}</math>]</b>	<b><math>s=0.5r</math></b> <b>No Taper</b> <b>[<math>\mu\text{m}</math>]</b>	<b><math>s=0.5r</math></b> <b>With Taper</b> <b>[<math>\mu\text{m}</math>]</b>	<b><math>s=0.5r</math></b> <b>With Taper</b> <b>[<math>\mu\text{m}</math>]</b>
<b>50% Coupling Length, <math>L_c/2</math></b>	1270	5260	480	480
<b>1 Taper Length, <math>L_t</math></b>	None	None	210	In separation region
<b>1 Separation Length, <math>L_s</math></b>	1570	390	390	390
<b>Device length, <math>L_c/2+2L_t+2L_s</math></b>	4420	6040	1680	1239

## 4.2 Fabrication

### 4.2.1 GaN material growth

The GaN samples used in this work were grown in-house by a horizontal-flow, low-pressure, Aixtron 200/4 RF-S single wafer MOCVD reactor. 3.8  $\mu\text{m}$  c-plane GaN was grown directly on a 500- $\mu\text{m}$ -thick (0001)-oriented sapphire substrate. Sapphire is a common substrate for GaN crystal growth due to high temperature requirements and minimal lattice mismatch [35]. However, GaN can be grown on a range of substrates including silicon, or as free-standing wafers [35]. Free-standing GaN may offer the lowest defect density, however, the GaN-on-sapphire material system is more established, typically cheaper and was available for this work. For growth on sapphire C-plane (0001) GaN produces the lowest lattice mismatch (13%) of all GaN orientations and hence reduces dislocations at the GaN/sapphire interface. 4 inch wafer sizes were used and after growth were diced into 10mm squares commercially using a mechanical saw.

### 4.2.2 Waveguide definition

A fabrication process similar to that described in chapter 3 was used in order to define the waveguide design into the GaN layer. This fabrication was carried out by Y. Zhang and further details are available in ref. [36].

500 nm of SiO<sub>2</sub> was deposited using plasma enhanced chemical vapour deposition (PECVD) onto the GaN-on-sapphire samples to act as a hard mask. It was important to ensure this layer was thick enough to allow sufficient etching of the GaN layer.

The desired thickness of S1805 photoresist was deposited on the 10×10 mm<sup>2</sup> samples using a standard spin-coating process. The desired waveguide design was patterned into the photoresist using a Karl Suss MA-6 contact mask aligner. The photolithographic masks used were commercially sourced and custom-designed according to the desired waveguide circuit. The SiO<sub>2</sub> layer was etched using reactive ion etching following the recipe detailed in Table 4. 2. Excess photoresist was removed with acetone and methanol.

Table 4. 2: ICP recipe for GaN etching and etching rate of GaN and SiO<sub>2</sub>.

Pressure	Cl <sub>2</sub> flow	Coil Power	Platen Power	GaN etching rate	SiO <sub>2</sub> etching rate
7 mTorr	50 sccm	700 W	300 W	905 nm/min	175 nm/min

The GaN waveguide etching depths were defined by either the 35% etch design for straight waveguides or the 50% etch design for the directional coupler device incorporating tapers, following the GaN etch recipe shown in Table 4. 2. Waveguide cross-section designs are shown in Figure 4. 1 and Figure 4. 4. For a 1.33 μm (35%) etch, ICP etching took 88 second and for a 1.9 μm (50%) etch, ICP etching took 126 seconds. The residual SiO<sub>2</sub> mask was removed with a buffered HF etch.

The cleaving of GaN is not a trivial task due to different crystal structure of GaN (wurtzite) and sapphire (3m), resulting in a reorientation of the GaN with respect to the sapphire, and has been the subject of research [37]. In order to aid with the manual cleaving process for revealing the waveguide facets the sapphire substrates were commercially thinned by mechanical polishing to 80 μm. Samples were then manually cleaved ~2-3mm from each edge to reveal optical quality facets and leave ~5 mm × 10 mm samples.

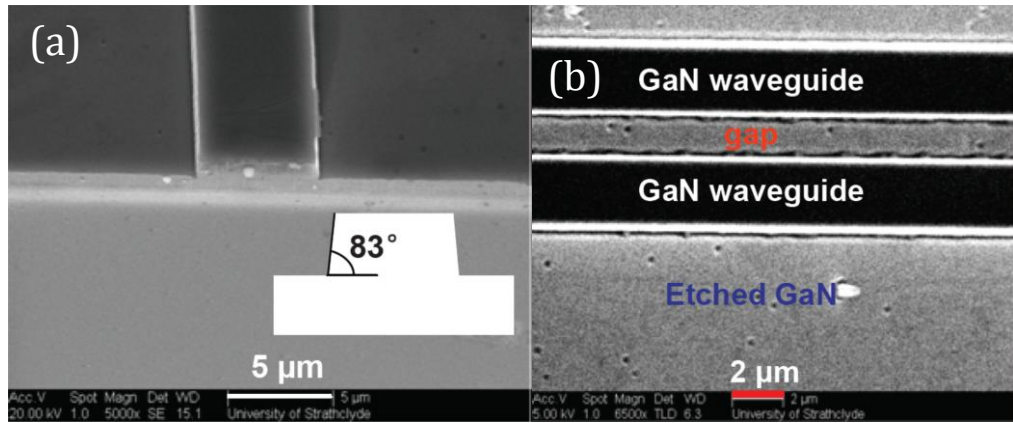


Figure 4. 7: SEM images of (a) the waveguide facet after cleaving and (b) the top-down view of the coupling region revealing the 7 degree sloped sidewalls.

Scanning electron microscope (SEM) inspections were conducted and revealed high waveguide quality facets as shown in Figure 4. 7 a). Stylus profilometer measurements confirmed that the etching depths of the GaN directional couplers were 1.9 μm and the straight waveguides were 1.33 μm.

The fabricated directional couplers exhibited a well-defined coupling region gap shown by SEM inspection in Figure 4. 7 b). This image shows an increased waveguide width of 2.2 μm and sloped sidewalls 7 degrees off verticality. BPM simulations were carried out to identify what effects this may have on device performance. The new mode profiles in the coupling region were calculated and are shown in Figure 4. 8. The coupling length was calculated for the new profile and was found to increase from 960 μm to 1150 μm. The 50% coupling length is thus increased by 90 μm and the overall DC device length will also be increased by this amount.

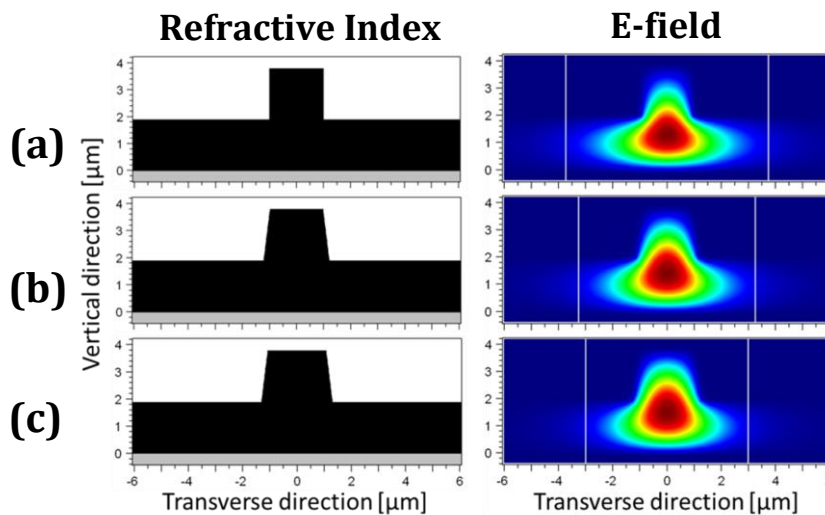


Figure 4. 8: (a) Standard design as shown in Figure 4. 4 with vertical sidewalls, (b) with 7 degree sloped sidewalls and (c) with 7 degree sloped sidewalls and an increased width to 2.2 μm. The vertical white line in the E-field plots shows the 1/e transverse position.

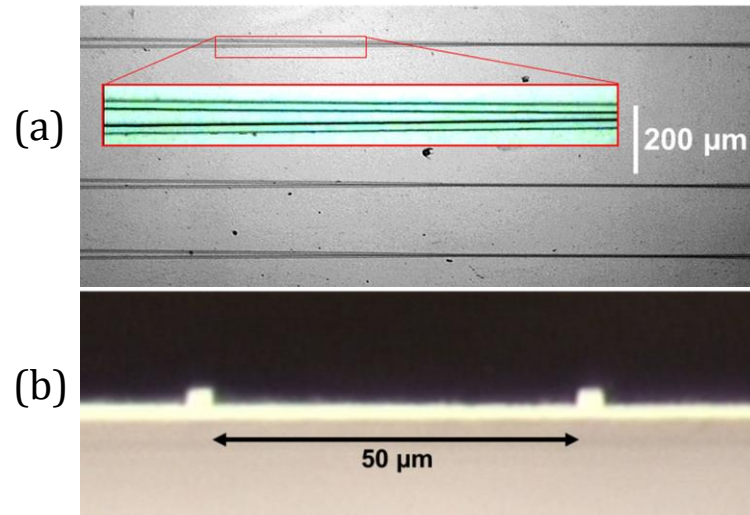


Figure 4. 9: Optical images of **(a)** plan view of directional couplers including a magnified inset of the tapers to the coupler region and **(b)** side view of the cleaved facets showing high optical quality and a 50% etch depth.

Optical microscopy images were taken of the cleaved facets and directional coupler region and are shown in Figure 4. 9. The port separation of these fabricated devices did not reach the requirements for standard fibre bundles and the separation distance was dependent on the precise cleave position. A novel coupling strategy was employed to efficiently couple in and out of both ports using microscope objectives and is detailed in Section 4.4.2.

## 4.3 Optical characterisation

### 4.3.1 Mode profiling

The guided mode profiles of the GaN waveguides were measured using the setup shown in Figure 4. 10. A single-mode fibre was used to clean the mode profile from an 800 nm diode laser and make it circular to increase the coupling efficiency to the waveguide. The 800 nm wavelength is of interest to this work as single photons produced by SPDC of GaN diode lasers output operating at 400 nm will be at 800 nm. Coupling was optimised by selecting appropriate collimation lenses from the fibre in order to produce a spot size after the 50X objective which matches that of the guided mode.

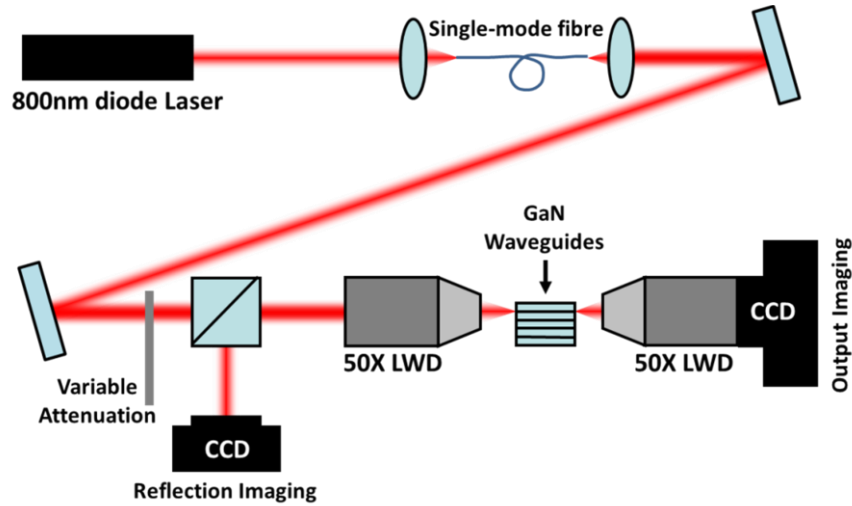


Figure 4. 10: Schematic of experimental setup used to measure the guided mode profile of the GaN waveguides.

In order to confirm that the waveguide designs were single-mode, the coupling conditions were varied, with use of a translation stage in order to excite a range of possible guided modes. The sample and output imaging optics were kept fixed. No change in mode profile was observed for the waveguide confirming the single-mode nature of the waveguide.

An example of a measured guided mode profile is shown in Figure 4. 11. The mode profile was measured with the same objective as the facet and thus could be scaled appropriately. The measured mode profile is shown overlaid on the facet image in b).

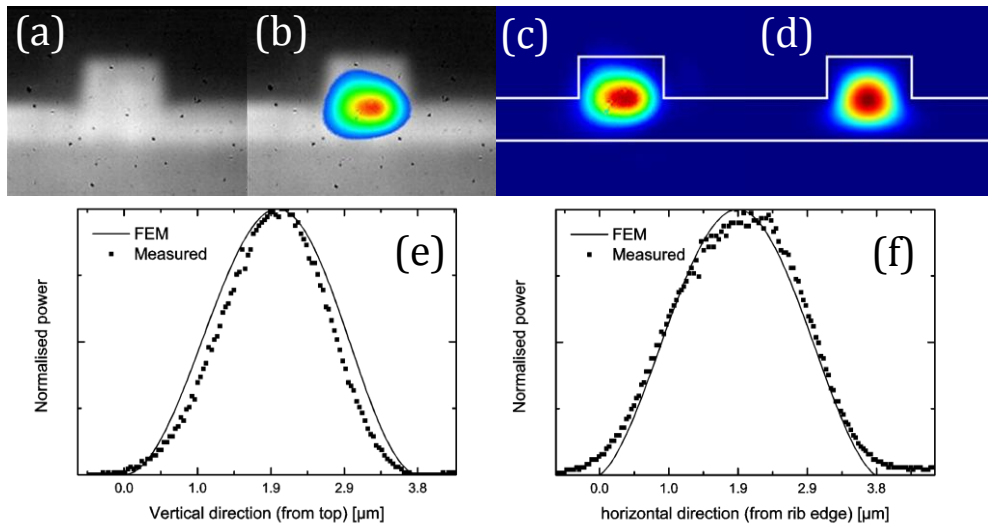


Figure 4. 11: Optical image of (a) the GaN facet and (b) GaN facet with overlay of measured mode profile. (c) Measured mode profile with outline of waveguide matching dimensions in Figure 4. 4. (d) FEM simulation of waveguide with the same dimensions. (e) Normalised power of vertical cross-section through centre of waveguide. (f) Normalised power of horizontal cross-section through the centre of the waveguide.

The measured mode profile was compared to FEM analysis and a close match was observed. The measured mode is confined slightly more in the vertical direction compared with simulation predictions.

### 4.3.2 Directional coupler splitting ratios

The splitting ratio describes how much power remains in one arm and how much is transferred to the other arm by the DC device. The splitting ratio is the key functional property of the DC that determines its practical use. As described in chapter 1, a range of splitting ratios are required to implement functional integrated quantum photonics circuits. The splitting ratio may be defined by a reflectivity,  $R$ , that represents the fraction of power that remains in the same arm. Conversely, it may also be defined by the power transferred to the adjacent guide,  $1-R$ .

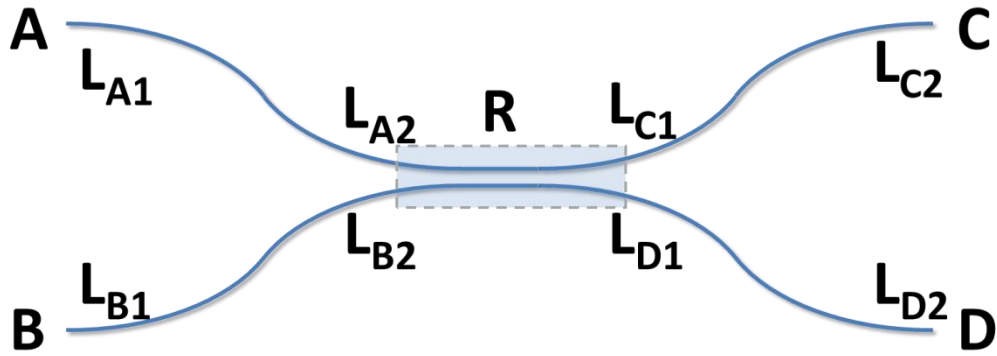


Figure 4. 12: Schematic of directional coupler including terms for loss  $L$ , reflectivity  $R$  and port identification.

By separately probing both input arms and recording the output power from both output arms a number of loss terms can be removed from the calculation of  $R$ :

$$\begin{aligned} P_{D_A} &= P_A L_{A1} L_{A2} L_{RAD} L_{D1} L_{D2} (1-R), & P_{C_A} &= P_A L_{A1} L_{A2} L_{RAC} L_{C1} L_{C2} R, \\ P_{D_B} &= P_B L_{B1} L_{B2} L_{RBD} L_{D1} L_{D2} R, & P_{C_B} &= P_B L_{B1} L_{B2} L_{RBC} L_{C1} L_{C2} (1-R) \end{aligned} \quad (4.6)$$

Where  $R$  is the reflectivity of the directional coupler and  $L$  are loss coefficients. All loss terms include both propagation loss and loss due to coupling into radiation modes. The subscript is used to identify arms and loss terms. For example:  $L_{A1}$  is the propagation loss term for arm A,  $L_{A2}$  is the coupling loss into the coupler region,  $L_{RAD}$  is the loss in the coupler region for light coupling from arm A to arm D,  $L_{RAC}$  represents loss in the coupler region for light coupling from arm A to C and  $P_{D_A}$  is the power measured at port

D when power  $P_A$  is coupled into port A. With some algebra, Equation (4.6) can be rewritten to find the reflectivity:

$$\begin{aligned} \frac{P_{D_A}}{P_{C_A}} &= \frac{L_{RAD}L_{D1}L_{D2}(1-R)}{L_{RAC}L_{C1}L_{C2}R}, & \frac{P_{C_B}}{P_{D_B}} &= \frac{L_{RBC}L_{C1}L_{C2}(1-R)}{L_{RBD}L_{D1}L_{D2}R}, \\ \frac{P_{D_A}P_{C_B}}{P_{C_A}P_{D_B}} &= \frac{L_{RAD}L_{RBC}(1-R)^2}{L_{RAC}L_{RBD}R^2} \\ \sqrt{\frac{P_{D_A}P_{C_B}}{P_{C_A}P_{D_B}}} &= \frac{L_T(1-R)}{L_S R} & (4.7) \\ R &= \frac{1}{\sqrt{\frac{P_{D_A}P_{C_B}}{P_{C_A}P_{D_B}} \frac{L_S}{L_T} + 1}} \end{aligned}$$

Where two new terms are introduced:  $L_T$  is the loss for light transferred across the coupling region and  $L_S$  is the loss for power which remains on the same side. These terms represent loss due to coupling to radiation modes in the coupler region and cannot be eliminated from the equation. These terms mean that simple measurement of the output power will not provide details of the true splitting ratio unless all other values of loss can be identified and eliminated from Equation (4.6).

From BPM simulations it was identified that no coupling to radiation losses occurred in the coupler region for perfectly symmetric directional couplers with no defects or surface roughness. For an estimation of the directional coupler reflectivity,  $R$ , the devices were assumed to be defect free so that  $L_S=L_T$ . In practice further analysis and measurements of the individual loss contributions should be carried out to confirm this assumption.

The fabricated directional couplers with different coupling lengths were measured in order to ascertain how much power was transferred by the coupling region. Using Equation (4.7),  $1-R$  is plotted for different directional couplers in Figure 4. 13. Using Equation (4.1) two possible trends are shown alongside the measured data: one that matches the design perfectly from Figure 4. 4 with  $L_c = 960\mu\text{m}$  and one matches the resulting fabricated structure inferred from Figure 4. 7 and simulated in Figure 4. 8 with  $L_c = 1148 \mu\text{m}$ .

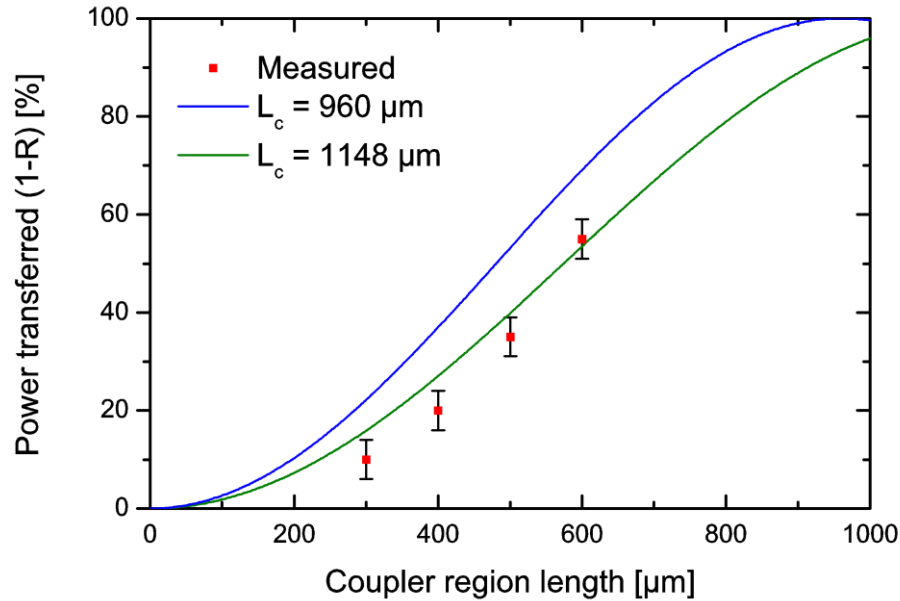


Figure 4. 13: Measured power transferred (1-R) for four fabricated directional couplers assuming  $L_S=L_T$  as described in the main text. Two theory plots are shown based on Equation (4.1) for the planned design with  $L_c = 960 \mu\text{m}$  and the modified design based on the fabrication related effects of an increased width and sloped sidewalls with  $L_c = 1148 \mu\text{m}$ .

Results show splitting ratios of 10:90, 20:80, 35:65 and 55:45 for coupling region lengths of  $300 \mu\text{m}$ ,  $400 \mu\text{m}$ ,  $500 \mu\text{m}$  and  $600 \mu\text{m}$ , respectively. The measured coupling length is consistent with the fabricated waveguides structure having a larger width and sloped sidewalls. These fabrication effects act to reduce the mode overlap between the adjacent waveguides in the coupler region due to the higher mode confinement under the rib. A range of splitting ratios should be obtained by appropriate fabrication of different length devices.

### 4.3.3 Propagation loss

Propagation loss is a key parameter in the design of integrated optical devices. For the design of waveguide lasers, as discussed in chapter 3, it is a crucial factor in obtaining efficient laser operation. For integrated circuits, such as multiple directional couplers for quantum information applications, the propagation loss limits the number of devices that can be combined on one chip before the signal reduces below a reliable value. Most quantum computational circuits require the integration of a vast number of devices for functionality. The measurement of waveguide propagation losses is a non-trivial task. The main issue lies with separating the measurement of coupling losses from propagation losses.

The simplest and most reliable method to measure propagation loss is the cut-back method [38], which evaluates the loss coefficient by output power measurements on guides of progressively shorter length. This method results in complete destruction of the device and is unsuitable for the GaN devices in this work due to the difficulty in making successive, repeatable, cleaves. A method involving prism coupling at various positions along the waveguide [39, 40] is well known and continued modifications [41, 42] make this technique practical and reliable. There is limited implementation of this technique for rib waveguides as it requires a spot size at the coupling position which is the same size as the guided mode. This is difficult to obtain as the prism must be within the working distance of the objective. Other novel techniques include using phase-conjugation [43], which requires the appropriate phase-conjugate materials, measuring fluorescence [44, 45], which requires either a doped or naturally fluorescing waveguide material and suitable pump sources, and reflectometer methods [46] that require suitable equipment and cm-long low single-pass loss waveguides. The two techniques used in this work are the scattered light method and the Fabry-Perot method, both of which will be described hereafter. They also have limitations, but are considered most practical for the type of waveguides used in this work.

### **a) Scattered light method**

It is possible to calculate the propagation loss of the waveguide by measuring the scattered light from the waveguide. Light is coupled into the waveguide and, rather than monitoring the waveguide output, the scattered light is measured transverse to the waveguide direction. This scattered light is then considered to be proportional to the power in the waveguide. Measurement can be done with either a CCD camera [47] or by collecting light with a fibre [48]. These techniques continue to find practical use where the scattered light is of interest and due to the ease of implementation [49]. The technique is simple and may only require one image for each waveguide. However, it assumes that the scattering points are uniformly distributed along the waveguide length and width. For accuracy, this technique requires a significant fraction of the power to be lost within the waveguide propagation distance and thus is only accurate for a range of waveguides/propagation losses.

Another limiting factor with this technique is that, for large-area rib waveguides, the unguided diffracting light contributes to scattered light. As discussed in chapter 3, leaky modes can remain guided for significant lengths due to their complex integration with

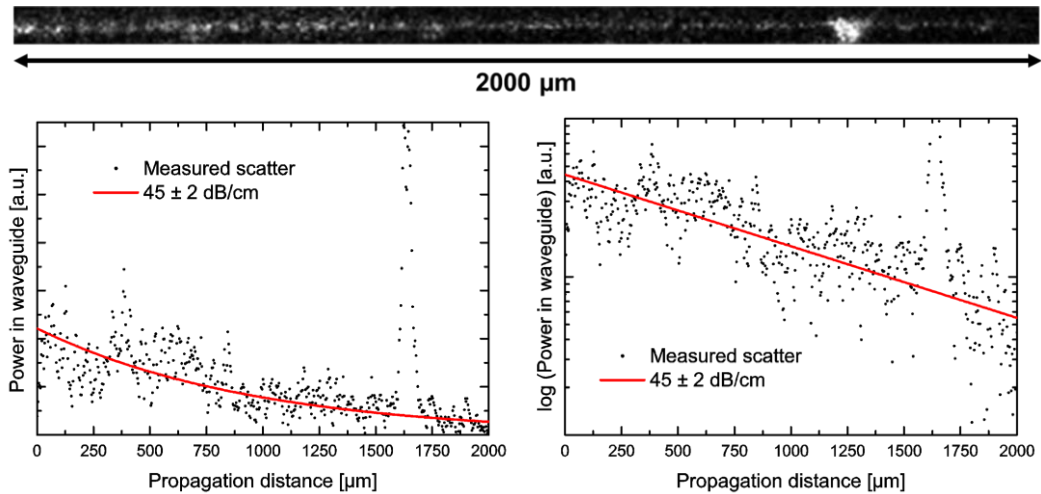


Figure 4. 14: **(top)** Measured 800 nm scattered light from the waveguide for a 2 mm propagation distance away from the coupling facet. **(graph left)** Measured scattered light, from the image (top), averaged over the waveguide width with least squares fit and linear regression error analysis. **(graph right)** Logarithm plot of graph on left.

the slab. Consequently there is a large section near the coupling facet where scattered light is produced by a range of leaky modes and so scattered light in this region is not proportional to fundamental mode loss. Care must be taken to avoid this section of the waveguide.

The scattered light from a straight GaN fabricated waveguide with  $s=0.65r$  was measured using the setup shown in Figure 4. 10 with an additional 5X plan-view microscope to image the waveguide from above. Results are shown in Figure 4. 14 in both measured and logarithmic form. Data was taken far from the coupling facet, towards the end of the waveguide where only the fundamental mode remained. Using a least-squares fit and linear regression error analysis the propagation loss was calculated to be  $45 \pm 2$  dB/cm. The intensity of scattering points was highly irregular, which was a cause for concern. This technique could not be applied with confidence to a range of waveguides due to the irregularity of scattering points.

### b) Fabry-Perot method

Another well-established technique for measuring loss is the Fabry-Perot resonance technique [50, 51]. This technique involves considering the entire waveguide as a resonator with the Fresnel reflection at the facets providing reflectivity and finds continued use due to the simplicity and reliability [52, 53]. Interference between the standing-waves in the cavity can be described by the well-established Fabry-Perot equations [54].

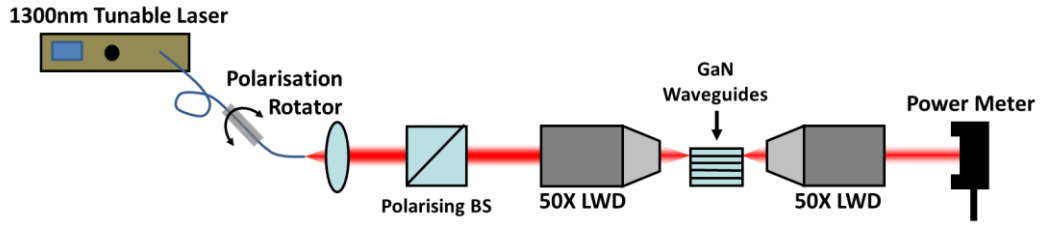


Figure 4. 15: Schematic of setup used for measuring loss with the Fabry-Perot technique. The 1300 nm tunable source is an Agilent 8167B laser.

A number of straight waveguides were measured using the setup shown in Figure 4. 15. An Agilent 8167B tunable laser source was programmed to output a range of wavelengths sweeping from 1300 to 1300.4 nm. This was achieved with 0.001 nm steps with a pause of 0.5ms at each wavelength. This type of measurement was possible due to the high coherence of the laser, offering a linewidth of 100 kHz. Polarisation was controlled using a fibre polarisation rotator to excite only one of the transverse modes. Particular care was taken to collect all of the output coupled light from the waveguide and not scattered/diffracted light with use of an aperture. The measured power for one waveguide is shown in Figure 4. 16.

The propagation loss was determined by analysing the visibility of the fringes from the equations that describe the transmission through a Fabry-Perot etalon. Here a propagation loss was introduced to the reflectivity term:

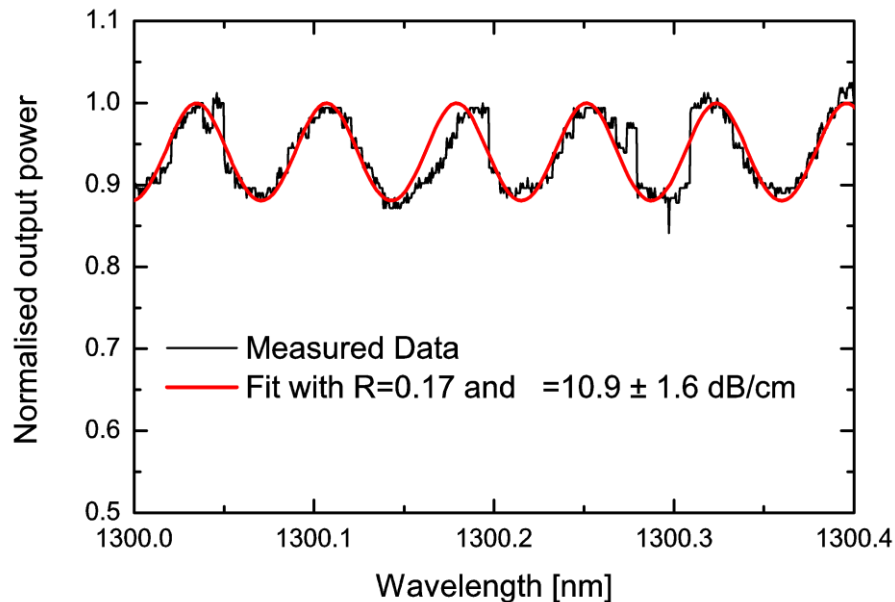


Figure 4. 16: Fabry-Perot fringes of a GaN straight waveguide. Black shows measured normalised data and red shows the least squares fit with linear regression error analysis used to predict the propagation loss.

$$T = \frac{(1-r)^2}{1+r^2-2r\cos(2kNL)}, \quad r = R \exp(-\alpha L) \quad (4.8)$$

Where  $R$  is the reflectivity of the facet,  $k$  is the free-space propagation constant,  $N$  is the guided mode effective index and  $L$  is the length of the waveguide. By normalising the peak transmission power to unity, the propagation loss,  $\alpha$ , was found, after some algebra, from the minimum transmission power,  $P_{min}$ :

$$\alpha = -\frac{1}{L} \ln \left( \frac{1 - \sqrt{P_{min}}}{R(1 + \sqrt{P_{min}})} \right) \quad (4.9)$$

By inspection of the waveguide facet, the reflection  $R$  was assumed to be that of the perpendicular Fresnel reflectivity of the waveguide:

$$R = \frac{N-1}{N+1}^2 \quad (4.10)$$

One drawback of this technique is the limited range of loss values that can be measured with high accuracy, as it relies on suitable reflectivity of the facets. Due to mechanical vibrations, laser stability and power meter accuracy, the error in  $P_{min}$  was calculated using the linear regression error analysis to be 2.8% due to the noise in Figure 4. 16. The percentage error in the measurement of propagation loss can be calculated from Equation (4.9). This error is shown for three example GaN waveguides of different lengths, where the cross-sectional design does not affect the result, in Figure 4. 17.

Taking the maximum acceptable error as 100%, for a 6 mm long GaN waveguide only loss values between 0.5-30 dB/cm can be measured. Higher propagation losses can be measured with shorter waveguides, with the minimum length limited by the practical waveguide criteria as discussed in Chapter 3. Lower propagation loss can be measured with longer waveguides however the coherence of the laser will create an upper length limit. All propagation loss measurements in this system are expected to have a minimum error of 14% due to the error in  $P_{min}$ .

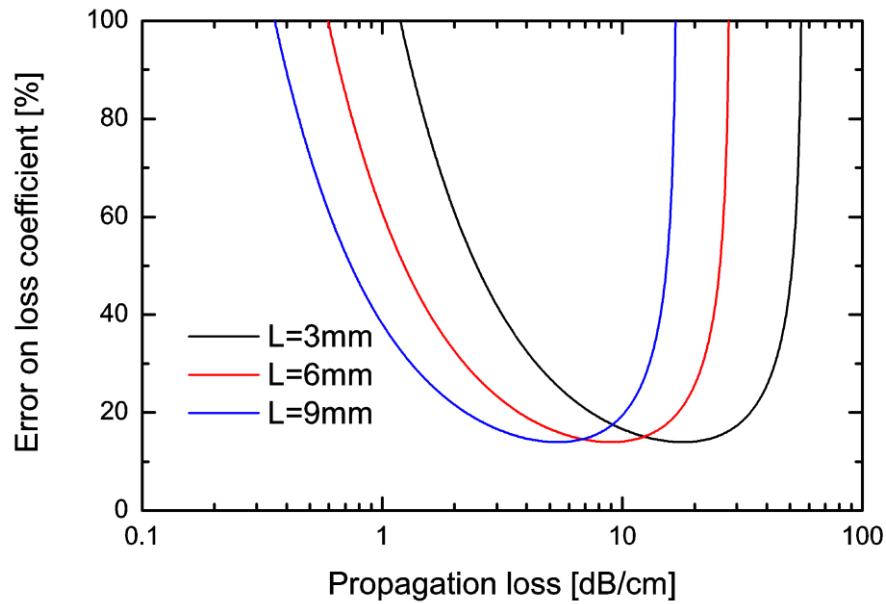


Figure 4. 17: Error on determined loss coefficient for different waveguide lengths based on a 6% error in measuring  $P_{\min}$ . The facet reflectivity is assumed to be for GaN waveguides and is  $R=0.17$ .

The cause for such high error is likely to be due to the relative wavelength accuracy of the tunable laser. The Agilent 8167B laser offers a relative accuracy of  $\pm 0.05$  nm at 1300 nm which is not far from the 0.09 nm free-spectral range. A shorter waveguide will reduce this source of error but may increase overall error due to the lower loss per round-trip as indicated in Figure 4. 17.

The propagation losses of a number of straight waveguides were measured with this technique and are shown in Table 4. 3. Results show that there is a large range in the measurement of propagation loss between 10-20 dB/cm. All these waveguides are expected to have similar surface scattering losses and so one possible cause for the differences between these measurements could be specific surface scattering points due to the fabrication process. Alternatively, the differences could be due to differing facet quality. These measured fabrication losses are large, more than should be typical of this type of waveguide, however they are lower than those previously reported in GaN, specifically 34 dB/cm at 1550 nm in reference [21]. It is proposed that these losses could be the result of high loss from the interface layer between the GaN and Sapphire which could be significantly reduced with appropriate growth methods [55, 56].

Table 4. 3: Measured propagation loss for a number of waveguides using the Fabry-Perot technique. In all cases  $s=2.47\mu\text{m}$ ,  $r=3.8\mu\text{m}$  and the wavelength was 1300 nm.

No.	Width [ $\mu\text{m}$ ]	Length [mm]	Loss [dB/cm]	
			TE	TM
1	2.5	5.8	$11.7 \pm 1.7$	$14.3 \pm 2.4$
2	2.5	5.9	$16.9 \pm 3.3$	$13.9 \pm 2.2$
3	3.0	5.8	$18.7 \pm 4.3$	$10.9 \pm 1.6$
4	3.0	5.8	$20.0 \pm 5$	$15.6 \pm 2.8$

It is important that the facet is perpendicular to the waveguide to assume all reflected power is coupled into the waveguide. For large cross-sectional area rib waveguides the weak horizontal guidance means that few degrees offset will cause a significant reduction in reflection-coupling. In order to estimate the expected loss from non-perpendicular facets, BPM simulations were carried out at 800 nm for the straight waveguide design. By launching the guided mode at an angle, an estimate of the reflection losses could be obtained by observing how much power is coupled into the guided mode. Results for angles from 0 to 3.5 degrees are shown in Figure 4. 18. The Fresnel reflectivity over a 5 degree range varies between 0.17 and 0.21 for the TM case and 0.17 and 0.13 for the TE case and is small in comparison to the reflection-coupling loss. Results show that significant care must be taken during orientation and cleaving for straight resonators to ensure that high cavity quality can be maintained.

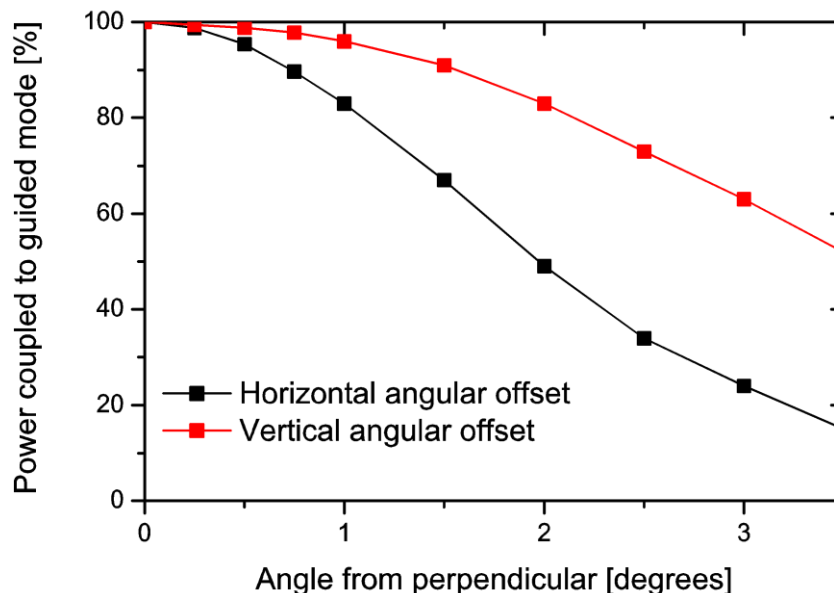


Figure 4. 18: Percentage of power coupled into the guided mode from angled launch conditions. Calculations carried out with BPM simulations. The drop in power represents additional loss for reflection from a non-perpendicular facet. Calculated for the design shown in Figure 4. 1 at 800 nm.

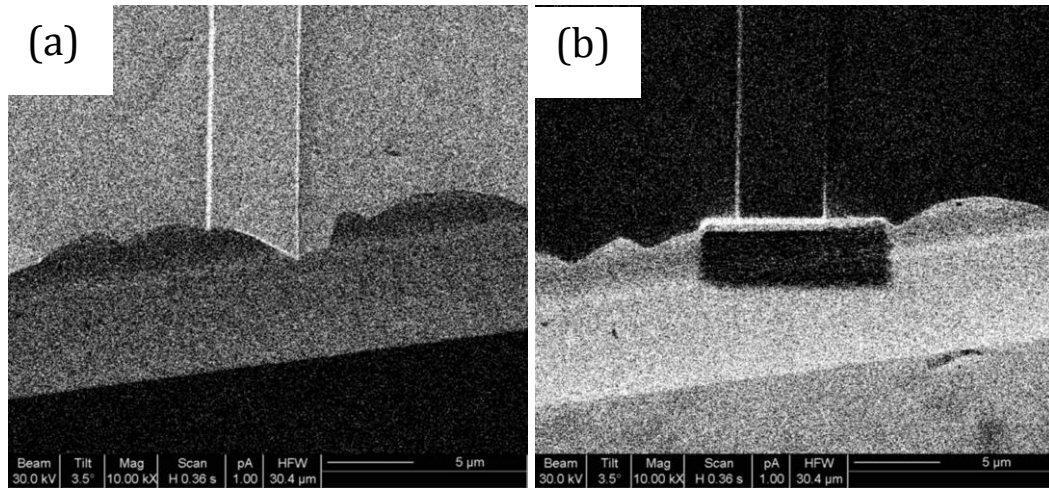


Figure 4. 19: Ion beam images of **(a)** damaged facet created by a poor cleaving process and **(b)** facet FIB milled for improved coupling or Fresnel reflectivity. Taken at Bristol University.

The manual cleaving process of thinned GaN samples was rather unreliable, leaving many samples with facets which were unsuitable for optical transmission. One such damaged facet is shown in Figure 4. 19 a). One method to resolve this problem and recover devices that would otherwise be unusable is to clean the facet with a focussed ion beam (FIB) milling process. In collaboration with Bristol University some straight waveguide facets were FIB milled to clean/straighten them. Damaged facets were removed with the milling process and new perpendicular facets were defined further back from the sample edge. An image of one facet and the new milled facet is shown in Figure 4. 19.

Four waveguide facets were cleaned, creating two waveguides with facets that should offer reflectivity near that of the Fresnel reflectivity. The propagation losses of these waveguides were measured using the Fabry-Perot technique and the results are shown in Table 4. 4.

The method was successful in creating resonators that after cleaning show a propagation loss at the lower end of those measured without cleaning in Table 4. 3. The difference between these waveguides and the lowest propagation loss of 10.9 dB/cm may be the result of a rough facet in comparison with the cleaving process which is expected to produce a smoother facet.

Table 4. 4: Measured propagation losses for waveguides with FIB milled facets using the Fabry-Perot technique. In all cases  $s=2.47\mu\text{m}$ ,  $r=3.8\mu\text{m}$  and the wavelength was 1300 nm.

No.	Width [ $\mu\text{m}$ ]	Length [mm]	Loss [dB/cm]	
			TE	TM
5	3.5	5.4	13.8 $\pm$ 2.2	15.9 $\pm$ 2.9
6	4.0	5.3	14.5 $\pm$ 2.5	14.4 $\pm$ 2.5

#### 4.3.4 Two-mode waveguide

With appropriate cross-sectional design, it is possible to fabricate a waveguide that is capable of supporting two-modes horizontally. A two-mode waveguide, when excited offset, causes the light to oscillate between the modes in a process directly analogous to what occurs inside a directional coupler. The length required to complete one full cycle is referred to as the beat-length.

A two-mode GaN waveguide was fabricated by increasing the width of the waveguide to 5  $\mu\text{m}$  compared to 3.8  $\mu\text{m}$  in the standard design in Figure 4. 1. The oscillatory behaviour of the light travelling down the waveguide was observed by imaging the waveguide from above in a similar method to that used to measure propagation losses and is shown in Figure 4. 20. Direct observation and measurement of this oscillatory behaviour with a CCD camera, between modes, is not known to be reported previously. Similar observations have been reported for beating between different polarisation modes in fibres and waveguides [57, 58], but not higher order modes. Observation in this instance could be unique due to the precise dimensions of the waveguide, creating an oscillation length that can be practically measured and is helped by the large scattering from the rib sidewalls.

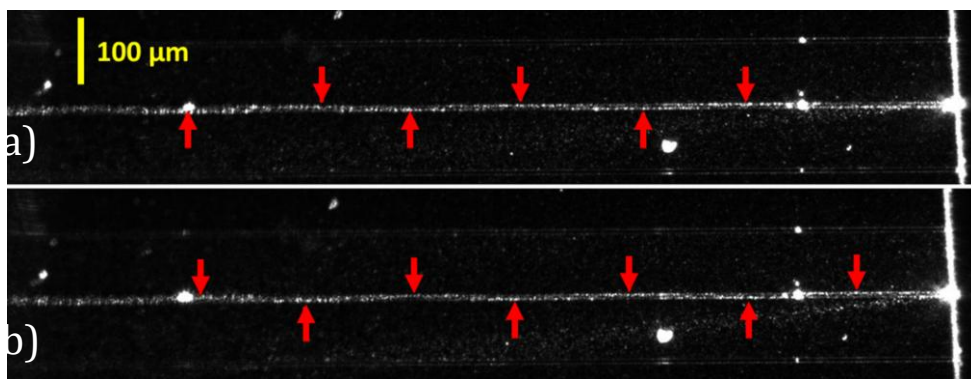


Figure 4. 20: The scattered light from a two-mode waveguide after coupling 800 nm light. Image (a) and (b) are of the same waveguide with different coupling conditions with light propagating from left to right. (a) and (b) were excited horizontally offset to the centre in either direction. The oscillatory behaviour is clear by observing the waveguide edges which scatter more light than the centre when the guided light is concentrate on one side of the waveguide.

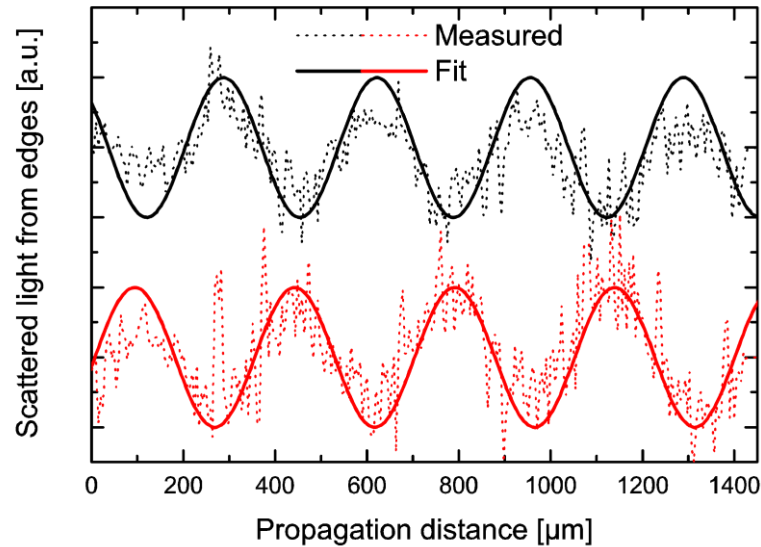


Figure 4. 21: Data extracted from Figure 4. 20 using a 4×4 pixel average along the edges of the waveguide. Shown is the difference in intensity between either edge of the waveguide, thus removing any background light. Red corresponds to Figure 4. 20 a) and black corresponds to Figure 4. 20 b) and are shown vertically displaced. A least squared fit is shown which corresponds to a beat length of  $342 \pm 19 \mu\text{m}$  with linear regression error analysis.

In order to precisely extract data from Figure 4. 20, the image was analysed along both waveguide edges in both excitation situations and the measured scattered light intensity is plotted in Figure 4. 21. A sinusoidal fit was applied in order to extract the beat-length. The beat-length is defined in an analogous way to the coupling-length and depends on the index difference between the fundamental mode and the second guided mode:

$$L_B = \frac{\lambda}{\Delta N} \quad (4.11)$$

The change in the effective index between the two modes was calculated from Equation (4.11). The beat length was calculated using averaging between the measurements to be  $342 \pm 19 \mu\text{m}$  with linear regression error analysis. This information may be used to calculate the refractive index or dimensions of the waveguide, solving for one unknown. This type of analysis may find application in the field of waveguide sensors, for instance to measure refractive index change. It is expected the accuracy of this technique could be improved with greater imaging resolution and a longer waveguide.

Using the measured beat length the overall height of the waveguide was confirmed assuming other parameters are well known. The overall height of the GaN layer had the highest uncertainty because the transition between Sapphire/GaN is not always abrupt

and the guided mode may sit significantly above this interface. FEM simulations were used with a well-defined wavelength, refractive index, etch depth and rib width. The overall height of the waveguide was altered until the difference between the effective indices of the two guided modes led to a beat length which matched the measurement using Equation (4.11). Using the measured width of the waveguide,  $5\mu\text{m}$ , and the measured etch depth,  $1.33\mu\text{m}$ , the overall height of the waveguide was determined. The measured beat length of  $342 \pm 19 \mu\text{m}$  corresponds to an overall height of  $3.61 \pm 0.20 \mu\text{m}$  or a waveguide mode that sits  $190 \pm 9.5 \text{ nm}$  above the GaN/sapphire interface. This particular scenario is consistent with a densification of the GaN material above the more dislocated (i.e. lower index) GaN buffer layer. This may act to explain the tighter mode confinement in the vertical direction, shown in Figure 4. 11, compared to simulations. Measurement of refractive index could be carried out in a similar way.

### 4.4 Two-Photon quantum interference

In order to confirm the suitability of the directional couplers for use as part of an integrated quantum photonics circuit, the fabricated directional coupler was tested with single-photon pairs in collaboration with the University of Bristol. The theory and motivation for integrated quantum photonics was discussed in Chapter 1.

#### 4.4.1 The Hong-Ou-Mandel (HOM) effect

In a classical description, when two beams of light are incident upon a beam splitter their power will be split between the exit paths of the beam splitter according to the reflectivity  $R$ . Even in the single-photon regime, where no interference occurs, this holds true and the output counts can be described by the same simple classical formula as shown in Figure 4. 22. When the two photons are indistinguishable however, such that they have the same frequency and polarisation, and arrive at a beam splitter at the same time, they will constructively interfere with each other and travel along the same path. This is a two-photon interference effect that can only be explained by the quantised nature of light [59].

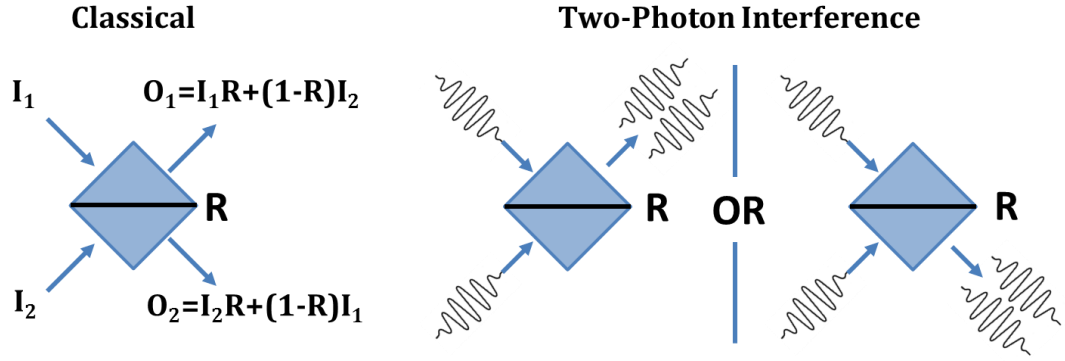


Figure 4.22: Schematic of the difference between classical and two-photon quantum interference.

For a 50-50 beam-splitter ( $R=0.5$ ), when two-photon interference occurs the probability of detecting photons simultaneously at both exits of the beam splitter drops to zero. The finite bandwidth of the photons used results in a finite temporal overlap which causes interference over a small range of arrival times. When a Gaussian temporal spread is assumed, which is appropriate for this work, the number of simultaneous counts at both exits of the beam splitter can be described by Equation (4.12). This drop in simultaneous counts is known as the Hong-Ou-Mandel (HOM) dip [60].

$$N_c = C(T^2 + R^2) \left[ 1 - \frac{2RT}{T^2 + R^2} \exp(-\Delta\omega\delta\tau)^2 \right] \quad (4.12)$$

where  $N_c$  is the number of simultaneous counts,  $C$  is a constant,  $T$  is the transmission ( $1-R$ ),  $R$  is the reflectivity,  $\Delta\omega$  is the bandwidth of the photons and  $\delta\tau$  is the time delay. When  $\delta\tau=0$ , the peak in interference is observed which drops the coincidence counts to a minimum which is defined by the reflectivity of the beam splitter alone:

$$N_{c\min} = 1 - \frac{2RT}{T^2 + R^2} \quad (4.13)$$

Only systems with highly correlated photon pairs, and low noise will be able to achieve this drop in coincidence counts and so a visibility term,  $V$ , is introduced to describe the quality of the beam-splitter, the measurement system and the photon pair. A visibility of 1 corresponds to a perfect system:

$$N_c = C(T^2 + R^2) \left[ 1 - \frac{2RTV}{T^2 + R^2} \exp(-\Delta\omega\delta\tau)^2 \right] \quad (4.14)$$

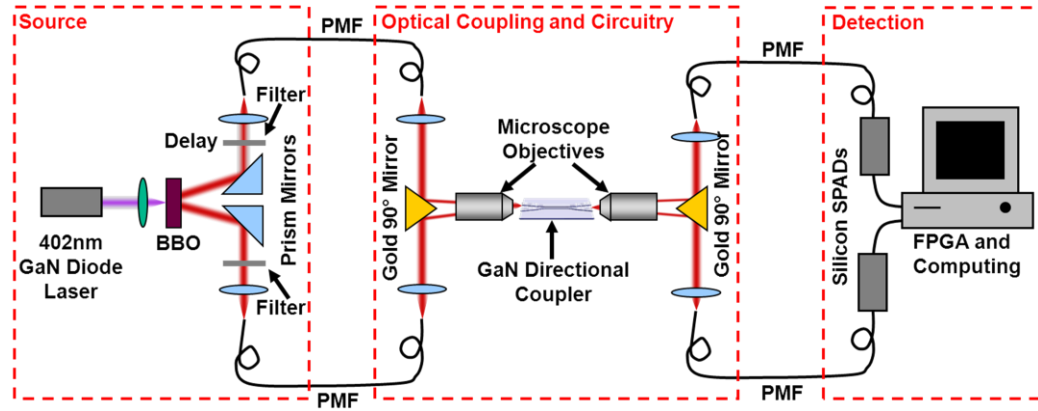


Figure 4. 23: Schematic of experimental setup for two-photon interference in a GaN direction coupler. Acronyms are defined in the main text or appendix. The system was arranged at Bristol University.

#### 4.4.2 Experimental setup

Single photon pairs were produced by type-2 spontaneous parametric down-conversion using a beta barium borate (BBO) crystal. This process produced single-photon pairs that were, when collected appropriately, perfectly correlated. Correlation for this work was when photons-pairs had wavevectors, wavelengths and polarisations that precisely related to each other. Spontaneous parametric down-conversion produced photon pairs with wavevectors that were the same in magnitude, thus had the same wavelength but were emitted at opposite angles, thus the precise collection angle was important. Photon pairs had linear polarisation, but were opposite such that one was vertical and the other horizontal. This process was highly inefficient with one pair produced for every  $\sim 10^{12}$  pump photons. Photon pairs were collected from a specific angle from the BBO crystal with prism mirrors which reflected all the light in a transverse direction. Narrow (3 nm) band interference filters were used to remove pump light and other unwanted noise. An adjustable time/distance delay was introduced into one arm of the photon pair source such that the photon pairs could be tuned to arrive at the same time at the directional coupler. They were then coupled into appropriately oriented polarisation maintaining fibre (PMF) and the fibres were rotated to align the polarisation for constructive interference.

Photon pairs were coupled into the two input arms of the directional coupler using free-space coupling, as the port separation was too small for standard fibre-bundles. This was achieved with a gold coated 90 degree mirror to maintain polarisation. Output from the PMFs were collimated and coupled into a microscope objective via the 90 degree mirror such that they coupled into different ports of the directional coupler. The

spot size produced by the microscope objectives was tuned to match that of the guided mode. Photon pairs were collected from the directional coupler in a similar free-space manner and coupled into PMFs. Photons were then detected with silicon single photon avalanche detectors (SPADs). Photon counting and coincidence logic was achieved with field programmable gate array (FPGA) hardware controlled with a computer [61]. The full schematic of the experimental setup is shown in Figure 4. 23.

The Hong-Ou-Mandel dip was measured in a 45:55 splitting GaN directional coupler by altering the delay in one arm. The delay was incremented in 15  $\mu\text{m}$  steps, corresponding to a 0.05 ps temporal delay, and coincidences were counted during a 30 second integration period. Figure 4. 24 shows the measured data which follows shows a characteristic Gaussian HOM dip, the first such measurement in GaN.

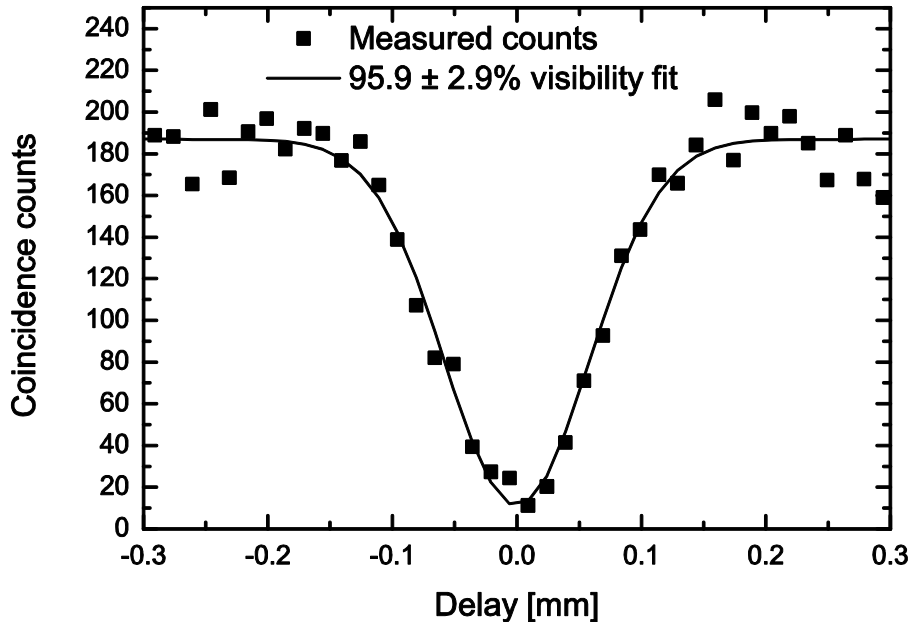


Figure 4. 24: Hong-Ou-Mandel dip with  $95.9 \pm 2.9\%$  visibility fit. Each point was taken after an integration time of 30 seconds. The 15  $\mu\text{m}$  steps correspond to a 0.05 ps temporal delay. The fit was applied using Equation (4.14) with linear regression error analysis.

By fitting Equation (4.14) to the data, a visibility of  $95.9 \pm 2.9\%$  was calculated with aid of the jack-knife technique for error analysis [62]. Single detector counts ranged from 129000 to 133000 for each data point, showing minimal drift throughout the measurement. Drift due to thermal or mechanically induced movement was a concern due to the long integration time and large number of xyz stages (9) used in the experiment. Background noise coincidence counts were measured by blocking one input port of the directional coupler and were found to be negligible for this

measurement. It is expected that the 2.9% error is due to the mechanical stability of the system which used nine xyz mechanical stages for input and output coupling between fibres and the waveguide. The deviation from maximum visibility is likely due to the quality of the source.

This measured visibility is similar in magnitude to other quantum interference measurements made with a BBO single-photon source; silica-on-silicon circuits by Politi et al. ( $94.8 \pm 0.5\%$ ) [19], laser written waveguides by Marshall et al. ( $95.8 \pm 0.5\%$ ) [63], glass waveguides by Sansoni et al. ( $93.7 \pm 0.9\%$ ) [64] and UV written waveguides by Smith et al. ( $95.0 \pm 1.4\%$ ) [65]. The high visibility measured in this work confirms the optical quality and single-mode nature of the direction coupler.

This measurement leads the way for the fabrication of integrated quantum photonics circuits in GaN. These circuits can be made from a number of directional couplers that offer 1/3 or 1/2 splitting ratios as described in detail in Chapter 1. With appropriate path length control, two-photon interference should occur at each of the directional couplers to achieve quantum logic.

### 4.5 Conclusions

A single-mode directional coupler was designed and simulated that allowed for compatibility with contact photolithography, a single etch step and a minimum feature size of 2  $\mu\text{m}$ . This device used novel inverse tapers that allowed a significant reduction in footprint and a circular mode at the coupling facets. This offered a mechanism to reduce coupling length without reduction of the coupling gap. The design had a smaller footprint than that offered by standard e-beam, sub-micron gap directional couplers [21]. This is the first known report of the use of inverted tapers to enhance coupling and may provide a route to high density integrated optics.

A range of straight and directional coupler waveguides were fabricated using the described process. Optical and SEM images have shown that these devices were fabricated to design requirements. These devices add to the small range of GaN devices demonstrated to date and are among the few that have been designed to operate in the optical/NIR wavelength range. The devices were characterised to confirm single-mode behaviour for a range of wavelengths, owing to the relaxed criteria of the rib-waveguide design.

## Chapter 4 – Gallium Nitride Waveguides

Propagation loss was measured with the scattering and Fabry-Perot methods. Results showed significant losses compared with similar designs for other materials, however, propagation loss remains small compared to demonstrated GaN devices:  $10.9 \pm 1.6$  dB/cm at 1300 nm in this work compared with 34 dB/cm at 1550 nm in ref. [21]. It is possible that the high losses measured in this work are due to underlying material loss which could be significantly reduced with appropriate growth methods [55, 56].

The splitting ratios of a number of directional couplers were measured using a method that compensates for loss in individual arms. Results demonstrate that a range of splitting ratios can be obtained by altering the length of the device. Results show a coupling length that is slightly longer than expected from simulations and this may be due to the slightly wider waveguide with sloped sidewalls due to fabrication effects.

A two-mode waveguide was fabricated and observed to oscillate ('beat') between the modes by measurement of the scattered light with a CCD camera. This is the first known measurement of the beat-length of a waveguide with the scattered light from the sides of the waveguide. This measurement technique may have applications in the field of waveguide sensors.

Two-photon interference was observed with down-converted single-photon pairs within a 45:55 GaN directional coupler. A novel free-space coupling system was used in order to address ports that were close together on the chip. Results show a visibility near the theoretical limit confirming the quality of the directional coupler. This result is the first within the GaN material system and may have implications for the field of integrated quantum photonics. The recent demonstration of single-photon pairs in lithium niobate waveguides via SPDC leads the way for similar developments in GaN [65].

## References

- [1] Y. F. Zhang, L. McKnight, E. Engin, I. M. Watson, M. J. Cryan, E. D. Gu, M. G. Thompson, S. Calvez, J. L. O'Brien, and M. D. Dawson, "*GaN directional couplers for integrated quantum photonics*," *Applied Physics Letters*, **99**, (2011).
- [2] E. A. J. Marcatili, "*Dielectric Rectangular Waveguide and Directional Coupler for Integrated Optics*," *Bell System Technical Journal*, **48**, 2071 (1969).
- [3] A. W. Snyder, "*Coupled-Mode Theory for Optical Fibers*," *Journal of the Optical Society of America*, **62**, 1267-1277 (1972).
- [4] A. Yariv, "*Coupled-Mode Theory for Guided-Wave Optics*," *IEEE Journal of Quantum Electronics*, **Qe 9**, 919-933 (1973).
- [5] H. Kogelnik, "*Introduction to Integrated Optics*," *IEEE Transactions on Microwave Theory and Techniques*, **Mt23**, 2-16 (1975).
- [6] S. E. Miller, "*Coupled Wave Theory and Waveguide Applications*," *Bell System Technical Journal*, **33**, 661-719 (1954).
- [7] S. Somekh, E. Garmire, A. Yariv, H. L. Garvin, and Hunsperg, "*Channel Optical Waveguide Directional Couplers*," *Applied Physics Letters*, **22**, 46-47 (1973).
- [8] J. C. Campbell, F. A. Blum, D. W. Shaw, and K. L. Lawley, "*GaAs Electro-Optic Directional-Coupler Switch*," *Applied Physics Letters*, **27**, 202-205 (1975).
- [9] Y. C. Shi, S. L. He, and S. Anand, "*Ultracompact directional couplers realized in InP by utilizing feature size dependent etching*," *Optics Letters*, **33**, 1927-1929 (2008).
- [10] G. B. Cao, F. Gao, J. Jiang, and F. Zhang, "*Directional couplers realized on silicon-on-insulator*," *IEEE Photonics Technology Letters*, **17**, 1671-1673 (2005).
- [11] V. M. N. Passaro, "*Optimal design of grating-assisted directional couplers*," *IEEE Journal of Lightwave Technology*, **18**, 973-984 (2000).
- [12] E. Paspalakis, "*Adiabatic three-waveguide directional coupler*," *Optics Communications*, **258**, 30-34 (2006).
- [13] A. Martinez, F. Cuesta, and J. Marti, "*Ultrashort 2-D photonic crystal directional couplers*," *IEEE Photonics Technology Letters*, **15**, 694-696 (2003).
- [14] T. Fujisawa, and M. Koshiba, "*Polarization-independent optical directional coupler based on slot waveguides*," *Optics Letters*, **31**, 56-58 (2006).
- [15] A. M. Streltsov, and N. F. Borrelli, "*Fabrication and analysis of a directional coupler written in glass by nanosecond femtosecond laser pulses*," *Optics Letters*, **26**, 42-43 (2001).
- [16] M. Olivero, and M. Svalgaard, "*Direct UV-written broadband directional planar waveguide couplers*," *Optics Express*, **13**, 8390-8399 (2005).
- [17] S. H. Xiao, L. F. Shen, and S. L. He, "*A novel directional coupler utilizing a left-handed material*," *IEEE Photonics Technology Letters*, **16**, 171-173 (2004).
- [18] Y. Enami, D. Mathine, C. T. DeRose, R. A. Norwood, J. Luo, A. K. Y. Jen, and N. Peyghambarian, "*Hybrid electro-optic polymer/sol-gel waveguide directional coupler switches*," *Applied Physics Letters*, **94**, 213513 (2009).
- [19] A. Politi, M. J. Cryan, J. G. Rarity, S. Y. Yu, and J. L. O'Brien, "*Silica-on-silicon waveguide quantum circuits*," *Science*, **320**, 646-649 (2008).
- [20] R. Hui, S. Taherion, Y. Wan, J. Li, S. X. Jin, J. Y. Lin, and H. X. Jiang, "*GaN-based waveguide devices for long-wavelength optical communications*," *Applied Physics Letters*, **82**, 1326-1328 (2003).
- [21] R. Q. Hui, Y. T. Wan, J. Li, S. X. Jin, J. Y. Lin, and H. X. Jiang, "*III-nitride-based planar lightwave circuits for long wavelength optical communications*," *IEEE Journal of Quantum Electronics*, **41**, 100-110 (2005).
- [22] M. Heiblum, and J. H. Harris, "*Analysis of Curved Optical-Waveguides by Conformal Transformation*," *IEEE Journal of Quantum Electronics*, **Qe11**, 75-83 (1975).
- [23] M. K. Smit, E. C. M. Pennings, and H. Blok, "*A Normalized Approach to the Design of Low-Loss Optical Wave-Guide Bends*," *IEEE Journal of Lightwave Technology*, **11**, 1737-1742 (1993).
- [24] J. Rayleigh, "*The problem of the whispering gallery*," *The London, Edinburgh, and Dublin Philos. Mag. J. Sci.*, **6**, 1001 (1910).

- [25] E. G. Neumann, "Curved Dielectric Optical-Waveguides with Reduced Transition Losses," IEE Proceedings-H Microwaves Antennas and Propagation, **129**, 278-280 (1982).
- [26] L. Faustini, and G. Martini, "Bend loss in single-mode fibers," IEEE Journal of Lightwave Technology, **15**, 671-679 (1997).
- [27] A. Sakai, G. Hara, and T. Baba, "Propagation characteristics of ultrahigh-Delta optical waveguide on silicon-on-insulator substrate," Japanese Journal of Applied Physics Part 2- Letters, **40**, L383-L385 (2001).
- [28] E. A. J. Marcatili, "Bends in Optical Dielectric Guides," Bell System Technical Journal, **48**, 2103 (1969).
- [29] H. G. Unger, "Circular Waveguide Taper of Improved Design," Bell System Technical Journal, **37**, 899-912 (1958).
- [30] E. A. J. Marcatili, "Dielectric Tapers with Curved Axes and No Loss," IEEE Journal of Quantum Electronics, **21**, 307-314 (1985).
- [31] I. Moerman, P. P. Van Daele, and P. M. Demeester, "A review on fabrication technologies for the monolithic integration of tapers with III-V semiconductor devices," IEEE Journal of Selected Topics in Quantum Electronics, **3**, 1308-1320 (1997).
- [32] J. N. Walpole, "Semiconductor amplifiers and lasers with tapered gain regions," Optical and Quantum Electronics, **28**, 623-645 (1996).
- [33] V. R. Almeida, R. R. Panepucci, and M. Lipson, "Nanotaper for compact mode conversion," Optics Letters, **28**, 1302-1304 (2003).
- [34] G. H. Ren, S. W. Chen, Y. P. Cheng, and Y. Zhai, "Study on inverse taper based mode transformer for low loss coupling between silicon wire waveguide and lensed fiber," Optics Communications, **284**, 4782-4788 (2011).
- [35] L. Liu, and J. H. Edgar, "Substrates for gallium nitride epitaxy," Materials Science & Engineering R-Reports, **37**, 61-127 (2002).
- [36] Y. F. Zhang, Phd Thesis, "Diamond and GaN Waveguides and Microstructures for Integrated Quantum Photonics," (Institute of Photonics, University of Strathclyde, 2012).
- [37] R. Sink, Phd Thesis, "Cleaved-facet group-iii nitride lasers, Ph.D. thesis," (2000).
- [38] A. Rickman, G. T. Reed, B. L. Weiss, and F. Namavar, "Low-Loss Planar Optical Wave-Guides Fabricated in Simox Material," IEEE Photonics Technology Letters, **4**, 633-635 (1992).
- [39] F. Zernike, J. W. Douglas, and D. R. Olson, "Transmission Measurements in Optical Waveguides Produced by Proton Irradiation of Fused Silica," Journal of the Optical Society of America, **61**, 678 (1971).
- [40] H. P. Weber, F. A. Dunn, and W. N. Leibolt, "Loss Measurements in Thin-Film Optical Waveguides," Applied Optics, **12**, 755-757 (1973).
- [41] A. Boudrioua, and J. C. Loulergue, "New approach for loss measurements in optical planar waveguides," Optics Communications, **137**, 37-40 (1997).
- [42] J. Wei, X.-F. Xu, Y. Ding, Z.-H. Kang, Y. Jiang, and J.-Y. Gao, "Improved method for loss measurements in planar waveguides," Optics and Lasers in Engineering, **45**, 419-422 (2007).
- [43] S. Brulisauer, D. Fluck, C. Solcia, T. Pliska, and P. Gunter, "Nondestructive Wave-Guide Loss-Measurement Method Using Self-Pumped Phase-Conjugation for Optimum End-Fire Coupling," Optics Letters, **20**, 1773-1775 (1995).
- [44] M. Weisser, F. Thoma, B. Menges, U. Langbein, and S. Mittler-Neher, "Fluorescence in ion exchanged BK7 glass slab waveguides and its use for scattering free loss measurements," Optics Communications, **153**, 27-31 (1998).
- [45] A. Kahn, Y. Kuzminykh, H. Scheife, and G. Huber, "Nondestructive measurement of the propagation losses in active planar waveguides," Journal of the Optical Society of America B-Optical Physics, **24**, 1571-1574 (2007).
- [46] S. W. Chen, Q. F. Yan, Q. Y. Xu, Z. C. Fan, and J. W. Liu, "Optical waveguide propagation loss measurement using multiple reflections method," Optics Communications, **256**, 68-72 (2005).
- [47] Y. Okamura, S. Yoshinaka, and S. Yamamoto, "Measuring Mode Propagation Losses of Integrated Optical-Waveguides - a Simple Method," Applied Optics, **22**, 3892-3894 (1983).

- [48] S. Dutta, H. E. Jackson, J. T. Boyd, R. L. Davis, and F. S. Hickernell, "Co<sub>2</sub>-Laser Annealing of Si<sub>3</sub>N<sub>4</sub>, Nb<sub>2</sub>O<sub>5</sub>, and Ta<sub>2</sub>O<sub>5</sub> Thin-Film Optical-Waveguides to Achieve Scattering Loss Reduction," *IEEE Journal of Quantum Electronics*, **18**, 800-806 (1982).
- [49] F. T. Wang, F. H. Liu, G. K. Chang, and A. Adibi, "Precision measurements for propagation properties of high-definition polymer waveguides by imaging of scattered light," *Optical Engineering*, **47**, 024602 (2008).
- [50] R. Regener, and W. Sohler, "Loss in Low-Finesse Ti-Linbo<sub>3</sub> Optical Wave-Guide Resonators," *Applied Physics B-Photophysics and Laser Chemistry*, **36**, 143-147 (1985).
- [51] R. G. Walker, "Simple and Accurate Loss Measurement Technique for Semiconductor Optical Wave-Guides," *Electronics Letters*, **21**, 581-583 (1985).
- [52] M. Gaidi, L. Stafford, J. Margot, M. Chaker, R. Morandotti, and M. Kulishov, "Microfabricated SrTiO<sub>3</sub> ridge waveguides," *Applied Physics Letters*, **86**, 221106 (2005).
- [53] C. S. Seibert, D. C. Hall, D. Liang, and Z. A. Shellenbarger, "Reduction of AlGaAs Heterostructure High-Index-Contrast Ridge Waveguide Scattering Loss by Sidewall Smoothing Through Oxygen-Enhanced Wet Thermal Oxidation," *IEEE Photonics Technology Letters*, **22**, 18-20 (2010).
- [54] C. Fabry, and A. Perot, "Sur les franges des lames minces argentées et leur application a la mesure de petites épaisseurs d'air," *Ann. Chim. Phys.*, **12**, 459 (1897).
- [55] A. Stolz, E. Cho, E. Dogheche, Y. Androussi, D. Troadec, D. Pavlidis, and D. Decoster, "Optical waveguide loss minimized into gallium nitride based structures grown by metal organic vapor phase epitaxy," *Applied Physics Letters*, **98**, (2011).
- [56] R. Geiss, A. Chowdhury, C. M. Staus, H. M. Ng, S. S. Park, and J. Y. Han, "Low loss GaN at 1550 nm," *Applied Physics Letters*, **87**, 132107 (2005).
- [57] A. Papp, and H. Harms, "Polarization Optics of Index-Gradient Optical-Waveguide Fibers," *Applied Optics*, **14**, 2406-2411 (1975).
- [58] M. Szczurowski, W. Urbanczyk, M. Napiorkowski, P. Hlubina, U. Hollenbach, H. Sieber, and J. Mohr, "Differential Rayleigh scattering method for measurement of polarization and intermodal beat length in optical waveguides and fibers," *Applied Optics*, **50**, 2594-2600 (2011).
- [59] H. Fearn, and R. Loudon, "Theory of 2-Photon Interference," *Journal of the Optical Society of America B-Optical Physics*, **6**, 917-927 (1989).
- [60] C. K. Hong, Z. Y. Ou, and L. Mandel, "Measurement of Subpicosecond Time Intervals between 2 Photons by Interference," *Physical Review Letters*, **59**, 2044-2046 (1987).
- [61] H. Dautet, P. Deschamps, B. Dion, A. D. Macgregor, D. Macsween, R. J. McIntyre, C. Trottier, and P. P. Webb, "Photon-Counting Techniques with Silicon Avalanche Photodiodes," *Applied Optics*, **32**, 3894-3900 (1993).
- [62] J. Shao, and D. Tu, "The Jackknife and Bootstrap" (Springer, 1995).
- [63] G. D. Marshall, A. Politi, J. C. F. Matthews, P. Dekker, M. Ams, M. J. Withford, and J. L. O'Brien, "Laser written waveguide photonic quantum circuits," *Optics Express*, **17**, 12546-12554 (2009).
- [64] L. Sansoni, F. Sciarrino, G. Vallone, P. Mataloni, A. Crespi, R. Ramponi, and R. Osellame, "Polarization Entangled State Measurement on a Chip," *Physical Review Letters*, **105**, 200503 (2010).
- [65] B. J. Smith, D. Kundys, N. Thomas-Peter, P. G. R. Smith, and I. A. Walmsley, "Phase-controlled integrated photonic quantum circuits," *Optics Express*, **17**, 13516-13525 (2009).

# Chapter 5

## Guiding and Laser Operation in KYbW

---

### Abstract

This chapter presents guiding and laser operation experimental work using the stoichiometric crystal  $\text{KYb}(\text{WO}_4)_2$ , referred to as KYbW. Mechanisms of optically induced refractive index change and their guiding effects are introduced. Optically-induced guiding at 633 nm is performed allowing calculation of refractive index change from the electronic and thermal contributions. The results of quasi-continuous-wave laser operation are presented with analysis of the power transfers, mode profiles, cavity stability and thermal effects.

### Preliminaries

Some of the work presented in this chapter has been presented at the Europhoton 2010 and ECIO 2012 conferences [1, 2]. The motivation and background to this work is detailed in Chapter 1. In this work only trivalent ytterbium ions are used, typically referred to as  $\text{Yb}^{3+}$ , and for convenience are simply referred to as Yb.

### 5.1 Optically-induced guiding effects

The absorption of light in a dielectric material can create guiding or anti-guiding effects through either changes in refractive index or the introduction of gain. The change in refractive index has a range of origins including thermal, electronic and elastic, the introduction of gain can create effects analogous to a change in refractive index. These guiding effects can be used to create a waveguide without fabrication, where the guiding properties are purely defined by the pump beam. The inclusion of these guiding effects within a laser cavity can change a range of laser characteristics such as threshold, stability and cavity profiles. It is important to consider the origin of various guiding effects to understand the significance of their contribution. This section does not attempt to be a complete review of the topic and further reading can be found in Boyd [3] and the following references within this section. In this thesis, a distinction is made between guiding and a waveguide: a waveguide must offer a mode volume smaller than that offered by diffraction for a length longer than the Rayleigh range. A

guiding effect may offer lens-like properties and change the profile of a beam for a short length, and may not offer the same amount of confinement as a waveguide.

### 5.1.1 Gain guiding

Gain guiding [4-6] and aperture guiding [7] describe the effects of gain and/or loss in shaping beam profiles, usually within laser cavities. These guiding characteristics have been observed in amplifiers [8] and in laser cavities including in fibre lasers [9, 10], disk lasers [11] and diodes that rely on the gain to form the cavity [12]. In practice, all of these systems will also observe a refractive index change due to absorption following a Kramers–Kronig relationship: this is referred to as the electronic guiding mechanism and discussed in 5.1.3. In this work, a distinction is made between these guiding mechanisms. Purely gain-related guiding effects can be used in a laser cavity to compensate for diffraction losses and/or change the stability regions.

Gain and aperture guiding are effects that describe a system with on-axis/within-core gain or off-axis/outside-core loss. Gain guiding describes a system where gain is used to increase light intensity within a specific core region relative to the surroundings. Aperture guiding describes a system where loss is used to remove intensity outside a specific core region. Aperture guiding is usually considered as a type of gain guiding.

Gain guiding does not prevent diffraction of light like a typical waveguide, but may compensate for diffractive loss. Light which spreads beyond the core region weakens relative to the core such that only light within the core region remains. In the case of gain guiding, the power within the core region may increase dramatically during propagation. In the case of pure aperture guiding the core region may experience large attenuation as the diffracted light is removed from the system.

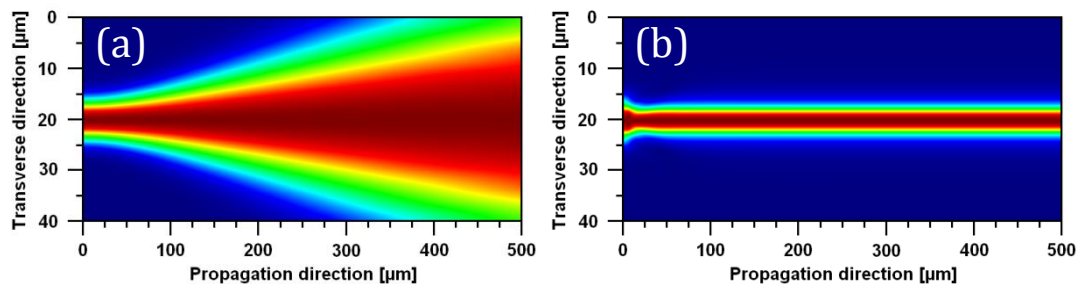


Figure 5. 1: Field amplitude from BPM simulations in air ( $n=1$ ).  $16\ \mu\text{m}$  wide circular Gaussian profile  $633\ \text{nm}$  light was launched into **(a)** free-space with a constant loss coefficient of  $50/\text{cm}$  throughout the simulation region and **(b)** a  $10\ \mu\text{m}$  wide circular core section with a reduced loss of  $0.5/\text{cm}$  surrounded by a higher loss coefficient of  $50/\text{cm}$ . Amplitude has been normalised along the propagation direction. There was no real refractive index variation in either simulation.

## Chapter 5 – Guiding and Laser Operation in KYbW

Beam propagation method (BPM) simulations were carried out for illustrative purposes to demonstrate the guiding-effects of variable gain/loss. Figure 5. 1 a) shows the propagation of light with equal transverse loss; the spread of the light can be described by Gaussian propagation equations. Figure 5. 1 b) shows propagation of light with reduced loss in a core region. Light that diffracts out of this region experiences larger loss, thus the remaining light in the core region appears as if it were guided.

Pure gain guiding can be observed in a 4-level system where there is no significant reabsorption loss at the signal/laser wavelength. A combination of gain and aperture guiding can be observed in most 3-level laser systems due to significant reabsorption the signal/laser wavelength. Within an unstable cavity, the gain-guiding effect can be used to compensate for diffraction losses; extending the operation range of the laser. This gain-guiding effect can be used to create laser operation in a plane-plane mirror cavity such as in some broad-area lasers [12].

Gain/population gratings are well-known dynamic structures that rely on the guiding effects of gain to shape beams. They find applications in fibre waveguides [13] and bulk systems such as self-conjugation in laser cavities [14]. Many of these gratings, however, also rely on the electronic refractive index change that accompanies the gain in order to operate; this is described in section 5.1.3.

### 5.1.2 Thermal guiding

The absorption of light produces heat due to the generation of acoustic and optical phonons: vibration of the lattice structure. Phonons are produced as the excited ions decay non-radiatively as part of the relaxation process that usually involves the generation of a lower energy photon. This heating produces three separate guiding effects: a direct change in refractive index through the thermo-optic effect, thermally induced mechanical stress and then refractive index change through the photoelastic effect, and deformation/bulging of crystal surfaces due to expansion, creating a lens-like structures.

The thermal guiding effect may act like a lens depending on the pump geometry and this is known as thermal lensing. Thermal lensing is well documented for high power lasers [15, 16] and most high power CW lasers involve thermal management [17, 18] in order to allow for laser operation without compensating the cavity for the lensing effects.

Thermal refractive index changes have been shown to play an important role in active waveguides. Thermal effects have been shown to dominate over fabricated refractive index changes in some fibres [19], waveguide lasers [20] and waveguide amplifiers [21]. However, it should be noted that in many of these cases no consideration was given to other components of refractive index change or gain-guiding.

The strength of thermal guiding strongly depends on the heat extraction from the pump region. This is defined by the pump geometry, the thermal conductivity and the heat capacity of the crystal. Even at low pump powers with a high heat extraction rate, thermal guiding will occur due to the change in temperature between the pump and non-pumped regions. As the heat generation rate begins to approach the efficient heat extraction rate, further build up in local and average temperature acts to greatly change the nature of the thermal guiding.

### 5.1.3 Electronic guiding

The refractive index of an optically-pumped material undergoes a refractive index change that does not relate to thermal causes [22-24]. As the optically active ions are excited through absorption of photons, the electrons are redistributed causing a direct change in refractive index. This change in electron distribution can be quantified by an optical polarisability which is characterised by a real third-order optical susceptibility. This causes a nonlinear refractive index which follows a Kramers-Kronig relationship [25].

This redistribution of charge also creates electrostriction – mechanical stress induced by the redistribution of charge. This mechanical stress can act to further change the refractive index through the photo-elastic effect. It has been calculated that as much as 19% of the electronic refractive index change can be attributed to this effect in fibres [26, 27]. Stimulated Raman scattering also relies on a high optical polarisability of molecules. It has been shown [28] that the Raman susceptibility can contribute 15% to the electronic refractive index change, however in practice could vary hugely and the contribution is poorly documented.

The optical Kerr effect [29] describes the change in refractive index by an applied optical intensity. The optical Kerr effect by definition does not specify the cause of the refractive index change, but in the literature is typically used to refer to the electronic

index change. The optical Kerr effect finds application in Kerr lens mode-locking [30] for which the electronic index change is required for fast modulation of the refractive index. Kerr lensing is typically used to describe self-lensing properties but the refractive index is changed for a range of wavelengths and has the possibility to guide other beams.

The contribution of the electronic component of refractive index to the overall refractive index change by optical absorption is well documented [3, 23, 31-33], and has been shown recently to dominate over thermal effects in certain materials [33]. As many authors refer to this index change as either Kerr lensing or gain-guiding it is often hard to pinpoint from the literature the precise contribution.

### 5.1.4 Guiding effects in KYbW

There are currently no published reports, known to the author, of optical guiding in KYbW. Furthermore, there are no known reports that document optically-induced refractive index changes in KYbW. However, there are a large number of reported material properties that indicate optically-induced guiding effects could be very strong. KYbW is stoichiometric and as such, all optical properties are enhanced due to the large density of Yb ions.

Yb in KYbW offers intrinsically high absorption and emission cross-sections. These are at least 10 times larger than in YbAG or YbVO<sub>4</sub> as compared in chapter 1. This offers the possibility for high gain under appropriate pumping conditions and crystal orientation. As a consequence, gain guiding is expected to be particularly prevalent. Aperture guiding will further enhance the gain guiding effect as the 3-level system has high absorption for a range of signal/laser wavelengths when not optically pumped. Optical absorption coefficients are as high as 6 cm<sup>-1</sup> at the laser wavelength of 1040 nm creating a single-pass loss through a 4 mm sample of 90%. The effects of gain and absorption at 1040 nm are compared to Nd:YAG in Table 5. 2.

The thermal guiding properties of Yb:KYW and other double-tungstates are poorly documented with many conflicting measurements in the literature [34-36]. Most recently [37] the thermo-optical coefficients have been confirmed in Yb:KYW to be strongly negative for a large range of wavelengths. This produces an anti-guiding effect with increasing temperature. It is not clear what contribution the photo-elastic tensors play in thermal refractive index changes in Yb:KYW and recently high acousto-optic

## Chapter 5 – Guiding and Laser Operation in KYbW

coupling efficiencies suggest it may be considerable [38]. Some of the material properties that contribute to thermal (anti)guiding are shown in Table 5. 1.

Table 5. 1: Approximated comparison of thermal properties of KYbW with typical laser crystals.

Property	Nd:YAG [39]	Ti:Sapphire [39]	KYbW [37]
Quantum defect	0.75 (800/1064)	0.67 (532/800)	0.94 (980/1040)
Thermal conductivity [W/mK]	12	33	3.5
dN/dT [ $\mu\text{K}^{-1}$ ]	8	13	-10
Young's modulus [GPa]	280	335	150

The quantum defect can be particularly low for KYbW laser systems and so the heat generation may be lower than other systems such as Nd:YAG/Ti:Sapphire. The thermal conductivity is average/poor which may act to counter any benefit of a reduced quantum defect at high powers unless heat-extractors are used. The Young's modulus is low, suggesting that there could be significant crystal deformation with temperature leading to bulging/lensing effects. A thermal guide factor is defined to allow comparison between the materials:

$$\text{Thermal guide factor} = \frac{dN}{dT} \frac{1}{\text{quantum defect} \times \text{thermal conductivity}} \quad (4.15)$$

This term is calculated for Nd:YAG and KYbW in Table 5. 2. It may be multiplied by the density of Yb ions, as the Yb ions are the source of heat during optical pumping.

The electronic refractive index change due to optical pumping can be determined from the optical polarisability. The optical polarisability has been determined by measurement of refractive index changes of  $2 \times 10^{-5}$  in 20% doped Yb:KYW using optically induced gratings [33]. It is found to be five times stronger in Yb:KYW than in Yb:YAG [33]. The electronic effect has shown to be more significant than thermal guiding under certain pumping geometries [24]. The high optical polarisability of Yb:KYW is due to the high cross-sections and high Raman susceptibility of KYW [40] which can be a significant contributor. The real refractive index change,  $\Delta n$ , can be calculated using [24]:

$$\Delta n = 2\pi \left( \frac{n_0^2 + 2}{3n_0} \right) \Delta p \Delta N \quad (4.16)$$

## Chapter 5 – Guiding and Laser Operation in KYbW

Where  $n_0$  is the initial refractive index,  $\Delta p$  is the polarisability and  $\Delta N$  is the change in population of the upper level ( ${}^2F_{5/2}$  for KYbW at 1040 nm). Assuming KYbW has the same optical polarisability as KYW,  $\Delta p = 8.2 \times 10^{-26} \text{ cm}^{-3}$ , and 50% of the ions are in the upper state,  $\Delta N = 3.2 \times 10^{21} \text{ cm}^{-3}$ , a refractive index change of  $1.6 \times 10^{-3}$  is possible. With this high refractive index change it is possible to confine light to <10 micrometre sized waveguides. The electronic guiding effect has been used to demonstrate highly efficient Kerr-lens mode-locking laser systems in Yb:KYW [41, 42]. The electronic refractive index change is compared to Nd:YAG in Table 5. 2.

The most important contribution to strong optically-induced guiding arises from the very high Yb concentration in KYbW of  $6.4 \times 10^{21} \text{ cm}^{-3}$ . This is much higher than typical laser crystals. For numerical comparison 1% doped Nd:YAG, a typical crystal for high power lasers, is considered in Table 5. 2. The high Yb concentration acts to enhance each guiding mechanism.

Table 5. 2: Material properties of KYbW that enhance guiding compared to Nd:YAG.

Guiding type	Property	Nd:YAG (1%)	KYbW (100%)
		At 1064 nm	At 1040 nm
Gain	Em. Cross-section [ $\times 10^{-20} \text{ cm}^2$ ]	[39] 28	[43] 0.15
	Laser gain [ $\text{cm}^{-1}$ ]	38	60
Aperture	Abs. cross-section [ $\times 10^{-20} \text{ cm}^2$ ]	0	[43] 0.15
	Laser absorption [ $\text{cm}^{-1}$ ]	0	6
Thermal	Thermal guide factor [ $\times 10^{-9} \text{ W}^{-1}$ ]	[39] 0.9	[37] -3
	guide factor $\times$ density [ $\times 10^{11} \text{ cm}^{-3}$ ]	1.2	-190
Electronic	Polarisability [ $\times 10^{-26} \text{ cm}^3$ ]	[24] 3.5	[33] 8.2
	polarisability $\times$ density [ $\times 10^{-6}$ ]	4.7	525

All guiding factors are significantly higher in KYbW compared to 1% Nd:YAG. Both the thermal and electronic guiding mechanisms are  $\sim 100$  times larger at the laser wavelength. Gain and aperture guiding would be enhanced significantly if the KYbW laser wavelength was at 980 nm where peak absorption and emission cross-sections occur, roughly 100 times larger than at 1040 nm.

## 5.2 Gain-free guiding at 633 nm

It is interesting to remove the effects of gain and aperture guiding in order to estimate the refractive index change by optical absorption. Both the thermal and electronic contribution to index change can be calculated away from the laser wavelength. It has been shown that electronic refractive index change mechanisms in Yb:KYW occur for wavelengths far from peak absorption in the visible regime where KYbW is transparent [33]. It has been identified that the polarisability change is due to excited state absorption bands from 200-300 nm and the wavelength dependence of the polarisability can be predicted [44]. The electronic refractive index change has been calculated from a spectroscopic relationship to be the same at 1040 nm as at 633 nm [44]. The thermo-optic coefficients in Yb:KYW have been determined at both 633 nm and at 1064 nm and the thermal effects are estimated to be 10% larger at 1064 nm [37]. The thermal and electronic guiding mechanisms at laser wavelengths can thus be estimated from guiding at 633 nm through use of a He-Ne laser. If this refractive index is large enough and positive, a transient waveguide can be formed by optical pumping.

### 5.2.1 Experimental setup

A 4×4.5×5 mm<sup>3</sup> KYbW crystal was cut to the optical axes  $N_m$ ,  $N_p$  and  $N_g$  as defined in reference [43]. The optical axes are shown in relation to the crystallographic axes in Chapter 1. The crystal was orientated such that it could be pumped along the  $N_p$ -axis with the E-field parallel to the  $N_m$  axis for maximum absorption. The sample was mounted on a copper pillar that allowed for adequate heat extraction for the minimal average pump powers used in this work without the use of water cooling. Three faces of the crystal could be easily accessed with the mounting arrangement to allow pumping in one face and probing and collection from perpendicular faces. The experimental setup for side pumping and a photograph is shown in Figure 5. 2.

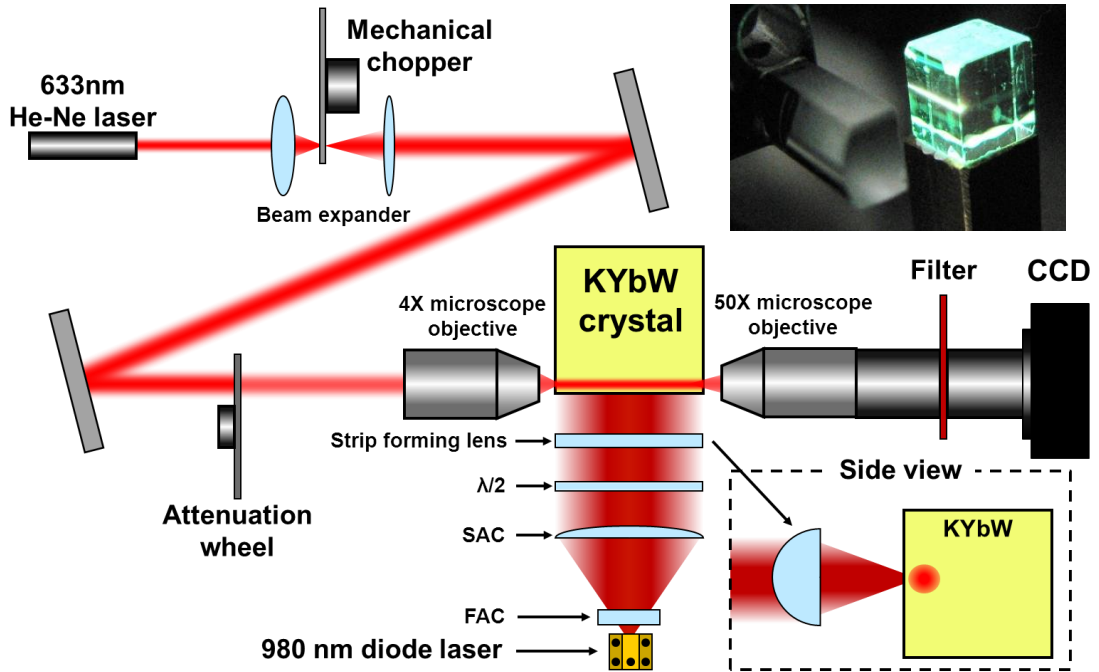


Figure 5. 2: Schematic of the experimental setup used to establish and probe a pump induced waveguide in KYbW. The waveguide forming system uses a fast-axis collimator (FAC) a slow-axis collimator (SAC) a half-wave plate ( $\lambda/2$ ) and a strip forming lens. **(bottom right)** A side view schematic of the strip forming lens and crystal which is positioned at the focus. **(top right)** A photograph of the strip forming lens and crystal during pumping.

A 981 nm single-emitter diode laser was used to provide up to 10 W optical power at the maximum absorption peak. The pump optics are shown separately in Figure 5. 3. Diode laser light was collimated vertically with a fast-axis collimator with an effective focal length of 0.91 mm. Slow-axis collimation was achieved with a cylindrical lens with focal length 30 mm. Through use of a 980 nm half-wave plate the polarisation was rotated to offer maximum absorption. The diode laser was temperature tuned in order to ensure the wavelength was maintained at 981 nm even during low average power operation. Laser light was then focussed to a strip through use of a cylindrical lens of focal length 5 mm which can be seen inset in Figure 5. 2 (photograph top right and schematic bottom right). The pump profile on the crystal surface was chosen to occupy the full 4 mm length of the crystal with a fraction ( $\sim 10\%$ ) of the power clipped to provide a near constant pump power long the length of the strip.

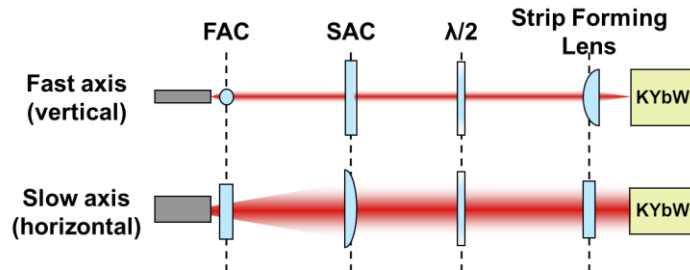


Figure 5. 3: Schematic of direct-diode pump system. Components include a fast-axis collimator (FAC), slow-axis collimator (SAC), half-wave plate ( $\lambda/2$ ) and a strip forming lens.

The output spectrum of the diode was compared to published measurements of the absorption data of KYbW and is shown in Figure 5. 4 a). It should be noted that the diode lasers used as part of this work output a broad output spectrum in cw and pulsed operation which is not ideal for this work. The diode lasers do however offer a large output power for a single emitter which is necessary for the high Yb density in the crystal. A Lorentzian fit was found to be appropriate for the absorption peak at 981 nm. Absorption at 981 nm for  $E$  parallel to  $N_m$  is  $747 \text{ cm}^{-1}$  and for  $E$  parallel to  $N_g$  is  $107 \text{ cm}^{-1}$ . The peak absorption wavelength of KYbW was measured elsewhere to be 980.8nm however the spectral resolution of these measurements mean it may lie anywhere from 980-982 nm [43]. The fitted Lorentzian width was found to be 1.8 nm, providing a narrow absorption band which is typically much smaller than the diode output spectrum.

The absorption length of the diode laser output was estimated by comparing the spectrum to absorption data. The diode spectral output was subdivided into 0.03 nm sections each of which observed a different absorption rate according to the wavelength. This provided 833 different absorption coefficients ranging from 55 to

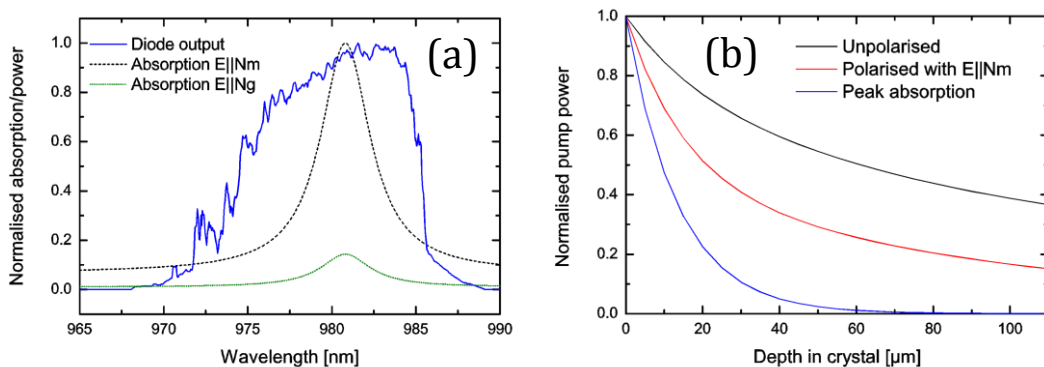


Figure 5. 4: **(a)** The spectrum of the diode output compared to a Lorentzian fit to the absorption peak at 981 nm in KYbW for the  $N_m$  and  $N_g$  optical axis from [42] and shown in Chapter 1. **(b)** Pump power vs. propagation distance in the crystal. The high absorption in KYbW acts to absorb the pump in a short micrometre distance.

$747\text{cm}^{-1}$  for  $E||N_m$  and  $8$  to  $107\text{cm}^{-1}$  for  $E||N_g$ . The results as shown in Figure 5. 4 b) indicate an effective absorption depth of  $35\ \mu\text{m}$  for diode output with  $E||N_m$ , and  $110\ \mu\text{m}$  for polarisation-unaligned diode output (50% for each  $N_m/N_g$ ). Shown for comparison is the  $13.3\ \mu\text{m}$  absorption depth at a wavelength of  $980.8\ \text{nm}$  with  $E||N_m$ .

### 5.2.2 Guided mode analysis

The Yb luminescence  $>1000\ \text{nm}$  due to  $981\ \text{nm}$  optical pumping was measured from the crystal face perpendicular to the pumping face. This luminescence was most intense near the pumping face, due to the short absorption length in KYbW. Imaging was achieved with a  $50\times$  long working distance objective and a CCD camera in the position shown in Figure 5. 2. A long-pass  $1000\ \text{nm}$  filter was used to remove scattered pump light. To correctly profile the luminescence, the length of the pump strip was reduced such that only a small region near the imaging face was pumped. This ensured the measured luminescence originated from the imaging plane. The measurement of the luminescence is shown in Figure 5. 6 a).

This luminescence profile can be considered to describe the electronic refractive index change profile. The luminescence results from a spontaneous photon emission and thus is representative of the change in upper state population as described in Section 5.1.4. The thermal index change is also essentially proportional to the luminescence, as the thermal load is due to phonon generation in the relaxation process involved in spontaneous emission.

The crystal was observed to luminesce green light as well as infrared light which is a well-known effect of up-conversion and resonant energy transfer to erbium impurity ions. This effect is noticeable for high density Yb systems and adds parasitic loss to the system [45]. This luminescence is visible in the photograph in Figure 5. 2.

A He-Ne laser was used to probe the pumped region, perpendicular to the pump direction. Using a beam expander and a  $4\times$  microscope objective the output of the He-Ne laser was tailored to have a focus spot which overlaps with the pumped region of the crystal with a full width half maximum of  $16\ \mu\text{m}$ . The input coupling objective was mounted on an xyz-translation stage and the beam-steering mirrors allowed for coupling optimisation.

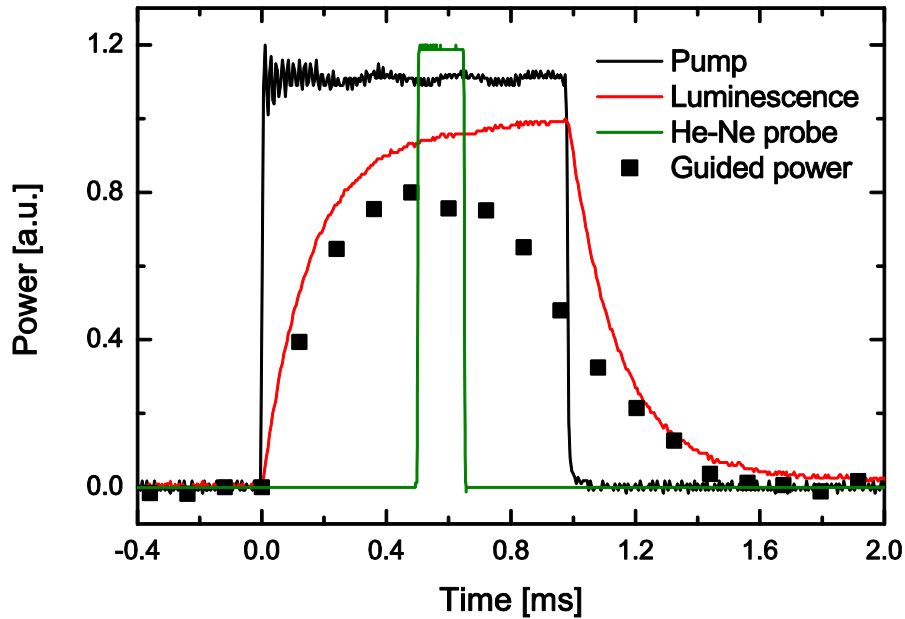


Figure 5. 5: The temporal characteristics of the pump probe system. Measurements were made with a detector collecting light transverse to the pump direction in the position of the CCD shown in Figure 5. 2. Data has been normalised to offset values to allow good visibility. The guided power was measured by temporally offsetting the He-Ne pulse with respect to the pump pulse. The guided power is maximum when the He-Ne probe is shown in the position in the Figure.

The pump diode laser was operated quasi-continuous-wave with pulse durations longer than the lifetime of Yb in KYbW and a low duty cycle to prevent significant thermal load. Pump pulsing was achieved with an electrical driver offering pulse lengths from 1 ms to 2.5 ms and variable duty cycle. For mode analysis, the He-Ne was also operated pulsed using a mechanical chopper with a duty cycle of 1.5% creating a He-Ne pulse of 150  $\mu$ s at 100 Hz. By using a delay and trigger system, the pump diode laser was temporally locked to the mechanical chopper such that the He-Ne pulse arrived at the crystal after formation of the waveguide and before removal of the diode laser pulse. Timing jitter between the pulses was negligible in comparison to the length of the pulses and was most accurate when triggering the diode laser from the mechanical chopper.

Typical temporal characteristics are shown in Figure 5. 5. The detector used was a Thorlabs PDA10CS-EC InGaAs detector and has a 20.6 ns rise time which is considered negligible for the luminescence decays measured as part of this work. The He-Ne probe pulse was delayed with respect to the pump pulse in order to observe the maximum guiding effect. The guiding effect was observed to be maximum after 480  $\mu$ s of pumping, as shown with the points in Figure 5. 5. This is consistent with the lifetime of

Yb in KYbW which will not create significant upper-level populations within the lifetime and will reach a steady-state after continuous pumping.

He-Ne probing resulted in observable guiding along the strip caused by an increase in refractive index as no gain is available at this wavelength. The guided mode profile was measured with the CCD camera. Appropriate long- and low-pass filters were used to ensure only He-Ne light arrived at the camera. This measurement is shown in Figure 5. 6 b). Coupling into the waveguide was optimised by observing this guided mode profile and increasing its intensity by altering the coupling position and the temporal position of the pump/probe system. In order to confirm that the unguided He-Ne light diffracts beyond pumped region, the unguided light was measured by removing the pump and is shown in Figure 5. 6 c).

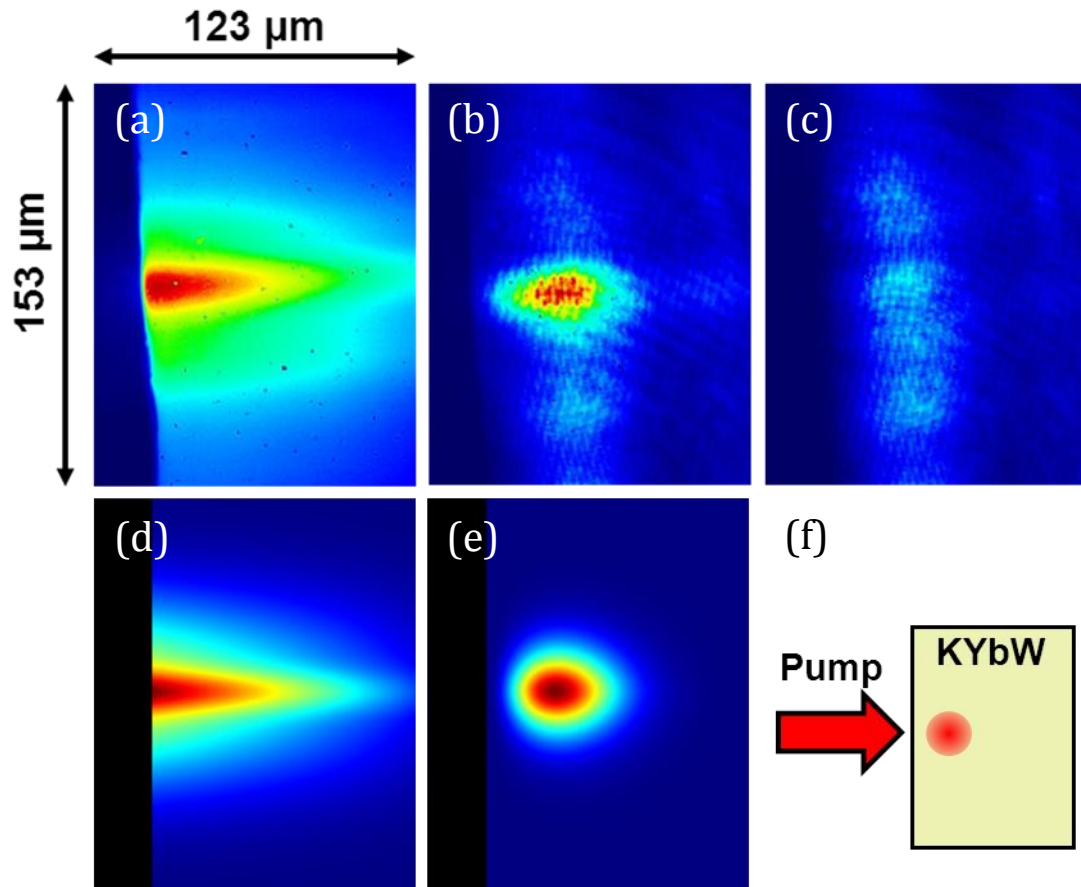


Figure 5. 6: **(a)** >1000 nm luminescence measured with a long pass filter. **(b)** Measured guided He-Ne light with a 660 nm low-pass filter to remove pump and luminescence and 600 nm long-pass filter to remove green luminescence. **(c)** The same setup as b) without pumping. **(d)** FEM simulated refractive index profile selected to match a). **(e)** FEM simulated guided mode profile selected to match b) based on the refractive index profile shown in d). **(f)** Schematic showing pump direction and crystal used in a)-e). The waveguide propagation direction is out of the page.

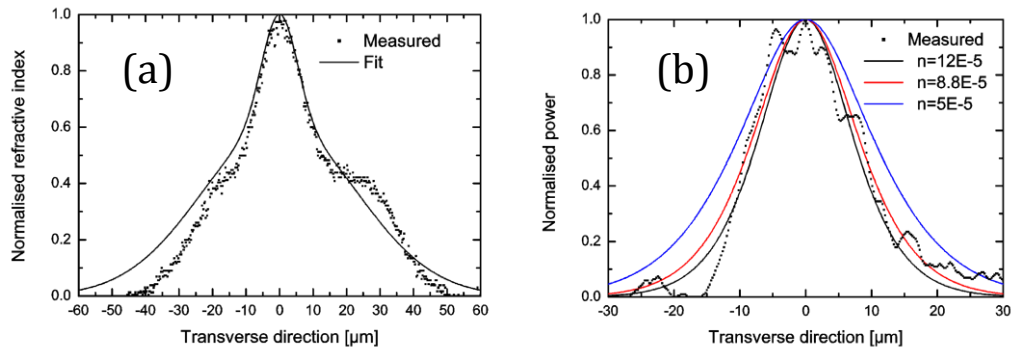


Figure 5. 7: Cross-section across the waveguide (the vertical direction in Figure 5. 6); **(a)** Refractive index 10µm from the crystal surface. Points show measured data from Figure 5. 6 a). Black line shows the approximated fit of two Gaussians used to determine the refractive index profile shown in Figure 5. 6 d). **(b)** Guided mode profile at maximum width. Points show measured data from Figure 5. 6 b). Lines show three FEM simulation results for different peak refractive index changes. Red is shown in Figure 5. 6 e).

In order to estimate the refractive index change required to produce the measured guided mode profile, a reverse FEM analysis method was used. This is a simple and well-established technique for estimating the refractive index change of waveguides [46].

A 2D refractive index profile was selected that matched the measured luminescence in Figure 5. 6 a) by Gaussian fitting across the guide and exponential fitting in the pump direction. The approximated refractive index profile is shown for a cross-section across the guide, 10 µm from the crystal edge in Figure 5. 7 a). The full colour-coded 2D fit is shown in Figure 5. 6 d).

FEM analysis was performed at a wavelength of 633 nm, a KYbW refractive index of 2 and an air index of 1. The FWHM of the guided mode, across the waveguide, was measured to be  $16 \pm 2$  µm using a Gaussian approximation fit and the measured data is shown in Figure 5. 7 b). The peak refractive index was adjusted until the FEM calculated guided mode profile matched the measured one. The results of three simulations for different peak refractive indices are shown in Figure 5. 7 b). The full 2D plot of the FEM simulated guided mode is shown in Figure 5. 6 e) and is intended to match Figure 5. 6 b).

The peak refractive index change found to match the mode profiles was  $\Delta n = 8.8 \pm 3.2 \times 10^{-5}$ . This value of refractive index change is low for typical waveguides which have cross-sections below 10 µm, as such dimensions require higher refractive index changes.  $10^{-5}$ - $10^{-4}$  refractive index changes are suitable for >10 µm waveguide

confinement which can still offer considerable advantages to many waveguide laser systems.

The large error in this result is due to the mode width having a small sensitivity to the refractive index change, because the guided mode sits well confined in the pumped region. The measured mode profile was of particularly poor quality due to the two filters required to block crystal luminescence. An improvement in the filter selection may reduce the error significantly. Improvements to the measurement technique and algorithm may also reduce the error [47]. Alternative techniques may be more suitable to measure this low refractive index change. This includes techniques associated with measuring thermal lensing effects in lasers, including classical interferometry, shearing-interferometry or wavefront sensing [16].

The positive refractive index change is measured to be roughly 4 times higher than that measured in 20% doped Yb:KYW using an alternative grating measurement technique [33]. A further increase in refractive index change is expected for smaller strip widths of the pump due to higher upper-state populations for higher pump intensities. In particular, the sidelobes of the strip act to reduce the potential for light confinement and are due to poor pump optics selection. A four-lens pumping scheme should offer a reduced strip-width in comparison to the current two-lens scheme.

### 5.2.3 Time-resolved guiding analysis

By monitoring the power exiting the waveguide, during pump pulsing, it is possible to ascertain the transient behaviour of the waveguide. This transient analysis may be used to calculate the contribution from electronic and thermal components of refractive index change.

Time-resolved analysis was carried out by modifying the experimental setup shown in Figure 5. 2. The mechanical chopper was removed such that He-Ne probe light was always illuminating the crystal whilst the pump power and therefore the induced waveguide was continually modulated. As a consequence, He-Ne light was only guided when the waveguide was established. The waveguide output power was monitored by replacing the CCD with a detector that captures light from the waveguide core (pumped) region of the crystal by spatially filtering the unguided diffracted light using an aperture. Appropriate low- and long-pass filters were used to block the scattered

pump and the green and infrared luminescence from the crystal. This is shown with the simplified schematic in Figure 5. 8 a).

The coupling objective was replaced with a 10X objective such that the power within the waveguide could be related to the refractive index of the waveguide. As the weak waveguide had a particularly small acceptance cone, only a small fraction of the coupled light was guided. Similarly weak waveguides have a known relationship between the power within the core (pumped) region and the power in the cladding (unpumped) region. BPM simulations were carried out to confirm this relationship for a waveguide with properties similar to that measured in section 5.2.2 and are shown in Figure 5. 8 b). This relationship is shown to be linear for a large range of refractive index changes, similar to that measured in 5.2.2. This linear relationship allows for calculation of the temporal characteristics of the refractive index change.

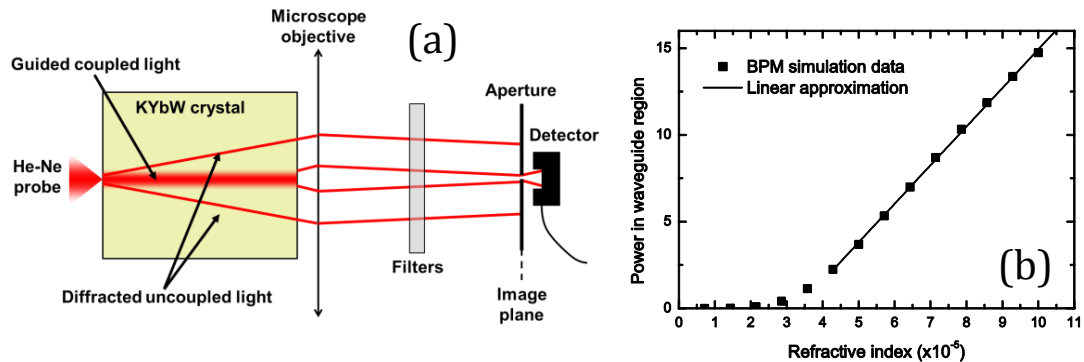


Figure 5. 8 **(a)** Schematic of the crystal and collection optics used for time-resolved analysis. **(b)** BPM simulation showing power in core region of a 15  $\mu\text{m}$  wide circular waveguide for 4- $\mu\text{m}$ -wide Gaussian coupling and varying refractive index changes at a wavelength of 633 nm. Fitted line is a linear approximation – only valid for a range of refractive index changes.

The power in the waveguide core region was monitored as the pump pulse was removed from the crystal. At this time the waveguide slowly ceased to exist and the He-Ne light was no longer guided. The removal of the pump pulse was considered to be instantaneous due to the much shorter timescales of the diode response than the Yb lifetime, as shown in Figure 5. 5.

In a similar method to that used for gratings [33], the refractive index change can be considered to be described by two transient properties: the electronic lifetime,  $\tau_e$ , and the thermal lifetime,  $\tau_T$ . Each will have a particular weighting factor,  $\eta$ , defining the contribution of each guiding mechanism to the refractive index change. The power in the waveguide after removal of the pump can then be approximated by:

$$\Delta n \propto \text{power in waveguide}$$

$$\Delta n \propto \eta_e \exp\left[-\frac{t}{\tau_e}\right] + \eta_T \exp\left[-\frac{t}{\tau_T}\right] \quad (4.17)$$

The measured decay vs. time of the guided He-Ne power is shown in Figure 5. 9. Equation (4.17) was fitted to the top 90% of the power levels, below which the linear approximation is not considered valid according to Figure 5. 8 b). The least-squares fit was carried out for the dataset shown in Figure 5. 9 b). A single exponential decay was also applied to the latter slower part of the decay, this agreed with the second part of the double exponential fit. In logarithm form the deviation from a single exponential fit at the beginning of the decay (after removal of the pump) can be clearly seen. The fit parameters are shown in Table 5. 3.

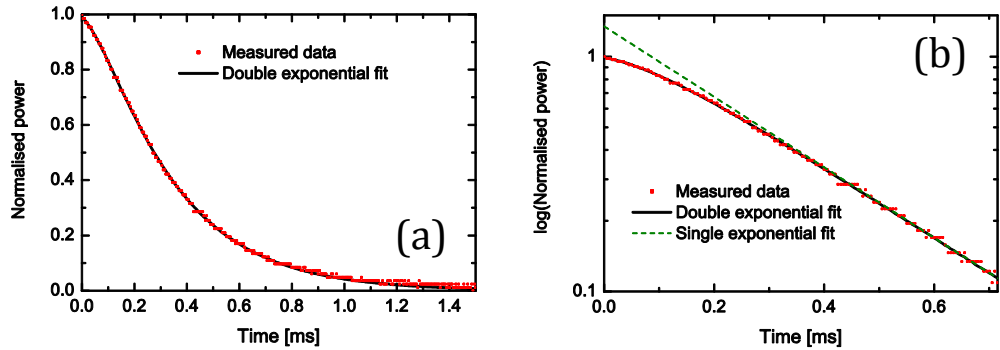


Figure 5. 9: **(a)** (points) Normalised measured He-Ne power guided by the waveguide after removal of the pump. (lines) Fit using double exponential shown in equation (4.17) with fit parameters shown in Table 5. 3. **(b)** Logarithm form of a) showing the double exponential fit and a single (electronic) fit.

Table 5. 3: Fitting parameters for equation (4.17) for data shown in Figure 5. 9 with jack-knife error analysis.

parameter	Least squares fit	Linear regression	Jack-Knife
$\eta_e$	1.35	$\pm 0.01$	$\pm 0.02$
$\tau_e$ [ $\mu\text{s}$ ]	290	$\pm 5$	$\pm 2$
$\eta_T$	-0.35	$\pm 0.07$	$\pm 0.02$
$\tau_T$ [ $\mu\text{s}$ ]	94	$\pm 5$	$\pm 5$

Errors were calculated using the method of standard deviation of the slope from linear regression, separating both decay components. In addition to this, errors were calculated using the Jack-knife error analysis method where the algorithm is detailed in Appendix C. The Jack-knife error analysis method is an alternative way to measure errors and is particularly useful if the relationship between the terms is largely unknown. The jack-knife error analysis will remove any bias from the calculation of the

## Chapter 5 – Guiding and Laser Operation in KYbW

errors. It is shown here to confirm that the errors calculated from linear regression are correct in magnitude and thus provides confidence in the fitting function. It involves removal of each data point, performing a fit on the remaining points and calculating a standard deviation of all the fits.

Results show a large positive decay component that has a lifetime similar to that of the Yb lifetime in KYbW. The intrinsic Yb lifetime in KYbW has been measured to be 200  $\mu\text{s}$ , however the lifetime including radiation trapping and without total internal reflection effects was measured to be 350  $\mu\text{s}$  [43]. Radiation trapping will play a role in extending the electronic lifetime of the refractive index change component. Significant reabsorption acts to extend the electronic lifetime and thus refractive index change beyond the intrinsic Yb value.

There is a smaller negative component of the refractive index change which is considered to be that of the thermal refractive index change. The  $dn/dT$  of 20% doped Yb:KYW is known to be large and negative; -6.6 to -12.3 at 633 nm [37]. KYbW is expected to have similar values. The negative sign on the thermal contribution shows that the thermal effects are anti-guiding and act to remove the positive guiding effects. It is possible to estimate the thermal lifetime from the pumping geometry of the crystal by solving the heat-transport equation:

$$\rho C \frac{dT}{dt} - \kappa \left( \frac{d^2T}{dy^2} + \frac{d^2T}{dz^2} \right) = 0 \quad (4.18)$$

where,  $\rho$  is the crystal density,  $C$  is the heat capacity per unit mass,  $T$  is the temperature,  $\kappa$  is the thermal conductivity. The z- direction is the pump direction and the y-direction is across the guide. The x- direction (along the strip) is ignored as a heat transfer direction because constant pumping is assumed along the strip. An estimate of the thermal lifetime can then be made from known quantities of the crystal.

The transient thermal properties can be analysed in similar manner to a longitudinally pumped bulk laser [3]. Due to the short absorption length, the pumped strip region is roughly cylindrical in shape (see Figure 5. 6). Heat flow is away from the centre of this region. A cylindrical approximation may be used for the pump region for a rough estimate. This is defined using terms of  $R_x$  and  $R_y$  to define the size of the pump region. The remaining approximations are taken directly from reference [3]:

$$\frac{dT}{dt} \approx \frac{T}{\tau}, \quad \frac{d^2T}{dy^2} + \frac{d^2T}{dz^2} \approx \frac{2T}{R_y^2 + R_z^2} \quad (4.19)$$

$$\tau_T \approx \frac{\rho C}{\kappa} \left( \frac{R_y^2 + R_z^2}{2} \right)$$

Using the parameters of KYW [37];  $\kappa=3.5 \text{ Wm}^{-1}\text{K}^{-1}$ ,  $C=0.4 \text{ Jg}^{-1}\text{K}^{-1}$ ,  $\rho=6.6 \text{ gcm}^{-3}$  and FWHM dimensions taken from Figure 5. 6,  $R_y=8.2 \pm 1.2 \text{ }\mu\text{m}$  and  $R_z=20.5 \pm 3.1 \text{ }\mu\text{m}$ . An estimate of the thermal lifetime is  $\approx 180 \mu\text{s}$ . This is of a similar order of magnitude to that measured ( $94 \pm 5 \mu\text{s}$ ) by analysing the transient behaviour of the waveguide. A more precise analysis may be carried out with transient finite element thermal modelling.

Using the coefficients of the electronic and thermal components, the contribution to the refractive index change can be calculated. The thermal contribution is anti-guiding and acts to reduce the guiding properties of the waveguide. Using the measured coefficients of  $\eta_e = 1.35$  and  $\eta_T = -0.35$ , the thermal anti-guiding effect acts to remove 26% of the guide strength. The refractive index change due to electronic mechanisms alone can thus be recalculated from Section 5.2.2 to be increased by 26% from  $8.8 \pm 3.2 \times 10^{-5}$  to  $11.1 \pm 4.0 \times 10^{-5}$ .

The time-resolved analysis has produced results that are consistent with the Yb electronic and thermal lifetime in KYbW. These results are also consistent with alternative time resolved analysis based on pump induced gratings in Yb:KYW [33]. The thermal anti-guiding effect of 26% is high and could be reduced with a smaller strip width to improve surface/volume heat extraction. Further heat extraction could be employed by bonding a transparent heat-spreader to the pumping-face crystal surface. Alternatively the crystal may be cut to athermal directions [33] to remove anti-guiding effects.

The positive guiding effects measured in Section 5.2.2 and confirmed to result from electronic mechanisms in this section offer the possibility for guided laser operation. Spectroscopic work by Moncorge et al. [44] has shown that the polarisability change and thus positive refractive index change at 1040 nm is the same as at 633 nm. By confining the mode of the laser, properties analogous to waveguide lasers can be expected and alternative cavity geometries can be employed.

### 5.3 Laser operation

Laser operation in KYbW and heavily doped Yb:KYW has been reported by others as discussed in Chapter 1. Work presented in this section utilises the positive guiding effect of the electronic refractive index change and gain-guiding in order to change cavity stability and allow novel pumping and cavity geometries. In Section 5.2 the electronic refractive index change was measured to be positive without the influence of gain. Gain will act to further increase guiding and change the cavity stability region, this will be shown with laser operation.

#### 5.3.1 Fibre pumped system

Using the crystal and orientation described in section 5.2.1, with a similar setup to that shown in Figure 5. 2, a laser cavity was established. A labelled setup photograph is shown in Figure 5. 10. Pumping was achieved with a fibre-coupled diode laser from Lumics offering 10W at peak power operating in the region of peak absorption at 981 nm. Diode laser output was polarisation-scrambled by the fibre, offering a spectral output at peak power similar to that offered by the diode-laser shown in Figure 5. 4. The fibre facet was angled at 9 degrees to minimise back reflection and therefore a suitable angled mount was fabricated to hold the fibre and a triplet lens to offer collimation. This was mounted on an xyz-translation stage with additional off-axis pitch, yaw and roll control offered by a custom made mount.

Laser light was focussed to a strip through use of a cylindrical lens of focal length 6.8 mm. The pump profile on the crystal surface was chosen to occupy the full 4 mm length of the crystal, creating a Gaussian profile along the cavity direction, slightly clipping the edges for optimised performance. Strip rotational control was obtained by rotating the  $f=6.8$  lens mount. The strip profile was measured with a commercial Coherent BeamMaster to have an  $e^{-2}$  length of 4 mm and an  $e^{-2}$  width of  $60\mu\text{m}$ . The strip length and width could be adjusted during laser operation by de-collimating the pump beam and repositioning the mount system.

To prevent crystal damage and to prevent build-up of negative thermal lens effects, the pump beam was mechanically chopped after collimation with a 5% duty cycle. Optically-induced damage was observed on a separate identical crystal with the same pumping scheme at  $\sim 5\text{W}$  of incident continuous power and again at  $\sim 10\text{W}$  50% chopped. Water cooling was provided by placing the sample on a copper mount and the crystal was kept at  $10^\circ\text{C}$ . However, this method of cooling offered no improvement to

heat-extraction from the pumped region and was only used as a method of controlling the average temperature of the crystal.

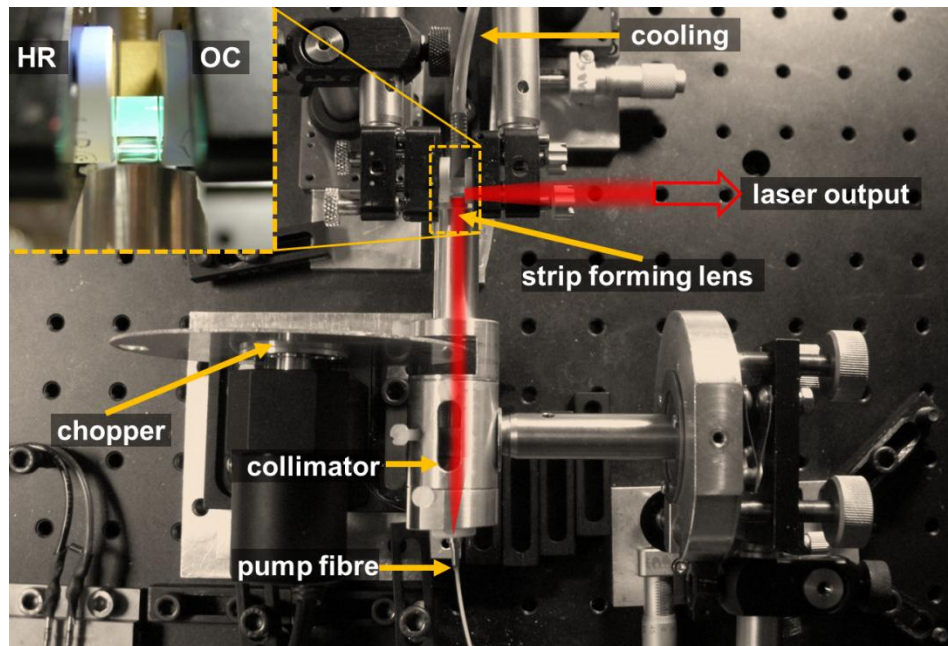


Figure 5. 10: Plan view photograph of the KYbW laser system with fibre-coupled pump setup. (top left) An image of the cavity including the highly reflective (HR) mirror and output coupler (OC).

Laser action was achieved with a simple plane-plane mirror cavity to allow the pump profile to determine the output profile. Electronic refractive index changes and gain acted to increase the stability region of the laser. Without refractive index change or gain guiding effects, the cavity would sit on a stability edge and the mode size would tend to infinity. One mirror was highly reflective, >99.9%, and the other output coupling mirror was selected from a range of 92% to 99.5% reflective. Mirrors were aligned parallel to the crystal edges and were moved close to, near touching, the crystal. If guiding is assumed to create a constant signal beam profile in the crystal, flat mirrors are required to be touching to eliminate diffraction losses. Figure 5. 10, inset top left, shows a magnified image of the 4 mm long laser cavity.

### 5.3.2 Laser performance

Quasi-continuous-wave laser operation was achieved with output couplers of 0.5%, 2%, 3%, 5% and 8%. On-time, averaged for the pulse duration, output powers of up to 320 mW were obtained for 7.4 W of pump power. The output was observed with chopper frequencies from 20Hz to 100Hz corresponding to pump pulse durations of 2.5 ms to 0.5 ms respectively. The power transfer curves are shown in Figure 5. 11. All powers may be divided by 20 to provide total average powers, taking into account the off-time.

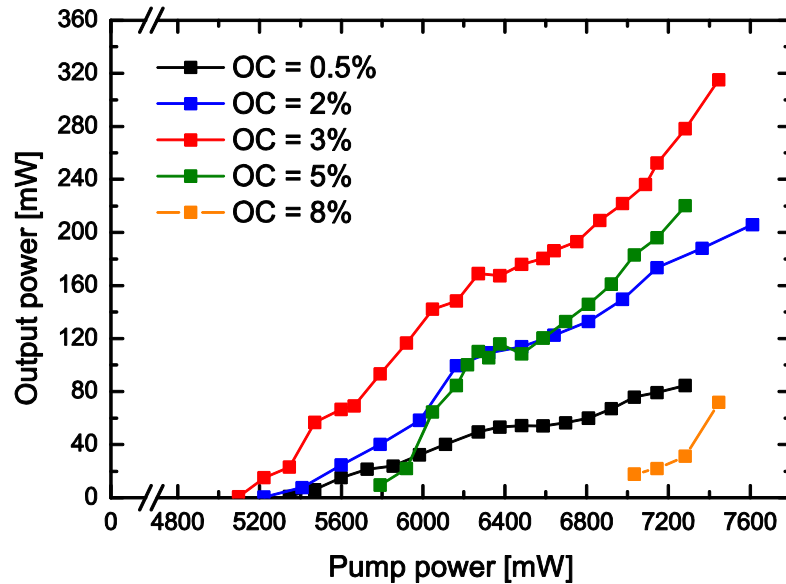


Figure 5. 11: Measured power transfer characteristics showing average powers during pump on-time. A duty cycle of 5% was used, thus all powers may be divided by 20 to provide average powers including pump off-time. All the pump power was absorbed within the crystal due to the long length, however not necessarily within the cavity mode region.

This demonstration of laser operation adds to the very few laser operation reports in KYbW and offers similar output powers to that demonstrated by Klopp et al. [48, 49]. However, the recorded threshold values are much higher and slope efficiencies are much lower. The difference between the laser characteristics are considered to be because of the different cavity and pumping geometry. Klopp et al. operated lasers in thin-disk like geometries with longitudinal pumping. This work uses side-pumping in a large bulk crystal.

The slope efficiency was found to change during laser operation with a nonlinear relationship between the output and pump powers. This is a well-known characteristic of three-level laser systems. The laser will find a lower threshold at longer wavelengths and then move towards shorter wavelengths, where more gain is available. This causes a progressive increase in the slope efficiency.

The nonlinear power transfer is also caused by the power dependent guiding properties of the cavity. Above threshold, the upper state population is not clamped but increases at a slow and reducing rate as the laser blue-shifts. The electronic guiding effects can be considered to be directly proportional to the population in the upper state. The thermal load is considered to be directly proportional to the absorbed pump power. The two guiding effects compete and increased pump power acts to reduce the

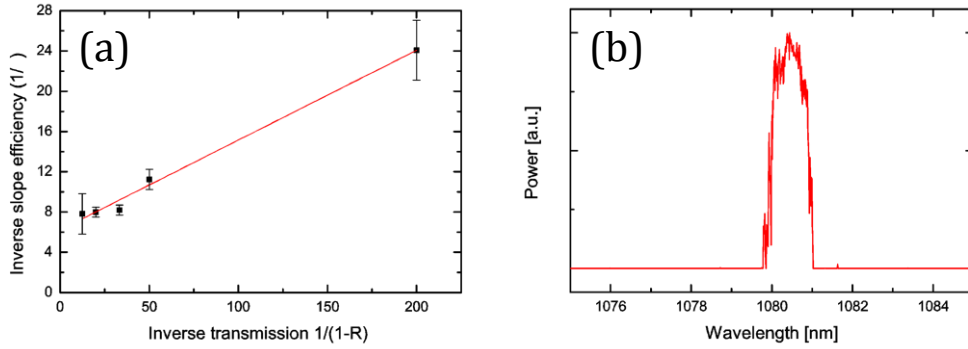


Figure 5. 12: **(a)** Caird analysis performed using equation (4.20) using the maximum slope efficiencies from Figure 5. 11 including errors **(b)** Laser output wavelength spectrum for the 2% output coupler. Laser wavelength measured to change by only 2 nm.

positive guiding effect. The reabsorption, electronic guiding and thermal anti-guiding act to create a complicated relationship between the output power and pump power.

Caird analysis, a laser performance analysis technique, was carried out by examining the slope efficiency during the latter half of the power transfer curve and is shown in Figure 5. 12. Caird analysis [50] using equation (0.6) was selected because the threshold of three-level laser systems depends greatly on reabsorption making Findlay-Clay analysis unsuitable. Caird analysis is only suitable for 3-level laser systems when the pump and cavity modes have good overlap and the laser output wavelength does not change with output coupler value. However, the laser was found to operate at a long wavelength where reabsorption is near-negligible and the output wavelength is found to marginally change  $\sim 4$  nm between output coupler values. This allows Caird analysis to hold some validity but the results should be confirmed with alternative techniques in future work.

$$\frac{1}{\eta_s} = \frac{1}{\eta_p} \left( 1 + \frac{L}{T} \right) \quad (4.20)$$

Where  $\eta_s$  is the measured slope efficiency,  $T$  is the output-coupler mirror transmission,  $\eta_p$  is the pumping efficiency including the quantum defect, and  $L$  is the passive intracavity round-trip loss. Results are shown in Figure 5. 12 a). Results indicate a roundtrip passive loss of  $1.4 \pm 0.1\%$  and a pump efficiency of  $16 \pm 2\%$  using least square fitting and jack-knife error analysis. The accuracy of this technique is further compromised by the nonlinear power transfer.

The round-trip passive loss of  $1.4 \pm 0.1\%$  is low and typical of most solid-state laser systems, suggesting that diffraction loss and crystal reflections do not contribute

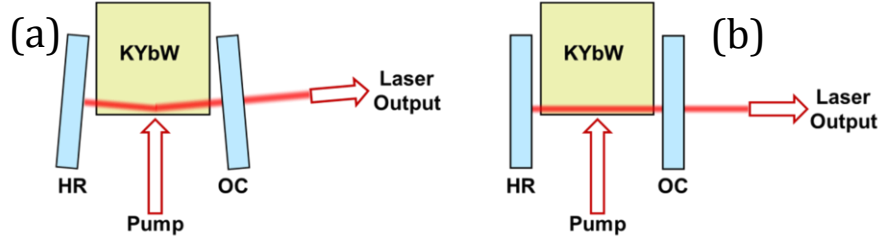


Figure 5. 13: Schematic of (a) tilted mirror 'bounce' cavity operation and (b) parallel mirror (perpendicular to pump face) operation.

significantly to the round-trip loss. The pump efficiency of  $16\pm 2\%$  is very low compared to typical solid-state laser systems. It is comprised of a 91% quantum defect, an 11% back reflection from uncoated facets, 10% pump clipping to provide a near constant power along the strip. The remaining discrepancy must be the result of poor pump/signal overlap with a large fraction of pumped crystal not contributing to laser output.

The laser was observed to operate at a wavelength of 1080 nm and the emission wavelength is shown for the 2% output coupler in Figure 5. 12. This wavelength is particularly long for Yb laser systems and confirms that significant reabsorption prevents laser operation at lower wavelengths. The output was observed to blue-shift  $\sim 2$  nm from 6W to 7.5W pump powers. The effects of reabsorption can be quantified by examining the threshold at 1040 nm in comparison to 1080 nm. The threshold may be estimated with use of the space-independent model for quasi-three level laser systems [51]:

$$P_{th} = \frac{\gamma_L + \gamma_O + 2\sigma_a NL}{2\eta_p} \frac{h\nu}{\tau} \frac{A}{\sigma_e + \sigma_a} \quad (4.21)$$

Where  $\gamma_L$  is the roundtrip passive loss,  $\gamma_O$  is the output-coupling ratio,  $\sigma$  is the cross-section, where the subscript denotes a – absorption and e – emission,  $N$  is the ground state population at room temperature,  $L$  is the length of the crystal,  $h$  is Planck's constant,  $\nu$  is the laser frequency,  $\tau$  is the upper-state lifetime,  $A$  is the area of the laser beam and  $\eta_p$  is the pumping efficiency.

Using measured values of  $\gamma_L=0.014$ ,  $\eta_p=0.16$  from Caird analysis, the intrinsic Yb lifetime of  $200\mu s$  and the ground state population of  $4 \times 10^{21} \text{cm}^{-3}$  from Pujol et al. [43] for an output coupler of  $\gamma_O=0.02$  and a crystal length of  $L=4$  mm. The beam area was

## Chapter 5 – Guiding and Laser Operation in KYbW

calculated with a strip width of 60  $\mu\text{m}$  and an absorption depth of 100  $\mu\text{m}$  due to the unpolarised pump (see Figure 5. 4).

The absorption and emission cross-sections were taken from Pujol et al. [43] and are shown in Chapter 1. At 1040 nm  $\sigma_e(1040)=1.5\times 10^{-20}\text{cm}^2$  and  $\sigma_a(1040)=0.15\times 10^{-20}\text{cm}^2$  providing a threshold of 55.7W. At 1080 nm reabsorption was considered to be negligible and  $\sigma_e(1080)=0.125\times 10^{-20}\text{cm}^2$  providing a threshold of 5.2W, close to the measured value.

Significant reduction in threshold and increase in slope efficiency is expected for an improvement in the pumping efficiency. This can include a reduced strip width, a polarisation aligned pumping scheme and anti-reflection coating on the crystal. The thermal anti-guiding is expected to dominate over electronic guiding for powers well above threshold due to the onset of upper-level population clamping and the increased thermal load. The guiding mechanism can still be enhanced for high pump and output powers by using high output coupling ratios.

### 5.3.3 Transverse cavity modes and temporal stability

Laser operation was achieved for a small range of mirror angles by rotating the output coupling and high reflective mirrors with respect to the crystal. Two distinct modes of operation could be distinguished and are shown in Figure 5. 13.

The laser cavity was tuned to operate in shallow angle bounce geometry shown in Figure 5. 13 a) for an angular separation of 2 degrees providing the results detailed in section 5.3.1. This position offered the highest output power of all angles. The bounce geometry laser is known to offer very high operating efficiencies for appropriate cavity design for four-level gain materials [52]. The in-crystal grazing angle (1 degree) was much lower than in typical bounce geometry lasers (7.5 degrees [52]). The bounce geometry relies on pump induced lensing in order to provide stability in the pump direction. As the thermal lens is known to be negative, operation must be relying on electronic index changes for operation. The temporal characteristics of the bounce geometry are shown in Figure 5. 14 and indicate a range of oscillatory instabilities suggesting that the cavity is operating on a stability edge. The signal to noise ratio of the bounce geometry was measured using average-power/peak-power to 0.7 (1.5dB).

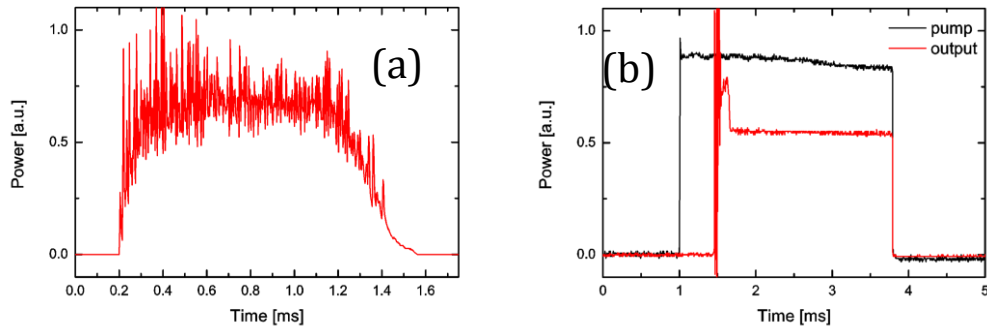


Figure 5. 14: Temporal characteristics of the laser output power for **(a)** bounce cavity and **(b)** parallel mirror cavity.

The laser was also tuned to operate with parallel mirror alignment. A higher temporal stability was obtained with the parallel plane-plane mirror cavity and is shown in Figure 5. 14 b). The signal to noise ratio of the parallel mirror geometry was measured to be 0.06 (0.2dB). This suggests that the cavity is well within the stability region for these pump powers.

The beam quality was assessed using the beam propagation  $M^2$  parameter. This parameter represents the deviation from a diffraction limited beam and is optimally 1 [53]. The  $M^2$  was measured by focussing the output beam with a lens and measuring the beam width at the waist and at a number of distances beyond the Rayleigh range. The beam widths were measured with a CCD camera using adequate attenuation with one or two high reflectors to ensure that the camera was not saturated. Accurate attenuation tuning was obtained by tilting the HR mirror to obtain an appropriate output power. The method was confirmed to agree with a more typical knife-edge method for this experiment. The beam diameter was defined using the  $e^{-2}$  power width. Although the standard definition requires the second moment width [53], the  $e^{-2}$  width was suitable for the beam profiles measured in this work as they were Gaussian-like.

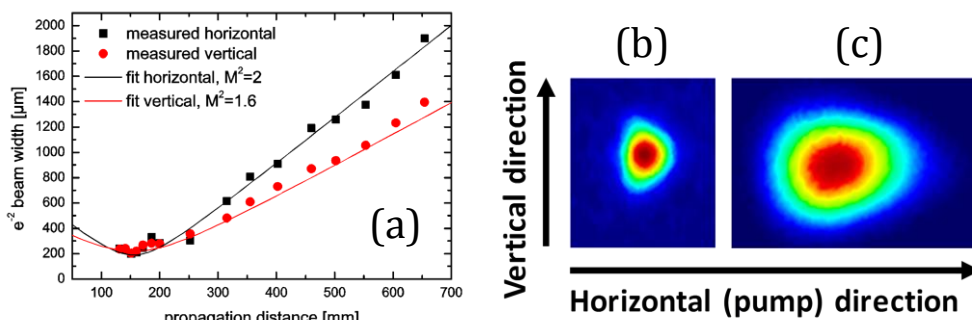


Figure 5. 15: **(a)** Laser output beam  $e^{-2}$  width during focus by a lens. **(b)** Laser spatial mode profile in an image plane of the cavity, (crystal/pump edge on left). **(c)** Far-field profile of the laser output.

A range of  $M^2$  parameters were measured for different cavity mirror alignments and were as high as 20 for particularly highly multimode cavities that showed a temporal noise similar to that shown in Figure 5. 14 a). The  $M^2$  was minimised with parallel mirrors during low noise operation similar to that shown in Figure 5. 14b). Figure 5. 15 a) shows the measured beam widths during propagation of laser output through a lens. The horizontal (pump direction)  $M^2$  was measured to be 2 and the vertical to be 1.6. The output profile is shown at the laser output in Figure 5. 15 b) and in the far-field in Figure 5. 15 c).

This profile may or may not be single-mode as it is possible to generate Gaussian-like modes from a number of higher order modes. The laser output profile in the pump direction is not Gaussian as shown in Figure 5. 15 b). The shape of this profile is significant because free-space cavity modes will be most efficient in Gaussian form. The profile is distorted in an asymmetric way such that the side closest to the crystal edge observes a rapid change in power and the right hand side, away from the crystal edge, observes a slow change in power. This profile is typical of a waveguide geometry in which there is an increase in refractive index towards the crystal edge. As a consequence, this distortion produces a higher  $M^2$  value as it diffracts more rapidly than the vertical direction as visible in Figure 5. 15 c).

### 5.3.4 Curved mirror cavity

In order to further investigate the optically-induced guiding effects during laser operation, a hemispherical cavity was setup. The cavity schematic is shown in Figure 5. 16 where the pump direction is into the page. A hemispherical cavity has a well-defined stability range from a cavity length of zero to a cavity length that matches the curvature of the mirror. It is possible to achieve laser operation between those cavity lengths, with optimal performance often achieved at the centre of the two. As the cavity length is increased from maximum stability, the spot size of the signal beam on the flat mirror is reduced. As the spot size on the flat mirror drops to zero the cavity is no longer stable. If the cavity length can be extended beyond this theoretical stability limit then there must be guiding effects within the crystal. This technique has been used previously [54, 55] with fabricated waveguide lasers in order to confirm their guiding properties. A similar technique is used here to confirm the pump-induced guiding characteristics (without waveguide fabrication).

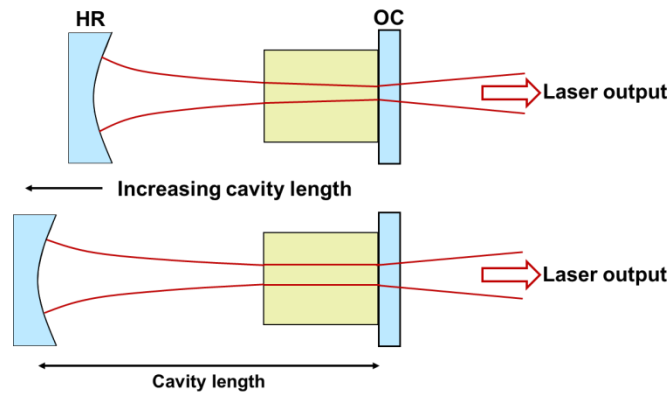


Figure 5. 16: Schematic of hemispherical mirror cavity. Laser output may be achieved for a range of cavity lengths. As the cavity length is increased beyond the curved mirror’s radius of curvature guiding is required to maintain laser operation.

A hemispherical cavity was set up using a curved HR mirror at the laser wavelength with a radius of curvature of 18 mm. Laser operation was achieved using a 3% output coupler. The length of the cavity was controlled by precisely moving the curved mirror with a translation stage. The unguided/bulk stability limit was calculated by considering 4 mm propagation through a refractive index of 2 which increases the range of stability from 18 mm to 20 mm. The output power was measured for different cavity lengths and is shown normalised in Figure 5. 17. Results show that the cavity length can be extended beyond the unguided limit of 20 mm up to 22 mm. This is beyond the predicted range of the stability limit for a bulk system and confirms the presence of positive guiding effects.

Two models are shown alongside the measured data calculated using commercial software WinLase™ which implements solutions to the ABCD matrix of a cavity mode [56]. One model was based on an unguided cavity, shown in Figure 5. 17 in red, considering a radius of curvature of 18 mm and 4 mm propagation through a refractive index of 2. The other model, shown in Figure 5. 17 in green, was based on a waveguide cavity that assumed no change in beam radius throughout the crystal. The models calculate the radius of the signal beam at the output-coupler position which drops to zero at the stability edge. The unguided model calculates a stability limit of 20 mm and the waveguide model extends this cavity length by 2 mm to 22 mm.

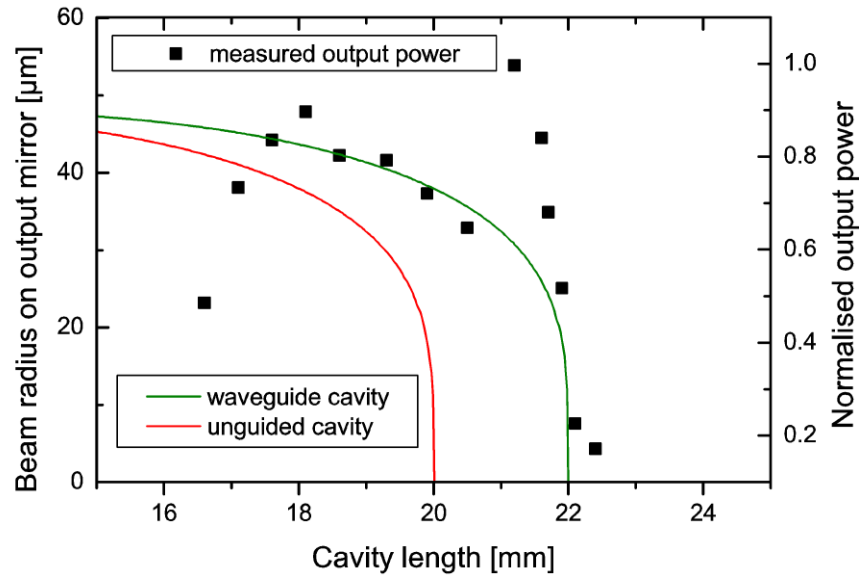


Figure 5. 17: **(Points - right axis)** Normalised output power for a range of cavity lengths with a hemispherical cavity shown in Figure 5. 16 Figure 5. 0**(lines - left axis)** Beam radius on the flat mirror calculated by WinLase™ considering the same hemispherical cavity for (red) no guiding effects within the crystal and (green) diffractionless propagation within the crystal.

The measured output power shows a clear increase in power for cavity lengths beyond the 20 mm bulk limit up to the theoretical limit of the guided cavity length. There is a large change in the output power at a cavity length of 21 mm indicating a change in the transverse mode properties within the cavity. The variation in output power can be linked to the overlap between the pump and signal beams. The pump profile was fixed with a constant beam radius of 30 μm. Output power was maximised when the signal/laser beam radius is close to the pump radius for both unguided and guided models. Power was observed to drop for short cavity lengths as a consequence of poor overlap between pump and cavity modes. Optimal output power was obtained when the beam radius in the crystal matched that of the pump strip width a radius ~30 μm as a result of guiding.

The hemispherical cavity was circularly symmetric. This cavity geometry did not offer the best performance due to the asymmetric nature of the pump profile as measured in section 5.3.3. To optimise the cavity for large mirror separations it is appropriate to insert cylindrical lenses or mirrors into the cavity to compensate for the elliptical nature of the laser profile. Better performance was achieved with the plane-plane mirror geometry.

### 5.3.5 Thermal analysis

The high Yb density is expected to make thermal anti-guiding effects significant in KYbW laser systems, because thermal loads can be highly concentrated. Poor thermal conductivity has been identified as a property which may limit the performance of this laser crystal in section 5.1. Previous reports on laser operation in KYbW have noted the anti-guiding effects of the thermal lens which has prevented efficient operation at high powers [48, 49]. By increasing the thermal load, the anti-guiding effects on the laser system can be observed. In section 5.2.3 analysis at 633 nm showed that thermal anti-guiding effects represented 26% of the index change and worked against the electronic guiding mechanism. The thermal refractive index change at the laser wavelength has been calculated to be 10% higher [37]. The clamping of the upper state population during laser operation is considered to reduce the magnitude of the electronic refractive index change in relation to the thermal anti-guiding and thus the overall guiding effect.

Work presented in this chapter has been based on quasi-continuous-wave operation with a duty cycle of 5%. This prevented the build-up of average temperature in the pump region allowing for sufficient extraction of the heat between pulses. By increasing the duty cycle it is possible to increase the average temperature in the pump region as the KYbW crystal is not capable of efficient heat extraction. This method can be used to ascertain properties of the thermal lens.

A plane-plane mirror cavity was setup with mirrors near-touching to reduce diffraction effects within the cavity. Laser operation was achieved with a 3% output coupler using electronic diode control to modify the duty cycle. The pump pulse duration was fixed at 1 ms whilst the period between pulses was varied electronically to provide duty cycles from 15% and upwards. The upper limit of 0.5 for the duty cycle was chosen as crystal damage had been previously observed beyond this point. The output power was monitored, normalised and divided by the duty cycle to calculate the power efficiency (output average / input average). Results are shown in Figure 5. 19.

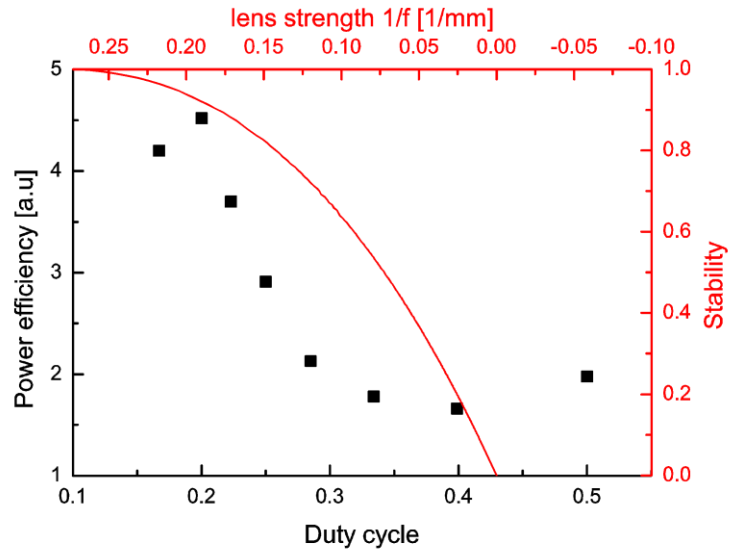


Figure 5. 18: **(Points – bottom/left axis)** Power efficiency (output power/input power) for various duty cycles of the pump. **(line – top/right axis)** Single lens cavity stability model with decreasing lens strength for increasing duty cycle.

The power efficiency was observed to drop as the duty cycle was increased. This drop in power efficiency had the effect of preventing CW operation before risk of crystal damage. The thermo-optic coefficients are known to be negative [37] in all directions and thus excessive thermal load is expected to cause anti-guiding effects and prevent laser operation.

The strength of the thermal anti-guiding effect can be modelled with a single lens cavity. Early models of waveguides used an analogy to a train of lenses which produced the effect of continual refocusing of the light to produce a beam profile which was near constant during propagation [57, 58]. Here it is proposed that both the cavity stability and waveguide properties can be described by a single lens which sits in the centre of the cavity as shown in Figure 5. 18.

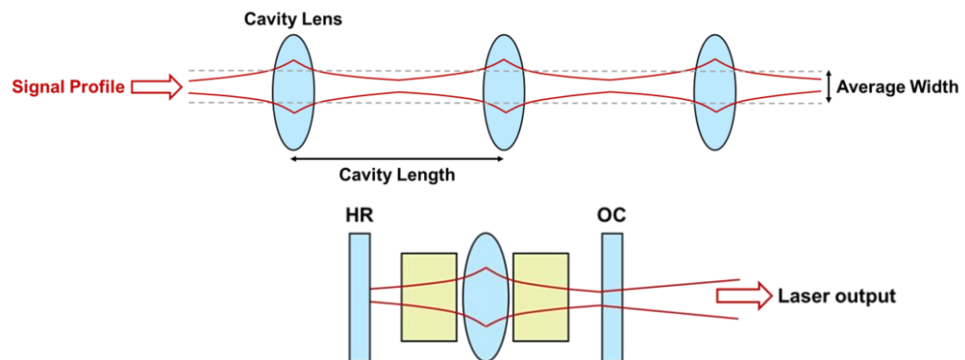


Figure 5. 19: **(top)** Waveguide model schematic based on a train of lenses. **(bottom)** Single lens cavity model to describe the guiding effects within the crystal.

The negative thermal lens acts to reduce the guide strength of the cavity. This reduces the stability of the cavity as diffraction effects can no longer be compensated and significantly increases the signal/laser mode radius.

The optically induced lens strength was modelled at the centre of the cavity and is shown alongside the measured output power in Figure 5. 17. From this model, strong positive lensing effects are required to keep the cavity stable. Maximum stability occurs at around  $f=4$  mm for which the signal/laser beam radius is around  $30\ \mu\text{m}$ . The positive guiding effect is reduced as thermal anti-guiding is introduced. The single-lens model assumes a linear reduction in lens strength with increased pump power however in practice it would be a non-linear relationship.

### 5.4 Conclusions

Optically induced guiding effects were observed at a wavelength of 633 nm without the effects of gain. Transient waveguides with a mode full-width-half-maximum of  $16\ \mu\text{m}$  were demonstrated by optical pumping at a wavelength of 981 nm. This is the first known demonstration of an optically induced gain-free waveguide outside a laser cavity and is only possible due to the high density of Yb ions. This waveguide formation technique is fabrication-free and as such will not suffer from traditional fabrication-related propagation loss. This waveguide formation technique may find applications in reconfigurable integrated optics or for waveguide laser operation.

The guided mode profile was fitted with a reverse FEM analysis method and the refractive index change was calculated to be  $8.8 \pm 3.2 \times 10^{-5}$  including all guiding mechanisms. This is four times higher than measured in previous studies with gratings in 20% doped Yb:KYW [33]. The contribution to refractive index changes from electronic and thermal mechanisms was measured from the transient behaviour. Thermal anti-guiding was calculated to reduce the positive electronic guiding effect by 26%. It is proposed that thermal anti-guiding could be compensated for with use of efficient heat spreaders bonded to the crystal.

Laser operation in KYbW is reported in a novel side-pumped flat-flat mirror cavity where the optically induced guide effects define the stability of the cavity. This is the first known report of a side-pumped KYbW laser. The short absorption length of KYbW

allows for a near-circular beam profile without the requirement for lenses in the cavity which differentiated it from traditional bounce cavity lasers.

The cavity length was increased beyond that of typical bulk-cavities, confirming the optically induced guiding properties of KYbW at the laser wavelength and within the cavity. Thermal analysis showed that significant anti-guiding effects prevented continuous wave operation of the laser and acts to prevent high power operation. The optically induced guiding effects observed in KYbW may lead to the use of novel laser cavities which have the characteristics of waveguide lasers but are fabrication free.

### References

- [1] L. J. McKnight, and S. Calvez, "*Gain-guided KYb(WO<sub>4</sub>)<sub>2</sub> Laser*," in EuroPhoton (Hamburg, 2010).
- [2] L. J. McKnight, and S. Calvez, "*Reconfigurable Integrated Optics: Diode-Laser induced waveguides for visible wavelengths in KYb(WO<sub>4</sub>)<sub>2</sub>*," in European Conference on Integrated Optics (Barcelona, 2012).
- [3] R. Boyd, "*Nonlinear Optics: 4. The Intensity-Dependent Refractive Index*" (Academic Press., 2008).
- [4] W. O. Schlosser, "*Gain-Induced Modes in Planar Structures*," Bell System Technical Journal, **52**, 887-905 (1973).
- [5] F. R. Nash, "*Mode Guidance Parallel to Junction Plane of Double-Heterostructure Gaas Lasers*," Journal of Applied Physics, **44**, 4696-4707 (1973).
- [6] F. Salin, and J. Squier, "*Gain Guiding in Solid-State Lasers*," Optics Letters, **17**, 1352-1354 (1992).
- [7] T. Y. Fan, "*Aperture Guiding in Quasi-3-Level Lasers*," Optics Letters, **19**, 554-556 (1994).
- [8] Z. Xiang, D. Wang, S. Q. Pan, Y. T. Dong, Z. G. Zhao, T. Li, J. H. Ge, C. Liu, and J. Chen, "*Beam quality improvement by gain guiding effect in end-pumped Nd:YVO<sub>4</sub> laser amplifiers*," Optics Express, **19**, 21060-21073 (2011).
- [9] A. E. Siegman, "*Propagating modes in gain-guided optical fibers*," Journal of the Optical Society of America a-Optics Image Science and Vision, **20**, 1617-1628 (2003).
- [10] X. Wang, C. Xiong, and M. Bass, "*Single mode operation of elliptical gain guided and index antiguided fibers*," Applied Physics B-Lasers and Optics, **106**, 385-392 (2012).
- [11] A. J. Kemp, R. S. Conroy, G. J. Friel, and B. D. Sinclair, "*Guiding effects in Nd : YVO<sub>4</sub> microchip lasers operating well above threshold*," IEEE Journal of Quantum Electronics, **35**, 675-681 (1999).
- [12] W. Streifer, R. D. Burnham, and D. R. Scifres, "*An Analytic Study of (Gaal) as Gain Guided Lasers at Threshold*," IEEE Journal of Quantum Electronics, **18**, 856-864 (1982).
- [13] S. Stepanov, "*Dynamic population gratings in rare-earth-doped optical fibres*," Journal of Physics D-Applied Physics, **41**, 224002 (2008).
- [14] M. J. Damzen, R. P. M. Green, and K. S. Syed, "*Self-Adaptive Solid-State Laser-Oscillator Formed by Dynamic Gain-Grating Holograms*," Optics Letters, **20**, 1704-1706 (1995).
- [15] W. Koechner, "*Thermal Lensing in a Nd-Yag Laser Rod*," Applied Optics, **9**, 2548 (1970).
- [16] S. Chenais, F. Druon, S. Forget, F. Balembois, and P. Georges, "*On thermal effects in solid-state lasers: The case of ytterbium-doped materials*," Prog. Quantum Electron., **30**, 89-153 (2006).
- [17] M. P. MacDonald, T. Graf, J. E. Balmer, and H. P. Weber, "*Reducing thermal lensing in diode-pumped laser rods*," Optics Communications, **178**, 383-393 (2000).
- [18] A. J. Kemp, G. J. Valentine, J. M. Hopkins, J. E. Hastie, S. A. Smith, S. Calvez, M. D. Dawson, and D. Burns, "*Thermal management in vertical-external-cavity surface-emitting lasers*:"

- Finite-element analysis of a heatspreader approach,* IEEE Journal of Quantum Electronics, **41**, 148-155 (2005).
- [19] F. Jansen, F. Stutzki, H. J. Otto, T. Eidam, A. Liem, C. Jauregui, J. Limpert, and A. Tunnermann, "Thermally induced waveguide changes in active fibers," Optics Express, **20**, 3997-4008 (2012).
- [20] H. X. Kang, H. T. Zhang, and D. S. Wang, "Thermal-induced refractive-index planar waveguide laser," Applied Physics Letters, **95**, 181102 (2009).
- [21] A. I. Bawamia, B. Eppich, K. Paschke, H. Wenzel, F. Schnieder, G. Erbert, and G. Trankle, "Experimental determination of the thermal lens parameters in a broad area semiconductor laser amplifier," Applied Physics B-Lasers and Optics, **97**, 95-101 (2009).
- [22] R. C. Powell, S. A. Payne, L. L. Chase, and G. D. Wilke, "Index-of-Refractive Change in Optically Pumped Solid-State Laser Materials," Optics Letters, **14**, 1204-1206 (1989).
- [23] G. D. Baldwin, and E. P. Riedel, "Measurements of Dynamic Optical Distortion in Nd-Doped Glass Laser Rods," Journal of Applied Physics, **38**, 2726 (1967).
- [24] O. L. Antipov, O. N. Ereneykin, A. P. Savikin, V. A. Vorob'ev, D. V. Bredikhin, and M. S. Kuznetsov, "Electronic changes of refractive index in intensively pumped Nd : YAG laser crystals," IEEE Journal of Quantum Electronics, **39**, 910-918 (2003).
- [25] D. C. Hutchings, M. Sheikbahae, D. J. Hagan, and E. W. Vanstryland, "Kramers-Kronig Relations in Nonlinear Optics," Optical and Quantum Electronics, **24**, 1-30 (1992).
- [26] E. L. Buckland, and R. W. Boyd, "Electrostrictive contribution to the intensity-dependent refractive index of optical fibers," Optics Letters, **21**, 1117-1119 (1996).
- [27] A. Martinez-Rios, A. N. Starodumov, Y. O. Barmenkov, V. N. Filippov, and I. Torres-Gomez, "Influence of the symmetry rules for Raman susceptibility on the accuracy of nonlinear index measurements in optical fibers," Journal of the Optical Society of America B-Optical Physics, **18**, 794-803 (2001).
- [28] P. Mamyshev, and S. Chernikov, "Recent developments in the ultrashort pulse Raman effect in optical fibers," Soviet Lightwave Communications, **2**, 97-111 (1992).
- [29] R. H. Stolen, and A. Ashkin, "Optical Kerr Effect in Glass Waveguide," IEEE Journal of Quantum Electronics, **Qe 8**, 548 (1972).
- [30] D. E. Spence, P. N. Kean, and W. Sibbett, "60-Fsec Pulse Generation from a Self-Mode-Locked Ti-Sapphire Laser," Optics Letters, **16**, 42-44 (1991).
- [31] O. L. Antipov, A. S. Kuzhelev, D. V. Chausov, and A. P. Zinov'ev, "Dynamics of refractive-index changes in a Nd : YAG laser crystal under excitation of Nd<sup>3+</sup> ions," Journal of the Optical Society of America B-Optical Physics, **16**, 1072-1079 (1999).
- [32] O. L. Antipov, D. V. Bredikhin, O. N. Ereneykin, A. P. Savikin, E. V. Ivakin, and A. V. Sukhadolau, "Electronic mechanism for refractive-index changes in intensively pumped Yb : YAG laser crystals," Optics Letters, **31**, 763-765 (2006).
- [33] E. V. Ivakin, A. V. Sukhadolau, O. L. Antipov, and N. V. Kuleshov, "Transient grating measurements of refractive-index changes in intensively pumped Yb-doped laser crystals," Applied Physics B-Lasers and Optics, **86**, 315-318 (2007).
- [34] V. V. Filippov, and I. T. Bodnar, "Thermo-optical parameters and dispersion of pure and Yb<sup>3+</sup>-doped KY(WO<sub>4</sub>)<sub>2</sub> laser crystals," Applied Optics, **46**, 6843-6846 (2007).
- [35] S. Biswal, S. P. O'Connor, and S. R. Bowman, "Thermo-optical parameters measured in ytterbium-doped potassium gadolinium tungstate," Applied Optics, **44**, 3093-3097 (2005).
- [36] S. Vatnik, M. C. Pujol, J. J. Carvajal, X. Mateos, M. Aguilo, F. Diaz, and V. Petrov, "Thermo-optic coefficients of monoclinic KLu(WO<sub>4</sub>)<sub>2</sub>," Applied Physics B-Lasers and Optics, **95**, 653-656 (2009).
- [37] P. A. Loiko, K. V. Yumashev, N. V. Kuleshov, and A. A. Pavlyuk, "Thermo-optical properties of pure and Yb-doped monoclinic KY(WO<sub>4</sub>)<sub>2</sub> crystals," Applied Physics B-Lasers and Optics, **106**, 663-668 (2012).
- [38] M. M. Mazur, F. A. Kuznetsov, L. I. Mazur, A. A. Pavlyuk, and V. I. Pustovoi, "Elastic and photoelastic properties of KY(WO<sub>4</sub>)<sub>2</sub> single crystals," Inorganic Materials, **48**, 67-73 (2012).
- [39] R. Paschotta, "Encyclopedia of Laser Physics and Technology" (Wiley, 2008).

## Chapter 5 – Guiding and Laser Operation in KYbW

- [40] T. T. Basiev, A. A. Sobol, P. G. Zverev, V. V. Osiko, and R. C. Powell, "Comparative spontaneous Raman spectroscopy of crystals for Raman lasers," *Applied Optics*, **38**, 594-598 (1999).
- [41] K. V. Yumashev, N. N. Posnov, P. V. Prokoshin, V. L. Kalashnikov, F. Mejid, I. G. Poloyko, V. P. Mikhailov, and V. P. Kozich, "Z-scan measurements of nonlinear refraction and Kerr-lens mode-locking with Yb<sup>3+</sup>: KY(WO<sub>4</sub>)(<sub>2</sub>)," *Optical and Quantum Electronics*, **32**, 43-48 (2000).
- [42] A. A. Lagatsky, C. T. A. Brown, and W. Sibbett, "Highly efficient and low threshold diode-pumped Kerr-lens mode-locked Yb : KYW laser," *Optics Express*, **12**, 3928-3933 (2004).
- [43] M. C. Pujol, M. A. Bursukova, F. Guell, X. Mateos, R. Sole, J. Gavalda, M. Aguilo, J. Massons, F. Diaz, P. Klopp, U. Griebner, and V. Petrov, "Growth, optical characterization, and laser operation of a stoichiometric crystal KYb(WO<sub>4</sub>)(<sub>2</sub>)," *Physical Review B*, **65**, 165121 (2002).
- [44] R. Moncorge, O. N. Eremeykin, J. L. Doualan, and O. L. Antipov, "Origin of athermal refractive index changes observed in Yb<sup>3+</sup> doped YAG and KGW," *Optics Communications*, **281**, 2526-2530 (2008).
- [45] X. Mateos, F. Guell, M. C. Pujol, M. A. Bursukova, R. Sole, J. Gavalda, M. Aguilo, F. Diaz, and J. Massons, "Green luminescence of Er<sup>3+</sup> in stoichiometric KYb(WO<sub>4</sub>)(<sub>2</sub>) single crystals," *Applied Physics Letters*, **80**, 4510-4512 (2002).
- [46] F. Caccavale, F. Segato, I. Mansour, and M. Gianesin, "A finite differences method for the reconstruction of refractive index profiles from near-field measurements," *J Lightwave Technol*, **16**, 1348-1353 (1998).
- [47] W. S. Tsai, S. C. Piao, and P. K. Wei, "Refractive index measurement of optical waveguides using modified end-fire coupling method," *Optics Letters*, **36**, 2008-2010 (2011).
- [48] P. Klopp, U. Griebner, V. Petrov, X. Mateos, M. A. Bursukova, M. C. Pujol, R. Sole, J. Gavalda, M. Aguilo, F. Guell, J. Massons, T. Kirilov, and F. Diaz, "Laser operation of the new stoichiometric crystal KYb(WO<sub>4</sub>)(<sub>2</sub>)," *Applied Physics B-Lasers and Optics*, **74**, 185-189 (2002).
- [49] P. Klopp, V. Petrov, U. Griebner, V. Nesterenko, V. Nikolov, M. Marinov, M. A. Bursukova, and M. Galan, "Continuous-wave lasing of a stoichiometric Yb laser material: KYb(WO<sub>4</sub>)(<sub>2</sub>)," *Optics Letters*, **28**, 322-324 (2003).
- [50] J. A. Caird, S. A. Payne, P. R. Staver, A. J. Ramponi, L. L. Chase, and W. F. Krupke, "Quantum Electronic-Properties of the Na<sub>3</sub>Ga<sub>2</sub>Li<sub>3</sub>F<sub>12</sub>-Cr-3+ Laser," *IEEE Journal of Quantum Electronics*, **24**, 1077-1099 (1988).
- [51] O. Svelto, "Principles of Lasers" (Springer, 1st Ed. 1976, 5th Ed. 2010).
- [52] A. Minassian, B. Thompson, and M. J. Damzen, "Ultrahigh-efficiency TEM<sub>00</sub> diode-side-pumped Nd : YVO<sub>4</sub> laser," *Applied Physics B-Lasers and Optics*, **76**, 341-343 (2003).
- [53] A. E. Siegman, "How to (Maybe) Measure Laser Beam Quality," in Tutorial presentation at the Optical Society of America Annual Meeting (1997).
- [54] U. Griebner, and H. Schonngel, "Laser operation with nearly diffraction-limited output from a Yb : YAG multimode channel waveguide," *Optics Letters*, **24**, 750-752 (1999).
- [55] Y. E. Romanyuk, C. N. Borca, M. Pollnau, S. Rivier, V. Petrov, and U. Griebner, "Yb-doped KY(WO<sub>4</sub>)(<sub>2</sub>) planar waveguide laser," *Optics Letters*, **31**, 53-55 (2006).
- [56] H. Kogelnik, and T. Li, "Laser Beams and Resonators," *Applied Optics*, **5**, 1550 (1966).
- [57] G. S. Goubau, F., "On the Guided Propagation of Electromagnetic Wave Beams," *IRE Transactions on Antennas and Propagation*, **9**, 248 (1961).
- [58] P. K. Tien, J. P. Gordon, and J. R. Whinnery, "Focusing of a Light Beam of Gaussian Field Distribution in Continuous and Periodic Lens-Like Media," *Proceedings of the Institute of Electrical and Electronics Engineers*, **53**, 129 (1965).

# Chapter 6

## Summary and Future Perspectives

---

The work presented in this thesis has focused on waveguides and their application in diamond, GaN and KYbW photonics. Section 6.1 summarises the theory and optical characterisation presented in Chapters 2-5. Section 6.2 outlines some of the future perspectives of the work presented in this thesis. This includes a few highlighted application areas and some suggested work that should be carried out for presented devices to reach their full potential.

### 6.1 Summary

#### 6.1.1 Theory and waveguide design; throughout thesis

Theory, modelling and simulation work was carried out to consider a range of waveguide designs that may be suitable for materials and applications presented in this work. This involved the consideration of the transverse resonance condition, the effective index method, Marcatili's approximation, the beam propagation method and the finite element method. A modification was proposed to the effective index method to more accurately describe behaviour of modes in a rib waveguide. The large cross-sectional area waveguide design was considered to be highly suitable for the work presented in this thesis, due to the relaxed fabrication requirements for single-mode operation it offers. This waveguide geometry was then used for fabrication of diamond and GaN waveguides and was presented in Chapters 3 and 4.

The transverse mode characteristics of large cross-sectional area rib waveguides were considered in Chapter 3 and waveguide confinement was compared to bulk. Criteria for a useful waveguide were developed based on confinement and waveguide length. Beam propagation method simulations have shown that higher order modes can remain guided in rib waveguides for significant distances, even though the cross-section of the waveguide suggests that the waveguide should be single mode. This work has shown the propagation length must be taken into account when defining the single-mode criteria of a waveguide.

## Chapter 6 – Summary and Future Perspectives

In chapter 4, a single-mode directional coupler was designed and simulated for compatibility with contact photolithography, a single etch step and a minimum feature size of 2  $\mu\text{m}$ . This device used novel inverse tapers that allowed a four times reduction in footprint and a circular mode at the coupling facets. This offered a mechanism to reduce coupling length without reduction of the coupling gap.

### 6.1.2 Diamond devices; Chapter 3

Diamond rib waveguides were designed and fabricated using a large cross-sectional area rib waveguide design. Fabrication was carried out by Y. Zhang [1]. A novel fabrication method was developed to extend the waveguide to the sample edge without the requirement for facet polishing. The waveguide design and fabrication method provides a much simpler alternative to existing fabrication methods for diamond.

The waveguides were optically characterised and were shown to support two modes, the fundamental and second vertical mode, over the 2 mm sample length. Simulations have shown that the second guided mode should be removed over longer propagation distances. Diamond waveguides fabricated in this manner may find applications in quantum optics or as a Raman waveguide laser material.

### 6.1.3 Analytical modelling of a diamond Raman waveguide laser; Chapter 3

The Payne and Lacey theory [2] of waveguide surface scattering propagation loss was extended to provide a full description from all surfaces of a rib waveguide. An analytical solution was proposed using Marcatili's approximation and was found to be suitable for a range of large cross-sectional area waveguide designs.

An analytical solution to the coupled equations to describe a Raman waveguide laser [3] was extended for large cross-sectional rib waveguides. This solution was combined with analytical solutions for scattering loss to provide a full description of the Raman waveguide laser system.

Optimisations have shown that thresholds as low as 100mW with a 1% output coupler could be obtained for optimised waveguides with a cross-section of  $(4-8)^2 \mu\text{m}^2$  for 2-5 mm sample lengths and 532 nm continuous wave pumping. Alternatively, continuous wave output power could be optimised to above 15 W for 20 W pump power at 532 or 1064 nm for waveguides with a cross-section above  $2 \times 2 \mu\text{m}^2$ .

An iterative solution to the coupled equations for a bulk Raman laser was developed considering a changing beam waist throughout the crystal. Results show that waveguide lasers can outperform bulk alternatives by significant factors for a range of conditions.

### 6.1.4 GaN devices; Chapter 4

A range of straight and directional coupler waveguides were designed and fabricated using the rib waveguide design. Fabrication was carried out by Y. Zhang [1]. These devices add to the small range of GaN devices reported to date and are among a small number that have been designed to operate in the visible/NIR wavelength range.

The devices were optically characterised to confirm single-mode behaviour for a range of wavelengths, owing to the relaxed criteria of the rib-waveguide design. Propagation loss was measured with the scattering and Fabry-Perot methods. Results show significant losses compared with similar designs for other materials however propagation loss remains small compared to demonstrated GaN devices;  $10.9 \pm 1.6$  dB/cm at 1300 nm in this work compared with 34 dB/cm at 1550 nm by [4]. It is suggested that the high losses measured in this work are due to underlying planar loss which could be significantly reduced with appropriate growth methods [5, 6].

The splitting ratios of a number of directional couplers were measured using a method that compensates for loss in individual arms. A range of splitting ratios from 10:90 to 55:45 were measured for different coupler region lengths following an expected relationship.

A two-mode waveguide was fabricated and observed to oscillate ('beat') between the modes by measurement of the scattered light with a CCD camera. This is the first known measurement of two-transverse-mode beat-length of a waveguide with the scattered light from the edges of the waveguide. This technique may provide alternative ways of measuring device properties such as physical dimensions or refractive indices.

Two-photon interference was observed with down-converted single-photon pairs within a 45:55 GaN directional coupler. A novel free-space coupling system was used in order to address ports that were close together on the chip. Results show a visibility of  $95.9 \pm 2.9\%$  which is near the theoretical limit and confirms the quality of the directional coupler.

GaN waveguide devices may find applications in integrated quantum optics involving integration with single-photon sources, perhaps with diamond. GaN waveguide devices are also of interest for nonlinear optics based on the high  $\chi^{(2)}$ .

### 6.1.5 KYbW; Chapter 5

Optically induced guiding effects were observed at a wavelength of 633 nm without the effects of gain. 16- $\mu\text{m}$ -sized transient waveguides were demonstrated by optical pumping at a wavelength of 981 nm. This is the first known demonstration of an optically induced gain-free waveguide outside a laser cavity and is only possible due to the high density of  $\text{Yb}^{3+}$  ions.

The guided mode profile was fitted with a reverse FEM analysis method and the refractive index change was calculated to be  $8.8 \pm 3.2 \times 10^{-5}$  including all guiding mechanisms. This is four times higher than measured in previous studies with gratings in 20% doped Yb:KYW [7]. The contribution to refractive index changes from electronic and thermal mechanisms was measured from the transient behaviour. Thermal anti-guiding was calculated to reduce the positive electronic guiding effect by 26%.

Laser operation in KYbW is reported in a novel side-pumped plane-plane mirror cavity where the optically induced guide effects define the stability of the cavity. This is the first known report of side-pumped KYbW laser. The short absorption length of KYbW allows for a circular-like beam profile without the requirement for lenses in the cavity which differentiates it from bounce cavity lasers.

The cavity length was increased beyond that of typical bulk-cavities, confirming the optically induced guiding properties of KYbW at the laser wavelength and within the cavity. Thermal analysis showed that significant anti-guiding effects prevented continuous wave operation and high power operation of the laser. The optically induced guiding effects observed in KYbW may lead to the use of novel laser cavities which have the characteristics of waveguide lasers but are fabrication free.

### 6.2 Future perspectives

The work presented in this thesis has been geared towards a broad range of applications of guided optics in diamond, GaN and KYbW. However, there has been a focus on a number of distinct topics including integrated quantum optics, nonlinear applications and novel guiding techniques. Further progress towards continued applications in these areas from devices demonstrated in this thesis is considered.

#### 6.2.1 Diamond and GaN for integrated quantum optics

##### a) An all-diamond solution

An all diamond solution with source, circuit and detector on-chip is one desirable route to achieve integrated quantum optics. This will require integration with a deterministic single-photon source, probably the N-V centre. This single-photon source will need to be within a cavity, either a photonic crystal or ring-resonator to achieve the zero-phonon line enhancement required [8]. Waveguide routing may take advantage of the high refractive index for compact circuits and transparency of diamond. Single-photon detectors may also take the form of colour centres and cavities will again be required to enhance their response.

This goal is rather ambitious and may not come to fruition for some time. The limited availability of suitable samples as part of this work restricted the fabrication of suitable components for this architecture. The integration of an N-V single-photon source with a circuit is the next clear step and some groups have made some progress in this direction [8, 9]. Resonators and directional couplers will require small waveguide dimensions  $\sim 1\text{-}5\ \mu\text{m}$  in size in order to achieve circuitry within a single sample. Recently the availability of  $5\ \mu\text{m}$  thick  $3\ \text{mm}^2$  optical quality diamond samples via Element 6 (Holland) may allow fabrication of complex circuits on-chip. N-V centre coupling to ring resonators has been demonstrated in these samples [9].

##### b) A GaN solution

The demonstration of a probabilistic single-photon source in GaN is considered as the next step towards integrated quantum photonics in GaN. The high  $\chi^{(2)}$  of GaN makes it suitable for spontaneous parametric down-conversion. With suitably designed waveguide structures and phase matching, photon pairs can be generated in a similar manner to that demonstrated in lithium niobate [10]. An integrated GaN laser/LED may be down-converted on-chip. In a similar manner, up-conversion single-photon

detectors could be explored. This could lead to fully integrated room temperature integrated quantum photonics with a probabilistic operation.

A waveguide structure with lower propagation loss is required to fully exploit the potential for GaN integrated optics. This may include appropriate growth of lattice matched layers to form the guiding mechanism [5]. This could also be achieved with other widely used waveguide fabrication techniques such as laser writing or ion implantation.

### **c) A hybrid solution**

Due to the refractive index match between GaN and diamond, a hybrid device consisting of the two materials is an interesting option. An N-V centre single-photon source could be combined with a GaN circuit. This could take the form of a cavity or resonant structure in diamond to enhance the zero phonon line. This cavity could be coupled to GaN by bonding with use of appropriate waveguide tapers to ensure a transition between the materials.

Alternatively a resonant structure could be fabricated in GaN. An N-V centre could be coupled to these structures either through bonding or through placing nanoparticles on a waveguide. GaN microdisk cavities have been fabricated within the Institute of Photonics and further work could involve the use of these devices.

## **6.2.2 Diamond and GaN nonlinear waveguide devices**

### **a) Diamond Raman waveguide laser**

Work as part of chapter 3 discussed the possibility for a diamond Raman waveguide laser. This design was shown to be feasible for a range of dimensions. Diamond has a high Raman gain and thus in combination with waveguide geometry may offer low threshold or high power devices. If threshold can be reduced significantly it may be possible to consider novel pump sources that are not currently possible with bulk Raman lasers. Raman cascading is also an area in which waveguides may benefit laser systems.

The fabrication of suitable devices is required to demonstrate a working laser system. This fabrication procedure must produce low loss waveguide devices for long lengths and small cross-sections. The samples used as part of this work were not suitable for

the Raman laser device due to the large cross-sectional area and short length. However, the increasing availability of diamond samples may lead to progress in this area.

### **b) GaN nonlinear frequency converters**

GaN has been reported to have a high  $\chi^2$  and as such is suitable for nonlinear frequency conversion. Second harmonic generation has been enhanced with use of a photonic crystal waveguide [11]. With use of a waveguide, phase matching can be achieved to produce doubling or optical parametric oscillator operation on-chip. Nonlinear conversion efficiency can be improved compared to bulk with the waveguide geometry due to intensity enhancement over long lengths.

The GaN waveguide devices fabricated as part of this work exhibited high propagation loss, limiting their application to efficient non-linear conversion. A fabrication route involving lower propagation losses should be investigated. This may include appropriate growth of lattice matched layers to form the guiding mechanism or using other standard fabrication techniques [5, 6]. From there the phase-matching requirements should be established for work to progress in this area.

### **6.2.3 Novel guiding techniques for laser operation**

In chapter 5, guided laser operation was demonstrated in KYbW through optical pumping. The electronic guiding mechanism was identified as the cause for waveguide formation. Other recent reports have shown pump induced guiding with the thermal mechanism suggested for waveguide formation [12]. The fabrication-free formation of waveguides for laser or non-linear applications may provide a route to lossless waveguides; a highly interesting prospect for laser operation.

Within the KYbW material system there are a number of improvements to the pump scheme that may be implemented. The use of a 4f pump system may reduce the strip width significantly and enhance the waveguide confinement. The butt-coupling of a diode stack may offer an alternative route to waveguide based laser operation without pump optics.

In general there are a number of novel waveguide formation techniques that are poorly reported. Thermally induced waveguides may offer a route to confinement in a number of material systems. Such systems may take advantage of the thermal lens behaviour in a controlled manner. Stress formed waveguides [13], either through fabrication or directly applied have not been explored fully and could offer a number of advantages

over more traditional methods. Many laser written waveguides rely on stress for waveguide formation and have demonstrated low propagation losses. Optical pumping may provide the means to produce such waveguides. The pump could then fulfil two purposes; the laser system optical pump and the waveguide formation method.

### References

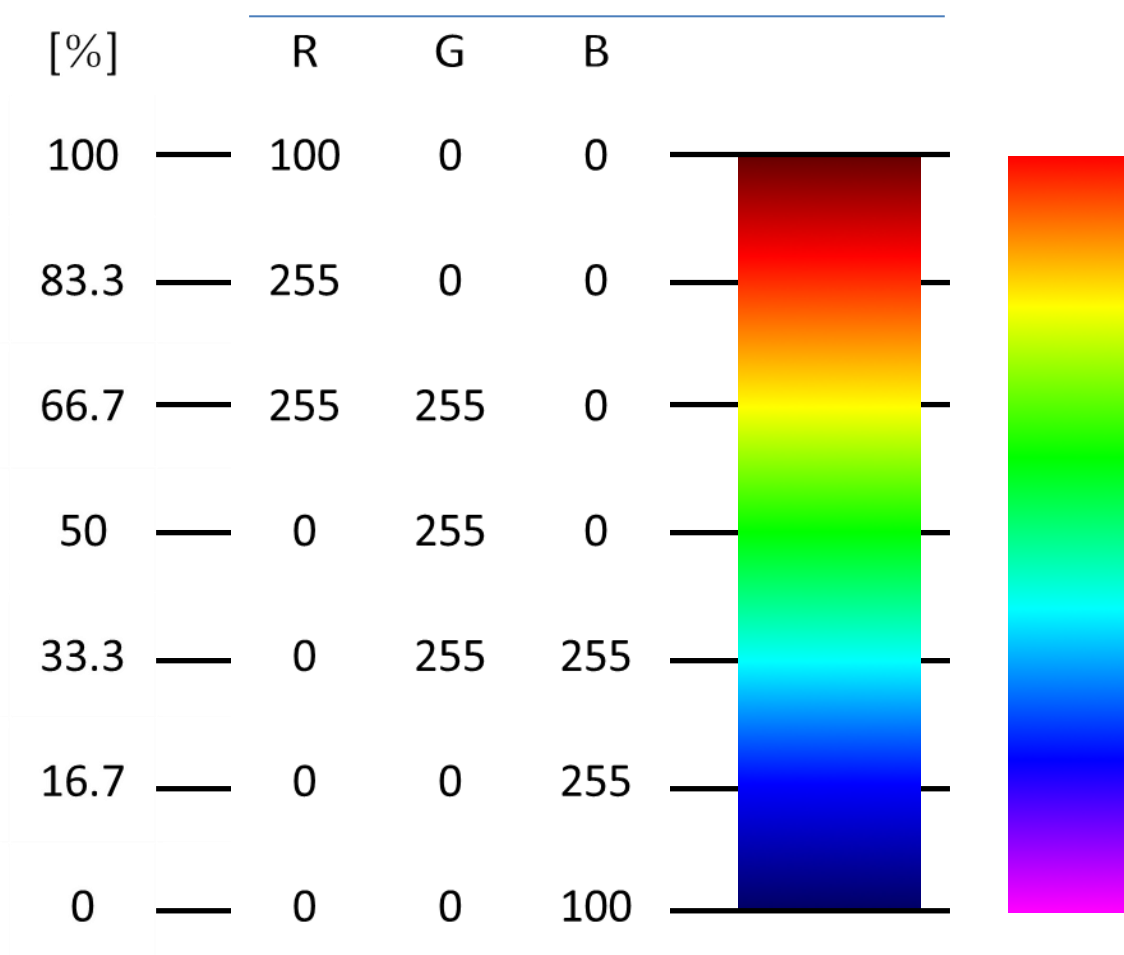
- [1] Y. F. Zhang, Phd Thesis, "*Diamond and GaN Waveguides and Microstructures for Integrated Quantum Photonics*," (Institute of Photonics, University of Strathclyde, 2012).
- [2] F. P. Payne, and J. P. R. Lacey, "*A Theoretical-Analysis of Scattering Loss from Planar Optical Wave-Guides*," *Optical and Quantum Electronics*, **26**, 977-986 (1994).
- [3] J. H. Zhou, J. P. Chen, X. W. Li, G. L. Wu, and Y. P. Wang, "*Exact analytical solution for Raman fiber laser*," *IEEE Photonics Technology Letters*, **18**, 1097-1099 (2006).
- [4] R. Q. Hui, Y. T. Wan, J. Li, S. X. Jin, J. Y. Lin, and H. X. Jiang, "*III-nitride-based planar lightwave circuits for long wavelength optical communications*," *IEEE Journal of Quantum Electronics*, **41**, 100-110 (2005).
- [5] A. Stolz, E. Cho, E. Dogheche, Y. Androussi, D. Troadec, D. Pavlidis, and D. Decoster, "*Optical waveguide loss minimized into gallium nitride based structures grown by metal organic vapor phase epitaxy*," *Applied Physics Letters*, **98**, 161903 (2011).
- [6] R. Geiss, A. Chowdhury, C. M. Staus, H. M. Ng, S. S. Park, and J. Y. Han, "*Low loss GaN at 1550 nm*," *Applied Physics Letters*, **87**, 132107 (2005).
- [7] E. V. Ivakin, A. V. Sukhadolau, O. L. Antipov, and N. V. Kuleshov, "*Transient grating measurements of refractive-index changes in intensively pumped Yb-doped laser crystals*," *Applied Physics B-Lasers and Optics*, **86**, 315-318 (2007).
- [8] A. D. Greentree, B. A. Fairchild, F. M. Hossain, and S. Praver, "*Diamond integrated quantum photonics*," *Nature Today*, **11**, 22-31 (2008).
- [9] A. Faraon, P. E. Barclay, C. Santori, K. M. C. Fu, and R. G. Beausoleil, "*Resonant enhancement of the zero-phonon emission from a colour centre in a diamond cavity*," *Nat Photonics*, **5**, 301-305 (2011).
- [10] G. Fujii, N. Namekata, M. Motoya, S. Kurimura, and S. Inoue, "*Bright narrowband source of photon pairs at optical telecommunication wavelengths using a type-II periodically poled lithium niobate waveguide*," *Opt Express*, **15**, 12769-12776 (2007).
- [11] D. Coquillat, G. Vecchi, C. Comaschi, A. M. Malvezzi, J. Torres, and M. L. d'Yerville, "*Enhanced second- and third-harmonic generation and induced photoluminescence in a two-dimensional GaN photonic crystal*," *Applied Physics Letters*, **87**, 101106 (2005).
- [12] H. X. Kang, H. T. Zhang, and D. S. Wang, "*Thermal-induced refractive-index planar waveguide laser*," *Applied Physics Letters*, **95**, 181102 (2009).
- [13] M. J. Liu, and H. K. Kim, "*Strain-induced channel waveguiding in bulk sapphire substrates*," *Applied Physics Letters*, **79**, 2693-2695 (2001).

# Appendix A

## Colour map scale

---

Within this thesis all 2D plots are shown with a specific colour scale. The colours in this scale represent a real numbered scale when normalised from 0 to 1 and sometimes normalised to be -1 to 1 where 0 is at the centre. Data calculated numerically with a range of software packages and data measured with a CCD camera has been converted into the same scale to allow comparison. The mapping is shown below, the visible spectrum which is the typical mapping used by commercial software RSoft:



# Appendix B

## Chapter 3, Equation 3.16

---

The analytical solution to the Raman laser coupled equations using the Lambert function from [1]:

$$P_p^+(z, P_{in}) = P_{in} \exp\left[-\frac{zP_{in}}{L} \gamma_p^0\right], \quad P_p^-(z) = P_p^+(L-z, P_p^+(L, P_{in}))$$

$$P_s^+(z) = \frac{\lambda_p}{\lambda_s} \frac{a}{2gL_{eff-s}} \left(\gamma_p^0 - \delta_p\right) \exp(\gamma_s^0 z), \quad P_s^-(z) = \left(\frac{\lambda_p}{\lambda_s} \frac{a}{2gL_{eff-s}} \left(\gamma_p^0 - \delta_p\right)\right)^2 \frac{1}{P_s^+(z)}$$

Where  $P$  is the power in the waveguide where the subscript  $p$  and  $s$  denotes the pump and the Stokes beams respectively, the superscript  $+$  and  $-$  denote the forwards and backwards directions respectively and the superscript  $0$  and  $L$  denote either end of the waveguide ( $0$  being the coupling position). Where  $\gamma$  is the gain factor and  $\delta$  is the single-pass loss coefficient defined below.  $P_{in}$  is the power coupled into the waveguide,  $L$  is the length of the waveguide,  $g$  is the Raman gain coefficient and  $a$  is the effective area of the guided mode. The single-pass loss coefficients  $\delta$  are defined:

$$\delta_s = \alpha_s L - \frac{\ln(R_s^0 R_s^L)}{2}, \quad \delta_p = \alpha_p L$$

Where  $\alpha$  is the propagation loss and  $R$  is the reflectivity. The effective lengths of the Stokes and pump beams are defined:

$$l_{eff-s} = \frac{\sinh(\gamma_s^L) - \sinh(\gamma_s^0)}{\gamma_s^L - \gamma_s^0}, \quad l_{eff-p} = \frac{\sinh(\gamma_p^L) - \sinh(\gamma_p^0)}{\gamma_p^L - \gamma_p^0}$$

Gain factors at the boundaries and with  $z$  dependence are defined:

$$\gamma_p^0 = \frac{P_{in} g L}{\delta_s} + 0.5 \text{Lb} \left\{ \frac{-2P_{in} g L}{a \delta_s} \exp\left(\frac{-2P_{in} g L}{a \delta_s}\right) \right\}, \quad \gamma_p^L = 0, \quad \gamma_s^0 = \frac{\ln(R_s^0)}{2}, \quad \gamma_s^L = \frac{-\ln(R_s^L)}{2}$$

$$\gamma_s^z = -\alpha_s z + \gamma_s^0 + \frac{\delta_s}{l_{eff-p}} \frac{\sinh(\gamma_p^z) - \sinh(\gamma_p^0)}{\gamma_p^L - \gamma_p^0}, \quad \gamma_p^z = \frac{1}{2} \ln \left( \frac{P_p^+(z, P_{in})}{P_p^-} \right)$$

Where  $\text{Lb}\{\}$  is the Lambert  $W$  function.

- [1] C. H. Huang, Z. P. Cai, C. C. Ye, and H. Y. Xu, "Explicit solution for Raman fiber laser using Lambert  $W$  function," *Optics Express*, **15**, 4671-4676 (2007)

# Appendix C

## Jack-knife error analysis

---

Within this thesis a simple version of the jack-knife algorithm for calculating errors from a dataset was used. Here a least-squares linear or nonlinear fit was always used for the data based on equations shown throughout the thesis. A further discussion on the applicability of this method is available in Ref. [1]. Here it is shown for calculating the gradient and can similarly be used to calculate other variables:

n = number of data points

i = counter

m<sub>a</sub> = calculate gradient using all data points

For i= 0 to n

    Remove data point 'i'

    m<sub>i</sub> = calculate gradient with remaining data points

    Replace data point 'i'

End loop

$$\text{Jack-knife error} = \sqrt{\frac{n-1}{n} \sum_{i=0..n} (m_i - m_a)^2}$$

[1] J. Shao, and D. Tu, *The Jackknife and Bootstrap* (Springer, 1995).

# Abbreviations

---

<b>BBO</b>	Barium borate
<b>BPM</b>	Beam propagation method
<b>CCD</b>	Charged coupled device
<b>CVD</b>	Chemical vapour deposition
<b>cw</b>	Continuous wave
<b>DC</b>	Directional coupler
<b>EIM</b>	Effective index method
<b>FAC</b>	Fast-axis collimator
<b>FDTD</b>	Finite difference time domain
<b>FEM/FEA</b>	Finite element method/analysis
<b>FIB</b>	Focused ion beam
<b>FPGA</b>	Field programmable gate array
<b>HF</b>	Hydrofluoric
<b>HOM</b>	Hong-Ou-Mandel
<b>HR</b>	High reflector
<b>ICP</b>	Inductively coupled plasma
<b>LED</b>	Light emitting diode
<b>MBE</b>	Molecular beam epitaxy
<b>MEIM</b>	Modified effective index method
<b>MOCVD</b>	Metalorganic chemical vapour deposition
<b>N-V</b>	Nitrogen-vacancy
<b>OC</b>	Output coupler
<b>PECVD</b>	Plasma enhanced chemical vapour deposition
<b>PMF</b>	Polarisation maintaining fibre
<b>RIE</b>	Reactive ion etching
<b>SAC</b>	Slow-axis collimator
<b>SEM</b>	Scanning electron microscope
<b>SPAD</b>	Single photon avalanche diode
<b>SPDC</b>	Spontaneous parametric down-conversion
<b>TE</b>	Transverse electric
<b>TM</b>	Transverse magnetic
<b>TPA</b>	Two-photon absorption

# Publications

---

## c) Journal Papers

### **GaN directional couplers for integrated quantum photonics**

Applied Physics Letters 99, 161119 (2011)

Y. Zhang, [L. J. McKnight](#), E. Engin, I. M. Watson, M. J. Cryan, E. Gu, M. G. Thompson, S. Calvez, J. L. O'Brien, and M. D. Dawson

### **Diamond Raman Waveguide Lasers: Completely Analytical Design Optimization Incorporating Scattering Losses**

Journal of Quantum Electronics, 47, 1069 (2011)

[L. J. McKnight](#), M.D. Dawson, S. Calvez

### **Large cross-section edge-coupled diamond waveguides**

Diamond and Related Materials, 20, 564 (2011)

Y. Zhang, [L. J. McKnight](#), Z. Tian, S. Calvez, E. Gu, M. D. Dawson

### **GaNNAs semiconductor disk lasers as pump sources for Tm<sup>3+</sup> (,Ho<sup>3+</sup> )-doped glass, crystal and fibre lasers**

Proceedings of SPIE, 7193, 719317 (2009)

S. L. Vetter; [L. J. McKnight](#); S. Calvez; M. D. Dawson; F. Fusari; A. A. Lagatsky; W. Sibbett; C. T. A. Brown; V. Korpijärvi; M. D. Guina; B. Richards; G. Jose; A. Jha

## d) Conference Presentations

### **Reconfigurable Integrated Optics: Diode-Laser induced waveguides for visible wavelengths in KYb(WO<sub>4</sub>)<sub>2</sub>**

European Conference on Integrated Optics, Sitges Barcelona, 18th Apr 2012, Poster

[L. J. McKnight](#), S. Calvez

### **Optimised GaN Directional Couplers with Mode Converters**

Frontiers in Optics, San Jose, 16th Oct 2011, Oral

[L. McKnight](#), Y. Zhang, I. M. Watson, E. Gu, S. Calvez, M. D. Dawson

### **Compact Large-Cross-Section GaN Directional Coupler**

IEEE Photonics, Virginia, 9th Oct 2011, Oral

Y. Zhang, [L. J. McKnight](#), I. M. Watson, E. Gu, S. Calvez and M. D. Dawson

### **GaN Waveguides: towards a New Platform for Integrated Quantum Photonics**

9th International Conference on Nitride Semiconductors, Glasgow, 10th Jul 2011, Poster

L. J. McKnight, Y. Zhang, I. M. Watson, E. Gu, S. Calvez, M. D. Dawson

### **Large cross-section diamond waveguides**

Diamond 2010, Budapest, 5th Sep 2010, Oral

Y. Zhang, L. J. McKnight, S. Calvez, E. Gu, and M. D. Dawson,

### **Gain-guided KYb(WO<sub>4</sub>)<sub>2</sub> Laser**

Europhoton, Hamburg, 29th Aug 2010, Poster

L. J. McKnight, S. Calvez

### **Large Cross-Section Diamond Waveguides**

Photon 2010, Southampton, 23rd Aug 2010, Oral

L. J. McKnight, Y. Zhang, Z. Tian, E. Gu, S. Calvez, M. D. Dawson

## **e) Symposia, Consortium Meetings and Student Conferences**

IONS (International OSA network of students) - 11, Paris, 22nd Feb 2012, Poster

UK Nitride Consortium Conference, Bath, 4th Jan 2012, Oral (best student talk)

IONS NA-3, Stanford, 13th Oct 2011, Poster

MUSIC Workshop, Next-generation of ultrafast lasers, Glasgow, 5th April 2011, Poster

IONS 9, Salamanca, 7th Apr 2011, Poster

SUZP - Scottish/Stanford University Partnership, St. Andrews, 28th Mar 2011, Poster

IONS 7, Galway, 4th Mar 2010, Oral

IONS 6, Glasgow, 9th July 2009, Poster

# Acknowledgements

---

To begin, I would like to give a special thanks to my supervisor Dr Stephane Calvez. He was there to offer assistance through all stages of this PhD for which he was engaged with genuine interest. He was there to discuss new and exciting ideas for many hours which I will always remember. His support as a supervisor and a friend will always be remembered. He has been an inspiration to pursue novel research without forgetting a solid foundation.

I would also like thank to Prof. Martin Dawson for letting me pursue this PhD and giving me support and direction throughout. He was the mastermind behind many of my projects and his experience and advice was much appreciated. He has taught me not to shy away from those challenging projects and his continued enthusiasm is inspiring.

I am very grateful to my collaborators in this project. Firstly Dr Yanfeng Zhang; her fabrication skills, dedication and friendly work attitude helped make this project a success. Dr Erdan Gu and Dr Ian Watson were able to offer fabrication and GaN advice throughout this project. A special thanks to Dr David Massoubre and Dr Benoit Guilhabert who were always available to try out those experimental fabrication ideas that, although this thesis did not have space to detail, were and will be a great help.

The laser specialists at the institute of photonics were always able to offer advice and support, thank you all. Dr Vasili Savitski, Dr Alan Kemp, Dr David Burns and Dr John-Mark Hopkins, Dr Nicolas Laurand and Dr Jennifer Hastie were always available for discussions.

A special note must go to the working attitude at the Institute of Photonics. Everyone was willing to offer technical advice and practical assistance. In particular the short loan of equipment between all groups allowed those unplanned experiments to go ahead... which is what a good research environment should allow for.

All the students during my time at the Institute of Photonics, many now finished their PhDs, were there not only in a work capacity but as friends each in their different way. My lab partner Sharon was able to show me some tricks in the lab and certainly made those long days of alignment more enjoyable. Jonathan, Peter S., Peter R., Antony, Rolf and David E. initiated me in the luxuries of Lord Todd's soup! More recently Caroline F., Gerald, Johannes, Brynmor, David G., Sean, Shuailong, Pengfei, Enyuan, Daniel, Ewan, Anne-Marie and Abigail have all supported me as friends. The people who started with me made the last four years in Glasgow most enjoyable; Daniele, Elliot, Yanfeng and Yujie. Caroline M. deserves a special mention, putting up with me from day one until those long evenings of writing in the end!

To my family and friends; you have always offered support. I am impressed you managed to locate the back page of my thesis.